Magneto-optical spectroscopy of *d*- and *f*-ferromagnetic materials: recent theoretical progress (Review Article)

V. N. Antonov, A. N. Yaresko, A. Ya. Perlov, and V. V. Nemoshkalenko

Institute of Metal Physics, 36 Vernadsky Street, 252142 Kiev, Ukraine

P. M. Oppeneer and H. Eschrig

Institute of Theoretical Physics, University of Technology, D-01062 Dresden, Germany

The current status of theoretical understanding of the optical and magneto-optical (MO) spectra of $3d$, $4f$ and $5f$ compounds is reviewed. Energy band theory based upon the local spin-density approximation (LSDA) describes the optical and MO spectra of transition metal compounds reasonably well. Examples which we examine in detail are XPt_3 compounds (with $X = 3d$ V, Cr, Mn, Fe, and Co) in the $AuCu_3$ structure, ternary Heusler alloys NiMnSb, PdMnSb, PtMnSb, and MnBi compound. The LSDA, which is capable of describing the spectra of transition-metal alloys with high accuracy, does not suffice for lanthanide compounds having a correlated $4f$ shell. A satisfactory description of the optical spectra could be obtained by using a generalization of the LSDA, in which explicitly f electron Coulomb correlations are taken into account (LSDA+U approach). As examples of this group we consider CeSb and CeBi. For CeSb a record Kerr angle of 90° was very recently reported, 90° is the absolute maximum value that can be measured. It is two orders of magnitude larger than the values that are commonly measured for transition-metal compounds, and about one order of magnitude larger than values maximally achieved for other lanthanide and actinide compounds. A third group consist of uranium $5f$ compounds. In those compounds where the $5f$ electrons are rather delocalized, the LSDA describes the MO spectra reasonably well. As examples of this group we consider UAsSe and URhAl. Particular difficulties occur for the uranium compounds where the $5f$ electrons are neither delocalized nor localized, but more or less semilocalized. Typical examples are US, USe and UTe. The semilocalized $5f$'s are, however, not inert, but their interaction with conduction electrons plays an important role. Recently achieved improvements for describing such compounds are discussed. © *1999 American Institute of Physics.* [S1063-777X(99)00106-1]

INTRODUCTION

It was first observed in 1877 by J. Kerr[1] that when linearly polarized light is reflected from a magnetic solid, its polarization plane becomes rotated over a small angle with respect to that of the incident light. This discovery has become known as the magneto-optical (MO) Kerr effect. The Kerr effect is closely related to other anomalous spectroscopic effects, like the Faraday effect and the circular dichroism. These effects all have in common that they are due to a different interaction of left- and right-hand circularly polarized light with a magnetic solid. The Kerr effect has now been known for more than a century, but it was only in recent times that it became the subject of intensive investigations. The reason for this recent development two-fold: first, the Kerr effect gained considerable interest due to modern data storage technology, because it can be used to «read» suitably stored magnetic information in an optical manner[2] and second, the Kerr effect has rapidly developed into an appealing spectroscopic tool in materials research. The technological research on the Kerr effect was initially motivated by the search for good magneto-optical materials that could

be used as information storage medium. In the sequence of this research, the Kerr spectra of many ferromagnetic materials were investigated. Over the years the Kerr spectra of many ferromagnetic materials have been investigated. An overview of the experimental data collected on the Kerr effect can be found in the review articles by Buschow,[3] Reim and Schoenes,[4] and Schoenes.[5] The quantum mechanical understanding of the Kerr effect began as early as 1932 when Hulme[6] proposed that the Kerr effect could be attributed to spin-orbit (SO) coupling (see, also Kittel[7]). The symmetry between left- and right-hand circularly polarized light is broken due to the SO coupling in a magnetic solid. This leads to different refractive indices for the two kinds of circularly polarized light, so that incident linearly polarized light is reflected with elliptical polarization, and the major elliptical axis is rotated by the so called Kerr angle from the original axis of linear polarization. The first systematic study of the frequency dependent Kerr and Faraday effects was developed by Argyres[8] and later Cooper presented a more general theory using some simplifying assumptions.[9] The very powerful linear response techniques of Kubo[11] gave general

formulas for the conductivity tensor which are being widely used now. A general theory of frequency dependent conductivity of ferromagnetic (FM) metals over a wide range of frequencies and temperatures was developed in 1968 by Kondorsky and Vediaev.[12]

The main problem afterward was the evaluation of the complicated formulas involving MO matrix elements using electronic states of the real FM system. With the tremendous increases in computational power and the concomitant progress in electronic structure methods the calculation of such matrix elements became possible, if not routine. Subsequently many earlier, simplified calculations have been shown to be inadequate, and only calculations from ''first-principles'' have provided, on the whole, a satisfactory description of the experimental results.[13] The existing difficulties stem either from problems using the local spin density approximation (LDA) to describe the electronic structure of FM materials containing highly correlated electrons, or simply from the difficulty of dealing with very complex crystal structures. For 15 years after the work of Wang and Callaway[13] there was a lull in MO calculations until MO effects were found to be important for magnetic recording and the computational resources had advanced. Different reliable numerical schemes for the calculation of optical matrix elements and the integration over the Brillouin zone have been implemented, giving essentially identical results.[14] Prototype studies have been performed using modern methods of band theory for Fe, Co and Ni. Following the calculations for the elemental $3d$ ferromagnets, a number of groups have evaluated the MO spectra for more interesting compounds[15–33] and multilayers.[34–40] While the calculations showed there is good agreement between theory and experiment in case of d-band magnetic materials, attempts to describe MO properties of materials using the same formalism failed to create a consistent physical picture. This has been attributed to the general failure of the LDA in describing the electronic structure of f-state materials ($4f$ especially). To overcome the LDA limitations to study MO spectra a so called E^3 correction for correlations was implemented but gave inconsistent results.[30] The more consistent LDA+U scheme has been used to describe the Kerr angle of CeSb.[31,32] Since then several papers implementing the LDA+U scheme for MO calculations have been published with for $4f$- and $5f$-materials.[20,28,30,32,33]

With the above as background, we have performed calculations to evaluate the MO properties for a number of $3d$, $4f$, and $5f$ FM materials. Besides the inherent interest in the materials studied, the use of similar methods to study materials with different degrees of localized electronic states helps to establish the limitations of the LDA approach and to identify where techniques like the LDA+U method are needed.

The paper is organized as follows. The theoretical framework is explained in Sec. 1. Section 2 presents the electronic structure and MO spectra of $3d$ transition metal compounds XPt$_3$ ($X=$ V, Cr, Mn, Fe and Co), Heusler alloys (NiMnSb, PdMnSb and PtMnSb) and MnBi compound calculated in the LDA. Section 3 devoted to MO properties and electronic structure of $4f$ compounds (CeSb and CeBi)

calculated in LDA and LDA+U approximations. Section 4 considers uranium compounds UAsSe, URhAl, US, USe and UTe. Finally, we present a Summary.

1. THEORETICAL FRAMEWORK

Using straightforward symmetry considerations it can be shown that all MO phenomena are caused by the symmetry reduction—compared to the paramagnetic state—caused by magnetic ordering.[41] Concerning optical properties this symmetry reduction only has consequences when SO coupling is considered in addition. To calculate MO properties one therefore has to account for magnetism and SO coupling at the same time when dealing with the electronic structure of the material considered. Performing corresponding band structure calculations it is normally sufficient to treat SO coupling in a perturbative way. A more rigorous scheme, however, is obtained by starting from the Dirac equation set up in the framework of relativistic spin density functional theory[42]:

$$[c\boldsymbol{\alpha}\cdot p + \beta mc^2 + IV + V_{sp}\beta\sigma_z]\psi_{n\mathbf{k}} = \varepsilon_{n\mathbf{k}}\psi_{n\mathbf{k}} \qquad (1)$$

with $V_{sp}(\mathbf{r})$ the spin-polarized part of the exchange-correlation potential corresponding to the z quantization axis. All other parts of the potential are contained in $V(\mathbf{r})$. The 4×4 matrices α, β and I are defined by

$$\alpha=\begin{pmatrix}0 & \sigma \\ \sigma & 0\end{pmatrix}, \quad \beta=\begin{pmatrix}1 & 0 \\ 0 & -1\end{pmatrix}, \quad I=\begin{pmatrix}1 & 0 \\ 0 & 1\end{pmatrix}, \qquad (2)$$

with σ the standard Pauli matrices, and 1 the 2×2 unit matrix.

There are quite a few band structure methods available now that are based on the above Dirac equation.[43] In the first scheme the basis functions are derived from the proper solution to the Dirac equation for the various single-site potentials.[44,45] In the second one, the basis functions are obtained initially by solving the Dirac equation without the spin-dependent term[46,47] and then this term is accounted for only in the variational step.[17,44] In spite of this approximation used, the second scheme nevertheless gives results in very good agreement with the first one,[43] while being very simple implemented. We also mention the quite popular technique when SO coupling is added variationally[46] after the scalar relativistic magnetic Hamiltonian has been constructed. In this case only the Pauli equation with SO coupling is being solved. All three techniques yield similar results.

In the polar geometry, where the z-axis is chosen to be perpendicular to the solid surface, and parallel to the magnetization direction, the expression for the Kerr angle can be obtained easily for small angles and is given by[4]

$$\theta_K(\omega) + i\varepsilon_K(\omega) = \frac{-\sigma_{xy}(\omega)}{\sigma_{xx}(\omega)[1 + (4\pi i/\omega)\sigma_{xx}(\omega)]^{1/2}}, \quad (3)$$

with θ_K the Kerr rotation and ε_K the so-called Kerr ellipticity. $\sigma_{\alpha\beta}$ ($\alpha,\beta\equiv x,y,z$) is the optical conductivity tensor, which is related to the dielectric tensor $\varepsilon_{\alpha\beta}$ through

$$\varepsilon_{\alpha\beta}(\omega) = \delta_{\alpha\beta} + \frac{4\pi i}{\omega}\sigma_{\alpha\beta}(\omega). \qquad (4)$$

The optical conductivity tensor, or equivalently, the dielectric tensor is the important spectral quantity needed for the evaluation of the Kerr effect.[5] The optical conductivity can be computed from the energy band-structure by means of the Kubo-Greenwood[11] linear-response expression[13]:

$$\sigma_{\alpha\beta}(\omega) = \frac{-ie^2}{m^2\hbar V_{uc}}$$

$$\times \sum_{\mathbf{k}} \sum_{nn'} \frac{f(\varepsilon_{n\mathbf{k}}) - f(\varepsilon_{n'\mathbf{k}})}{\omega_{nn'}(\mathbf{k})} \frac{\Pi_{n'n}^{\alpha}(\mathbf{k})\Pi_{nn'}^{\beta}(\mathbf{k})}{\omega - \omega_{nn'}(\mathbf{k}) + i\gamma} \quad (5)$$

with $f(\varepsilon_{n\mathbf{k}})$ the Fermi function, $\hbar\omega_{nn'}(\mathbf{k}) \equiv \varepsilon_{n\mathbf{k}} - \varepsilon_{n'\mathbf{k}}$, the energy difference of the Kohn-Sham energies $\varepsilon_{n\mathbf{k}}$, and γ is the lifetime parameter, which is included to describe the finite lifetime of excited Bloch electron states. The $\Pi_{nn'}^{\alpha}$ are the dipole optical transition matrix elements, which in a fully relativistic description are given by[49]

$$\Pi_{nn'}(\mathbf{k}) = m\langle\psi_{n\mathbf{k}}|c\,\alpha|\psi_{n'\mathbf{k}}\rangle \quad (6)$$

with $\psi_{n\mathbf{k}}$ the four-component Bloch electron wave-function.

Equation (5) for the conductivity contains a double sum over all energy bands, which naturally separates in the so called interband contribution, i.e., $n \neq n'$, and the intraband contribution, $n = n'$. The intraband contribution to the diagonal components of σ may be rewritten for zero temperature as

$$\sigma_{\alpha\alpha}(\omega) \equiv \frac{(\omega_{p,\alpha})^2}{4\pi} \frac{i}{\omega + i\gamma_D}, \quad (7)$$

with $\omega_{p,\alpha}$ the components of the plasma frequency, which are given by

$$(\omega_{p,\alpha})^2 \equiv \frac{4\pi e^2}{m^2 V_{uc}} \sum_{n\mathbf{k}} \delta(\varepsilon_{n\mathbf{k}} - E_F)|\Pi_{nn}^{\alpha}|^2, \quad (8)$$

and E_F is the Fermi energy. For cubic symmetry, we furthermore have $\omega_p^2 \equiv \omega_{p,x}^2 = \omega_{p,y}^2 = \omega_{p,z}^2$. Equation (7) is identical to the classical Drude result for the ac conductivity, with $\gamma_D = 1/\tau_D$, and τ_D the phenomenological Drude electron relaxation time. The intraband relaxation time parameter γ_D may be different from the interband relaxation time parameter γ. The latter can be frequency dependent,[48] and, because excited states always have a finite lifetime, will be non-zero, whereas γ_D will approach zero for very pure materials. Here we adopt the perfect crystal approximation, i.e., $\gamma_D \to 0$. For the interband relaxation parameter, on the other hand, we shall use, unless stated otherwise, $\gamma = 0.2\,\text{eV}$. This value has been found to be on average a good estimate of this phenomenological parameter. The contribution of interband transitions to the off-diagonal conductivity usually is not considered. Also we did not study the influence of local field effects on the MO properties.

We mention, lastly, that the Kramers-Kronig transformation has been used to calculate the dispersive parts of the optical conductivity from the absorptive parts.

The application of standard LDA methods to *f*-shell systems meets with problems in most cases, because of the correlated nature of the *f* electrons. To account better for the on-site *f*-electron correlations, we have adopted as a suitable

model Hamiltonian that of the LDA+U approach.[50] The main idea is the same as in the Anderson impurity model[51]: the separate treatment of localized *f*-electrons for which the Coulomb *f*-*f* interaction is taken into account by a Hubbard-type term in the Hamiltonian $\frac{1}{2}U\Sigma_{i\neq j}n_i n_j$ (n_j are *f*-orbital occupancies), and delocalized *s,p,d* electrons for which the local density approximation for the Coulomb interaction is regarded as sufficient.

Let us consider the *f* ion as an open system with a fluctuating number of *f* electrons. The formula for the Coulomb energy of *f*-*f* interactions as a function of the number of *f* electrons N given by the LDA is $E = UN(N-1)/2$. If we subtract this expression from the LDA total energy functional, add a Hubbard-like term and take into account the exchange interaction we obtain the following functional[50]:

$$E = E_{LDA} + \frac{1}{2}U\sum_{m,m',\sigma} n_{m\sigma}n_{m'-\sigma} + \frac{1}{2}(U-J)$$

$$\times \sum_{m\neq m',m',\sigma} n_{m\sigma}n_{m'\sigma} - \text{d.c.}, \quad (9)$$

where

$$\text{d.c.} = U\frac{N(N-1)}{2} - \frac{JN^{\uparrow}(N^{\uparrow}-1)}{2} - \frac{JN^{\downarrow}(N^{\downarrow}-1)}{2},$$

N is the total number of localized *f* electrons; $N^{\uparrow}$ and $N^{\downarrow}$ are the number of *f* electrons with spin-up and spin-down, respectively; U is the screened Coulomb parameter; J is the exchange parameter.

The orbital energies ε_i are derivatives of (9) with respect to orbital occupations n_i:

$$\varepsilon_i = \frac{\partial E}{\partial n_i} = E_{LDA} + (U-J)\left(\frac{1}{2} - n_i\right)$$

$$= E_{LDA} + U_{\text{eff}}\left(\frac{1}{2} - n_i\right). \quad (10)$$

This simple formula gives the shift of the LDA orbital energy $-U_{\text{eff}}/2$ for occupied *f* orbitals ($n_i = 1$) and $+U_{\text{eff}}/2$ for unoccupied *f* orbitals ($n_i = 0$). A similar formula is found for the orbital dependent potential $V_i(\mathbf{r}) = \delta E/\delta n_i(\mathbf{r})$, where variation is taken not on the total charge density $\rho(\mathbf{r})$ but on the charge density of a particular *i*th orbital $n_i(\mathbf{r})$:

$$V_i(\mathbf{r}) = V_{LDA}(\mathbf{r}) + U_{\text{eff}}\left(\frac{1}{2} - n_i\right). \quad (11)$$

The advantage of the LDA+U method is the ability to treat *simultaneously* delocalized conduction band electrons and localized 4*f*-electrons in the same computational scheme. With regard to these electronic structure calculations, we mention that the present approach is still essentially a single particle description, even though intraatomic 4*f*-Coulomb correlations are explicitly taken into account.

The LDA+U method has proven to be a very efficient and reliable tool in calculating the electronic structure of systems containing localized orbitals where the Coulomb interaction is much larger than the band width. It works not only for 4*f* orbitals of rare-earth ions, but also for such

systems as transition metal oxides, where localized $3d$ orbitals hybridize quite strongly with oxygen $2p$ orbitals (see review article Ref. 52). The LDA+U method was recently applied to heavy-fermion compounds YbPtBi[53] and Yb_4As_3[54] and it has also to explain the nature of colossal polar Kerr rotation of the maximal possible rotation of 90° in CeSb (Ref. 33).

We should also note that for large Kerr rotation, it is not possible to use the approximate expression (3) for the polar Kerr rotation. This equation is valid only for small θ_K, ε_K, and $|\varepsilon_{xy}| \ll |\varepsilon_{xx}|$. Instead one must use the exact expression

$$\frac{1+\tan\varepsilon_k}{1-\tan\varepsilon_K}e^{2i\theta_K} = \frac{1+n_+}{1-n_+}\frac{1-n_-}{1+n_-} \qquad (12)$$

with $n_\pm = (\varepsilon_{xx} \pm i\varepsilon_{xy})^{1/2}$, the complex indices of refraction. From Eq. 12 it can be seen that the maximal observable θ_K is $\pm 90°$.

2. 3d-TRANSITION-METAL COMPOUNDS

Transition-metal alloys consisting of a ferromagnetic $3d$ elements have drawn attention over the last years because of their good magneto-optical (MO) properties (see, e.g., Refs. 55–57). Especially multilayers of Co and Pt or Pd are at present intensively studied because of their potential application as optical storage material in MO storage devices[58–60] In addition to this, it has recently been discovered that the compound $MnPt_3$ exhibited a very large MO Kerr rotation, of about −1.2° at 1 eV photon energy.[61,62] This discovery indicates that the whole group of transition-metal-platinum alloys is exceptionally interesting within MO research, and also that large Kerr effects might still be found in materials which were previously not considered for their MO properties.

With the aim of undertaking a systematic investigation of the trends in transition-metal alloys, we study (in the present work) theoretically the MO Kerr spectra of the series XPt_3 compounds (with X= V, Cr, Mn, Fe, and Co), Heusler alloys (PtMnSb, PdMnSb and NiMnSb) and MnBi.

2.1. XPt_3 compounds (X= V, Cr, Mn, Fe, and Co)

The calculated polar Kerr spectra of VPt_3, $CrPt_3$, and $MnPt_3$ are shown in Fig. 1, and those of $FePt_3$ and $CoPt_3$ in Fig. 2. All Kerr spectra given in Figs. 1 and 2 pertain to the (001) magnetization direction, and are due to the interband optical conductivity tensor only, i.e., no free-electron contributions to the conductivity are considered. A Lorentzian broadening with a half width at a half maximum of 0.4 eV, taking account of the effects of finite lifetimes and of the experimental resolution, has been applied to all optical conductivity spectra. In Fig. 1, the recently measured Kerr spectra of $MnPt_3$ are also shown.[61] As one can see from Figs. 1 and 2, the Kerr spectra of VPt_3, $CrPt_3$, and $MnPt_3$ are very similar, as are those of $FePt_3$ and $CoPt_3$. This is the reason why we show the spectra in this combination together. The theoretical Kerr rotations of VPt_3, $CoPt_3$, and $MnPt_3$ have their minimum at the same photon energy of 0.8 eV, followed by a zero crossing at 2 eV. This similarity is partially observed in the Kerr ellipticity too. The Kerr rotations of
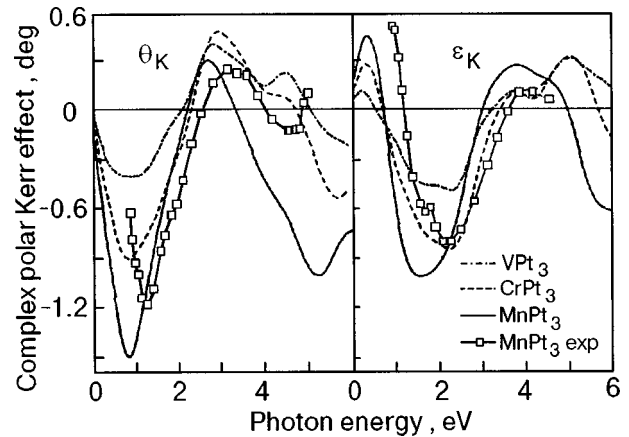

FIG. 1. Calculated polar Kerr rotation (θ_K) and Kerr ellipticity (e_K) spectra of VPt_3, $CrPt_3$, and $MnPt_3$ in the $AuCu_3$ crystal phase with (001) magnetization orientation. The theoretical spectra are all calculated with a relaxation-time broadening of 0.4 eV and result from the interband optical conductivity only. The experimental data shown are those of $MnPt_3$ (Ref. 61).

$FePt_3$ and $CoPt_3$, however, are distinctly different, as they have no zero crossing, and exhibit two minima, one smaller minimum at 1.3 eV, and a larger one at 4.7 eV. Noticeable further are the large Kerr rotations that are predicted by density-functional theory for these compounds. The largest Kerr rotation is found for $MnPt_3$ which reaches a value of −1.5° at 0.8 eV. But also the Kerr rotation of the $CrPt_3$ alloy as yet not investigated is surprisingly large, being with a peak value of −0.9° at 0.8 eV larger than that of the transition metals Fe and Co. Further the Kerr rotations predicted for $FePt_3$ and $CoPt_3$ are with peak values of −1.0° to −1.1° at 4.7 eV also substantial. (The term «peak» is used for a maximal Kerr rotation, irrespective of whether it is of positive or negative sign.) With respect to the magnitudes of the Kerr rotations displayed in Figs. 1 and 2, there are three points to be mentioned. First, the precise peak magnitude depends on the applied broadening parameter. A larger broadening than 0.4 eV would generally lead to slightly smaller, but broader spectral peaks. However, so far it is our experience that the broadening parameter of 0.4 eV gives a
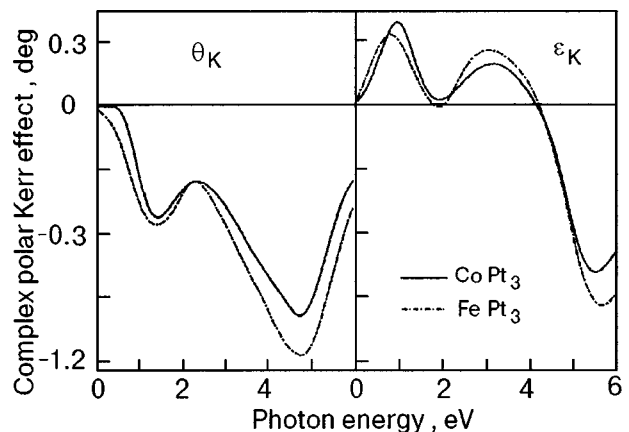

FIG. 2. As Fig. 1, but for the theoretical polar Kerr spectra of $FePt_3$ and $CoPt_3$.

physically adequate description.[21] Second, the neglect of an intraband contribution to the optical conductivity can play a role for VPt$_3$, CrPt$_3$, and MnPt$_3$. An intraband or free-electron contribution to the optical conductivity can be of importance for the Kerr rotation spectrum at small photon energies. As the main Kerr rotation peak of the compounds in Fig. 1 occurs at a small energy, the size of this peak will become reduced when a large intraband contribution is present. For CoPt$_3$ and FePt$_3$, the intraband contribution is less important, because these compounds already have a relatively small Kerr rotation at low energies (see Fig. 2). Third, it should be noted that the *ab initio* Kerr spectra are essentially calculated for zero temperature. If the Kerr spectra are measured at room temperature, where the magnetization is smaller, then the over-all size of the thus measured Kerr rotation will be smaller too. In Fig. 1 also the recently measured Kerr spectra of ordered MnPt$_3$ are shown.[61,62] These spectra were measured from an annealed thin film of MnPt$_3$ on a quartz substrate, but from the substrate side, i.e., through quartz.[61] This implies that these can be enhanced over the Kerr spectra measured in air by a factor of about one and a half. Within the limitations concerning the size of the Kerr rotation mentioned above, and the possible influence of the quartz substrate on the Kerr spectra, it can only be concluded that the shape of the theoretical and experimental Kerr rotation and ellipticity spectra are in good agreement as yet.

Density-functional theory predicts a large Kerr effect in the XPt$_3$ alloys. Noticeably, the Kerr rotations predicted are much larger than those calculated for, e.g., Fe, Co, or Ni, where the same broadening parameter of 0.4 eV was used. An important issue is therefore to identify the origin of the large Kerr effect in these compounds. To this end, we examine the dependence of the MO spectra on the exchange splitting, the SO interaction, and the optical transition matrix elements. As it can be expected that the Kerr effect in each of these compounds is of the same origin, we do this only for one compound, CrPt$_3$. The exchange splitting and the SO coupling are studied by scaling the corresponding terms in the Hamiltonian artificially with a constant prefactor. This is done in a non-self-consistent way, i.e., after self-consistency has been achieved, only one iteration is performed with the modified Hamiltonian (a self-consistent calculation would lead to a different band structure). From the resulting band structure the optical spectra are then computed. These modifications can in addition be done atom dependent, i.e., within each atomic sphere, so that we can investigate the separate effects of these quantities on Cr and on Pt. The outcomes of these model calculations for the Kerr rotation of CrPt$_3$ are shown in Fig. 3. In the upper panel, the importance of the exchange splitting is illustrated. When the exchange splitting on Pt is set to zero, the Kerr rotation remains as it is but when we do the same for the exchange splitting on Cr, the Kerr rotation totally vanishes. This implies that the exchange splitting due to Cr is crucial for the sizeable Kerr rotation, but that of Pt is unimportant. Furthermore, an enhancement of the exchange splitting on Cr by a factor of two (dashed line) leads to a much larger peak in the Kerr rotation. The middle panel in Fig. 3 shows the dependence on the SO
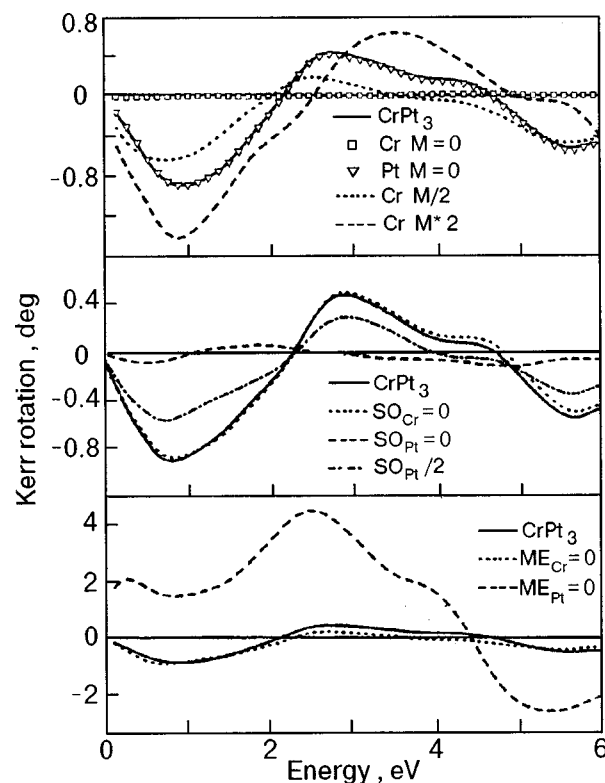

FIG. 3. Study of the influence of the exchange splitting (M), spin-orbit (SO) coupling, and optical transition matrix elements (ME) on the Kerr rotation of CrPt$_3$. The upper panel shows the effect of multiplying the spin-polarized part of the Dirac Hamiltonian with a constant factor, on the Cr site or on the Pt site. The middle panel shows the effect of multiplying the SO-coupling part of the Hamiltonian on Cr or on Pt with a constant prefactor (see text). The lower panel depicts the effect of setting the matrix elements on Cr or on Pt to zero.

coupling. If we set the SO coupling on Cr to zero, the Kerr rotation practically doesn't change (dotted line). On the other hand, when the SO coupling on Pt is zero, the Kerr rotation almost disappears (dashed line). Thus, the SO coupling of Pt is equally responsible for the large Kerr rotation as is the exchange splitting of Cr. An intermediate scaling of the SO coupling of Pt by a factor of 0.5 leads to an approximately half as large Kerr angle, thereby illustrating the almost linear dependence of the Kerr effect on the SO interaction of Pt in these compounds. The lower panel in Fig. 3, finally, displays the importance of the site-dependent matrix elements. Within an atomic sphere about one of the atomic positions, the optical transition matrix elements are set to zero. If this is done for the matrix elements on Cr, the Kerr rotation doesn't change much. But if the matrix elements on Pt vanish, a large impact on the Kerr rotation is found (dashed curve). This indicates that the matrix elements on the Pt site are more important for bringing about the large Kerr peak at 1 eV, than are those of Cr. Making the matrix elements zero gives only an impression of which site the main contribution comes from. To obtain information about the bands that are responsible for the Kerr peak, it is instructive to exclude a particular transition matrix element. Due to the selection rules for optical transitions, these transitions can only take place between band states with an angular momentum differ-
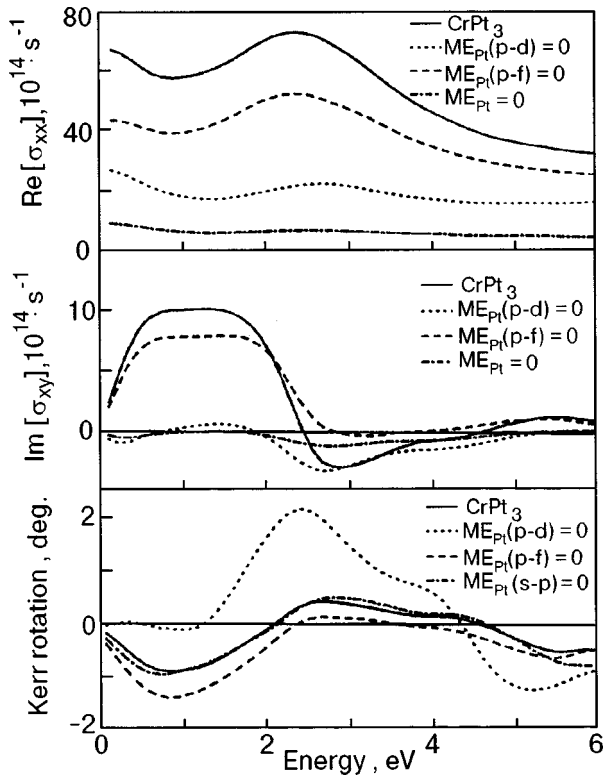
FIG. 4. Influence of the exclusion of various optical matrix elements on the Pt site on the real part of the diagonal optical conductivity ($[\mathrm{Re}|\sigma_{xx}]$), the imaginary part of the off-diagonal optical conductivity ($\mathrm{Im}[\sigma_{xy}]$) and Kerr rotation. The notation $ME_{Pt}(p-d)=0$ means that on the Pt site the p-d interband transitions and the d-p interband transitions are excluded from the optical matrix element.

ence of ± 1. By excluding for instance the p-d transition matrix element we can investigate the contribution of this type of transitions. However, as the transition matrix must be Hermitian, we have to exclude also the conjugated transition, i.e., both p-d and d-p transitions. The results of an investigation of the importance of the various transitions on Pt are shown in Fig. 4 for the real part of the diagonal optical conductivity, $\mathrm{Re}[\sigma_{xx}]$, the imaginary part of the off-diagonal conductivity, $\mathrm{Im}[\sigma_{xy}]$, and the Kerr rotation. The upper and middle panel in Fig. 4 show that both $\mathrm{Re}[\sigma_{xx}]$ and $\mathrm{Im}[\sigma_{xy}]$ are strongly reduced when the p-d and d-p interband transitions are excluded, more than when the d-f and f-d transitions are excluded. Especially the off-diagonal conductivity almost disappears in the energy region around 1 eV if the p-d and d-p transitions on the Pt sites are excluded. Because this peak in the off-diagonal conductivity at 1 eV is responsible for the peak in the Kerr rotation spectrum, this shows that the d-p and p-d transition matrix elements on Pt account for most of the Kerr effect in this frequency region. The other transitions, s-p and d-f, also have a minor influence, but excluding these still gives approximately the same Kerr rotation (see Fig. 4, lower panel). Thus, the d states of Pt, being subject to the strong SO interaction on the Pt site, contribute most to the optical transitions that lead to a large Kerr angle.

From these investigations the following picture of the Kerr effect in these compounds emerges: Pt is the magneto-

optically active element, and creates the large Kerr rotation through its large SO interaction. The important magneto-optical transitions are the p-d and d-p transitions on Pt. The $3d$ elements are magneto-optically not very active. Their role is to supply through their exchange splitting enough hybridized spin-split energy bands. This understanding suggests the following recipe for finding a material having a sizeable Kerr rotation: such material should contain elements with a large SO coupling, for instance Pt, Bi, or an actinide. Also should it contain an element having a sufficiently large magnetic moment, but this element needn't have a strong SO interaction, like for instance Mn. Also should there be a substantial hybridization between states of these two kinds of constituents. Elements having a large, but local atomic moment, like some of the $4f$-elements, are in the latter respect not suited, if the moment is due to unhybridized, localized $4f$-states.

The behavior of the peak magnitude in the Kerr rotation spectra with respect to the $3d$ element, as shown in Figs. 1 and 2, and also the dependence of the Kerr effect magnitude on the magnetization, can furthermore be understood on the basis of the model calculations. The increase of the peak in the Kerr angle at about 1 eV when going from VPt_3 to $MnPt_3$ (see Fig. 1) is caused by the corresponding increase in the exchange splitting. This is most clearly demonstrated by the scaling of the peak in the Kerr rotation of $CrPt_3$ with respect to the scaling of the exchange splitting (Fig. 3, upper panel). Also it can be understood from this behavior that a reduction of the magnetization at room temperature leads to a reduction of the Kerr rotation. This dependence on the magnetization also explains why the Kerr rotation of $FePt_3$ is larger than that of $CoPt_3$.

In concluding, we have further proven the important result that the total density of states cannot be used to derive information about the shape or magnitude of the Kerr spectra thereof. The dependence of the Kerr spectra in the XPt_3 compounds on the crystallographic direction of the magnetization is found to be very small. This finding corroborates with the high degree of isotropy of the $AuCu_3$ crystal structure. The agreement between the *ab initio* calculated Kerr spectra and the experimental result for $MnPt_3$ (Refs. 61 and 62) finally looks very promising. Further measurements on these compounds are desirable and needed, in order to obtain a complete picture of the correspondence between experimental and first-principles Kerr spectra.

2.2. Heusler alloys

The Heusler alloys NiMnSb, PdMnSb, and PtMnSb have been the subject of intensive experimental and theoretical investigations since the early 1980's.[55,63-65] The interest in these compounds arose first from the experimental discovery of an extremely large magneto-optical Kerr rotation of $-1.27°$ in PtMnSb at room temperature.[55] This value was for many years the record Kerr rotation observed in a transition metal compound at room temperature and therefore called ''gaint.'' Kerr effect (see, e.g., the recent surveys Refs. 3 and 5). Almost simultaneously with the experimental discovery, the theoretical finding of the so-called ''half-metallic'' na-

ture of PtMnSb was reported.[65] Half-metallicity means that according to (semirelativistic) bandstructure theory the material is metallic for majority, but insulating for minority spin electrons.[65] Such a gap for one spin type naturally may give rise to unusual magnetotransport and optical properties. Also the isoelectronic Heusler alloy NiMnSb was predicted to be half-metallic, whereas the isoelectronic compound PdMnSb was predicted not to be half-metallic.[65] The MO Kerr rotations in both NiMnSb and PdMnSb on the other hand, were experimentally found to be much smaller than that of PtMnSb, which resulted in a puzzling combination of features. Experimental efforts were undertaken to verify the proposed half-metallic character of NiMnSb and PtMnSb,[66–69] which was subsequently established in the case of NiMnSb.[66,69] Very recently, also experimental evidence in favor of half-metallicity in PtMnSb was reported.[70]

On the theoretical side, several model explanations of the MO spectra of the compounds were proposed.[71–73] One of those was based on a possible loss of the half-metallic character due to spin-orbit (SO) coupling which was suggested to lead to a symmetry breaking between the different m states of the Sb p bands in the vicinity of the Fermi energy E_F.[71] Another explanation was based on differences of the semirelativistic effects in NiMnSb and PtMnSb,[73] and another one on enhancement of the MO Kerr spectra near the plasma resonance.[72] While the proposed models contain interesting physical mechanisms themselves, one of the remaining major stumbling blocks was to explain the measured differences in the MO spectra of the isoelectronic NiMnSb, PdMnSb, and PtMnSb.

Only owing to the development of *ab initio* calculations of the MO spectra the detailed quantitative comparison between experiment and first-principles spectra became feasible.[15–17,74,75] The Heusler compounds are, of course, most attractive materials for *ab initio* calculations of their MO spectra on account of the mentioned unusual features. Several first-principles calculations for these compounds were reported very recently.[15,18,21,26,31] The various calculated MO Kerr spectra, however, spread rather widely. The origin of the differences in the spectra obtained in the various calculations traces back, first, to the fact that the MO Kerr effect is in calculations a tiny quantity, related to the difference of reflection of left- and right-hand circularly polarized light.[5] SO coupling in the presence of spontaneous magnetization is responsible for the symmetry breaking in the reflection of left- and right-hand circularly polarized light. Second, since the MO Kerr effect is only a tiny quantity in the first-principles calculations, numerical accuracy and the influence of approximations made in the evaluation gain an appreciable importance. For this reason, the evaluation of the MO Kerr spectra of the ferromagnetic $3d$ transition metals Fe, Co, and Ni have become bench mark test cases for MO calculation schemes.[16,17,75–79] Numerical accuracy plays normally not a decisive role if the physical mechanism is to be sought. However, it has been shown by several groups[16,75] that for the *ab initio* calculation of MO spectra an accurate evaluation of the dipole matrix elements is essential for obtaining numerically reliable MO Kerr spectra. Moreover, in the particular case of the Heusler alloys, the
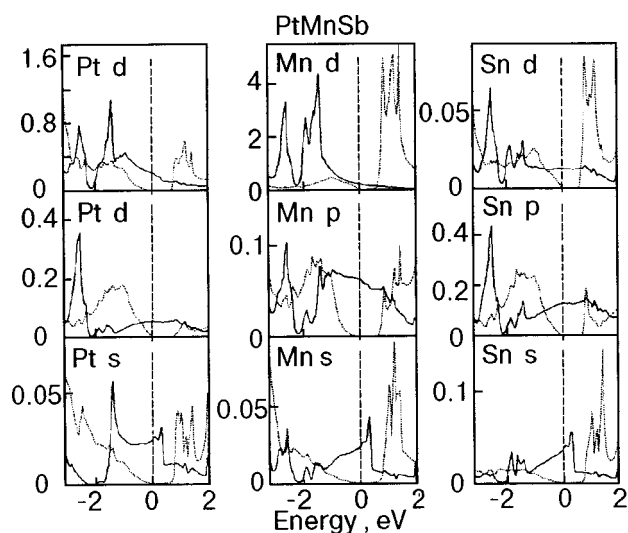

FIG. 5. Spin-projected, partial densities of state calculated for PtMnSb. Majority spin densities are given by the full curves, minority spin densities by the dotted curves. The half-metallic behavior can be seen from the band gap at the Fermi level, which is present for minority spin, but not for majority spin.

half-metallic band gap depends sensitively on technicalities of the band structure calculation, as, e.g., atomic sphere radii.[21]

In the present work we report a detailed investigation of the MO Kerr spectra of NiMnSb, PdMnSb, and PtMnSp.[26]

Figure 5 shows the spin projected, fully relativistic partial densities of states of PtMnSb. As can be recognized from Fig. 5, the partial densities of states for minority spin have evidently a gap at the Fermi level. A similar behavior we have found for NiMnSb, but, of course, not for PdMnSb. For all three Heusler compounds we show the calculated relativistic energy bands and total densities of state (DOS) in Fig. 6. In the case of PdMnSb, three spin-orbit split energy bands are just above the Fermi level at the Γ-point, therefore half-metallic behavior is not supported for PdMnSb by band-structure theory. In the case of NiMnSb and PtMnSb, these important bands are just below E_F, rendering the half-metallicity in these compounds. Our bandstructure results are in agreement with recent experiments on NiMnSb and PtMnSb, in which half-metallic behavior to a degree of nearly 100% was observed.[66,69,70]

After having verified the half-metallic bandstructure property we turn to the magneto-optical spectra. In Fig. 7 we show the calculated and experimental[55,64] MO Kerr spectra of the three isoelectronic Heusler compounds. There exists apparently a rather good agreement between the experimental Kerr spectra and the *ab initio* calculated ones. Overall, the experimental features are reasonably well reproduced, except for the magnitude of the Kerr rotation of PdMnSb, for which theory predicts larger values than are experimentally observed. The first and important conclusion which we draw from the correspondence between experimental and calculated Kerr spectra is: *the anomalous behavior of the MO Kerr spectra in these compounds is well described by normal bandstructure theory*. While the calculated MO Kerr spectra of these three Heusler compounds were recently shown in a
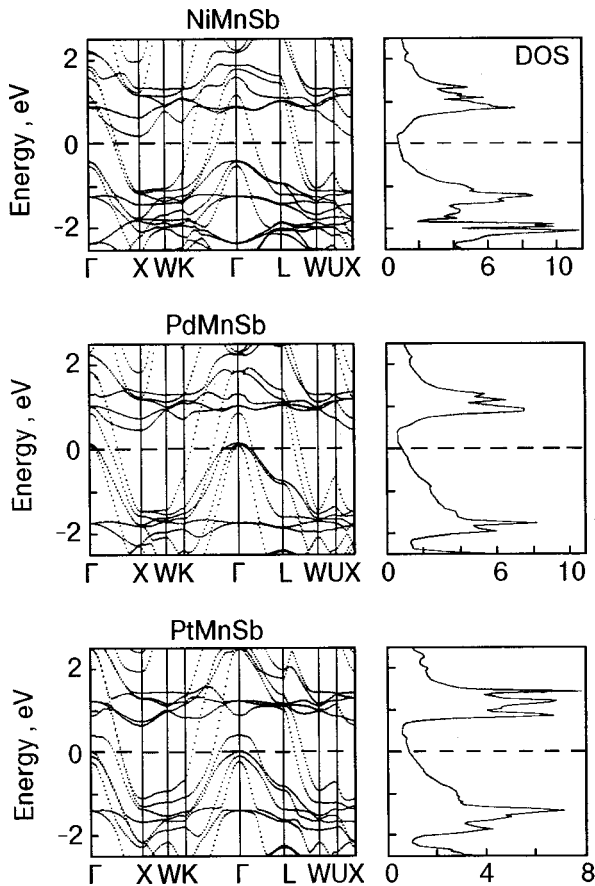
FIG. 6. Relativistic, spin polarized energy bandstructures and total densities of state (DOS) of NiMnSb, PdMnSb, and PtMnSb.

FIG. 7. Calculated and experimental Kerr rotation (θ_K) and Kerr ellipticity (ε_K) spectra of the Heusler compounds NiMnSb, PdMnSb, and PtMnSb. The experimental data are those of Refs. 55 and 64.

review paper,[18] an explanation in detail of the origin of the depicted spectra has not yet been given we shall give it in the following.

To investigate the origin of the Kerr spectra, we consider the separate contributions of both the numerator of Eq. (3), i.e., $\sigma_{xy}(\omega)$ and the denominator, $D(\omega) = \sigma_{xx}(1 + \sigma_{xx} 4\pi i/\omega)^{1/2}$. In Fig. 8 we show how the separate contributions of numerator and denominator bring about the Kerr angle of NiMnSb. The imaginary part of the inverse denominator (times the photon frequency), $\text{Im}[\omega D]^{-1}$, displays a typical resonance structure at about 1 eV. The imaginary part of $\omega\sigma_{xy}$, i.e., $\omega\sigma_{xy}^{(2)}$ displays a double peak structure. The double peak structure of the Kerr rotation results roughly as the product of $\text{Im}[\omega D]^{-1}$ and $\omega\sigma_{xy}^{(2)}$. The first peak in the Kerr rotation at 1.5 eV is predominantly caused by a minimum of the denominator, whereas the second peak in the Kerr rotation at 4 eV is due to a maximum in the off-diagonal conductivity, $\omega\sigma_{xy}^{(2)}$. The nature of the peak in $\text{Im}[\omega D]^{-1}$ can be understand from the top panel in Fig. 8, where the complex diagonal dielectric function is shown: its real part, $\varepsilon_{xx}^{(1)}$, becomes small at about 1 eV, and its imaginary part, $\varepsilon_{xx}^{(2)}$, has a shallow minimum at 1 eV. The second peak in the Kerr rotation, stems from the maximum in $\omega\sigma_{xy}^{(2)}$, which in turn is known to be due to the interplay of SO coupling and spin polarization.[8,18] Thus, the two similar looking peaks in the Kerr rotation arise in fact from quite a different origin.
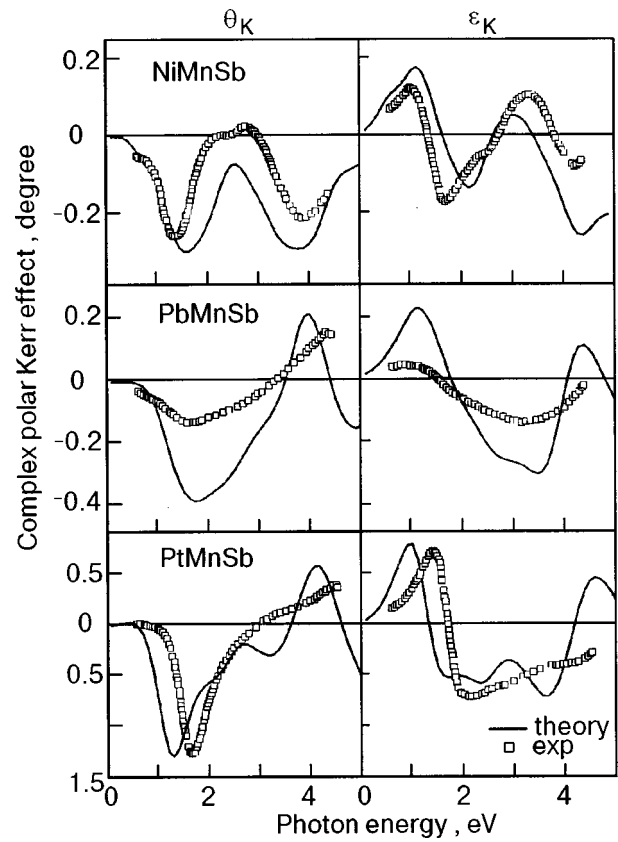
Next, we consider the spectra for the compound PdMnSb in more detail, which are shown in Fig. 9. In this compound $\omega\sigma_{xy}^{(2)}$ is larger than that of NiMnSb in the energy range 1–4 eV. This is simply due to the larger SO interaction on Pd as compared to that on Ni. The inverse denominator $\text{Im}[\omega D]^{-1}$, however, does not exhibit such a strong resonance as it does for NiMnSb. The latter is related to the particular shape of the $\varepsilon_{xx}^{(1)}$ and $\varepsilon_{xx}^{(2)}$ spectra. The Kerr rotation in effect displays the same shape as $\omega\sigma_{xy}^{(2)}$, being enhanced at 1–2 eV by the contribution from the denominator.

In Fig. 10 we show the spectral quantities for PtMnSb. The inverse denominator $\text{Im}[\omega D]^{-1}$ again displays for PtMnSb a strong resonance at 1 eV, which is even larger than that for NiMnSb. In addition, the off-diagonal conductivity $\omega\sigma_{xy}^{(2)}$ is for PtMnSb again larger than that of PdMnSb, in accordance with the larger SO coupling on Pt. The resulting Kerr rotation has a «giant» peak of −1.2° up to −2.0° depending on the applied lifetime parameter (see Fig. 10). These values are in good agreement with the available experimental Kerr peak values for PtMnSb, which range from about −1° to −2° depending on sample preparation and surface quality.[55,80–88] Careful investigations of the consequences of sample preparation have been performed by Takanashi *et al.*[83] and Sato *et al.*[87,88] These investigations showed that annealing of the PtMnSb sample rises the Kerr angle to a maximum value of −2°, whereas the nonannealed Kerr angle is only −1.2°. The off-diagonal conductivity
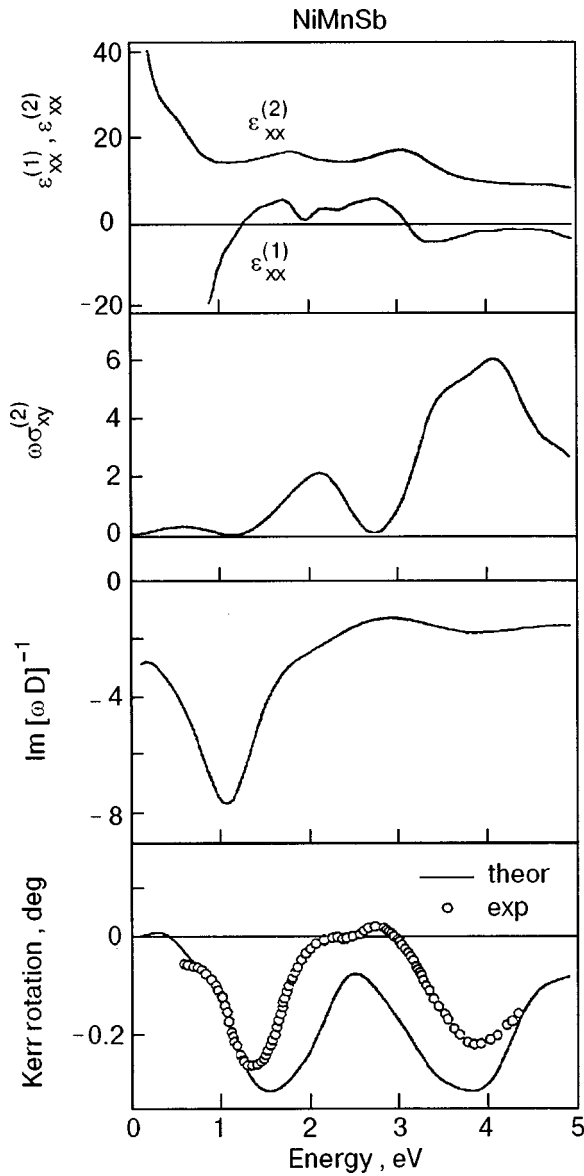
FIG. 8. Decomposition of the Kerr rotation spectrum of NiMnSb in separate contributions. Top panel: calculated real and imaginary part of the diagonal dielectric function, $\varepsilon_{xx}^{(1)}$ and $\varepsilon_{xx}^{(2)}$, respectively. Third panel from the top: the imaginary part of $[\omega D]^{-1}$ which results from $\varepsilon_{xx}^{(1)}$ and $\varepsilon_{xx}^{(2)}$. Bottom panel: the Kerr rotation which results as a combination of $\text{Im}[\omega D]^{-1}$ and $\omega\sigma_{xy}^{(2)}$ (second panel from the top). The experimental Kerr angle spectrum is after van Engen *et al.*[55]

FIG. 9. As Fig. 8, but for PdMnSb.

$\omega\sigma_{xy}^{(2)}$ was found to be rather insensitive to annealing (see Fig. 10).[87,88] The main impact of annealing thus evidently occurs in the denominator. The reason for the calculated resonance in the inverse denominator lies again in the frequency dependence of the diagonal dielectric function, which is shown in the top panel of Fig. 10. The calculated ε_{xx} compares reasonably well with the experimental one,[88] except for the important first root frequency of $\varepsilon_{xx}^{(1)}$ which is shifted by about 0.5 eV. This difference leads to a shifted position in the resonance peak of $\text{Im}[\omega D]^{-1}$, which in turn results in a shifted main Kerr rotation peak of just the same amount. The position of the maximum in $\text{Im}[\omega D]^{-1}$ thus predominantly determines the position of the main Kerr rotation peak. We mention in addition that the second maxi-
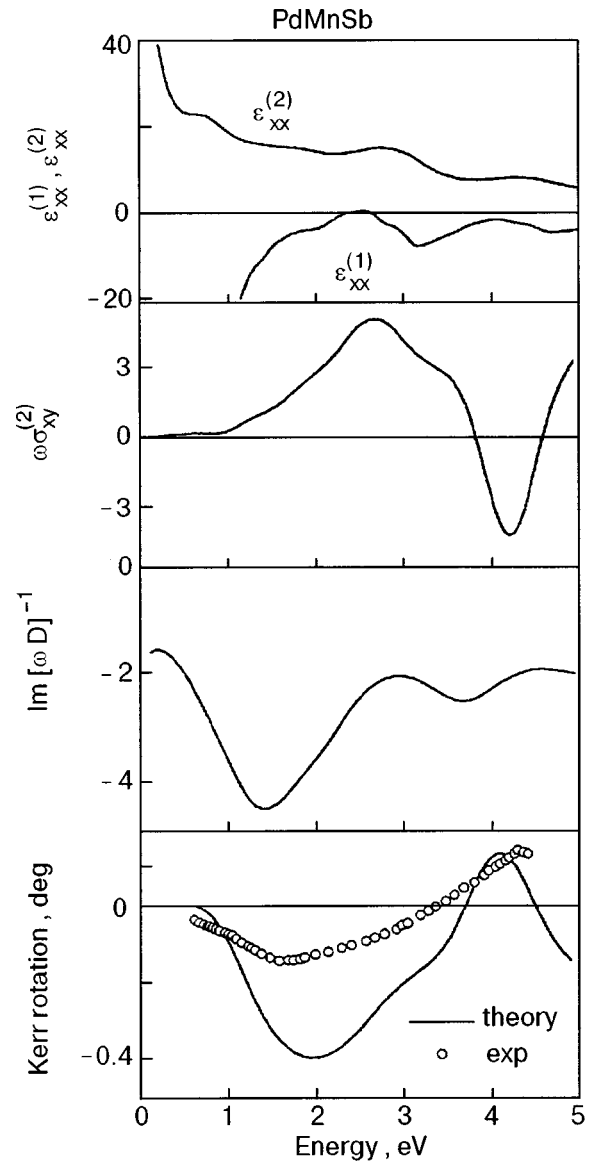
mum in the calculated $\omega\sigma_{xy}^{(2)}$ at 4.4 eV (see Fig. 10) is also present in the experimental spectrum, but at a higher energy of 5.2 eV.[88]

The origin of the giant Kerr angle in PtMnSb as compared to the Kerr angles in NiMnSb and PdMnSb can completely be understood from our calculations. First, in these three compounds the off-diagonal conductivities $\sigma_{xy}(\omega)$ are quite different, what is a direct result of the different relativistic electronic structure. Although both NiMnSb and PtMnSb are half-metallic, their $\omega\sigma_{xy}^{(2)}$ spectra are distinctly different, while on the other hand the $\omega\sigma_{xy}^{(2)}$ of PdMnSb and PtMnsb have a similar structure, but not a similar magnitude (see Figs. 8–10). Second, there is the influence of the denominators as exemplified in $\text{Im}[\omega D]^{-1}$. These are similar in shape and magnitude for NiMnSb and PtMnSb, but the magnitude of $\text{Im}[\omega D]^{-1}$ in PdMnSb is about a factor of two smaller. We find that this difference relates to the half-metallic nature of both NiMnSb and PtMnSb, which is not present for PdMnSb. From Fig. 6 it can be seen that for the
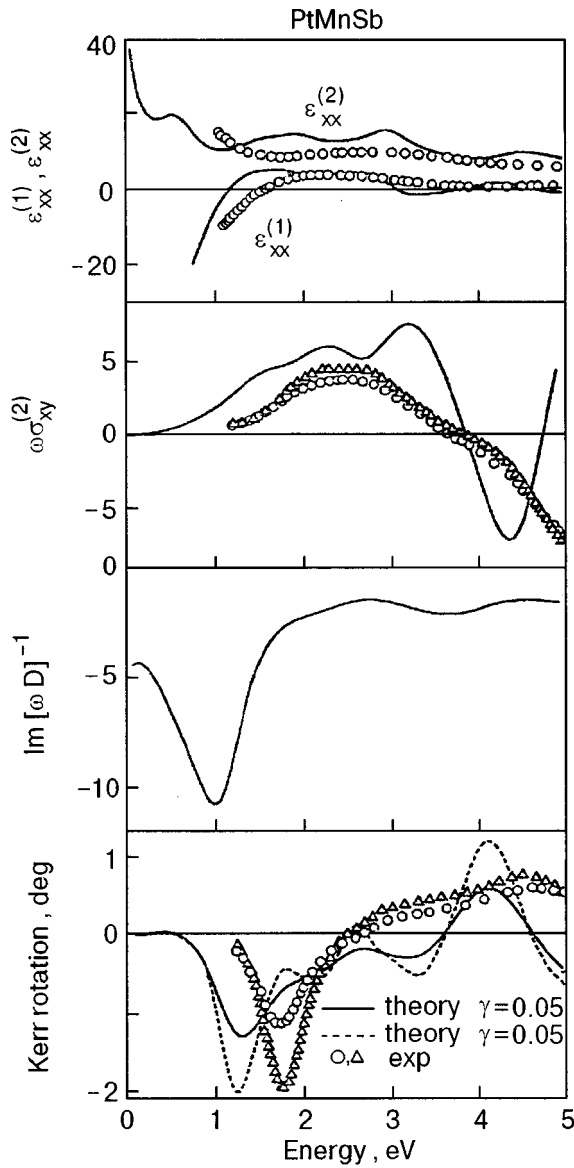
FIG. 10. As Fig. 8, but for PtMnSb. The experimental data are after Ikekame *et al.*[88] The data for annealed PtMnSb are denoted by △, and those for non-annealed, polished PtMnSb by ○. The calculated Kerr rotation spectrum is shown for two interband lifetime parameters, $\gamma = 0.05$ Ry and $\gamma = 0.02$ Ry.
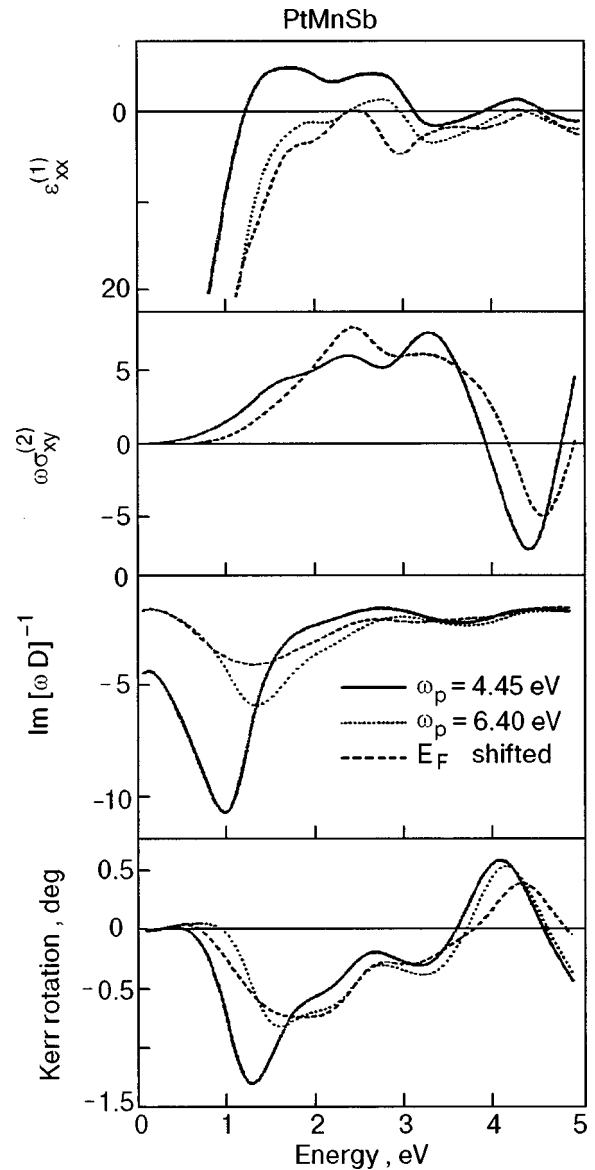
FIG. 11. Model investigation of the influence of the half-metallic character of PtMnSb on the optical and MO spectra. A non-half-metallic bandstructure has been modeled in two ways: by artificially shifting E_F in PtMnSb down, and by increasing the calculated plasma frequency $\omega_F = 4.45$ eV to 6.40 eV.

half-metallic compounds there are three lesser bands at E_F. One consequence is therefore that the intraband contribution to σ_{xx} will be smaller (see Eq. (8)). In Fig. 11 we show the impact of the half-metallic character of the bandstructure on the Kerr rotation of PtMnSb. The calculated plasma frequency in PtMnSb is small, $\hbar\omega_p = 4.45$ eV. Experimentally a somewhat bigger plasma frequency of (6.1 ± 0.4) eV was found for PtMnSb, and a smaller $\hbar\omega_p = (4.9 \pm 0.2)$ eV for NiMnSb.[89] One should, however, not forget that the sample purity can affect the plasma frequency through the position of E_F. To investigate the influence of the half-metallicity, we can artificially shift the Fermi energy down, and calculate the spectra for this position of E_F or we can leave E_F as it is and model a non-half-metallic bandstructure by adopting a larger ω_p. Both ways to mimic non-half-metallicity have a drastic impact on the resulting Kerr rotation, which becomes

reduced by a factor 2! As can be seen from the top panel in Fig. 11, in the absence of half-metallicity the shape of $\varepsilon_{xx}^{(1)}$ changes and resembles closely that of PdMnSb (see Fig. 9). This is especially so for the model where E_F is shifted, since this leads to the smaller $\mathrm{Im}[\omega D]^{-1}$ and also to a reduction of $\omega\sigma_{xy}^{(2)}$ at photon energies below 2 eV. The later is due to the exclusion of optical transitions from the SO split bands just below E_F. The consequence of both models for non-half-metallic behavior is that the maximum in $\mathrm{Im}[\omega D]^{-1}$ becomes about two times smaller. The Kerr angles derived in these models resemble now that of PdMnSb in shape, but are bigger, because $\omega\sigma_{xy}^{(2)}$ is larger than that of PdMnSb. Previously we have shown that if the SO coupling on Pt in PtMnSb is artificially set to zero, the Kerr rotation peak in PtMnSb becomes reduced by a factor of three.[21] We mention with respect to the influence of the denominator on the Kerr rotation
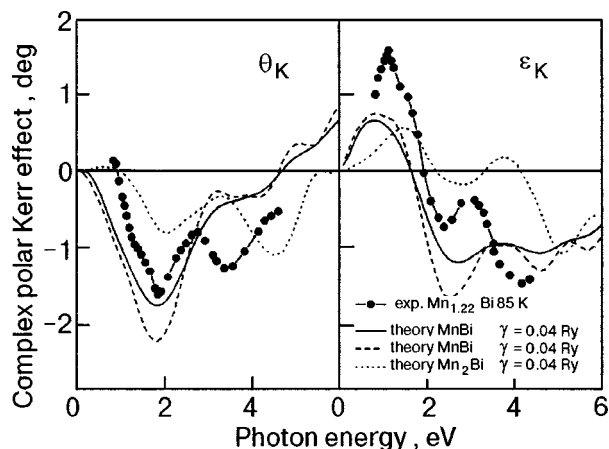
FIG. 12. Calculated and experimental Kerr spectra of Mn–Bi compounds. The Kerr rotation is denoted by θ_K, and the Kerr ellipticity by ε_K. The theoretical spectra are calculated for MnBi in the NiAs structure, for two lifetime broadenings, and for hypothetical Mn_2Bi in the Heusler C_{1b} structure. The experimental Kerr spectra were measured at 85 K on a $Mn_{1.22}Bi$ film.[90]

in PtMnSb, that experiments in which the stoichiometry and crystalline sample quality were varied also concluded that the denominator contributed appreciably to the giant Kerr rotation.[83,85–88]

In conclusion, we find that the Kerr spectra of NiMnSb, PdMnSb, and PtMnSb can be fully understood from their electronic structure. The puzzling anomalies in the Kerr spectra of these compounds arise from an interplay of compound related differences in the SO interaction, in the half-metallic character, and also in relative positions of energy bands.

2.3. MnBi

Although the MO Kerr effect in MnBi was measured already about twenty years ago, only very recently a thorough investigation of the spectral dependency of the Kerr effect under variation of the Mn-Bi composition.[90] These experimental Kerr spectra obtained at 85 K as well as the calculated ones are shown in Fig. 12. First-principles theory predicts a very large Kerr rotation in MnBi of about $-1.17°$ at 1.8 eV,[24] which is even larger than the measured peak value of $-1.6°$.[90] The lifetime broadening parameter γ used was 0.04 Ry (i.e., γ is the half-width at half maximum of a Lorentzian). However, we wish to point out that a smaller (but still reasonable) relaxation time broadening of 0.02 Ry would already result in a theoretical peak value of $-2.22°$. Therefore, according to theory, a larger Kerr effect than measured as yet should be possible. Experiment shows a second maximum in the Kerr angle at 3.4 eV, where theory only gives a smaller shoulder. A tentative explanation of this difference might be the sample composition, which is in experiment $Mn_{1.22}Bi$.[90,91] There is thus an excess of Mn in the sample. To examine the changes caused by the excess of Mn we performed test calculations for a hypothetical Mn_2Bi compound in the Heusler C_{1b} structure (i.e., MnMnBi), where each Mn atom is tetragonally surrounded by Bi. In the (111) direction this compound has a trigonal symmetry, like

the (0001) NiAs phase. The calculated Kerr spectra of Mn_2Bi are also shown in Fig. 12 (dotted curve). In its Kerr rotation there is a peak at about 4.3 eV and a smaller one at 2 eV, which is at the same position as the main peak of MnBi. As Mn_2Bi in this structure is only a hypothetical compound, we have used a guessed lattice constant. The position of the peak at about 4 eV is rather sensitive to the lattice constant value. Thus, if the stoichiometry shifts from MnBi to Mn_2Bi there appears to be a tendency to reduce the first peak at 1.8 eV and to enhance the peak at about 3.5 eV. This corresponds exactly to what is seen in the experimental Kerr spectrum of composition $Mn_{1.22}Bi$. Other recent experiments on MnBi samples with an almost 2:1 Mn-Bi ratio confirm the trend of an increased Kerr rotation above 3 eV.[92]

A further feature of the experimental Kerr rotation is that it exhibits a sign reversal at 0.9 eV. This sign reversal is actually also given by theory, but only for a smaller broadening parameter. This is consistent with the observation that experimentally it disappears in the room-temperature Kerr rotation.[90,93] Lastly, we mention that there appears to be a substantial intraband contribution to the conductivity present in the sample. In the calculations shown in Fig. 12 we accounted for the intraband conductivity by adding a Drude-type conductivity to the calculated interband conductivity. For this Drude conductivity we used the calculated plasma frequency and an estimated Drude broadening parameter (which is $\omega_p = 0.26$ Ry and $\gamma_D = 0.02$ Ry for MnBi). But, as adding a Drude conductivity shifts especially the Kerr ellipticity below 3 eV upwards, we would judge that in the sample there is likely a larger intraband contribution to the conductivity. This can be due to some disorder and the Mn-Bi stoichiometry.

The Kerr spectra depend on the MO conductivity spectra in an entangled way, so that it is difficult to assign features in the Kerr spectra to particular band transitions. The absorptive parts of the optical conductivity, $\sigma_{xx}^{(1)}$ and $\sigma_{xy}^{(2)}$, however, relate directly to the interband optical transitions, and provide therefore more physical insight. These absorptive parts of the conductivity tensor are shown for MnBi and Mn_2Bi in Fig. 13. The main peak in the Kerr rotation of MnBi is due to the maximum in $\sigma_{xy}^{(2)}(\omega)$ at 2 eV. Several kinds of dipolar optical transitions contribute to the broad structure in $\sigma_{xx}^{(1)}$. The main contributions originate from $p-d$ and $d-p$ transitions. The peak in $\sigma_{xy}^{(2)}$ is, however, mainly due to transitions from Bi p-like states.

As a first result, we conclude that first-principles electronic structure calculations give a satisfactory description of the giant Kerr rotation in MnBi. The difference between the experimental and *ab initio* Kerr rotation at 3.4 eV is anticipated to be related to the stoichiometry of the sample.

From these investigations the following picture of the Kerr effect in MnBi emerges: manganese has the required big magnetic moment of $3.71\mu_B$, while Bi has a small induced moment of $-0.10\mu_B$. In an applied field the small moment on Bi shifts to Mn (with sign reversed), so that then the total calculated moment compares well with the moment obtained from the saturation magnetization of $(3.84 \pm 0.03)\mu_B$.[94] Thus, in the interplay of exchange splitting
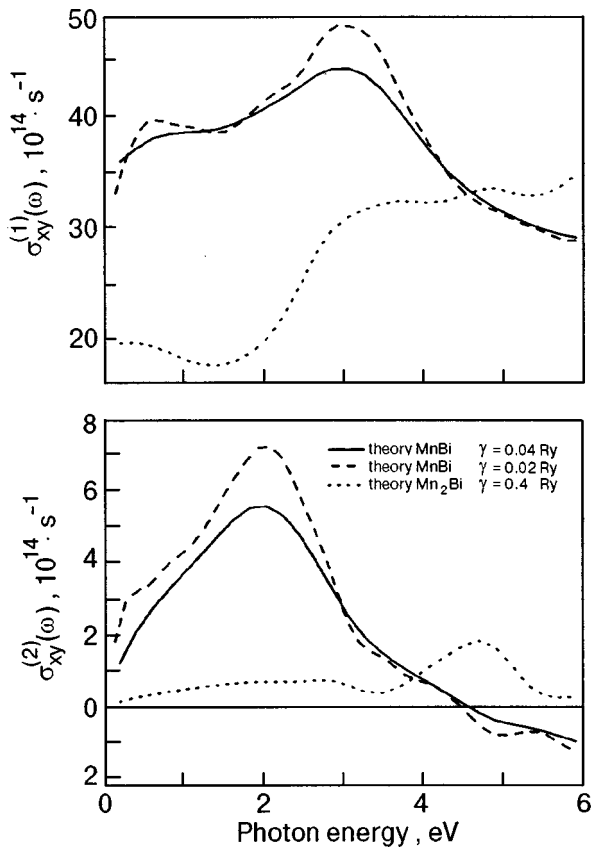
FIG. 13. Calculated absorptive parts of the optical conductivity, $\sigma_{xx}^{(1)}$ and $\sigma_{xy}^{(2)}$, for MnBi and Mn$_2$Bi.

FIG. 14. Partial densities of states for MnBi, in units of states/(atom-eV).

and spin-orbit coupling leading to the record Kerr effect, Mn brings in the exchange splitting and Bi the spin-orbit coupling. The degree of hybridization between Mn and Bi, furthermore, can be recognized from the partial densities of states, which are shown in Fig. 14. There is a strong hybridization between the Bi and Mn *p*-type states as well as Bi and Mn *d*-type states, as can be seen from the identical shape of the partial densities. The magneto-optically active transitions take place mainly on Bi, from occupied *p*- to unoccupied *d*-states, in the spin-down bands (dotted curves). It is worthwhile to consider also the partial densities of states of Mn$_2$Bi, which are shown in Fig. 15. For this compound the Bi *p*-states are shifted down and are higher in density, and the hybridization is also large. As a result, the Kerr rotation at 4 eV becomes bigger. In contrast to MnBi, Mn$_2$Bi has its Fermi energy right at a maximum in the partial density of states, which suggests that this hypothetical compound will be unstable.

3. LOCALIZED *f* ELECTRONS: THE CASE OF CeSb AND CeBi

Rare-earth compounds and alloys exhibit a great variety of unusual properties. Among them one finds heavy-fermion systems, intermediate valence compounds, Kondo metals, and Kondo insulators. To understand the physical properties of these materials correctly, it is necessary to investigate their electronic structure in detail. In this light, optical and MO spectroscopy has proven to be an extremely useful tool
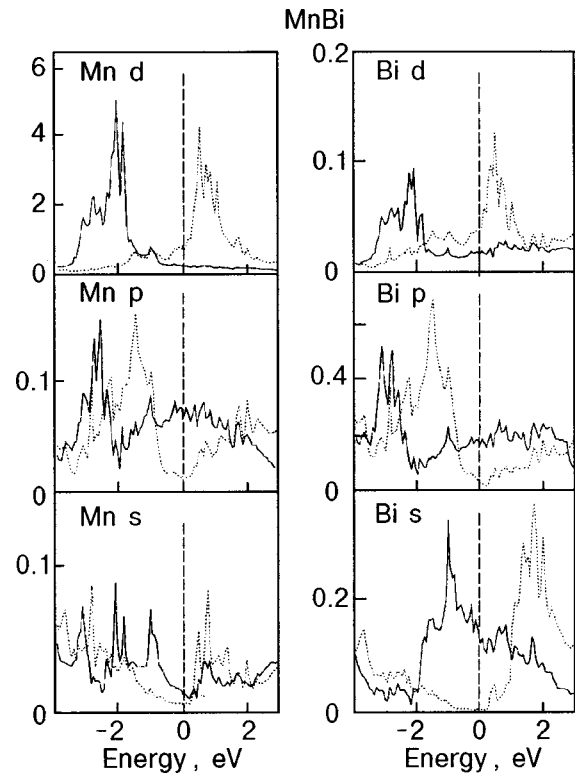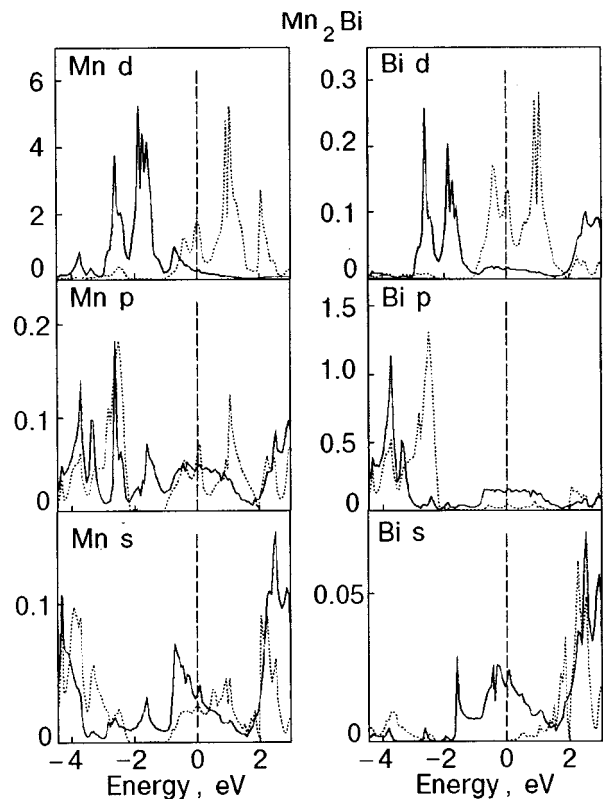

FIG. 15. As Fig. 14, but for Mn$_2$Bi.

for the study of the f states in rare-earth and actinide compounds.[4] Over last decade the MO properties of rare earth compounds have attracted large interest,[4] which increased after the discovery of the maximal observable rotation of 90° in CeSb by Pittini *et al.*[96] The majority of MO investigations deal with compounds and alloys of the light rare earth ions Ce^{3+} and Nd^{3+}, the half-filled shell ion Eu^{2+} and the heavy rare earths Tm^{2+} and Yb^{3+}. As with most lanthanides, cerium and neodymium form face centered cubic (FCC) rock-salt type binary chalcogenides with the VIA elements of the periodic table of the elements (S, Se, Te) and FCC poictides with the VA elements (N, P, As, Sb, Bi).[95] With the exception of the nitrides, all cerium and neodymium chalcogenides and pnictides order antiferromagnetically in zero magnetic field. CeN is disordered down to 1.5 K, while NdN orders ferromagnetically.[4] The MO properties of cerium chalcogenides are well investigated experimentally,[4,96,97] and also theoretically.[15,31,33]

For CeSb a record Kerr angle of 90° was very recently reported,[96] 90° is the absolute maximum value that can be measured. It is two orders of magnitude larger than the values that are commonly measured for transition-metal compounds, and about one order of magnitude larger than values maximally achieved for other lanthanide and actinide compounds.[4] To investigate the nature of a record polar Kerr rotation in CeSb, we have performed *ab initio* calculations of the optical spectra using the LDA and LDA+U approaches, with $U = 6$ eV.[33] In Fig. 16 we show theoretical and experimental results for the real part of σ_{xx} for CeSb, CeTe and CeSe. From Fig. 16 it can be seen that for CeSe and CeTe the inclusion of the Coulomb interaction U leads to a substantial improvement over the LDA result. The erroneous peak at 1.5 eV in the LDA spectra, which is due to an unphysical $4f$ band resonance near E_F, disappears in LDA+U spectra. Due to the Coulomb correlation, the occupied $4f^1$-levels are placed about 3–4 eV below E_F. In Fig. 17 we show the experimental[98] and LDA+U results for Kerr spectra of CeSe and CeTe. The results of the LDA approach are not shown here, but we mention that these do not by far reproduce the experimental data as good as LDA+U approaches.[33] The main peak in the Kerr rotation spectra in Fig. 17 is not found to be due to optical transitions stemming directly from the nearly localized $4f^1$-level. Instead, these peaks are due to a plasma minimum in the denominator of Eq. (3) and non-zero σ_{xy}, as will be discussed for CeSb below.

The LDA+U results for the Kerr spectra of CeSb are shown in Fig. 18. There is a giant Kerr rotation of 60° which is less than the observed value of 90°. Pittini *et al.*[96] observed that the maximum Kerr rotation depended on the magnetization and that therefore the intrinsic quantum state played an important role. In addition, the record Kerr effect occurs close to a plasma minimum. Both observations agree with what we find in our calculations. The denominator of Eq. (3) nearly vanishes due to the particular frequency dependence of σ_{xx}. A small denominator is not sufficient for obtaining a large Kerr rotation. Also σ_{xy}, which relates to the magnetic polarization, is important. The $4f^1$-level in CeSb is a completely spin and orbitally polarized state,
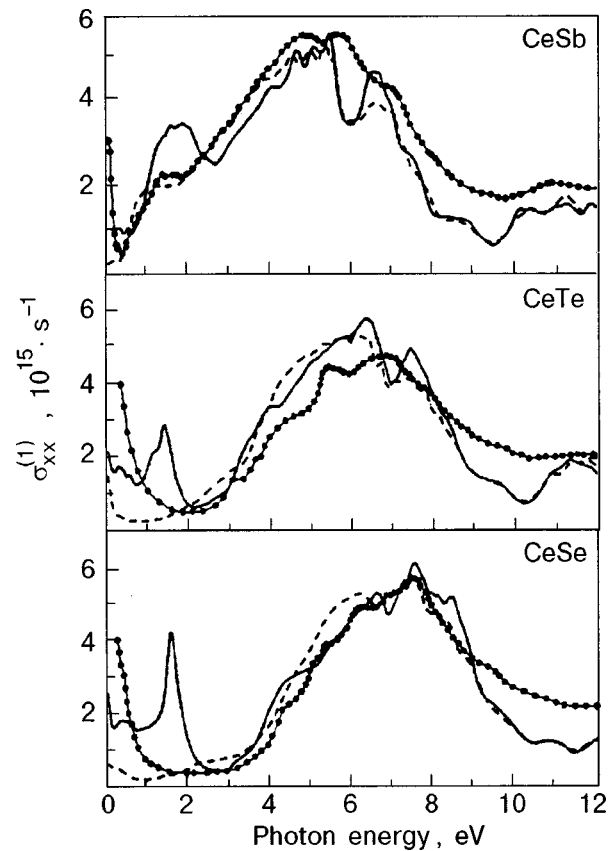

FIG. 16. Real part of diagonal optical conductivity, $\sigma_{xx}^{(1)}$, for CeSb, CeSe and CeTe. LDA results are depicted by the solid curves, LDA+U results by the dashed curves, and experimental results[98] are depicted by the solid dots.

which has a large magnetic moment of about $2\mu_B$. The $4f^1$-level is, however, located 3.6 eV beneath E_F in our calculations, and therefore it cannot contribute directly to the peak rotation. We find that the $4f^1$-level plays nevertheless a crucial role, because, due to hybridization of valence states with the anisotropically polarized $4f^1$-state, the valence bands become anisotropically polarized. This anisotropic polarization leads to an asymmetrical coupling of the left- and

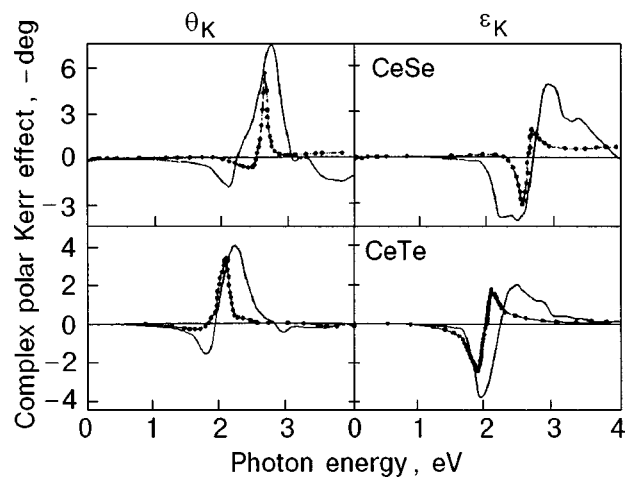FIG. 17. Theoretical and experimental[98] Kerr angle (θ_K) and Kerr ellipticity (ε_K) spectrum of CeSe and CeTe. The theoretical spectrum (solid curve) was calculated using the LDA+U approach with $U = 6$ eV.
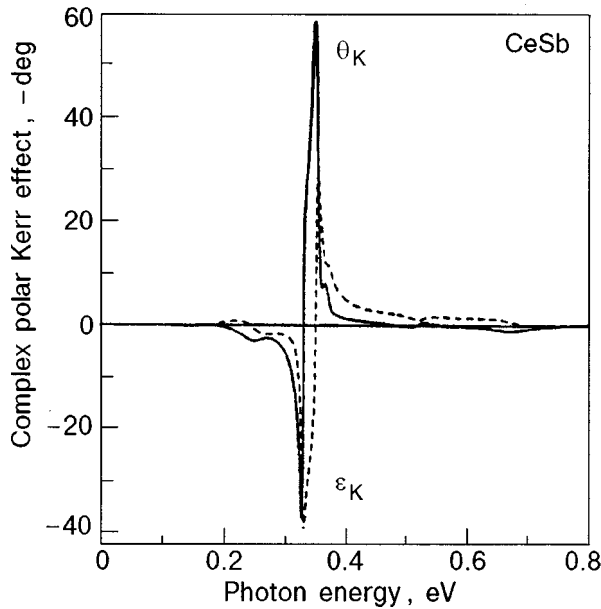
FIG. 18. Theoretical Kerr spectra of CeSb as calculated with LDA+U approach with $U=6$ eV.

right-hand circularly polarized light at small photon energies. The asymmetrical light coupling leads in turn to a relatively large σ_{xy}, which causes the huge Kerr rotation. To emphasize the importance of the anisotropic hybridization, we also performed quasi-core calculations for the $4f^1$-level. We obtained a very similar σ_{xx}, but due to the lack of anisotropic $4f$-hybridization, σ_{xy} becomes nearly zero. Consequently, only a very small Kerr rotation is obtained in quasi-core calculations.

The MO Kerr spectrum of CeBi has also a considerable interest. In most compounds the magnitude of the Kerr effect is proportional to the spin-orbit (SO) coupling interaction. The MO Kerr effect in MnBi is, for example, larger than that in MnSb, because the SO coupling on Bi is larger than that on Sb.[24] One could thus expect that the Kerr angle in CeBi should be as large as, or even larger, than that of CeSb. However, this is not found to be the case.[98] In Fig. 19 we
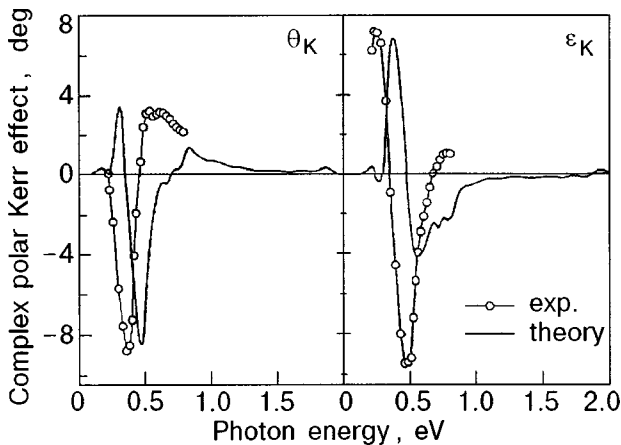

FIG. 19. Theoretical and experimental[98] Kerr angle (θ_K) and Kerr ellipticity (ε_K) spectrum of CeBi. The theoretical spectrum (solid curve) was calculated using the LDA+U approach with $U=6$ eV.

show the experimental[98] and theoretical Kerr spectra of CeBi. The measured maximal Kerr rotation amounts only to $-9°$, ten times less than that of CeSb. The LDA+U approach (with $U=6$ eV) explains the measured MO Kerr spectrum of CeBi fairly well. There is a small energy difference of 0.1 eV in the position of the rotation maximum, and the calculated Kerr ellipticity deviates above 0.5 eV from the experimental curve.

The fact that the Kerr rotation of CeBi is far less than that of CeSb is fully reproduced by our calculations,[28,33] but it is not consistent with our experience that the Kerr effect is proportional to the magnitude of SO coupling. The imaginary part of σ_{xy} is for CeBi as large as that of CeSb, but if we compare the σ_{xx} of CeBi to that of CeSb, then we find that the denominator does not become as small for CeBi. The resulting Kerr angle of CeBi is therefore not as large as that of CeSb.

We conclude that LDA+U approach provides an improved electronic structure for materials having deep-lying, nearly localized f's. The optical and MO spectra computed therefrom are in fair accord with experimental spectra. The overall agreement of the calculated and experimental spectra, however, emphasizes that improvements are still called for.

4. URANIUM COMPOUNDS

Intensive experimental and theoretical study over more than two decades[99–103] has revealed that $5f$ magnetism is quite complex, because Coulomb, spin-orbit, crystalline field and exchange energies in $5f$ systems are the same order of magnitude. Today it is well established that many unusual physical properties of the light actinide metals are a reflection of the particular nature of the $5f$ electrons. Many years ago Friedel[104] proposed that the bonding in these materials must involve the $5f$ electrons. The argument for $5f$ bonding can be understood as a consequence of the extended nature of the $5f$ wave function relative to the rare-earth $4f$ wave functions. This causes them to form in bandlike states.[105]

The itinerant nature of the $5f$ electrons in the light actinide metals are well known.[99] Their electronic structure and optical properties are well described by LDA band structure calculations.[106,107] On the other hand, the decreasing f-band width (W) and the increasing intraatomic Coulomb energy (U) results in a Mott localization in between plutonium and americium[100,108,109] and the correlation effects are not properly described in the local density approximation.[102,110]

Actinide compounds occupy an intermediate position between itinerant $3d$ and localized $4f$ systems[111,112] and one of the fundamental questions concerning the actinide materials is whether their f states are localized or itinerant. This question is most frequently answered by comparison between experimental spectroscopies and the different theoretical descriptions.

Optical spectroscopy provides a powerful, widely used tool to investigate in detail the electronic structure of actinides. Traditionally, one distinguishes the various existing kinds of spectroscopies according to the photon energy of the employed light, i.e., high-energy x-ray methods, and methods applying infrared, visible or medium-energy light ($\hbar\omega$

<10 eV). X-ray photoemission spectroscopy (XPS) has been applied to determine the energy position of the $5f$ states below E_F, and angle-resolved XPS has been used to map out the energy bands in the Brillouin zone (see, e.g., Ref. 113). Optical spectroscopy in the visible and infrared energy range has successfully been applied to many topics in the actinide research. Examples are the infrared absorption in the heavy-fermion state of URu_2Si_2[114] and UPd_2Al_3,[115] reflectivity spectroscopy on intermediate valence and dense Kondo materials.[116] A particular useful spectroscopic technique is MO Kerr spectroscopy.[4] Reflectivity spectroscopy can be used to determine relative energy level positions, but Kerr spectroscopy has the additional advantage that it couples to both the spin and orbital polarization of the electron states.[4] Kerr spectroscopy is therefore ideally suited for studying magnetic actinide compounds. On the other hand, actinide compounds are also excellent subjects for MO research. The participation of the $5f$ states in bonding is reflected in strongly hybridized bands near the Fermi level, with a high density of states and significant $f \rightarrow d$ oscillator strengths for optical transitions. The $5f$ delocalization favors higher ordering temperatures. In fact, many uranium compounds have ordering temperatures which are one order of magnitude larger than those in similar lanthanide compounds.[4,117] Regarding the magnitude of the MO effects compared to rare-earth materials, an enhancement due to the larger spin-orbit energy can be expected and is in part experimentally verified.[4,117] For actinide compounds the figure of merit $R^{1/2}(\theta_K^2 + \varepsilon_K^2)^{1/2}$, where R is the optical reflectivity, θ_K and ε_K are Kerr angle and Kerr ellipticity, respectively, is one order of magnitude larger than for the best transition or rare-earth compounds.[4] Besides the issue of radioactivity (minimal for depleted uranium) a hindrance for successful application of actinide compounds in storage devices is that the typical Curie temperature are below room temperature. This is not a fundamental problem, and can probably be overcome by suitable alloying.

As we mentioned above one of the most intriguing aspects of actinide compounds is the great variability in the localization degree of the $5f$ electrons. Varying from one actinide compound to another, the $5f$ electrons may range from being nearly localized to being practically itinerant. In this work we consider two groups of actinide compounds. The optical and MO spectra of the first group which contains UAsSe and URhAl compounds can be properly described within density functional theory in the local-density approximation, but such an approximation totally failed in the case US, USe, and UTe. This result puts forward further evidence for at least partly itinerant electron behavior in the first group compounds and at least partly localized one in the second group.

4.1. UAsSe and URhAl

UAsSe crystallizes in the tetragonal PbFCl crystal structure (also called ZrSiS structure, P4/nmm space group) and orders ferromagnetically below $T_C = 110$ K.[118,119] Magnetic susceptibility measurements[120] and photo-emission experiments[121] supplied evidence for localized $5f$ electrons in UAsSe. On the other hand, reflectivity and MO spectros-
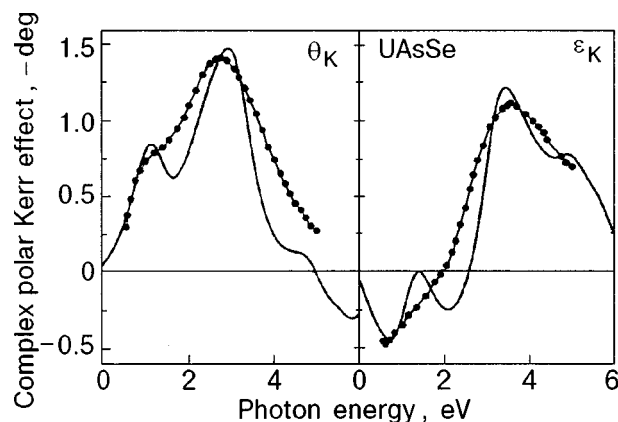

FIG. 20. Theoretical and experimental polar Kerr rotation and Kerr ellipticity spectra of UAsSe. The experimental data (■) are after Reim (Ref. 5).

copy revealed a pronounced spectral intensity at small photon energies (<2 eV) which was attributed to a $5f$ band located at the Fermi energy.[117] Also, the specific heat coefficient $\gamma = 41$ mJ/Mol·K^2 indicates a tendency to itinerancy.[122] These apparently contradicting observations show that the behavior of the $5f$ electrons and the related magnetic properties of UAsSe are not yet well understood.

As in other uranium compounds with non-cubic structures such as, e.g., the ternary UT_2X_2 compounds[123] there is the possibility of partially delocalized electrons in another sense. These compounds with a preferred c-axis tend to have the uranium atoms arranged in layers which leads to both anisotropic bonding and magnetic properties due to hybridization of $5f$ and p or d states. It is quite possible that the $5f$ electrons are delocalized in the planes but localized along the c-axis and we suspect that this may be the case in UAsSe. In this compound the uranium planes are perpendicular to the axis of the polar Kerr measurements, so that the polar MO Kerr effect selectively probes these planes which is a possible explanation[5] of why the response appears to be due to itinerant electrons.

A comparison of the theoretical and experimental spectra in Fig. 20 proves that there is a very good agreement between the band theory and experimental data: Both the position and height of the main peak in the Kerr angle (θ_K) at 3 eV are properly given by theory, with the usual (small) dependence of the theoretical peak height on the broadening. Energy-band theory predicts also a smaller peak in the Kerr rotation at 1 eV, where there is only a shoulder seen in the measured Kerr angle. A Kramers-Kronig related peak structure is visible in the Kerr ellipticity (ε_K) spectrum at 1.5 eV. In this energy region there will of course be the influence of the not included intraband conductivity which may change the pure interband spectra.

URhAl has also a layer crystal structure with U-Rh planes separated by Rh-Al planes. There are apparently several contradicting experimental observations on the nature of $5f$-electron localization in URhAl. Inelastic neutron scattering experiments on URhAl revealed a peak at 380 meV, which could be the signature of an intermultiplet transition.[124] The value of 380 meV is quite close to the intermultiplet transition energy of 390 meV measured for
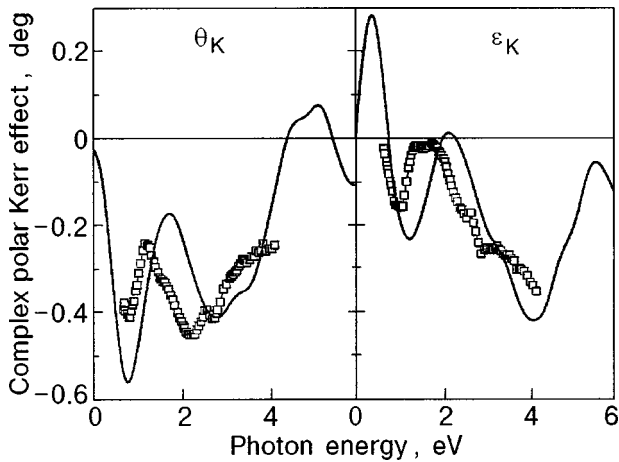
FIG. 21. Experimental[129] and theoretical Kerr spectrum of URhAl. The theoretical spectrum is calculated with the itinerant LDA approach.

UPd_3.[125] There are, however, several other properties of URhAl that would advocate rather delocalized $5f$ behavior in URhAl. A small U moment of only $0.94\mu_B$ was measured which does corresponds to the magnetic moment of neither a $5f^2$ nor a $5f^3$ configuration.[126] A significant amount of anisotropic $5f$-ligand hybridization was reported.[127] Also, the measured specific heat $\gamma = 60\,\mathrm{mJ \cdot mol^{-1} \cdot K^{-2}}$ is not particularly small.[128] These contradictory observations demonstrate that the $5f$ behavior in URhAl is not yet understood.

In Fig. 21 we show the experimental Kerr spectrum[129] of URhAl together with the theoretical spectrum calculated using the itinerant LDA approach.[28] The first spectral peak at 1 eV, and the second one at 2–3 eV in the Kerr angle are definitely reproduced in the theoretical spectrum. The theoretical Kerr rotation drops off between 4 and 5 eV, but it is yet not clear if this also occurs in the experimental θ_K spectrum. It can, nevertheless, be concluded that the itinerant $5f$ model explains the measured Kerr spectrum fairly well. Clearly, this supports the picture of delocalized $5f$ electrons in URhAl. The calculated electronic specific heat coefficient, $\gamma = 41\,\mathrm{mJ \cdot mol^{-1} \cdot K^{-2}}$, is quite reasonable since a many-body enhancement of 1.5 can be considered to be normal.

With respect to the signified intermultiplet transition, it could be speculated that the $5f$'s in URhAl divide into two groups, relatively delocalized, rather hybridized $5f$'s in the U-Rh plane, and more localized $5f$'s perpendicular to this plane, in accord with the observation of anisotropic f hybridization in URhAl.[127] The possible intermultiplet transition might correspond to the localized $5f$'s, whereas Kerr spectroscopy in the polar geometry probes the MO response in the U-Rh plane.

In conclusion, we find that the MO Kerr spectra of UAsSe and URhAl can be excellently described by a LDA band-structure approach to the $5f$ electrons.

4.2. US, USe and UTe

The uranium compounds US, USe, and UTe belong to the class of uranium monochalcogenides that crystallize in the NaCl structure and order ferromagnetically (on the uranium sublattice) at Curie temperatures of 178, 160, and 102

K, respectively (see, e.g., the review[130]). These uranium compounds exhibit several unusual physical phenomena, which are the reason for an as yet ongoing interest in these compounds. Despite their relatively simple and highly symmetrical NaCl structure, it has been found that the magnetic ordering on the uranium atoms is strongly anisotropic,[131,132] with the uranium moment favoring a (111) alignment. The magnetic anisotropy in US, e.g., is one of the largest measured in a cubic material, with a magnetic anisotropy constant K_1 of more than 2×10^8 erg/cm^3.[133] Also the magnetic moment in itself is unusual, consisting of an orbital moment that is about twice as large as the spin moment, and of opposite sign,[134–136] but it is not close to the atomic moment. In addition to this, these materials show with increasing mass of the chalcogenide atom evidence of correlated-electron behavior, with UTe being considered as a dense Kondo system.[137] Obviously, the uranium $5f$-electrons are to be held responsible for both features.

Schoenes and Reim,[4,77,117,138,139] investigated the magneto-optical (MO) spectra of these uranium salts and obtained three rather similar Kerr spectra, as one would expect from isochemical compounds. Besides, the measured Kerr rotation spectra are unusually large, with peak values of about 3 degrees. In a first interpretation of their measurements Reim and Schoenes gave an analysis of the Kerr spectra in terms of optical transitions on uranium.[117,139]

It has already been shown that first-principles band-structure theory using the local density approximation has failed in giving a satisfactory description of the optical spectra of the uranium monochalcogenides.[4,77] This failure was thought to be due to an insufficient treatment of the f-electron correlations by the LDA.[4] These many-body correlation effects can already be important for the proper description of ground state properties, but they should become imperative for describing optical excitations. For example, if a strong on-site Coulomb repulsion between electron and hole quasiparticles plays a dominating role.[140] Therefore, if the uranium $5f$ electrons are localized, then one would particularly expect to observe corresponding electron correlation effects in the optical spectra. The behavior of the $5f$ electrons ranges from nearly delocalized to almost localized: US is considered to be nearly itinerant,[141] while UTe is considered to be quasilocalized.[142] So the failure of LDA description of MO Kerr spectra in US comes as a surprise, because, if the $5f$-electrons are itinerant, one would expect the delocalized LDA approach to be applicable.

To find the appropriate description, we carried out various model calculations of the optical and MO spectra.[20,22] These included the orbital polarization[143] and the LDA+U approach, assuming $5f^2$ and $5f^3$ configurations for uranium (with $U = 2$ eV). However, using these approaches we could not obtain satisfactory agreement with the experimental spectra for all three compounds. In Fig. 22 we show theoretical and experimental results for the real part of $\sigma_{xx}^{(1)}$, for US, USe and UTe. From Fig. 22 it can be seen that for US and USe the inclusion of the Coulomb interaction U leads to a substantial improvement over LDA result. The erroneous peak at 3 eV in the LDA spectra disappears in LDA+U spectra. In Fig. 23 we show theoretical and experimental
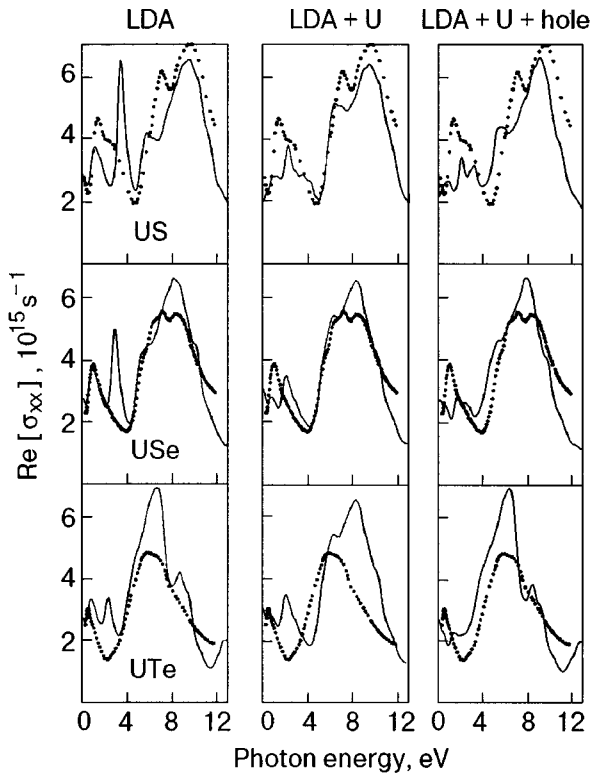
FIG. 22. Real part of diagonal optical conductivity, $\sigma_{xx}^{(1)}$, for US, USe and UTe in LDA, LDA+U approximations and with a screened hole in the $5f^2$-shell (LDA+U+hole). Theoretical results are depicted by the solid curves, and experimental results[4] are depicted by the solid dots.
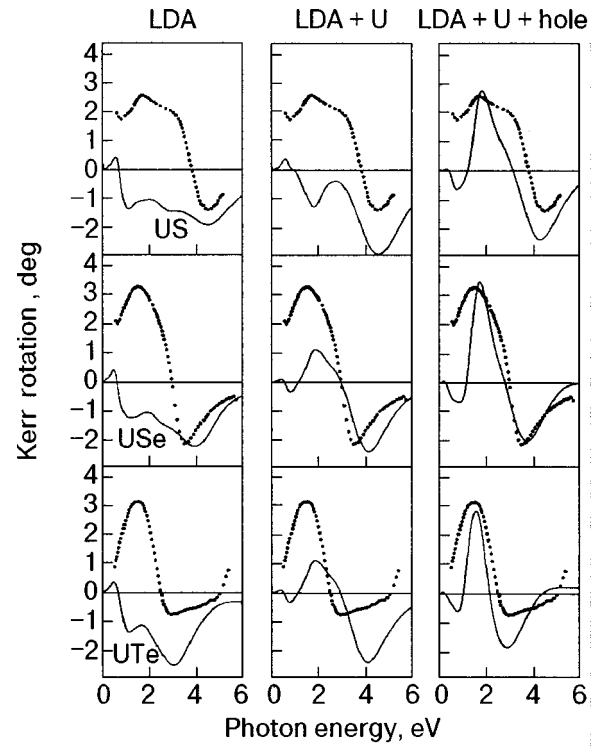

FIG. 24. Experimental[4] (solid dots) and theoretical (solid line) Kerr spectra of US, USe and UTe.
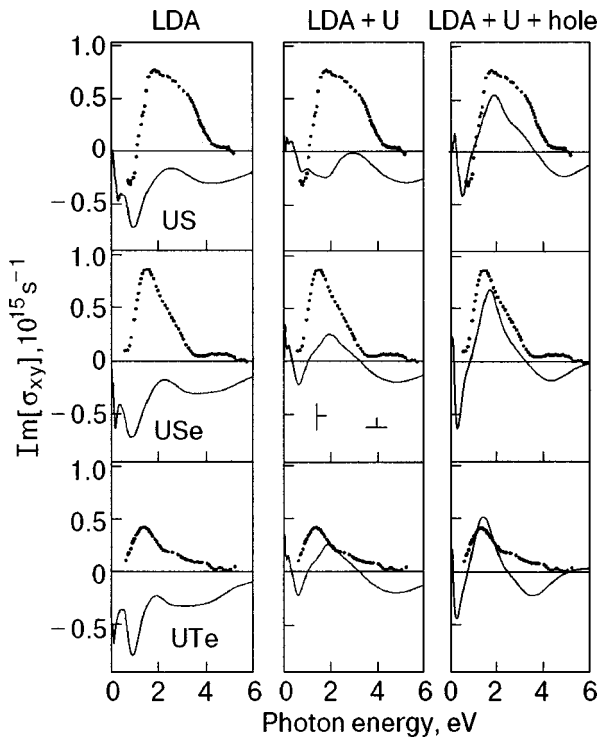
results for the imaginary part of offdiagonal part of optical conductivity $\sigma_{xy}^{(2)}$, for US, USe and UTe. It can be seen that LDA calculations gives completely inappropriate results LDA+U calculations are greatly improve the agreement between theory and experiment in the case of USe and UTe. This finding appears to be consistent with the quasilocalized nature of the $5f$-electrons in USe and UTe. As for US, the dynamical process of the optical excitations may provide a clue for understanding what happens: the photoemission of a $5f$-electron creates a long-living hole in the $5f$-shell, which will be rapidly screened. This hole in the broad, semilocalized $5f$-bands lies in the important spectral range. To test the influence of this process we performed LDA+U calculations (with $U = 2$ eV) and with a screened hole in the $5f^2$-shell. The physically motivated correction leads to an improved description of the optical conductivity (see Figs. 22 and 23) and also Kerr spectrum for US, USe and UTe (Fig. 24).

SUMMARY

Recent progress in first-principle calculations of optical spectra illustrates that optical and MO spectra are developing into a powerful tool for tracing the electronic structure of crystals. The density-functional theory in the local-density approximation gives a fully satisfactory explanation of the MO Kerr spectra of transition metal compounds and alloys in most cases. Moreover, theory can help to understand the nature of MO spectra and gives some recommendations how to create compounds with appropriate MO properties.

As can be seen from the consideration of MO properties of MnBi, XPt_3 compounds and Heusler alloys, large Kerr effects can be anticipated when compounds fulfill the follow-

FIG. 23. As Fig. 22, but for imaginary part of offdiagonal optical conductivity, $\sigma_{xy}^{(2)}$.

ing conditions: one of the constituting elements must be heavy, but this element need not be magnetic, for instance, Pt or Bi. One of the other elements must have a large moment, but this element need not be heavy, for instance, Mn, Fe or Co. In addition should there be a good hybridization between the states of the two kinds of atoms. Within such a composition, the large exchange splitting (i.e., a big magnetic moment) and the strong spin-orbit coupling lead through the hybridized bands to a big Kerr rotation. However, not in all cases does this ''rule of thumb'' apply, because sometimes the influence of the band structure can be such that dipolar transitions of different bands compensate each other.

In most of the $4f$ systems, the f electrons are localized and form a Hund's rule ground state. The application of plain LDA calculations to $4f$ electron systems encounters problems in most cases, because of the correlated nature of electrons in the f shell. To better account for strong on-site electron correlations the LDA+U approach should be used, in which a model Hamiltonian explicitly including the on-site Coulomb interaction, U, for localized states is combined with the standard band structure calculation Hamiltonian for extended states. The LDA+U method provides a rather good description of the electronic structure and the optical and MO properties of some lanthanide compounds.[20,28,32]

Actinide compounds occupy an intermediate position between itinerant $3d$ and localized $4f$ systems, and one of the fundamental questions concerning the actinide materials is whether their f states are localized or itinerant. This question is most frequently answered by comparison between experimental spectroscopies and the different theoretical descriptions. Optical and MO spectroscopy, like photoelectrons spectroscopy and bremsstrahlung isochromat spectroscopy supply direct information about the energy states (both occupied and unoccupied) around the Fermi energy, and can provide a means of discrimination between the two theoretical limits.

There are quite a few first-principle calculations of the MO spectra of uranium compounds.[9,19,20,22,144] The MO spectra of such compounds as UAsSe,[19] URhAl,[28] U_3P_4[144,145] and U_3As_4[145] are well described in the LDA and we can conclude that they have at least partially itinerant electron behavior. On the other hand, the MO spectra in UTe can be well described only in the LDA+U approximation[20] supporting the localized description for their $5f$ electrons. The most difficult case is US which is commonly classified to be itinerant. We find that a LDA+U approach supplemented with a screened hole in the $5f$-shell gives a reasonable description of the Kerr spectra of US and USe.

ACKNOWLEDGMENTS

[1] J. Kerr, Philos. Mag. **3**, 321 (1877).

[2] C. D. Mee and E. D. Daniel, *Magnetic Recording*, McGraw-Hill, New York (1987); M. Mansuripur, *The Physical Principles of Magneto-Optical Recording*, University Press, Cambridge (1995).

[3] K. H. J. Buschow, in *Ferromagnetic Materials*, E. P. Wohlfarth and K. H. J. Buschow (Eds.), North-Holland, Amsterdam (1988), Vol. 4, p. 588.

[4] W. Reim and J. Schoenes, in *Ferromagnetic Materials*, E. P. Wohlfarth and K. H. J. Buschow (Eds.), North-Holland, Amsterdam (1990), Vol. 5, p. 133.

[5] J. Schoenes, in *Materials Science and Technology*, Vol. 3A: *Electronic and Magnetic Properties of Metals and Ceramics*, K. H. J. Buschow, R. W. Cahn, P. Hassen and E. J. Kramer (Eds.), Verlag Chemic, Weinheim (1992), p. 147.

[6] H. R. Hulme, Proc. Roy. Soc. **A135**, 237 (1932).

[7] C. Kittel, Phys. Rev. **83**, A208 (1951).

[8] P. N. Argyres, Phys. Rev. **97**, 334 (1955).

[9] B. R. Cooper, Phys. Rev. **139**, A1504 (1965).

[10] G. S. Krinchik and E. A. Gan'sbina, Zh. Éksp. Teor. Fiz. **65**, 1970 (1913) [Sov. Phys. JETP **38**, 983 (1974)].

[11] R. Kubo, J. Phys. Soc. Jpn. **12**, 570 (1957).

[12] A. E. Kondorsky and A. V. Vediaev, J. Appl. Phys. **89**, 559 (1968).

[13] C. S. Wang and J. Callaway, Phys. Rev. B **B9**, 4897 (1974).

[14] G. H. O. Daalderop, F. M. Mueller, R. C. Albers, and A. M. Boring, J. Magn. Magn. Mater. **74**, 211 (1988); H. Ebert, P. Strange, and B. L. Gyorffy, J. Phys. C **CS**, 31 (1988); Yu. Uspenskii and S. V. Halilov, Zh. Éksp. Teor. Fiz. **95**, 1022 (1989) [Sov. Phys. JETP **68**, 588 (1989)].

[15] E. T. Kulatov, Yu. A. Uspenskii, and S. V. Khalilov, Phys. Lett. A **195**, 267 (1994); Yu. A. Uspenskii, E. T. Kulatov, and S. V. Khalilov, Zh. Éksp. Teor. Fiz. **1**, 1708 (1995) [JETP Lett. **80**, 952 (1995)]; Ya. A. Uspenskii, E. T. Kulatov, and S. V. Khalilov, Phys. Rev. B **54**, 474 (1996); E. T. Kulatov, Yu. A. Uspenski, and S. V. Khalilov, Fiz. Tverd. Tela. **38**, 3066 (1970) [Phys. Solid State **38**, 1677 (1996)].

[16] P. M. Oppeneer, J. Sticht, and F. Herman, J. Magn. Soc. Jpn. **15**, SI, 73 (1991); P. M. Oppeneer, T. Maurer, J. Sticht, and J. Kübler, Phys. Rev. B **B45**, 10924 (1992); I. Osterloch, P. M. Oppeneer, J. Sticht, and J. Kübler, J. Phys. Cond. Mat. **6**, 285 (1994); J. Kühler, L. Sandratskii, and J. Kübler, Physica B **253**, 272 (1998).

[17] V. N. Antonov, A. Ya. Perlov, A. P. Shpak, and A. N. Yaresko, J. Magn. Magn. Mater. **146**, 205 (1995).

[18] P. M. Oppeneer and V. N. Antonov, in *Spin-Orbit Influenced Spectroscopies of Magnetic Solids*, H. Ebert and G. Schiitz (eds.), Springer, Berlin (1996), p. 29.

[19] P. M. Oppeneer, M. S. S. Brooks, V. N. Antonov, T. Kraft, and H. Eschrig, Phys. Rev. B **53**, R10437 (1996).

[20] P. M. Oppeneer, V. N. Antonov, A. Ya. Perlov, A. N. Yaresko, T. Kraft, and H. Eschrig, Physica B **230-232**, 544 (1997).

[21] P. M. Oppeneer, V. N. Antonov, T. Kraft, H. Eschrig, A. N. Yaresko, and A. Ya. Perlov, Solid State Commun. **94**, 255 (1995).

[22] T. Kraft, P. M. Oppeneer, V. N. Antonov, and H. Eschrig, Phys. Rev. B **52**, 3561 (1995).

[23] P. M. Oppeneer, V. N. Antonov, A. N. Yaresko, A. Ya. Perlov, T. Kraf, and H. Eschrig, J. Magn. Soc. Jpn. **20 Suppl S1**, 41 (1996).

[24] P. M. Oppeneer, V. N. Antonov, T. Kraf, H. Eschrig, A. N. Yaresko, and A. Ya. Perlov, J. Appl. Phys. **80**, 1099 (1996).

[25] P. M. Oppeneer, V. N. Antonov, T. Kraf, H. Eschrig, A. N. Yaresko, and A. Ya. Perlov, J. Phys.: Condens. Matter **8**, 5769 (1996).

[26] V. N. Antonov, P. M. Oppeneer, A. N. Yaresko, A. Ya. Perlov, and T. Kraft, Phys. Rev. B **56**, 13012 (1997).

[27] A. Ya. Perlov, H. Ebert, A. N. Yaresko, V. N. Antonov, and D. Weller, Solid State Commun. **105**, 273 (1998).

[28] P. M. Oppeneer, A. Ya. Perlov, V. N. Antonov, A. N. Yaresko, T. Kraft, and M. S. S. Brooks, J. Alloys Compd. **271-273**, 831 (1998).

[29] A. N. Yaresko, L. Uba, S. Uba, A. Ya. Perlov, R. Gontarz, and V. N. Antonov, Phys. Rev. B **58**, 5043 (1998).

[30] S. P. Lim, D. L. Price, and B. R. Cooper, IEEE Trans. Magn. **27**, 3648 (1991); B. R. Cooper, S. F. Lim, and I. Avgin, J. Phys. Chem. Solids **56**, 1518 (1995).

[31] X. Wang, V. P. Antropov, and B. N. Harmon, IEEE Trans. Magn. **30**,

4458 (1994); V. P. Antropov, A. I. Liechtenstein, and B. N. Harmon, J. Magn. Magn. Mater. **140**, 1161 (1995); B. N. Harmon, V. P. Antropov, A. I. Liechtenstein, I. V. Soloviev, and V. I. Anisimov, J. Phys. Chem. Solids **56**, 1521 (1995); Yu. A. Uspenskii, V. P. Antropov, and B. N. Harmon, Phys. Rev. B **56**, R11396 (1997).

[32] A. I. Liechtenstein, V. P. Antropov, and B. N. Harmon, Phys. Rev. B **49**, 10770 (1995).

[33] A. N. Yaresko, P. M. Oppeneer, A. Ya. Perlov, V. N. Antonov, T. Kraft, and H. Eschrig, Europhys. Lett. **36**, 551 (1996).

[34] S. Uba, L. Uba, A. Ya. Perlov, A. N. Yaresko, V. N. Antonov, and R. Gontars, J. Exp. Zool. **9**, 447 (1997).

[35] H. Ebert, A. Ya. Perlov, A. N. Yaresko, V. N. Antonov, and S. Uba, in *Magnetic Ultrathin Films, Multilayers and Surfaces*, J. Tobin *et al.* (Eds.), Pittsburgh, Pennsylvania (1997), p. 407.

[36] S. Uba, L. Uba, R. Gontarz, V. N. Antonov, A. Ya. Perlov, and A. N. Yaresko, J. Magn. Magn. Mater. **144**, 575 (1995).

[37] S. Uba, L. Uba, A. N. Yaresko, A. Ya. Perlov, V. N. Antonov, and R. Gontarz, Phys. Rev. B **53**, 6526 (1996).

[38] S. Uba, A. N. Yaresko, L. Uba, A. Ya. Perlov, V. N. Antonov, and R. Gontarz, Phys. Rev. B **57**, 1534 (1997).

[39] S. Uba, L. Uba, A. N. Yaresko, A. Ya. Perlov, V. N. Antonov, and R. Gontarz, J. Phys.: Condens. Matter **10**, 7769 (1998).

[40] R. Gontarz, S. Uba, L. Uba, A. Ya. Perlov, A. N. Yaresko, and V. N. Antonov, in *Frontiers in Magnetism of Reduced Dimension Systems*. P. E. Wigen (Ed.), *Proc. of NATO Advanced Research Workshops, ASI*—Kiev, Ukraiane, 1997 KLUWER Academic Publishers, Netherlands (1998).

[41] W. H. Kleiner, Phys. Rev. **142**, 318 (1966).

[42] A. H. MacDonald and S. H. Vosko, J. Phys. C: Solid State Phys. **12**, 2977 (1979).

[43] H. Ebert, H. Freyer, A. Vernes, and G.-Y. Guo, Phys. Rev. B **53**, 7721 (1996).

[44] H. Ebert, Phys. Rev. B **38**, 9390 (1988).

[45] I. V. Solovyev, A. B. Shik, V. P. Antropov, A. I. Liechtenstein, V. A. Gubanov, and O. K. Andersen, Sov. Phys. Solid State **31**, 1285 (1989).

[46] O. K. Andersen, Phys. Rev. B **12**, 3060 (1975).

[47] V. V. Nemoshkalenko, A. E. Krasovskii, V. N. Antonov, Vl. N. Antonov, U. Fleck, H. Worm, and P. Ziesche, Phys. Status Solidi B **120**, 283 (1983).

[48] A. Santoni and F. J. Himpsel, Phys. Rev. B **43**, 1305 (1991).

[49] V. N. Antonov, A. I. Bagljuk, A. Ya. Perlov, V. V. Nemoshkalenko, Vl. N. Antonov, O. K. Andersen, and O. Jepsen, Low Temp. Phys. **19**, 494 (1993).

[50] V. I. Anisimov, J. Zaanen, and O. K. Andersen, Phys. Rev. B **44**, 943 (1991).

[51] P. W. Anderson, Phys. Rev. **124**, 41 (1961).

[52] V. I. Anisimov, F. Aryasetiawan, and A. I. Liechtenstein J. Phys.: Condens. Matter **9**, 767 (1997).

[53] P. M. Oppeneer, V. N. Antonov, A. N. Yaresko, A. Ya. Perlov, and H. Eschrig, Phys. Rev. Lett. **78**, 4079 (1997).

[54] V. N. Antonov, A. N. Yaresko, A. Ya. Perlov, P. Thalmeier, P. Fulde, P. M. Oppeneer, and H. Eschrig, Phys. Rev. B **58**, 9752 (1998).

[55] P. G. van Engen, K. H. J. Buschow, R. Jongebreur, and M. Erman, Appl. Phys. Lett. **42**, 202 (1983).

[56] B. M. Lairson and B. M. Clemens, Appl. Phys. Lett. **63**, 1438 (1993).

[57] G. R. Harp, D. Weller, T. A. Rabedeau, R. F. C. Farrow, and M. F. Toney, Phys. Rev. Lett. **71**, 2493 (1993).

[58] W. B. Zeper, F. J. A. M. Greidanus, P. F. Garcia, and C. R. Fincher, J. Appl. Phys. **65**, 4971 (1989).

[59] D. Weller, H. Brandle, G. Gorman, C.-J. Lin, and H. Notarys, Appl. Phys. Lett. **61**, 2726 (1992).

[60] K. Sato, H. Ikedame, Y. Tosaka, K. Tsuzukiyama, Y. Togami, and M. Fujisawa, J. Magn. Magn. Mater. **126**, 572 (1993).

[61] T. Kato, H. Kikuzawa, S. Iwata, S. Tsunashima, and S. Uchiyama, J. Magn. Magn. Mater. **140-144**, 713 (1995).

[62] T. Kato, S. Iwata, S. Tsumashima, and S. Uchiyama, J. Magn. Soc. Jpn. **19**, 205 (1995).

[63] P. G. van Engen, K. H. J. Buschow, and M. Erman, J. Magn. Magn. Mater. **30**, 374 (1983).

[64] P. G. van Engen, PhD thesis, Technical University Delft, (1983).

[65] R. A. de Groot, F. M. Mueller, P. G. van Engen, and K. H. J. Buschow, Phys. Rev. Lett. **50**, 2024 (1983).

[66] K. E. H. M. Hanssen, P. E. Mijnarends, L. P. L. M. Rabou, and K. H. J. Buschow, Phys. Rev. B **42**, 1533 (1990).

[67] E. Kisker, C. Carbone, C. F. Flipse, and E. F. Wassermann, J. Magn. Magn. Mater. **70**, 21 (1987).

[68] G. L. Bona, F. Meier, M. Taborelli, E. Bucher, and P. H. Schmidt, Solid State Commun. **56**, 391 (1985).

[69] J. S. Moodera and D. M. Mootoo, J. Appl. Phys. **76**, 6101 (1994).

[70] J. F. Bobo, P. R. Johnson, M. Kautzky, F. B. Mancoff, E. Tuncel, R. L. White, and B. M. Clemens, J. Appl. Phys. **81**, 4164 (1997).

[71] R. A. de Groot, F. M. Mueller, P. G. van Engea, and K. H. J. Buschow, J. Appl. Phys. **55**, 2151 (1984).

[72] H. Feil and C. Haas, Phys. Rev. Lett. **58**, 65 (1987).

[73] J. H. Wijngaard, C. Haas, and R. A. de Groot, Phys. Rev. B **40**, 9318 (1989).

[74] G. Y. Guo and H. Ebert, Phys. Rev. B **50**, 10377 (1994).

[75] G. Y. Guo and H. Ebert, Phys. Rev. B **51**, 12633 (1995).

[76] K. J. Kim, T. C. Leung, B. N. Harmon, and D. W. Lynch, J. Phys.: Condens. Matter **6**, 5069 (1994).

[77] T. Gasche, PhD. thesis, Uppsala (1993).

[78] T. Gasche, M. S. S. Brooks, and B. Johansson, Phys. Rev. B **53**, 296 (1996).

[79] N. Mainkar, D. A. Browne, and J. Callaway, Phys. Rev. B **53**, 3692 (1996).

[80] S. Shiomi, A. Ito, and M. Masuda, J. Math. Phys. **11**, S1, 221 (1987).

[81] M. C. Kautzky and B. M. Clemens, Appl. Phys. Lett. **66**, 1279 (1995).

[82] T. Inukai, N. Sugimoto, M. Matsuoka, and K. Ono, Appl. Phys. Lett. **49**, 52 (1986).

[83] K. Takanashi, H. Fujimori, J. Watanabe, M. Shoji, and A. Nagai, Jpn. J. Appl. Phys., Part 2 **27**, L2351 (1988).

[84] M. Naoe, N. Kitamura, M. Shoji, and A. Nagai, J. Appl. Phys. **63**, 3636 (1988).

[85] K. Takanashi, J. Watanabe, G. Kido, and H. Fujimori, Jpn. J. Appl. Phys., Part 2 **29**, L306 (1990).

[86] K. Takanashi, K. Sato, J. Watanabe, Y. Sato, and H. Fujimori, Jpn. J. Appl. Phys., Part 2 **30**, 52 (1991).

[87] K. Sato, H. Ikekame, H. Hongu, M. Fujisawa, K. Takanshi, and H. Fujimori, in *Proceedings of the Sixth Int. Conf. on Ferrites*, (Jpn. Society of Powder and Powder Metallurgy. Tokyo) (1992), p. 1647.

[88] H. Ikekame, K. Sato, K. Takanashi, and H. Fujimori, Jpn. J. Appl. Phys., Part 2 **32**, Suppl 32-3, 284 (1993).

[89] P. A. M. van der Heide, W. Baelde, R. A. de Groot, A. R. de Vroomen, P. G. van Engen, and K. H. J. Buschow, J. Phys. F: Metal Phys. **15**, L75 (1985).

[90] G. Q. Di, S. Iwata, S. Tsunashima, and S. Uchiyama, J. Math. Phys. **16**, 113 (1992).

[91] G. Q. Di, PhD. Thesis, Nagoya University (1992).

[92] C. H. Shang, Z. H. Guo, Y. Xu, and Y. J. Wang, in *Proceedings of the Third Int. Conf. on Phys. of Magn. Mater.* (Seoul, Korea, 1995), p. 515.

[93] G. Q. Di, S. Iwata, S. Tsunashima, and S. Uchiyama, J. Magn. Magn. Mater. **104-107**, 1023 (1992); G. Q. Di, S. Iwata, and S. Uchiyama, *ibid.* **131**, 242 (1994).

[94] Tu Chen and W. E. Stutius, IEEE Trans. Magn. **10**, 581 (1974).

[95] P. Villars and L. D. Calvert, *Pearson's Handbook of Crystallographic Data for Intermetallic Phases*, ASM International, Materials Park (1991).

[96] R. Pittini, J. Schoenes, O. Vogt, and P. Wachter, Phys. Rev. Lett. **77**, 944 (1996).

[97] R. Pittini, J. Schoenes, and P. Wachter, Phys. Rev. B **55**, 7524 (1997).

[98] R. Pittini, J. Schoenes, and P. Wachter, Physica B **206-207**, 92 (1995).

[99] A. J. Freeman and D. D. Koelling, *The Actinides: Electronic Structure and Related Properties*, A. J. Freeman and J. E. Darby (Eds.), Academic Press, New York (1974), Vol. 1; E. Warren, E. Picket, A. J. Freeman, and D. D. Koelling, Phys. Rev. B **22**, 2965 (1980).

[100] B. Johansson, Phys. Rev. B **11**, 2740 (1975).

[101] H. I. Skriver, O. K. Andersen, and B. Johansson, Phys. Rev. Lett. **41**, 42 (1978); *ibid.* **44**, 1230 (1980).

[102] M. S. S. Brooks, J. Magn. Magn. Mater. **29**, 257 (1982); J. Phys. **F13**, 103 (1983).

[103] *Handbook of Physics and Chemistry of the Actinides*, A. J. Freeman and G. H. Lander (Eds.), North-Holland, Amsterdam (1984).

[104] J. Friedel, J. Phys. Chem. Solids **1**, 175 (1956).

[105] R. C. Albers, A. M. Boring, J. M. Wills, L. E. Cox, O. E. Eriksson, and N. E. Christensen, Phys. Rev. B **54**, 14405 (1996).

[106] V. N. Antonov, A. I. Bagljuk, A. Ya. Perlov, V. V. Nemoshkalenko, Vl. N. Antonov, O. K. Andersen, and O. Jepsen, Low Temp. Phys. **19**, 792 (1993).

[107]T. Gasche, M. S. S. Brooks, and B. Johansson, Phys. Rev. B **54**, 2446 (1996).

[108]J. Kollar, L. Vitos, and H. L. Skriver, Phys. Rev. B **55**, 15353 (1997).

[109]P. Sderlind, J. M. Wills, B. Johansson, and O. Eriksson, Phys. Rev. B **55**, 1997 (1997).

[110]J. van Ek, P. A. Sterne, and A. Gonis, Phys. Rev. B **48**, 16 (1993).

[111]J. D. Becker, J. M. Wills, L. Cox, and B. R. Cooper, Phys. Rev. B **54**, 17265R (1996).

[112]L. M. Sandratskii and J. Kübler, Phys. Rev. B **55**, 11395 (1997).

[113]H. Kumigashira, S.-H. Yang, T. Yokoya, A. Chaiani, T. Takahashi, A. Uesawa, T. Suzuki, O. Sakai, and Y. Kaneta, Phys. Rev. B **54**, 9341 (1996).

[114]D. A. Bonn, J. D. Garrett, and T. Timusk, Phys. Rev. Lett. **61**, 1305 (1988).

[115]L. Degiorgi, M. Dressel, G. Griiner, N. Sato, and T. Komatsubara, Europhys. Lett. **25**, 311 (1994).

[116]P. Wachter, in: *Handbook on the Physics and Chemistry of the Rare Earths*, K. A. Gschneidner, Jr., L. Eyring, G. H. Lander, and G. R. Choppin (Eds.), North-Holland, Amsterdam (1994), Vol. 19, p. 177.

[117]W. Reim, J. Magn. Magn. Mater. **58**, 1 (1986).

[118]F. Hulliger, J. Less-Common Met. **16**, 113 (1968).

[119]J. Leciejewicz and A. Zygmunt, Phys. Status Solidi A **13**, 657 (1972).

[120]A. Zygmunt and M. Duczmal, Phys. Status Solidi A **9**, 659 (1972). K. P. Belov, A. S. Dmitrievsky, A. Zygmunt, R. Z. Levitin, and V. Trzebiatowski, Sov. Phys. JETP **64**, 582 (1973).

[121]J. Brunner, M. Erbudak, and F. Hulliger, Solid State Commun. **38**, 841 (1981).

[122]A. Blaise, R. Lagnier, A. Wojakowski, A. Zygmunt, and M. J. Mortimer, J. Low Temp. Phys. **41**, 61 (1980).

[123]V. Sechovsky and L. Havela, in *Ferromagnetic Materials*, E. P. Wohlfarth, and K. H. J. Buschow (Eds.), North-Holland, Amsterdam (1988), Vol. 4, p. 309. L. M. Sandratskii and J. Kiibler, Solid State Commun. **91**, 183 (1994).

[124]A. Hiess, L. Havela, K. Prokes, R. S. Eccleston, and G. H. Lander, Physica B **230-232**, 89 (1997).

[125]K. A. McEwen, U. Steigenberger, and J. L. Martinez, Physica B **186-188**, 670 (1993).

[126]J. A. Paixao, G. H. Lander, P. J. Brown, H. Nakotte, F. R. de Boer, and E. Brück, J. Phys.: Condens. Matter **4**, 829 (1992).

[127]J. A. Paixao, G. H. Lander, A. Delapalme, H. Nakotte, F. R. de Boer, and E. Brück, Europhys. Lett. **24**, 607 (1993).

[128]P. A. Veenhuizen, F. R. de Boer, V. Menovsky, V. Sechovsky, and L. Havela, J. Appl. Phys. **63**, 3064 (1988).

[129]P. Beránková, M. Kucera, M. Matyás, and A. A. Menovsky, in 26^{iemes} *Journées des Actinides*, Szklarska Poreba, Poland, (1996), p. 70.

[130]J.-M. Fournier and R. Troc, in *Handbook on the Physics and Chemistry of the Actinides*, A. J. Freeman, and G. H. Lander (Eds.), North-Holland, Amsterdam (1985), Vol. 2, p. 29.

[131]D. L. Tillwick and P. de V. du Plessis, J. Magn. Magn. Mater. **3**, 329 (1976).

[132]G. Busch, O. Vogt, A. Delpalme, and G. H. Lander, J. Phys. C **12**, 1391 (1979).

[133]G. H. Lander, M. S. S. Brooks, B. Lebech, P. J. Brown, O. Vogt, and K. Mattenberger, J. Appl. Phys. **69**, 4803 (1991).

[134]M. S. S. Brooks and P. J. Kelly, Phys. Rev. Lett. , 51 (1983).

[135]G. H. Lander, Physica B **186-188**, 664 (1993).

[136]M. M. S. Brooks, Physica B **130**, 6 (1985).

[137]J. Schoenes, B. Frick, and O. Volt, Phys. Rev. B **30**, 6578 (1984).

[138]J. Schoenes, Physica B & C **102**, 45 (1980).

[139]J. Schoenes, in *Handbook on the Physics and Chemistry of the Actinides*, A. J. Freeman, and CD. H. Lander (Eds.) North-Holland, Amsterdam (1984), Vol. 1, p. 341.

[140]B. R. Cooper, Q. G. Sheng, S. P. Lim, C. Sanchez-Castro, N. Kioussis, and J. M. Wills, J. Magn. Magn. Mater. **108**, 10 (1992).

[141]M. S. S. Brooks, T. Gasche, and B. Johansson, J. Phys. Chem. Solids **56**, 1491 (1995).

[142]B. Reihl, N. Martensson, and O. Vogt, J. Appl. Phys. **53**, 2008 (1982).

[143]L. Severin, M. S. S. Brooks, and B. Johansson, Phys. Rev. Lett. **71**, 3214 (1993).

[144]J. Köhler, L. M. Sandratskii, and J. Kuber, Phys. Rev. B **55**, 10153R (1997).

[145]V. N. Antonov, V. P. Antropov, B. N. Harmon, A. N. Yaresko, and A. Ya. Perlov, submitted to Phys. Rev. B (1999).

QUANTUM LIQUIDS AND QUANTUM CRYSTALS

Nonlinear second sound in He-II under pressure

V. B. Efimov, G. V. Kolmakov, L. P. Mezhov-Deglin, and A. B. Trusov

Institute of Solid State Physics, Russian Academy of Sciences, 142432 Chernogolovka, Moscow Region, Russia*
(Submitted December 24, 1998)
Fiz. Nizk. Temp. **25**, 551–553 (June 1999)

The dependence of the nonlinearity coefficient α for the roton second sound in superfluid He-II on pressure P is studied for the first time. It is found that as the value of P increases from saturated vapor pressure to 25 atm, the temperature T_α at which the coefficient α reverses its sign decreases from 1.88 to 1.58 K, i.e., there exists a wide temperature interval below T_λ in He-II at all pressures, in which the nonlinearity coefficient α is negative, and a temperature discontinuity (shock wave) is formed at the trailing edge of the second sound compression wave. © *1999 American Institute of Physics.* [S1063-777X(99)00206-6]

In this communication, we present the results of experimental and theoretical studies of the temperature dependence of the nonlinearity coefficient α of the second sound waves in superfluid helium (He-II). Measurements were made in HeII at temperatures 1.6–2.15 K under different pressures in the experimental cell (from saturated vapor pressure (svp) to $P = 14$ atm). The dependence $\alpha(P,T)$ is calculated theoretically down to the minimum pressure $P = 25$ atm corresponding to solidification of the superfluid liquid.

The emergence of second sound in He-II is characterized[1–3] by rather strong nonlinear properties. This leads to the formation of shock waves (temperature discontinuities) during propagation of a finite-amplitude wave in He-II at short distances from the source. The velocity of a travelling second sound wave depends on the amplitude and can be written in the first approximation in the following form:

$$c_2 = c_{20}(1 + \alpha \delta T), \tag{1}$$

where δT is the wave amplitude, c_{20} the velocity of second sound of small amplitude, and α the coefficient of nonlinearity of the second sound defined by the relation[1,2]

$$\alpha = \frac{\partial}{\partial T} \ln\left(c_{20}^3 \frac{C}{T} \right). \tag{2}$$

In the subsequent analysis, we shall assume that the amplitude of the second sound wave is not too large ($|\delta T| < 10^{-2}$ K) so that we can neglect the processes of creation of quantum vortices at the front of a travelling shock wave during a theoretical analysis of the evolution of the shape of a short-duration solitary pulse with distance. For such amplitudes, the description of the nonlinear evolution of the shape of the second sound wave can be confined to the first terms in the expansion of the velocity of sound c_2 in δT, as in Eq. (1).

It should be recalled that unlike the nonlinearity coefficient of the ordinary (first) sound, the nonlinearity coefficient α of the second sound in He-II may be positive or negative. Under saturated vapor pressure in the region of the second roton sound (i.e., at $T > 1$ K), the nonlinearity coefficient is positive ($\alpha > 0$) at temperatures $T < T_\alpha = 1.88$ K (like the nonlinearity coefficient of sound waves in ordinary media), passes through zero at $T = T_\alpha$, and becomes negative ($\alpha < 0$) in the interval $T_\alpha < T < T_\lambda$, where $T_\lambda = 2.187$ K is the temperature of transition of the liquid to the normal state. Hence during propagation ($\delta T > 0$) of a plane (one-dimensional) second-sound compression wave in He-II, the temperature discontinuity (shock wave) emerges at the front of the wave at temperatures 1 K $< T < T_\alpha$ and at the trailing edge of the wave at temperatures $T_\alpha < T < T_\lambda$ (see, for example, Ref. 4). The emergence of a discontinuity at the trailing edge of the compression wave (or at the front of a rarefaction wave for $\delta T < 0$) is a specific property of second sound in He-II, and is unknown in ordinary sound.[2]

All the numerical values mentioned above correspond to He-II under saturated vapor pressure. The characteristics of He-II, e.g., the heat capacity C of helium, the second sound velocity c_{20}, and the phase transition temperature T_λ change considerably upon an increase in pressure. Naturally, a change in pressure P must also affect the magnitude and temperature dependence of the nonlinearity coefficient α. The dependence $\alpha(P,T)$ was not studied earlier.

While carrying out numerical computations of the coefficient $\alpha(T)$ under different pressures right down to the minimum pressure $P = 25$ atm corresponding to solidification, we used the known dependences[3] $C(P,T)$ and $c_{20}(P,T)$. Figure 1 shows the temperature dependences $\alpha(T)$ calculated at the saturated vapor pressure, 5, 10, 15, and 25 atm (curves *1–5*).

In order to analyze the experimental results, say, for studying the evolution of the form of the second sound wave with an enhanced thermal flux density Q in the wave,[4,5] it is convenient to present the dependence (1) in the form
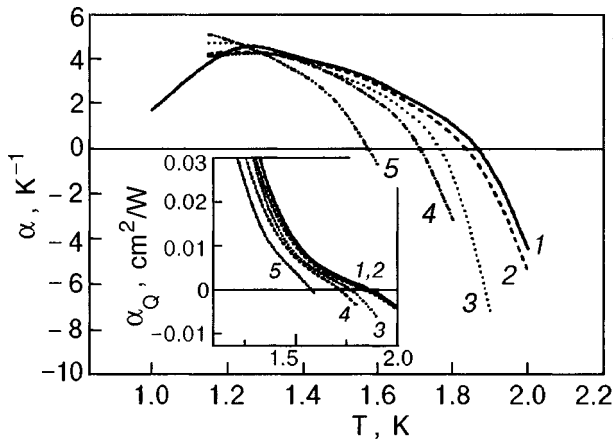
FIG. 1. Theoretical dependence of the second sound nonlinearity coefficient α on temperature under various pressures in the liquid. Curve *1* corresponds to the saturated vapor pressure, while curves *2–5* correspond to the pressures 5, 10, 15 and 25 atm respectively. The inset shows the dependence $\alpha_Q(T)$ for the same pressures.

$$c_2 = c_{20}(1 + \alpha_Q Q). \tag{3}$$

Within the admissible error limits, the flux Q in the wave can be expressed in terms of the amplitude δT by proceeding from the linearized fluid dynamics equations.[1] Since the heat capacity of He-II varies strongly with temperature and pressure, the dependence $\alpha(T)$ shown in Fig. 1 differs significantly from the dependence $\alpha_Q(T)$ shown in the inset to Fig. 1.

Experimental investigations of the pressure dependence of the nonlinearity coefficient in a superfluid liquid were carried out in a cylindrical cell of diameter 3 mm and length 30 mm placed in a high-pressure chamber. A film-type heater of area 2×2 mm and a superconductor rhenium bolometer having a resistance[6] $R = 130 \, \Omega$ attached to the endfaces of the cell were used for exciting and recording second sound waves. The sensitivity of the bolometer at temperatures 1.6–2 K was 6 V/K. The heater was attached to a generator of rectangular electric pulses. The duration τ of the exciting electric pulses varied in the interval 0.3–10 μs. The a.c. signal from the bolometer was amplified by a wideband amplifier and then stored in the memory of a digital oscillograph Tektronics TDS-340 for a subsequent digital analysis of the data.

The dependences $\alpha(T)$ under a fixed pressure in the liquid can be reconstructed by studying the evolution of shape of the second sound shock wave with a change in temperature T or the heat flux Q under consideration, say, with the help of the plots shown in Fig. 2. Here, the duration τ of the exciting pulse is 10 μs, the heat flux density $Q = 10 \, \text{W/cm}^2$, and the pressure P in the cell is equal to 3 atm. Curves *1–3* correspond to $\alpha > 0$ ($T = 1.744$, 1.783 and 1.81 K), while curves *4–7* correspond to $\alpha < 0$ ($T = 1.968$, 1.999, 2.044 and 2.071 K).

According to the results of our experiments, the estimates of $\alpha(P,T)$ are in accord with the results of theoretical calculations shown in Fig. 1.

Figure 3 shows the pressure dependence of the temperature T_α corresponding to the passage of the second sound
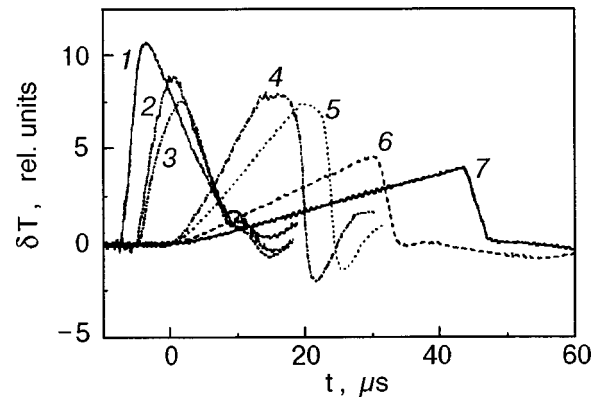

FIG. 2. Evolution of the shape of a quasi-one-dimensional second-sound wave in a cylindrical ampoule upon a change in temperature T, K; 1.744 (*1*); 1.783 (*2*); 1.81 (*3*); 1.968 (*4*); 1.999 (*5*); 2.044 (*6*); 2.071 (*7*) pressure $P = 3$ atm, $Q = 10 \, \text{W/cm}^2$, $\tau = 10 \, \mu$s.

nonlinearity coefficient in He-II through zero. The dotted curve corresponds to the theory, while the circles show the results of processing of the experimental data. Within the limits of the computational error, the experimental data are in good accord with the predictions of the theory. The solid curve in Fig. 3 was constructed from the data available in the literature,[3] and describes the variation in the temperature $T_\lambda(P)$ of transition of the liquid to the normal state upon an increase in pressure.

It follows from Fig. 3 that under all pressures right up to the value corresponding to the solidification of He-II, there exists a fairly wide temperature range in which the second sound nonlinearity coefficient α is negative. This is quite important since the thermal excitation of a second sound spherical wave of quite large amplitude in a superfluid liquid in the case $\alpha < 0$ leads to the formation of a *bipolar pulse of constant duration* determined by the duration τ of the exciting heat pulse *with a temperature discontinuity at the center of the travelling wave.*[5] The use of bipolar pulses propagating in a long waveguide[7] may turn out to be important in the investigation of nonlinear and dissipative processes in the
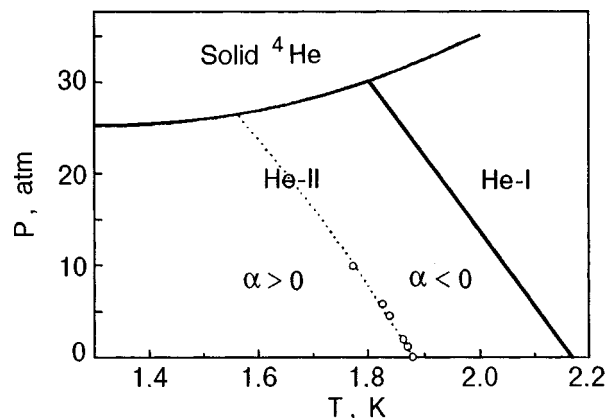

FIG. 3. Dependence of the temperature T_α on pressure: the dashed curve corresponds to the theory while the circles describe the experimental results. The solid curves show the temperature dependence of the pressure of solidification of liquid helium and the variation of phase transition temperature T_λ with pressure.

vicinity of T_λ,[8–10] since the width of the one-dimensional shock pulse in the case of monopolar pulses normally employed in such experiments increases rapidly (as $|\alpha|^{1/2}$) as the critical temperature is approached, thus making it difficult to register the pulses.

[*]E-mail: efimov@issp.ac.ru

[1]L. D. Landau and E. M. Lifshits, *Hydrodynamics* [in Russian], Nauka, Moscow (1986).

[2]I. M. Khalatnikov, *Introduction to the Theory of Superfluidity* [in Russian], Nauka, Moscow (1965).

[3]C. Putterman, *Superfluid Hydrodynamics*, North Holland, Amsterdam (1974).

[4]A. Yu. Iznankin and L. P. Mezhov-Deglin, Zh. Éksp. Teor. Fiz. **84**, 1378 (1983) [Sov. Phys. JETP **57**, 801 (1983)].

[5]A. Yu. Iznankin, L. P. Mezhov-Deglin, and V. P. Mineev, JETP Lett. **32**, 199 (1980).

[6]I. Yu. Borisenko, L. P. Mezhov-Deglin, and V. Zh. Rozenflants, Prib. Tekh. Eksp. No. 5, 137 (1987).

[7]V. B. Efimov, G. V. Kolmakov, A. S. Kuliev, and L. P. Mezhov-Deglin, Fiz. Nizk. Temp. **24**, 116 (1998) [Low Temp. Phys. **24**, 81 (1998)].

[8]L. C. Krysac and J. D. Maynard, J. Low Temp. Phys. **110**, 949 (1998); *ibid.* **113**, 1025 (1998); M. Mohazzad, N. Moulders, M. Larson, and Al Nash, J. Low Temp. Phys. **113**, 1031 (1998).

[9]F.-C. Liu and G. Ahlers, Phys. Rev. Lett. **76**, 1300 (1996).

[10]J. A. Lipa, D. R. Swanson, J. A. Nissen *et al.*, Phys. Rev. Lett. **76**, 944 (1996).

Translated by R. S. Wadhwa

SUPERCONDUCTIVITY, HIGH-TEMPERATURE SUPERCONDUCTIVITY

Lower critical fields of texturized high-T_c superconductors. II On the possibility of studying the anisotropy of H_{c1}

V. A. Finkel'

National Science Center ''Kharkov Physicotechnical Institute,'' 310108 Kharkov, Ukraine*

The concepts about the possibility of studying the anisotropy of lower critical fields of HTSC are developed by measuring the values of H_{c1} in texturized samples for different angles of rotation of the investigated sample relative to the axis perpendicular to the external magnetic field **H**. © *1999 American Institute of Physics.* [S1063-777X(99)00306-0]

Information about the lower (H_{c1}) and upper (H_{c2}) critical fields of high-temperature superconductors (HTSC) is vital for constructing the electrodynamics of this class of materials and for determining the origin of high-temperature superconductivity. Obviously, it should be interesting to measure not the averaged values of H_{c1} and H_{c2} for a poly-crystalline object, but rather the values of the critical fields along the principal axes of complex (tetragonal or rhombic) lattices which are characteristic of HTSC. The values of the critical fields along the principal axes (H_{c1}^c, H_{c2}^c) and at right angles to it (H_{c1}^{ab}, H_{c2}^{ab}) are directly related to the values of fundamental parameters of superconductivity, viz., the co-herence length ξ and the penetration depth λ in the same directions[1,2]:

$$H_{c1}^c/H_{c1}^{ab} = H_{c2}^{ab}/H_{c2}^c = \xi^{ab}/\xi^c = \lambda^c/\lambda^{ab} = (m^c/m^{ab})^{1/2}, \quad (1)$$

where m^c and m^{ab} are the ''effective mass tensor'' compo-nents of an electron along the principal axis and at right angles to it respectively in the Ginzburg–Landau anisotropic theory.

It should be borne in mind that although the values of critical HTSC fields depend (very strongly!) on direction, the critical fields themselves are not tensors, and the standard procedure of ''reducing the tensor to principal axes''[3] is not applicable in this case. Special studies must be carried out to determine the character of the orientational dependences of H_{c1} and H_{c2}. In the framework of the modern theoretical models concerning magnetic properties of type II anisotropic superconductors, which were developed even before the dis-covery of high-temperature superconductivity[4,5] and were applied successfully to HTSC (see, for example, Refs. 6–10), the following expressions were obtained for the de-pendence of lower and upper critical fields on the angle γ between the magnetic anisotropy axis and the external mag-netic field **H**:

$$H_{c1}(\gamma) = H_{c1}^c[\cos^2\gamma + (m^c/m^{ab})\sin^2\gamma]^{-1/2}, \quad (2)$$

$$H_{c2}(\gamma) = H_{c2}^c[\sin^2\gamma + (m^c/m^{ab})\cos^2\gamma]^{-1/2}. \quad (3)$$

It would seem that measurements on single crystals of different orientations provides the only real possibility of studying experimentally the anisotropy of critical fields for HTSC. Unfortunately, this possibility cannot be realized in all cases since many HTSC cannot be obtained in the form of single crystals (for example, the synthesis of single crystals with substitution of elements, e.g., in $YBa_2Cu_{3-x}M_xO_{7-\delta}$, where M is an element replacing copper in the lattice, is practically impossible). Moreover, the size and shape of single crystals are often unsuitable for fairly accurate mea-surements of H_{c1}, and the more so of H_{c2}.

Earlier, we proposed[11] that the anisotropy of lower criti-cal fields of HTSC should be determined by measuring H_{c1} in three mutually orthogonal directions in texturized samples, i.e., in objects displaying anisotropy of their elec-tromagnetic properties. In this case, it was not necessary to describe quantitatively the texture of the investigated object (i.e., to construct pole figures and to reconstruct the orienta-tion distribution functions for grains, etc.). The real textur-ized sample was put in correspondence with a certain single crystal with the same critical fields H_{c1}^{ab} and H_{c1}^c and with its magnetic anisotropy axis c forming angles α, β, and γ with the laboratory reference frame XYZ, such that the values of H_{c1} along the X-, Y-, and Z-axes coincide with the critical fields for the sample along the same directions. This analysis, which was confirmed experimentally in Ref. 11, provided information about the critical fields H_{c1}^{ab} and H_{c1}^c and the Euler angles of the magnetic anisotropy axis of the HTSC crystal in the reference frame of the crystal as a function of the ratio m^c/m^{ab} of effective masses. The available data (three values of H_{c1} and the orthogonality condition $\cos^2\alpha + \cos^2\beta + \cos^2\gamma = 1$ are insufficient for determining the abso-lute values of the five unknown quantities H_{c1}^{ab}, H_{c1}^c, α, β, and γ.

The aim of the present paper is to work out an algorithm for studying the lower critical fields of high-temperature su-perconductors, which would make it possible to determine the orientational dependence of H_{c1} from the results of mea-surements on texturized samples. The approach used for
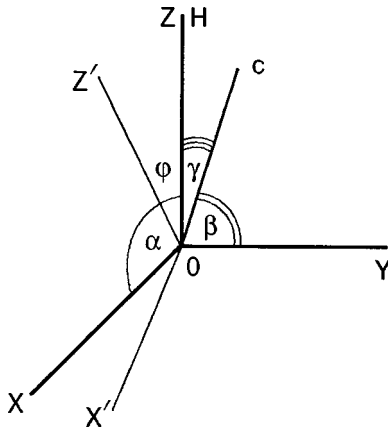
FIG. 1. Transformation of coordinate axes upon a rotation of the investigated sample about the Y-axis through an angle φ.

studying the anisotropy of the critical fields boils down to finding the quantities H_{c1}^{ab} and H_{c1}^{c} from the results of measurements for different orientations of the investigated sample relative to the external magnetic field vector **H** realized by rotating the texturized sample around one of the axes of the laboratory reference frame.

Suppose that the magnetic anisotropy axis (c-axis for HTSC) of a texturized sample (to be more precise, of the ''virtual'' crystal put in correspondence with the real sample, see above) forms angles α, β, and γ with the axes of the laboratory reference frame XYZ, and the magnetic field **H** is applied along the Z-axis. The direction in which H_{c1} is measured also coincides initially with this axis (Fig. 1). The initial value of the lower critical field $H_{c1}^{0}(\gamma)$ (for **H**∥Z) is defined by Eq. (2) written for the sake of convenience in the form

$$H_{c1}^{0} = H_{c1}^{c}[m+(1-m)\cos^2\gamma]^{-1/2}, \tag{4}$$

where $m = m^c/m^{ab}$.

Rotation of the crystal through an angle φ_i relative to the Y-axis of the laboratory reference frame transforms the orientation angles α, β, and γ to their new values (α_i, β_i, and γ_i) in accordance with the following familiar relations in crystal physics (see, for example, Ref. 12):

$$\begin{pmatrix} \cos\alpha_i \\ \cos\beta_i \\ \cos\gamma_i \end{pmatrix} = \begin{pmatrix} \cos\alpha \\ \cos\beta \\ \cos\gamma \end{pmatrix} \begin{pmatrix} \cos\varphi_i & 0 & \sin\varphi_i \\ 0 & 1 & 0 \\ -\sin\varphi_i & 0 & \cos\varphi_i \end{pmatrix}$$

$$= \begin{pmatrix} \cos\alpha\cos\varphi_i + \cos\gamma\sin\varphi_i \\ \cos\beta \\ -\cos\alpha\sin\varphi_i + \cos\gamma\cos\varphi_i \end{pmatrix}. \tag{5}$$

Naturally, the value of the critical field along the sample axis must also change in this case:

$$H_{c1}^{i}(\gamma_i) = H_{c1}^{c}[m+(1-m)(-\cos\alpha\sin\varphi_i$$
$$+ \cos\gamma\cos\varphi_i)^2]^{-1/2}. \tag{6}$$

We introduce the notation

$$h_i = [H_{c1}^{0}(\gamma)/H_{c1}^{i}(\gamma_i)]^2 = [m+(1-m)(-\cos\alpha\sin\varphi_i$$
$$+ \cos\gamma\cos\varphi_i)^2]/[m+(1-m)\cos^2\gamma].$$

Obviously, we have

$$m = \frac{(-\cos\alpha\sin\varphi_i + \cos\gamma\cos\varphi_i)^2 - h_i\cos^2\gamma}{h_i(1-\cos^2\gamma)-1+(-\cos\alpha\sin\varphi_i+\cos\gamma\cos\varphi_i)^2}. \tag{7}$$

It can be proved easily that the elimination of m from two equations of type (7) for $i=1,2$ (i.e., for a rotation of the sample through angles φ_1 and φ_2 relative to the Y-axis) leads to the equation

$$[(h_2-1)\sin^2\varphi_1 - (h_1-1)\sin^2\varphi_2]\cos^2\alpha + 2[(h_1$$
$$-1)\sin\varphi_2\cos\varphi_2 - (h_2$$
$$-1)\sin\varphi_1\cos\varphi_1]\cos\alpha[g\cos\gamma + (h_2-1)\cos^2\varphi_1$$
$$-(h_1-1)\cos^2\varphi_2 + h_1 - h_2]\cos^2\gamma = 0. \tag{8}$$

Using the notation

$$A_{12} = (h_2-1)\sin^2\varphi_1 - (h_1-1)\sin^2\varphi_2,$$

$$B_{12} = (h_1-1)\sin\varphi_2\cos\varphi_2 - (h_2-1)\sin\varphi_1\cos\varphi_1,$$

$$C_{12} = (h_2-1)\cos^2\varphi_1 - (h_1-1)\cos^2\varphi_2 + h_1 - h_2,$$

we can reduce Eq. (8) to a quadratic equation in $\cos\alpha$:

$$A_{12}\cos^2\alpha + 2B_{12}\cos\gamma\cos\alpha + C_{12}\cos^2\gamma = 0, \tag{9}$$

whose solution is given by

$$\cos\alpha = [-B_{12} \pm (B_{12}^2 - A_{12}C_{12})^{1/2}]\frac{\cos\gamma}{C_{12}} = D_{12}\cos\gamma, \tag{10}$$

where $D_{12} = [-B_{12} \pm (B_{12}^2 - A_{12}C_{12})^{1/2}]/C_{12}$.

Substituting the value of $\cos\alpha$ from (10) and repeating the procedure of eliminating m for $i=2,3$ ($\varphi_i = \varphi_2, \varphi_3$), we arrive at an equation linear in $\cos^2\gamma$ and having a solution in the form

$$\cos^2\gamma = \{h_2(-D_{12}\sin\varphi_3 + \cos\varphi_3)^2 - h_3(-D_{12}\sin\varphi_2$$
$$+ \cos\varphi_2)^2 + [(-D_{12}\sin\varphi_2 + \cos\varphi_2)^2 -$$
$$(-D_{12}\sin\varphi_3 + \cos\varphi_3)^2] + h_3 - h_2\}$$
$$\times [(-D_{12}\sin\varphi_2 + \cos\varphi_2)^4 - (-D_{12}\sin\varphi_3$$
$$+ \cos\varphi_3)^4]^{-1}. \tag{11}$$

Obviously, the case of conic texture,[13] for which a certain crystallographic direction (⟨001⟩, i.e., the c-axis for HTSC) forms a conic surface around a sample axis with the half-cone angle γ is more significant than the rather exotic case of an arbitrary texture. The ''limiting'' case for such a texture is a two-dimensional texture for which, say, the plane ab is parallel to the sample surface. (By the way, the actual situation in which HTSC ceramics are obtained by uniaxial compression of powders is quite close to this case.[14] More complex textures are obtained, for example, by applying a magnetic field to HTSC powders.[15]) Obviously, in this case $\alpha = \beta$ and
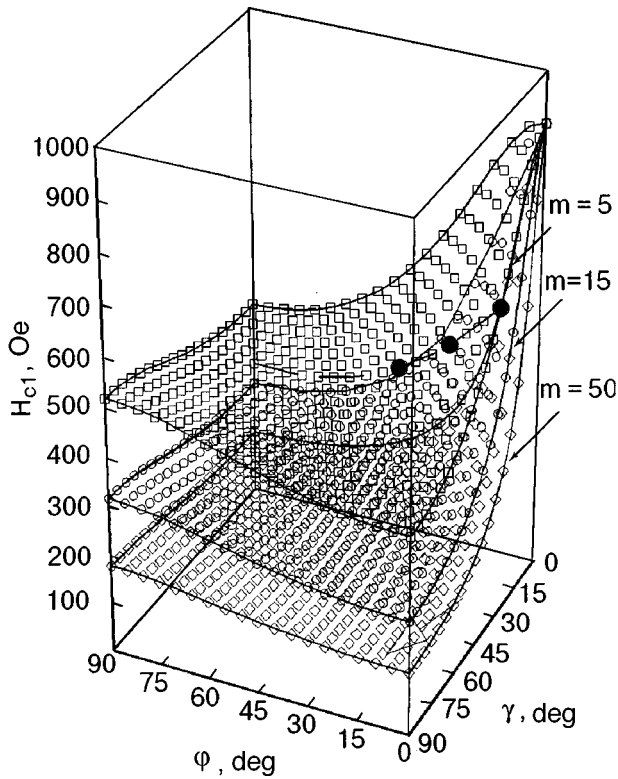
FIG. 2. Dependence of the lower critical field H_{c1} on the angle γ between the direction of the magnetic field **H** and the HTSC magnetic anisotropy axis c, as well as on the angle φ_i of rotation of the crystal about the Y-axis for various values of the parameter m^c/m^{ab}. The dashed curve was obtained as a result of scanning for $\gamma=$const in the interval $0<\varphi<90°$. The dark circles correspond to the values of $H_{c1}(\varphi_i)$ for which $\alpha, \beta, \gamma, H_{c1}^c, H_{c1}^{ab}, m^c/m^{ab}$ were calculated (see text).

$$\cos\alpha = \frac{1}{\sqrt{2}}\cos\beta\sin\gamma, \tag{12}$$

while the equation for the angular dependence of the critical field (6) is simplified considerably:

$$H_{c1}^i(\gamma) = H_{c1}^c\left[m + (1-m)\left(-\frac{1}{\sqrt{2}}\sin\gamma\sin\varphi_i + \cos\gamma\cos\varphi_i \right)^2 \right]^{-1/2}. \tag{13}$$

This equation describes the surface $H_{c1}(\gamma,\varphi)$ in the "experimental space" (γ,φ,H_{c1}). By way of an illustration, Fig. 2 shows the surfaces $H_{c1}(\gamma,\varphi)$ for a high-temperature superconductor with $H_{c1}^c = 900$ Oe and with the effective mass ratios m^c/m^{ab} equal to 5, 15, 50. The rotation of the object of investigation around the Y-axis of the laboratory reference frame corresponds to the motion over this surface along the plane curve $\gamma=$const.

Without going into details of calculations, we write the final result. Denoting

$$A_{12} = (h_2-1)\left(\cos^2\varphi_1 - \frac{1}{2}\sin^2\varphi_1 \right) - (h_1-1)\left(\cos^2\varphi_2 - \frac{1}{2}\sin^2\varphi_2 \right) + h_1 - h_2,$$

$$B_{12} = [(h_2-1)\sin^2\varphi_1 - (h_1-1)\sin^2\varphi_2]/2,$$

$$C_{12} = \sqrt{2}[(h_2-1)\sin\varphi_1\cos\varphi_1 - (h_1-1)\sin\varphi_2\cos\varphi_2],$$

we obtain the following equation in one unknown (γ)

$$A_{12}\cos^2\gamma + B_{12} = C_{12}\sin\gamma\cos\gamma, \tag{14}$$

which can be reduced to a simple biquadratic equation. The final solution has the form

$$\cos^2\gamma = \{ -(A_{12}B_{12}-C_{12}^2) \pm [(A_{12}B_{12}-C_{12}^2)^2 - (A_{12}^2 + C_{12}^2)B_{12}^2]^{1/2} \}/(A_{12}+C_{12}). \tag{15}$$

Thus, the measurement of the lower critical field for a texturized sample or nonoriented HTSC single crystal for four values of the angle of rotation ($\varphi_i=0, \varphi_1, \varphi_2, \varphi_3$) of the sample around an axis in the laboratory reference frame for an arbitrary texture, or for three values ($\varphi_i=0, \varphi_1, \varphi_2$) for a conic structure, allows us to determine the lower critical fields H_{c1}^c along the principal axis and H_{c1}^{ab} at right angles to it, as well as angles characterizing the orientation of the magnetic anisotropy axis c in the sample.

The results of mathematical simulation confirm the validity of the concepts developed here about the possibility of studying the anisotropy of lower critical fields of HTSC from the data on the critical fields for several angles of rotation of a statistically anisotropic (texturized) sample relative to an axis in the laboratory reference frame.[1)]

In conclusion, we can make the following remarks that are important in our opinion.

1. Apparently, the measurement of critical currents of texturized samples exposed to a magnetic field and oriented at different angles φ_i relative to the sample axes is the optimal approach for realizing the ideas developed here for studying the anisotropy of lower critical fields for HTSC.[11]
2. The approach developed for studying the anisotropy of H_{c1} requires a meticulous consideration of the demagnetization factor (it is assumed that the samples are close in shape to ellipsoids of revolution), i.e., a recalculation of all applied magnetic fields to "effective" fields H_{eff} according to the familiar relation

$$H_{eff} = H/(1-D), \tag{16}$$

where D is the demagnetization factor whose values are well known for ellipsoids.[16] For the case of rotation of an HTSC sample through an angle φ around the Y-axis of the laboratory reference frame considered by us (see Fig. 1), the quantity D_φ is defined as[17]

$$D_\varphi = D_Z \cos^2 \varphi + D_X \sin^2 \varphi, \qquad (17)$$

where D_Z and D_X are the values of D along Z- and X-axes respectively.[2)]

3. Obviously, the accuracy with which the quantities H_{c1}^c and H_{c1}^{ab} are determined depends on how strongly the statistical anisotropy (texture) is manifested in the object under investigation.

4. For any value of m^c/m^{ab}, the strongest angular dependence of critical fields must be observed for a field orientation close to $\mathbf{H} \| c$ (this can be seen clearly in Fig. 2).

5. Although we considered only the texture of HTSC samples, the values of H_{c1} are determined in actual practice by the type of surface texture for any measuring technique, which is much more perfect as a rule than the texture of the sample as a whole.[18]

At the present time, we are studying experimentally the anisotropy of lower critical fields on texturized HTSC samples of various compositions.

[*]E-mail: vasil@kipt.kharkov.ua(to:finkel)
[1)]Thus, an analysis of three ''experimental'' points on the surface m^c/m^{ab} = const (see Fig. 2) for the simpler case of a conic structure (the magnetic anisotropy axis c deviates by an angle γ from the Z-axis along which the magnetic field $\mathbf{H}$ was initially directed) based on the above formulas leads to the following initial values: $\alpha = \beta = 69.3°$, $\gamma = 30°$, $H_{c1}^c = 900$ Oe, $H_{c1}^{ab} = 402$ Oe, $m^c/m^{ab} = 5$.

[2)]Naturally, formula (17) is valid only when the applied field slightly exceeds H_{c1}, i.e., when the sample is in the Meissner region (except the surface layer of thickness $d \sim \lambda$.

[1] Y. Lye, Int. J. Mod. Phys. B **3**, 367 (1989); Comments Condens. Matter Phys. **16**, 89 (1992).

[2] E. Z. Meĭlikhov and V. G. Shapiro, Sverkhprovodimost: Fiz., Khim., Tekh. **4**, 1437 (1991).

[3] J. Nye, *Physical Properties of Crystals. Their Representation by Tensors and Matrices*, Oxford (1964).

[4] A. V. Balatskiĭ, L. I. Burlachkov, and L. P. Gor'kov, Zh. Éksp. Teor. Fiz. **90**, 1478 (1986) [Sov. Phys. JETP **63**, 866 (1986)].

[5] D. R. Tilley, Proc. Phys. Soc. **85**, 1177 (1965); E. I. Kats, Zh. Éksp. Teor. Fiz. **56**, 1675 (1969) [Sov. Phys. JETP **29**, 897 (1969)].

[6] W. Pint, M. Prohammer, and E. Schachinger, Physica C **162−164**, 801 (1989).

[7] C. Yang, J. S. Abell, and C. E. Gough, IEEE Trans. Supercond. **3**, 1671 (1993).

[8] D. Shaltiel, H. Bill, A. Grayevsky *et al.*, Phys. Rev. B **43**, 13 594 (1991).

[9] V. V. Moshchalkov, A. A. Zhukov, D. K. Petrov *et al.*, Physica C **166**, 185 (1990).

[10] I. M. Babich, G. P. Mikitik, and Yu. V. Sharlai, Fiz. Nizk. Temp. **20**, 227 (1994) [Low Temp. Phys. **20**, 220 (1994)].

[11] V. A. Finkel' and V. V. Toryanik, Fiz. Nizk. Temp. **23**, 824 (1997) [Low Temp. Phys. **23**, 618 (1997)].

[12] Yu. I. Sirotin and M. P. Shaskol'skaya, *Basic Principles of Crystal Physics* [in Russian], Nauka, Moscow (1975).

[13] Ya. S. Umanskiĭ, Yu. A. Skakov, A. N. Ivanov, and L. N. Rastorguev *Crystallography, X-ray Spectroscopy and Electron Microscopy* [in Russian], Metallurgiya, Moscow (1982).

[14] V. A. Finkel' and V. V. Toryanik, Functional Mater. **3**, 190 (1996).

[15] V. V. Toryanik and V. A. Finkel', Functional Mater. **1**, 5 (1994); V. V. Toryanik, V. A. Finkel', and V. V. Derevyanko, Fizika i Khimiya Obrabotki Mater. **No. 5**, 55 (1995).

[16] J. A. Osborn, Phys. Rev. **67**, 351 (1945).

[17] U. Yaron, I. Felner, and Y. Yeshurun, Phys. Rev. B **44**, 12 531 (1991).

[18] A. S. Kapcherin, I. I. Papirov, P. I. Stoev *et al.*, Sverkhprovodimost: Fiz., Khim., Tekh. **5**, 113 (1992).

Translated by R. S. Wadhwa

LOW-TEMPERATURE MAGNETISM

On the ground state of the Hubbard model with strong repulsion

Ju. V. Mikhailova

*State Research Institute of Thermal Engineering Instrumentation, 129085 Moscow, Russia**

The exact result is obtained for a square (cubic) Hubbard lattice with an infinitely large repulsion energy U: the ferromagnetic state with the maximum spin is not the ground state of the system if the number of holes is equal to two. © *1999 American Institute of Physics.*
[S1063-777X(99)00406-5]

INTRODUCTION

The Hubbard model that was initially introduced for explaining ferromagnetism is the simplest model describing compounds with a strong correlation coupling. The Hubbard Hamiltonian is usually written in the form

$$\hat{H} = -t \sum_{\langle i,j \rangle, \sigma} (\hat{c}_{i,\sigma}^+ \hat{c}_{j,\sigma} + \hat{c}_{j,\sigma}^+ \hat{c}_{i,\sigma}) + U \sum_i (n_{i\uparrow} n_{i\downarrow}),$$

where $c_{i,\sigma}^{(+)}(c_{i,\sigma})$ are the operators of electron creation (annihilation) at a lattice site i with a spin projection σ, $n_{i\sigma}$ is the number of electrons at site i with spin σ, and the summation over $\langle i,j \rangle$ is carried out over pairs of nearest neighbors. The presence of only two parameters (hopping t to an nearest site and the Coulomb repulsion energy U per site) makes the model extremely attractive for analysis.

The two-dimensional Hubbard model with infinite repulsion can be regarded as the zeroth approximation for the description of a large class of compounds with anomalous magnetic and electric properties, including high-temperature superconductors. For this reason, the origin of the ground state in this model is of utmost importance for understanding the mechanism of high-temperature superconductivity. The available data from the literature contain contradictory statements. All numerical investigations of cluster systems (see, for example, Refs. 1 and 2) give the same result: the ground state energy E_0 for a system with a fixed total spin S of particles is a monotonic function of S. In the case of a single hole, the ground state of the system corresponds to the maximum spin (saturated ferromagnetism) in the following cases: (1) free boundary; (2) even number of particles in each direction, and (3) positive hopping energy ($t > 0$). In this case, the ground-state energy is a monotonically decreasing function of S. If all the three conditions do not hold, the ground state corresponds to the minimum possible spin of particles, the value of $E_0(S)$ increasing with S. If the number of holes in the system is greater than unity, the ground state of the system corresponds to the minimum spin ($S = 0$ or $1/2$), and the ground-state energy is a monotonically increasing function of S. Nagaoka[3] considered a simple cubic (square) lattice only with periodic boundary conditions and even num-

ber of particles in each direction. He obtained an exact proof[3] of the maximum value of spin for the ground state energy for this case. The contents of the remaining part of Nagaoka's paper[3] is usually interpreted as follows: the ground state of a cubic lattice with a low concentration of holes is characterized by the maximum lattice spin (the state of saturated ferromagnetism) for all $U < U_{max}$. According to Nagaoka,[3] the limiting value U_{max} decreases upon an increase in the hole concentration. In fact, Nagaoka himself formulated his result in a somewhat different form: the ground state for a simple cubic lattice with a single hole and $U = \infty$ corresponds to the maximum spin; for finite values of U and the number of holes n, the ferromagnetic state with the maximum total spin is not the ground state if $\alpha n/N < t/U$ (N is the number of sites in the lattice), where α is a numerical parameter of the order of unity. This result was obtained by Nagaoka in the gas approximation for a low, but macroscopic hole concentration n/N. Formally, the case of two holes was not analyzed by him.[3]

In the present paper, the upper estimate of the difference $\Delta = E_0(S_{max} - 1) - E_0(S_{max})$ between the ground-state energy with a spin differing from the maximum spin by unity and the energy of the Nagaoka state is obtained for a periodic $3D$ ($2D$) lattice with an even number of sites in each direction. The estimate is obtained by the variational method. The value of $\tilde{\Delta} = \langle \Psi, (H - E_0(S_{max})) \Psi \rangle / \langle \Psi, \Psi \rangle$ is calculated, and the following results are obtained: $\Delta \leq -240\pi^2/227N^2$ for the $2D$ case and $\tilde{\Delta} \leq -120\pi^2/689N^{5/3}$ for a $3D$ lattice.

Thus, the spin of the ground state for a cubic (square) lattice does not have the maximum value if the number of holes is two.

BASIC EQUATIONS

We consider a rectangular $N_x \times N_y$ lattice and denoted by $N = N_x N_y$ the number of sites, by $\hat{a}^+(\hat{a})$ the creation (annihilation) operator of a particle with spin up at the ith site and by $\hat{b}_i^+(\hat{b}_i)$ the creation (annihilation) operator of a particle with spin down at the ith site. We assume that the system possesses translational invariance and consider states with a given quasimomentum $\alpha = (\alpha_x, \alpha_y, \alpha_z)$:

$$\alpha_x = \frac{2\pi}{N_x} i, \quad i = 0,1,..., N_x - 1;$$

$$\alpha_y = \frac{2\pi}{N_y} i, \quad i = 0,1,..., N_y - 1;$$

$$\alpha_z = \frac{2\pi}{N_z} i, \quad i = 0,1,..., N_z - 1.$$

For such states, we can indicate the complete set

$$\Phi_{ij} = \frac{1}{N^{1/2}} [1 + \exp(i\alpha_x)\hat{K}_x \exp(2i\alpha_x)\hat{K}_x^2 + ...$$

$$+ \exp(iN_{x-1}\alpha_x)\hat{K}_x^{N_x-1}][1$$

$$+ \exp(i\alpha_y)\hat{K}_y \exp(2i\alpha_y)\hat{K}_y^2 + ...$$

$$+ \exp(iN_{y-1}\alpha_y)\hat{K}_y^{N_y-1}][1$$

$$+ \exp(i\alpha_z)\hat{K}_z \exp(2i\alpha_z)\hat{K}_z^2 + ...$$

$$+ \exp(iN_{z-1}\alpha_z)\hat{K}_z^{N_z-1}]\hat{a}_i\hat{a}_j\Phi_0 \qquad (1)$$

or

$$\Phi_{ij} = \frac{1}{N^{1/2}} \sum_{j_x=1}^{N_x} \exp(ij_x\alpha_x)\hat{K}_x^{j_x} \sum_{j_y=1}^{N_y} \exp(ij_y\alpha_y)\hat{K}_y^{j_y}$$

$$\times \sum_{j_z=1}^{N_z} \exp(ij_z\alpha_z)\hat{K}_z^{j_z}\hat{a}_i\hat{a}_j\Phi_0, \qquad (1a)$$

where $\hat{K}_x(\hat{K}_y, \hat{K}_z)$ is the operator of translational shift by a site along $x(y,z)$; $\Phi_0 = \hat{b}_1^+ \hat{a}_2^+ ...\hat{a}_N^+ |\rangle$ being the empty state. The function Φ_{ij} describes a translation-invariant state with fixed distances between the flipped spin and each hole (equal to the separations between the first and the ith or jth lattice sites respectively). The translational shift operators $\hat{K}_x(\hat{K}_y, \hat{K}_z)$ are defined as

$$\hat{K}_x\Phi = \exp(-i\alpha_x)\Phi; \quad \hat{K}_y\Phi = \exp(-i\alpha_y)\Phi;$$

$$\hat{K}_z\Phi = \exp(-i\alpha_z)\Phi. \qquad (2)$$

The functions Φ_{ij} satisfy the following normalization conditions:

$$\langle\Phi_{ij}, \Phi_{lm}\rangle = \delta_{il}\delta_{jm} - \delta_{im}\delta_{jl}. \qquad (3)$$

We choose as base functions

$$\Omega_{\mathbf{k}_1,\mathbf{k}_2} = \frac{1}{N} \sum_{i,j} \Phi_{ij} \exp(i\mathbf{k}_1\mathbf{r}_i)\exp(i\mathbf{k}_2\mathbf{r}_j), \qquad (4)$$

where the set $\mathbf{k} = (k_x, k_y)$ coincides with the set of quasimomenta $\alpha = (\alpha_x, \alpha_y, \alpha_z)$ except for $k_x = k_y = k_z = 0$. The vector $\mathbf{k}$ can be treated as the momentum of a hole in the system in which the flipped spin is at rest.

The functions $\Omega_{\mathbf{k}_1,\mathbf{k}_2}$ are obviously antisymmetric in the indices $\mathbf{k}_1, \mathbf{k}_2$:

$$\Omega_{\mathbf{k}_1,\mathbf{k}_2} = -\Omega_{\mathbf{k}_1,\mathbf{k}_2}. \qquad (5)$$

Thus, the obvious requirement is satisfied: for a given quasimomentum α, we have $(N-1)(N-2)/2$ independent functions $\Omega_{\mathbf{k}_1,\mathbf{k}_2}$.

The following relations are worth noting:

$$\sum_{\mathbf{k}_1} \Omega_{\mathbf{k}_1,\mathbf{k}_2} = -\frac{1}{N} \sum_{i,j} \Phi_{ij} \exp(i\mathbf{k}_2\mathbf{r}_j) \qquad (6)$$

and similarly

$$\sum_{\mathbf{k}_2} \Omega_{\mathbf{k}_1,\mathbf{k}_2} = -\frac{1}{N} \sum_{i,j} \Phi_{ij} \exp(i\mathbf{k}_1\mathbf{r}_j), \qquad (7)$$

where the sum over $\mathbf{k}$ is taken over the $N-1$ quantities indicated above.

The functions Ω_{ij} satisfy the following normalization conditions:

$$\langle\Omega_{\mathbf{k}_1,\mathbf{k}_2}, \Omega_{\mathbf{p}_1,\mathbf{p}_2}\rangle = (\delta_{\mathbf{k}_1,\mathbf{p}_1}\delta_{\mathbf{k}_2,\mathbf{p}_1} - \delta_{\mathbf{k}_1,\mathbf{p}_2}\delta_{\mathbf{k}_2,\mathbf{p}_1})$$

$$-\frac{1}{N}(\delta_{\mathbf{k}_1,\mathbf{p}_1} + \delta_{\mathbf{k}_2,\mathbf{p}_2} - \delta_{\mathbf{k}_1,\mathbf{p}_2} - \delta_{\mathbf{k}_2,\mathbf{p}_1}). \qquad (8)$$

Besides, we can write

$$\langle\Omega_{\mathbf{k}_1,\mathbf{k}_2}, \Phi_{\mathbf{r}_1,\mathbf{r}_2}\rangle = \frac{1}{N}[\exp(-i\mathbf{k}_1\mathbf{r}_1 - i\mathbf{k}_2\mathbf{r}_2)$$

$$-\exp(-i\mathbf{k}_1\mathbf{r}_2 - i\mathbf{k}_2\mathbf{r}_1)]. \qquad (9)$$

Thus, the functions Φ_{ij} can be expressed in terms of $\Omega_{\mathbf{k}_1,\mathbf{k}_2}$ as follows:

$$\Phi_{ij} = \frac{1}{N} \sum_{\mathbf{k}_1,\mathbf{k}_2} \Omega_{\mathbf{k}_1,\mathbf{k}_2}[\exp(-i\mathbf{k}_1\mathbf{r}_i) - 1]$$

$$\times [\exp(-i\mathbf{k}_2\mathbf{r}_i) - 1]. \qquad (10)$$

The energy spectrum E is defined by the solution of the Schrödinger equation

$$\hat{H}\Psi = E\Psi, \qquad (11)$$

where $\hat{H}$ is the Hubbard Hamiltonian for $U = \infty$:

$$\hat{H} = t\sum_{i,j} [(\hat{a}_i^+\hat{a}_j + \hat{a}_j^+\hat{a}_i)(1 - \hat{b}_i^+\hat{b}_i)(1 - \hat{b}_j^+\hat{b}_j) + (\hat{b}_i^+\hat{b}_j$$

$$+ \hat{b}_j^+\hat{b}_i)(1 - \hat{a}_i^+\hat{a}_i)(1 - \hat{a}_j^+\hat{a}_j)] \qquad (12)$$

or

$$\hat{H} = t\sum_{i,j,\sigma} \hat{X}_i^{\sigma 0}\hat{X}_j^{0\sigma}, \qquad (12a)$$

where $\hat{X}_i^{\sigma 0}(\hat{X}_i^{0\sigma})$ are Hubbard operators. Summation in (12) and (12a) is carried out over nearest neighbors. In the subsequent analysis, we take the quantity t as the energy unit, i.e., we assume in (12) that $t = 1$.

We write the wave function Ψ in the form of an expansion in the set $\Omega_{\mathbf{k}_1,\mathbf{k}_2}$:

$$\Psi = \sum_{\mathbf{k}_1,\mathbf{k}_2} c_{\mathbf{k}_1,\mathbf{k}_2}\Omega_{\mathbf{k}_1,\mathbf{k}_2}. \qquad (13)$$

For the action of the operator $\hat{H}$ on the functions $\Omega_{\mathbf{k}_1,\mathbf{k}_2}$ we have

$$\Gamma_{\mathbf{k}_1,\mathbf{k}_2}=\hat{H}\Omega_{\mathbf{k}_1,\mathbf{k}_2};$$

$$\Gamma_{\mathbf{k}_1\mathbf{k}_2}=-\varepsilon_{\mathbf{k}_1,\mathbf{k}_2}\Omega_{\mathbf{k}_1,\mathbf{k}_2}+\Delta_{\mathbf{k}_1,\mathbf{k}_2}, \tag{14}$$

$$\Delta_{\mathbf{k}_1,\mathbf{k}_2}=\frac{2}{N}\sum_{\mathbf{p}}(\Omega_{\mathbf{k}_1\mathbf{p}}+\Omega_{\mathbf{p}\mathbf{k}_2})\{[\cos p_x-\gamma_x\cos(\alpha_x-k_{1x}$$

$$-k_{2x}-p_x)-1+\gamma_x\cos(\alpha_x-k_{1x}-k_{2x})]$$

$$+[\cos p_y-\gamma_y\cos(\alpha_y-k_{1y}-k_{2y}-p_y)-1$$

$$+\gamma_y\cos(\alpha_y-k_{1y}-k_{2y})]+[\cos p_z-\gamma_z\cos(\alpha_z$$

$$-k_{1z}-k_{2z}-p_z)-1+\gamma_z\cos(\alpha_z-k_{1z}-k_{2z})]\}. \tag{15}$$

Here

$$\varepsilon_{\mathbf{k}_1,\mathbf{k}_2}=\varepsilon_{\mathbf{k}_1}+\varepsilon_{\mathbf{k}_2}, \quad \varepsilon_{\mathbf{k}}=2(\cos k_x+\cos k_y). \tag{16}$$

VARIATIONAL ESTIMATES

If trial wave functions are used in the form (13), it is more convenient to obtain an estimate for the maximum eigenvalue of Hamiltonian (12).

In view of periodicity of the lattice and the evenness of the number of lattice sites in the given direction, the Hamiltonian of the system reverses its sign ($\hat{H}\leftrightarrow-\hat{H}$) upon the substitution $\hat{a}_i^+\leftrightarrow\hat{a}_i^+(-1)^i$, $\hat{a}_i\leftrightarrow\hat{a}_i(-1)^i$ and $\hat{b}_i^+\leftrightarrow\hat{b}_i^+(-1)^i$, $\hat{b}_i\leftrightarrow\hat{b}_i(-1)^i$. This means than the energy spectrum E does not depend on the choice of t. Consequently, the proof of the fact that the maximum eigenvalue $E_{\max}$ is larger than a certain quantity Λ automatically leads to the inequality $E_{\min}<-\Lambda$.

Let us consider trial wave functions for which $c_{\mathbf{k}_1,\mathbf{k}_2}$ differ from zero only if one of the vectors $\mathbf{k}_1$ or $\mathbf{k}_2$ is equal to $\mathbf{p}_0=(p_x,p_y,p_z)=(\pi,\pi,\pi)$, while the other is equal to any of the possible six vectors:

$$\mathbf{p}_1=(\pi,\pi,\pi+2\pi/L), \quad \mathbf{p}_2=(\pi,\pi,\pi-2\pi/L),$$

$$\mathbf{p}_3=(\pi,\pi+2\pi/L,\pi), \quad \mathbf{p}_4=(\pi,\pi-2\pi/L,\pi),$$

$$\mathbf{p}_5=(\pi+2\pi/L,\pi,\pi), \quad \mathbf{p}_6=(\pi-2\pi/L,\pi,\pi),$$

where $L=N^{1/3}$. (17)

The vectors $\mathbf{p}_i$ are chosen so that the energy of two free quasiparticles for any $\mathbf{p}_i$ is equal to the maximum energy of $N-2$ particles with the total spin $S=S_{\max}$:

$$\varepsilon_0=-\varepsilon_{\mathbf{p}_0,\mathbf{p}_i}=10+2\cos\frac{2\pi}{L}\cong12\left(1-\frac{\pi^2}{3N^{2/3}}\right). \tag{18}$$

Consequently, the following coefficients $c_{\mathbf{k}_1,\mathbf{k}_2}$ have nonzero values:

$$c_{\mathbf{p}_1,\mathbf{p}_0}=\gamma_1, \quad c_{\mathbf{p}_2,\mathbf{p}_0}=\gamma_2, \quad c_{\mathbf{p}_3,\mathbf{p}_0}=\delta_1,$$

$$c_{\mathbf{p}_4,\mathbf{p}_0}=\delta_2, \quad c_{\mathbf{p}_5,\mathbf{p}_0}=\lambda_1, \quad c_{\mathbf{p}_6,\mathbf{p}_0}=\lambda_2,$$

$$c_{\mathbf{p}_0,\mathbf{p}_1}=-\gamma_1, \quad c_{\mathbf{p}_0,\mathbf{p}_2}=-\gamma_2, \quad c_{\mathbf{p}_0,\mathbf{p}_3}=-\delta_1,$$

$$c_{\mathbf{p}_0,\mathbf{p}_4}=-\delta_2, \quad c_{\mathbf{p}_0,\mathbf{p}_5}=-\lambda_1, \quad c_{\mathbf{p}_0,\mathbf{p}_6}=-\lambda_2. \tag{19}$$

We shall treat the coefficients γ_i, δ_i, and λ_i as variational parameters. According to formula (A14) from Appendix, the quantity $\Delta=\langle\Psi,(H-E_0(S_{\max}))\Psi\rangle/\langle\Psi,\Psi\rangle$ can be calculated in terms of the quantities $f_i(\mathbf{p})$. For $X=\langle\Psi,\hat{H}\Psi\rangle$, we have

$$X-\varepsilon_0\langle\Psi,\Psi\rangle=\frac{8}{N}|f_0(\mathbf{p}_0)|^2\left[3-\left(1-\cos\frac{2\pi}{L}\right)\right]$$

$$+\frac{8}{N}[|f_2(\mathbf{p}_0)|+|f_4(\mathbf{p}_0)|^2+|f_6(\mathbf{p}_0)|^2]$$

$$+\frac{16}{N}\operatorname{Re}f_0(\mathbf{p}_0)[f_2^*(\mathbf{p}_0)+f_4^*(\mathbf{p}_0)$$

$$+f_2^*(\mathbf{p}_0)]-\frac{8}{N}\sum_{\mathbf{k}1}|f_2(\mathbf{k}_1)|^2[\cos(k_{1x}$$

$$-\alpha_x)+1]-\frac{8}{N}\sum_{\mathbf{k}1}|f_4(\mathbf{k}_1)|^2[\cos(k_{1y}$$

$$-\alpha_y)+1]-\frac{8}{N}\sum_{\mathbf{k}1}|f_6(\mathbf{k}_1)|^2[\cos(k_{1z}$$

$$-\alpha_z)+1]+\frac{16}{N}\operatorname{Re}f_2^*(\mathbf{p}_0)f_1(\mathbf{p}_0)\sin\alpha_x$$

$$+\frac{16}{N}\operatorname{Re}f_4^*(\mathbf{p}_0)f_3(\mathbf{p}_0)\sin\alpha_y$$

$$+\frac{16}{N}\operatorname{Re}f_6^*(\mathbf{p}_0)f_5(\mathbf{p}_0)\sin\alpha_z$$

$$-\frac{8}{N}|f_1(\mathbf{p}_0)|^2\cos\alpha_x$$

$$-\frac{8}{N}|f_3(\mathbf{p}_0)|^2\cos\alpha_y$$

$$-\frac{8}{N}|f_5(\mathbf{p}_0)|^2\cos\alpha_z. \tag{20}$$

Denoting $\Delta=X-\varepsilon_0\langle\Psi,\Psi\rangle$, $\beta=2\pi/L$, we obtain the following expression correct to $O(1/N^{5/3})$:

$$\Delta=-\frac{4}{N}|f_0(\mathbf{p}_0)|^2[\beta^2+\alpha_x^2+\alpha_y^2+\alpha_z^2]-\frac{4}{N}|f_0(\mathbf{p}_1)|^2[\alpha_x^2$$

$$+\alpha_y^2+(\beta-\alpha_z)^2]-\frac{4}{N}|f_0(\mathbf{p}_2)|^2[\alpha_x^2+\alpha_y^2+(\beta$$

$$+\alpha_z)^2]-\frac{4}{N}|f_0(\mathbf{p}_3)|^2[\alpha_x^2+\alpha_z^2+(\beta-\alpha_y)^2]$$

$$-\frac{4}{N}|f_0(\mathbf{p}_4)|^2[\alpha_x^2+\alpha_z^2+(\beta+\alpha_y)]-\frac{4}{N}|f_0(\mathbf{p}_5)|^2[\alpha_y^2$$

$$+\alpha_z^2+(\beta-\alpha_x)^2]-\frac{4}{N}|f_0(\mathbf{p}_6)|^2[\alpha_y^2+\alpha_z^2+(\beta$$

$$+\alpha_x)^2] - \frac{16}{N}\operatorname{Re}f_0^*(\mathbf{p}_0)\{[f_0(\mathbf{p}_5) - f_0(\mathbf{p}_6)]\alpha_x$$

$$+[f_0(\mathbf{p}_3) - f_0(\mathbf{p}_4)]\alpha_y + [f_0(\mathbf{p}_1) - f_0(\mathbf{p}_2)]\alpha_z\}$$

$$-\frac{8\beta^2}{N}\{[f_0(\mathbf{p}_1) - f_0(\mathbf{p}_2)]^2 + [f_0(\mathbf{p}_3) - f_0(\mathbf{p}_4)]^2$$

$$+[f_0(\mathbf{p}_5) - f_0(\mathbf{p}_6)]^2\}. \tag{21}$$

For $\alpha_x = 2\beta$ and $\alpha_y = \alpha_z = 0$, we have

$$\Delta = -\frac{20\beta^2}{N}\{|f_0(\mathbf{p}_0)|^2 + |f_0(\mathbf{p}_1)|^2 + |f_0(\mathbf{p}_2)|^2 + |f_0(\mathbf{p}_3)|^2$$

$$+|f_0(\mathbf{p}_4)|^2\} - \frac{4\beta^2}{N}|f_0(\mathbf{p}_5)|^2 - \frac{36\beta^2}{N}|f_0(\mathbf{p}_6)|^2$$

$$-\frac{32\beta^2}{N}\operatorname{Re}f_0^*(\mathbf{p}_0)[f_0(\mathbf{p}_5) - f_0(\mathbf{p}_6)] - \frac{8\beta^2}{N}\{[f_0(\mathbf{p}_1)$$

$$-f_0(\mathbf{p}_2)]^2 + [f_0(\mathbf{p}_3) - f_0(\mathbf{p}_4)]^2 + [f_0(\mathbf{p}_5)$$

$$-f_0(\mathbf{p}_6)]^2\}. \tag{22}$$

Let us suppose that $f_0(\mathbf{p}_1) = f_0(\mathbf{p}_2) = f_0(\mathbf{p}_3) = f_0(\mathbf{p}_4)$, $f_0(\mathbf{p}_6) = 0$. This gives

$$\Delta = -\frac{20\beta^2}{N}\{|f_0(\mathbf{p}_0)|^2 + 4|f_0(\mathbf{p}_1)|^2\} - \frac{4\beta^2}{N}|f_0(\mathbf{p}_5)|^2$$

$$-\frac{32\beta^2}{N}\operatorname{Re}f_0^*(\mathbf{p}_0)f_0(\mathbf{p}_5) - \frac{8\beta^2}{N}|f_0(\mathbf{p}_5)|^2. \tag{23}$$

We denote

$$f_0(\mathbf{p}_0) = -x; \quad f_0(\mathbf{p}_5) = y; \quad f_0(\mathbf{p}_1) = \frac{x - y}{4}, \tag{24}$$

so that

$$X - \varepsilon_0\langle\Psi,\Psi\rangle = -\frac{25\alpha^2}{N}\left(x - \frac{21}{25}y\right)^2 + \frac{16\alpha^2}{25N}y^2. \tag{25}$$

The maximum value of the quantity $\tilde{\Delta} = \max[(X - \varepsilon_0\langle\Psi,\Psi\rangle)/\langle\Psi,\Psi\rangle]$ is attained for $x - 21/25\,y \approx 4/625\,y$ and is equal to

$$\max\frac{X - \varepsilon_0\langle\Psi,\Psi\rangle}{\langle\Psi,\Psi\rangle} \approx \frac{100\beta^2}{629N}. \tag{26}$$

to a high degree of accuracy. Consequently, the maximum value of energy exceeds ε_0 by a quantity larger than

$$\Delta\varepsilon \cong \frac{400\pi^2}{629N^{5/3}}. \tag{27}$$

This means that a system with two holes is characterized by the energy level E^+ such that

$$E^+ \geq \varepsilon_0 + \frac{400\pi^2}{629N^{5/3}}. \tag{28}$$

In view of the symmetry of the energy spectrum relative to the sign reversal of t from (28) mentioned above, a system with two holes also has an energy level E^- such that

$$E^- \leq -\varepsilon_0 - \frac{400\pi^2}{629N^{5/3}}. \tag{29}$$

Similar calculations in the $2D$ case lead to

$$\tilde{\Delta} = \frac{\langle\Psi,[\hat{H} - E_0(S_{\max})]\Psi\rangle}{\langle\Psi,\Psi\rangle} \leq -\frac{240\pi^2}{227N^2}. \tag{30}$$

CONCLUSION

In accordance with inequalities (29) and (30), the ground state of a system with two holes corresponds to the total particle spin S smaller than the maximum possible value. In this paper, we choose trial functions with $S = S_{\max} - 1$. Even in this case, the ground state is smaller than the Nagaoka state. For states with smaller values of S the estimates (29) and (30) can probably be enhanced.

The results of this research prove that the state of saturated ferromagnetism is not the ground state for a system with two holes.

This conclusion does not at all contradict the results obtained by Nagaoka.[3] It should be emphasized in this connection that Nagaoka proved that the ground state of a system with $U = \infty$ and a single hole, which corresponds to saturated ferromagnetism, is characterized by a smaller S for a larger number of holes and for $U < U_0$. Thus, Nagaoka[3] proved the absence of saturated ferromagnetism. His proof was based on the assumption concerning the structure of the wave function, which is not necessarily correct

in the case when the ground state of a system with the maximum spin and a preset total value of spin projection is degenerate. Thus, Nagaoka formulated the sufficient ($U < U_0$) but not necessary condition for the absence of saturated ferromagnetism; the wave function under the condition of nondegeneracy of the ground state of a system with the maximum value of spin is sought in a quite definite form. In the case of two holes, the ground state of the system with the maximum spin is degenerate, and hence the wave function of the ground state can differ from that obtained by Nagaoka. This concerns the $2D$ as well as $3D$ cases. The trial function used by us here can be obtained as a solution of the secular equation for the zeroth-approximation function in the expansion in low density (in $1/N$ in the given case).

APPENDIX

In order to calculate the quantity

$$\Delta = \langle\Psi,\hat{H}\Psi\rangle/\langle\Psi,\Psi\rangle, \tag{A1}$$

we obtain expressions for the normalization $\langle\Psi,\Psi\rangle$ and $X = \langle\Psi,\hat{H}\Psi\rangle$ in terms of the coefficients $c_{\mathbf{k}_1,\mathbf{k}_2}$ in the expansion of the wave function (11).

Taking into account (6) and (7), we obtain the following expression for the normalization of the wave function $\langle\Psi,\Psi\rangle$:

$$\langle \Psi, \Psi \rangle = 2 \sum_{\mathbf{k}_1, \mathbf{k}_2} |c_{\mathbf{k}_1, \mathbf{k}_2}|^2 - \frac{4}{N} \sum_{\mathbf{k}_1} \left| \sum_{\mathbf{k}_p} c_{\mathbf{k}_1 \mathbf{k}_p} \right|^2. \tag{A2}$$

Denoting

$$\varepsilon(\mathbf{k}) = -2(\cos k_x + \cos k_y), \tag{A3}$$

$$f_0(\mathbf{k}) = \sum_{\mathbf{p}} c_{\mathbf{kp}}; \quad f_2(\mathbf{k}) = \sum_{\mathbf{p}} c_{\mathbf{kp}} \cos p_x;$$

$$f_4(\mathbf{k}) = \sum_{\mathbf{p}} c_{\mathbf{kp}} \cos p_y; \quad f_6(\mathbf{k}) = \sum_{\mathbf{p}} c_{\mathbf{kp}} \cos p_z, \tag{A4}$$

$$f_1(\mathbf{k}_1) = \sum_{\mathbf{p}} c_{\mathbf{k}_1 \mathbf{p}} \sin p_x; \quad f_3(\mathbf{k}_1) = \sum_{\mathbf{p}} c_{\mathbf{k}_1 \mathbf{p}} \sin p_y;$$

$$f_5(\mathbf{k}_1) = \sum_{\mathbf{p}} c_{\mathbf{k}_1 \mathbf{p}} \sin p_z, \tag{A5}$$

we obtain

$$\langle \Psi, \Psi \rangle = 2 \sum_{\mathbf{k}_1 \mathbf{k}_2} |c_{\mathbf{k}_1 \mathbf{k}_2}|^2 - \frac{4}{N} \sum_{\mathbf{k}_1} |f_0(\mathbf{k}_1)|^2. \tag{A6}$$

Similarly, for $X = \langle \Psi, \hat{H} \Psi \rangle$ we obtain

$$X = X_1 + X_2,$$

$$X_1 = -\sum_{\mathbf{k}_1 \mathbf{k}_2 \mathbf{p}_1 \mathbf{p}_2} c^*_{\mathbf{p}_1 \mathbf{p}_2} c_{\mathbf{k}_1 \mathbf{k}_2} \varepsilon_{\mathbf{k}_1 \mathbf{k}_2} \langle \Omega_{\mathbf{p}_2 \mathbf{p}_2}, \Omega_{\mathbf{k}_1 \mathbf{k}_2} \rangle$$

$$= -2 \sum_{\mathbf{k}_1 \mathbf{k}_2} \varepsilon_{\mathbf{k}_1 \mathbf{k}_2} |c_{\mathbf{k}_1 \mathbf{k}_2}|^2 - \frac{4}{N} \sum_{\mathbf{k}_1 \mathbf{k}_2 \mathbf{p}_1} \varepsilon_{\mathbf{k}_1 \mathbf{k}_2} c^*_{\mathbf{k}_1 \mathbf{p}_1} c_{\mathbf{k}_1 \mathbf{k}_2},$$

$$X_2 = \sum_{\mathbf{k}_1 \mathbf{k}_2 \mathbf{p}_1 \mathbf{p}_2} c^*_{\mathbf{p}_1 \mathbf{p}_2} c_{\mathbf{k}_1 \mathbf{k}_2} \langle \Omega_{\mathbf{p}_1 \mathbf{p}_2}, \Delta_{\mathbf{k}_1 \mathbf{k}_2} \rangle. \tag{A7}$$

Substituting expression (15) for $\Delta_{\mathbf{k}_1, \mathbf{k}_2}$, we get

$$X_2 = \frac{2}{N} \sum_{\mathbf{k}_1, \mathbf{k}_2, \mathbf{p}_1, \mathbf{p}_2, \mathbf{p}} c^*_{\mathbf{p}_1 \mathbf{p}_2} c_{\mathbf{k}_1 \mathbf{k}_2} \langle \Omega_{\mathbf{p}_1 \mathbf{p}_2}, \Omega_{\mathbf{k}_1 \mathbf{p}} + \Omega_{\mathbf{p} \mathbf{k}_2} \rangle$$

$$\times [\cos p_x + \cos p_y + \cos p_z - 3 - \gamma_x \cos(\alpha_x - k_{1x} - k_{2x} - p_x) - \gamma_y \cos(\alpha_y - k_{1y} - k_{2y} - p_y)$$

$$- \gamma_z \cos(\alpha_z - k_{1z} - k_{2z} - p_z) + \gamma_x \cos(\alpha_x - k_{1x} - k_{2x}) + \gamma_y \cos(\alpha_y - k_{1y} - k_{2y}) + \gamma_z \cos(\alpha_z - k_{1z} - k_{2z}]$$

or, using antisymmetry of the coefficients $c_{\mathbf{k}_1, \mathbf{k}_2}$ and the functions $\Omega_{\mathbf{k}_1, \mathbf{k}_2}$ as well as the symmetry of the expression in the brackets relative to the substitution $\mathbf{k}_1 \leftrightarrow \mathbf{k}_2$, we obtain

$$X_2 = \frac{4}{N} \sum_{\mathbf{k}_1, \mathbf{k}_2, \mathbf{p}_1, \mathbf{p}_2, \mathbf{p}} c^*_{\mathbf{p}_1 \mathbf{p}_2} c_{\mathbf{k}_1 \mathbf{k}_2} \langle \Omega_{\mathbf{p}_1 \mathbf{p}_2}, \Omega_{\mathbf{k}_1 \mathbf{p}} \rangle [\cos p_x$$

$$+ \cos p_y + \cos p_z - 3 - \gamma_x \cos(\alpha_x - k_{1x} - k_{2x} - p_x)$$

$$- \gamma_y \cos(\alpha_y - k_{1y} - k_{2y} - p_y) - \gamma_z \cos(\alpha_z - k_{1z} - k_{2z}$$

$$- p_z) + \gamma_x \cos(\alpha_x - k_{1x} - k_{2x}) + \gamma_y \cos(\alpha_y - k_{1y}$$

$$- k_{2y}) + \gamma_z \cos(\alpha_z - k_{1z} - k_{2z})]. \tag{A8}$$

Taking into account the normalization condition (6), we obtain

$$X_2 = X_2^1 + X_2^2, \tag{A9}$$

where

$$X_2^1 = \frac{8}{N} \sum_{\mathbf{k}_1, \mathbf{k}_2, \mathbf{p}} c^*_{\mathbf{k}_1 \mathbf{p}} c_{\mathbf{k}_1 \mathbf{k}_2} [\cos p_x + \cos p_y + \cos p_z - 3$$

$$- \gamma_x \cos(\alpha_x - k_{1x} - k_{2x} - p_x) - \gamma_y \cos(\alpha_y - k_{1y}$$

$$- k_{2y} - p_y) - \gamma_z \cos(\alpha_z - k_{1z} - k_{2z} - p_z) + \gamma_x \cos(\alpha_x$$

$$- k_{1x} - k_{2x}) + \gamma_y \cos(\alpha_y - k_{1y} - k_{2y}) + \gamma_z \cos(\alpha_z$$

$$- k_{1z} - k_{2z})],$$

$$X_2^2 = -\frac{8}{N^2} \sum_{\mathbf{k}_1, \mathbf{k}_2, \mathbf{p}_2, \mathbf{p}} c^*_{\mathbf{k}_1 \mathbf{p}_2} c_{\mathbf{k}_1 \mathbf{k}_2} [\cos p_x + \cos p_y + \cos p_z$$

$$- 3 - \gamma_x \cos(\alpha_x - k_{1x} - k_{2x} p_x) - \gamma_y \cos(\alpha_y - k_{1y}$$

$$- k_{2y} - p_y) - \gamma_z \cos(\alpha_z - k_{1z} - k_{2z} - p_z) + \gamma_x \cos(\alpha_x$$

$$- k_{1x} - k_{2x}) + \gamma_y \cos(\alpha_y - k_{1y} - k_{2y}) + \gamma_z \cos(\alpha_z$$

$$- k_{1z} - k_{2z})] \tag{A10}$$

or, carrying out summation over $\mathbf{p}$ for X_2^2, obtain

$$X_2^2 = \frac{8}{N} \sum_{\mathbf{k}_1, \mathbf{k}_2, \mathbf{p}_2} c^*_{\mathbf{k}_1 \mathbf{p}_2} c_{\mathbf{k}_1 \mathbf{k}_2} [3 - \gamma_x \cos(\alpha_x - k_{1x} - k_{2x})$$

$$- \gamma_y \cos(\alpha_y - k_{1y} - k_{2y}) - \gamma_z \cos(\alpha_z - k_{1z} - k_{2z})]. \tag{A11}$$

Consequently, we have

$$X_2 = \frac{8}{N} \sum_{\mathbf{k}_1, \mathbf{k}_2, \mathbf{p}} c^*_{\mathbf{k}_1 \mathbf{p}} c_{\mathbf{k}_1 \mathbf{k}_2} [\cos p_x - \gamma_x \cos(\alpha_x - k_{1x} - k_{2x}$$

$$- p_x) + \cos p_y - \gamma_y \cos(\alpha_y - k_{1y} - k_{2y} - p_y) + \cos p_z$$

$$- \gamma_z \cos(\alpha_z - k_{1z} - k_{2z} - p_z)]. \tag{A12}$$

The quantity X_2 can be expressed in terms of the quantities $f_i(\mathbf{k}_j)$ as follows:

$$X_2 = \frac{8}{N} \sum_{\mathbf{k}_1} (f_2^*(\mathbf{k}_1) + f_4^*(\mathbf{k}_1) + f_6^*(\mathbf{k}_1)) f_0(\mathbf{k}_1)$$

$$- \frac{8\gamma_x}{N} \sum_{\mathbf{k}_1} |f_2(\mathbf{k}_1)|^2 \cos(\alpha_x - k_{1x})$$

$$- \frac{8\gamma_y}{N} \sum_{\mathbf{k}_1} |f_4(\mathbf{k}_1)|^2 \cos(\alpha_{yx} - k_{1y})$$

$$- \frac{8\gamma_z}{N} \sum_{\mathbf{k}_1} |f_6(\mathbf{k}_1)|^2 \cos(\alpha_z - k_{1z})$$

$$- \frac{16\gamma_x}{N} \text{Re} \sum_{\mathbf{k}_1} f_2^*(\mathbf{k}_1) f_1(\mathbf{k}_1) \sin(\alpha_x - k_{1x})$$

$$- \frac{16\gamma_y}{N} \text{Re} \sum_{\mathbf{k}_1} f_4^*(\mathbf{k}_1) f_3(\mathbf{k}_1) \sin(\alpha_y - k_{1y})$$

$$-\frac{16\gamma_z}{N}\text{Re}\sum_{\mathbf{k}_1} f_6^*(\mathbf{k}_1)f_5(\mathbf{k}_1)\sin(\alpha_z-k_{1z})$$

$$-\frac{8\gamma_x}{N}\sum_{\mathbf{k}_1} |f_1(\mathbf{k}_1)|^2\sin(\alpha_x-k_{1x})$$

$$-\frac{8\gamma_x}{N}\sum_{\mathbf{k}_1} |f_3(\mathbf{k}_1)|^2\sin(\alpha_y-k_{1y})$$

$$-\frac{8\gamma_y}{N}\sum_{\mathbf{k}_1} |f_1(\mathbf{k}_1)|^2\cos(\alpha_y-k_{1y}). \tag{A13}$$

Consequently, for the quantity $X=\langle\Psi,\hat{H}\Psi\rangle$ we have

$$X=-2\sum_{\mathbf{k}_1\mathbf{k}_2} \varepsilon_{\mathbf{k}_1\mathbf{k}_2}|c_{\mathbf{k}_1\mathbf{k}_2}|^2+\frac{8}{N}\sum_{\mathbf{k}_1} (\cos k_{1x}+\cos k_{1y}$$

$$+\cos k_{1z})|f_0(\mathbf{k}_1)|^2+\frac{16}{N}\sum_{\mathbf{k}_1} \text{Re}\,f_0(\mathbf{k}_1)[f_2^*(\mathbf{k}_1)$$

$$+f_4^*(\mathbf{k}_1)+f_6^*(\mathbf{k}_1)]-\frac{8\gamma_x}{N}\sum_{\mathbf{k}_1} |f_2(\mathbf{k}_1)|^2\cos(k_{1x}$$

$$-\alpha_x)-\frac{8\gamma_y}{N}\sum_{\mathbf{k}_1} |f_4(\mathbf{k}_1)|^2\cos(k_{1y}-\alpha_y)$$

$$-\frac{8\gamma_z}{N}\sum_{\mathbf{k}_1} |f_6(\mathbf{k}_1)|^2\cos(k_{1z}-\alpha_z)$$

$$+\frac{16\gamma_x}{N}\text{Re}\sum_{\mathbf{k}_1} f_2^*(\mathbf{k}_1)f_1(\mathbf{k}_1)\sin(k_{1x}-\alpha_x)$$

$$+\frac{16\gamma_y}{N}\text{Re}\sum_{\mathbf{k}_1} f_4^*(\mathbf{k}_1)f_3(\mathbf{k}_1)\sin(k_{1y}-\alpha_y)$$

$$+\frac{16\gamma_z}{N}\text{Re}\sum_{\mathbf{k}_1} f_6^*(\mathbf{k}_1)f_5(\mathbf{k}_1)\sin(k_{1z}-\alpha_z)$$

$$+\frac{8\gamma_x}{N}\sum_{\mathbf{k}_1} |f_1(\mathbf{k}_1)|^2\cos(k_{1x}-\alpha_x)$$

$$+\frac{8\gamma_y}{N}\sum_{\mathbf{k}_1} |f_3(\mathbf{k}_1)|^2\cos(k_{1y}-\alpha_y)$$

$$+\frac{8\gamma_z}{N}\sum_{\mathbf{k}_1} |f_5(\mathbf{k}_1)|^2\cos(k_{1z}-\alpha_z). \tag{A14}$$

It is worth noting the case when the expansion (11) of the wave function Ψ contain only terms with hole momenta $\mathbf{p}_1$ and $\mathbf{p}_2$, i.e.,

$$c_{\mathbf{k}_1\mathbf{k}_2}=\delta_{\mathbf{k}_1\mathbf{p}_1}\delta_{\mathbf{k}_2\mathbf{p}_2}-\delta_{\mathbf{k}_1\mathbf{p}_2}\delta_{\mathbf{k}_2\mathbf{p}_1}. \tag{A15}$$

In this case, we have

$$f_0(\mathbf{p}_1)=1; \quad f_0(\mathbf{p}_2)=-1; \quad f_2(\mathbf{p}_1)=\cos p_{2x};$$

$$f_2(\mathbf{p}_2)=-\cos p_{1x}; \quad f_4(\mathbf{p}_1)=\cos p_{2y};$$

$$f_4(\mathbf{p}_2)=-\cos p_{1y}; \quad f_6(\mathbf{p}_1)=\cos p_{2x};$$

$$f_6(\mathbf{p}_2)=-\cos p_{1x}; \quad f_1(\mathbf{p}_1)=\sin p_{2x};$$

$$f_1(\mathbf{p}_2)=-\sin p_{2x};$$

$$f3(\mathbf{p}1)=\sin p2y; \quad f3(\mathbf{p}2)=-\sin p2y;$$

$$f_5(\mathbf{p}_1)=\sin p_{2z}; \quad f_5(\mathbf{p}_2)=-\sin p_{1z}, \tag{A16}$$

and, hence, $\langle\Psi,\Psi\rangle=4-8/N$; consequently,

$$X=-4\varepsilon_{p_1p_2}+\frac{8}{N}(\cos p_{1x}+\cos p_{1y}+\cos p_{1z}+\cos p_{2x}$$

$$+\cos p_{2y}+\cos p_{2z})+\frac{16}{N}(\cos p_{1x}+\cos p_{1y}+\cos p_{1z}$$

$$+\cos p_{2x}+\cos p_{2y}+\cos p_{2z})-\frac{8\gamma_x}{N}(\cos(2p_{2x}+p_{1x}$$

$$-\alpha_x)+\cos(2p_{1x}+p_{2x}-\alpha_x))-\frac{8\gamma_y}{N}\bigg(\cos(2p_{2y}$$

$$+p_{1y}-\alpha_y)+\cos(2p_{1y}+p_{2y}-\alpha_y)-\frac{8\gamma_z}{N}(\cos(2p_{2z}$$

$$+p_{1z}-\alpha_x)+\cos(2p_{1z}+p_{2z}-\alpha_z)). \tag{A17}$$

If $\gamma_x=\gamma_y=\gamma_z=1$ (even number of lattice sites in each direction), $p_{2x}+p_{1x}=\alpha_x$ and $p_{2y}+p_{1y}=\alpha_y$, which corresponds to the wave function of states with $S=S_{\max}$, we have $X=-4(1-2/N)\varepsilon_{\mathbf{p}_1\mathbf{p}_2}$ or $\langle\Psi,\Psi\rangle=4-8/N$, $X=-(\varepsilon_{\mathbf{p}_1}+\varepsilon_{\mathbf{p}_2})\langle\Psi,\Psi\rangle$ since $\langle\Psi,\Psi\rangle=4-8/N$. This should be expected since in this case we use the exact wave function with the eigenvalue $E=-(\varepsilon_{\mathbf{p}_1}+\varepsilon_{\mathbf{p}_2})$ of the Hamiltonian.

*E-mail: zam@niitp.mainet.msk.su

[1] Y. Takashashi, Prog. Theor. Phys. **41**, 228 (1972).
[2] R. O. Zaitsev and Ju. V. Mikhailova, Fiz. Nizk. Temp. **17**, 999 (1991) [Sov. J. Low Temp. Phys. **17**, 521 (1991)].
[3] Y. Nagaoka, Phys. Rev. **147**, 392 (1966).

Translated by R. S. Wadhwa

Long-period incommensurate structures in crystals with triangular arrangement of magnetic ions

Yu. D. Zavorotnev and L. I. Medvedeva

A. Galkin Institute of Physics and Technology, National Academy of Sciences of the Ukraine, 340114 Donetsk, Ukraine*
(Submitted September 18, 1998; revised January 21, 1999)
Fiz. Nizk. Temp. **25**, 567–574 (June 1999)

The possibility of formation of a long-period structure in crystals with triangular arrangement of magnetic atoms is considered. It is shown that two cycloid and one spiral structures are formed. The influence of a magnetic field and second-order magnetic crystallographic anisotropy is studied. Superstructures can be transformed into one another by turning the plane of irreducible vectors for which ''anticentrifugal'' effect takes place, and an intermediate structure called a ''rotating skew spiral'' (R$\widetilde{S}\widetilde{S}$) is formed. It is also shown that ''domains'' over whose length irreducible vectors turn through an angle of $\pi/2$ can emerge in the system. These ''domains'' can form structures with a jump in the phase of irreducible vectors at the boundary. © *1999 American Institute of Physics.* [S1063-777X(99)00506-X]

INTRODUCTION

The emergence of long-period structures in crystals is explained by the presence of invariants in the nonequilibrium potential, which contain first spatial derivatives of the order parameter to the first[1] and second[2] power. Such terms appear in the Hamiltonian due to inhomogeneities of the exchange[3] and exchange–relativistic[4,5] interactions. The rich material that can be used for an analysis of long-period structures in specific crystals is systematized in the reviews in Refs. 6 and 7.

It is well known[8] that the compound $(Fe_{1-x}Mn_x)_2P$ contains under certain conditions an incommensurate spiral structure with the vector of propagation in the [110] direction. The aim of the present paper is to determine the reasons behind the formation of such a structure and also to find all possible superstructures for a crystal of the given type. Usually, superstructures considered in uniaxial crystals propagate along the principal axis of the crystal. In this case, the solution of the problem is simplified if we direct the polar axis along the principal axis of the crystal and analyze the variation of only one of the two spherical angles. In the case under investigation, the propagation vector is directed at right angles to this axis, and the polar axis in the spherical system of coordinates is chosen as in the previous case. This complicates the solution of the problem, but allows us to analyze different types of superstructures and their superposition. Taking into account the variation of both spherical angles, we can consider the spiral and cycloidal structures as two limiting cases of a rotating skew spiral (R$\widetilde{S}\widetilde{S}$). The correlation between the structures is determined by the change in the rotation of the plane of rotation of irreducible vectors.

CYCLOIDAL AND SPIRAL STRUCTURE

Gufan *et al.*[9] proved that compounds of the Fe$_2$P type possessing the D_{3h} symmetry are characterized by the three irreducible vectors: $\mathbf{F}=\mathbf{S}_1+\mathbf{S}_2+\mathbf{S}_3$, $\mathbf{L}_1=(\sqrt{6})^{-1}(2\mathbf{S}_1-\mathbf{S}_2-\mathbf{S}_3)$, $\mathbf{L}_2=(\sqrt{2})^{-1}(\mathbf{S}_2-\mathbf{S}_3)$. The first (FM) vector is transformed according to a completely symmetric irreducible representation, while $\mathbf{L}_1$ and L_2 are transformed according to the same representation as x and y, the z-axis being directed along the third-order axis. It follows hence that we can compose an invariant of the Dzyaloshinskii type, after which the potential density assumes the form[10]

$$\Phi = \delta_1\mathbf{F}^2 + \delta_2\mathbf{L}_1^2 + \Delta\left(\mathbf{F}\frac{\partial\mathbf{L}_1}{\partial x} - \mathbf{L}_1\frac{\partial\mathbf{F}}{\partial x} + \mathbf{F}\frac{\partial\mathbf{L}_2}{\partial y} - \mathbf{L}_2\frac{\partial\mathbf{F}}{\partial y}\right)$$
$$+ \alpha_1\left(\frac{\partial\mathbf{F}}{\partial x}\right)^2 + \alpha_2\left(\frac{\partial\mathbf{L}_1}{\partial x}\right)^2 + \beta_1 F_z^2 + \beta_2 L_{1z}^2 + \alpha_3\left(\frac{\partial\mathbf{F}}{\partial y}\right)^2$$
$$+ \alpha_4\left(\frac{\partial\mathbf{L}_2}{\partial y}\right)^2 + \beta_3 L_{2z}^2 - \mathbf{FH}, \qquad (1)$$

where α_i $(i=1,2,3,4), \Delta$ are the nonuniform exchange interaction constants in the basal plane, $\delta_1=0.5(T-T_C)$ and $\delta_2=0.5(T-T_N)$ are the coefficients depending on the Curie (T_C) and Neel (T_N) temperatures, β_1, β_2, and β_3 are the constants of magnetic crystallographic anisotropy, and H the magnetic field strength. We introduce the spherical system of coordinates, considering modulations along the x-direction and assuming that the magnitudes of irreducible vectors do not depend on the variable x. This leads to the following expression for the density of the nonequilibrium potential:

$$\Phi = \delta_1\mathbf{F}^2 + \delta_2\mathbf{L}_1^2 + \Delta F L_1\{\theta'_{1,x}[-\cos\theta_3\sin\theta_1$$
$$+ \sin\theta_3\cos\theta_1\cos(\varphi_1-\varphi_3)] + \theta'_{3,x}[\cos\theta_1\sin\theta_3$$
$$- \sin\theta_1\cos\theta_3\cos(\varphi_1-\varphi_3)] + (\varphi'_{1x}$$
$$- \varphi'_{3x})\sin\theta_1\sin\theta_3\sin(\varphi_3-\varphi_1)\} + \mathbf{F}^2\alpha_1\{(\theta'_{3x})^2$$
$$+ (\varphi'_{3x})^2\sin^2\theta_3\} + \mathbf{L}_1^2\alpha_2\{(\theta'_{1x})^2 + (\varphi'_{1x})^2\sin^2\theta_1\}$$

$$+\beta_1 \mathbf{F}^2 \cos^2 \theta_3 + \beta_2 \mathbf{L}_1^2 \cos^2 \theta_1 - \mathbf{FH}, \qquad (2)$$

where θ and φ are the polar and azimuthal angles, the indices "1" and "3" correspond to the vectors $\mathbf{L}_1$ and F, $\theta_x' \equiv \partial\theta/\partial x$, and $\varphi_x' \equiv \partial\varphi/\partial x$. Here we assume that $\mathbf{H}\|\mathbf{z}$. The variation of such a functional has solutions in two limiting cases.

In the first case, for $\Delta\varphi = \varphi_3 - \varphi_1 = \pm \pi/2$, $\theta_1 = \theta_3 = \theta$, $\varphi_{1x}' = \varphi_{2x}' = \varphi'$ the Euler equations have the form

$$2(\mathbf{F}^2\alpha_1 + \mathbf{L}_1^2\alpha_2)\theta_x'' + \sin\theta\{[2\beta_1\mathbf{F}^2 + 2\beta_2\mathbf{L}_1^2 - 4\Delta FL_1\varphi_x'$$
$$-2(\mathbf{F}^2\alpha_1 + \mathbf{L}_1^2\alpha_2)(\varphi_x)^2]\cos\theta - \mathbf{FH} = 0;$$

$$(\mathbf{F}^2\alpha_1 + \mathbf{L}_1^2\alpha_2)\varphi_x''\sin\theta + 2\theta'\cos\theta[\varphi_x'(\mathbf{F}^2\alpha_1 + \mathbf{L}_1^2\alpha_2)$$
$$+\Delta FL_1] = 0. \qquad (3)$$

These equations have the same structure as those in Ref. 11. This set of equations is satisfied by functions of the type $\varphi(x) = k_1 x, \theta = \text{const}$ describing for $H=0$ a double cycloidal structure with the propagation vector $\mathbf{k}_1$ directed along the x-axis. In this case, we obtain for its modulus

$$k_1 = \frac{\Delta FL_1}{F^2\alpha_1 + L_1^2\alpha_2};$$

$$\cos\theta = \frac{FH(F^2\alpha_1 + L_1^2\alpha_2)}{2[(\beta_1 F^2 + \beta_2 L_1^2)(F^2\alpha_1 + L_1^2\alpha_2) + \Delta^2 F^2 L_1^2]}. \qquad (4)$$

If $H=0, \theta = \pi/2$, and the vectors $\mathbf{F}$ and $\mathbf{L}_1$ rotate in the $x0y$ plane (a structure of the SS type according to Izyumov[6]). For $H \neq 0$, a structure of the FS type is formed. However, in our case $\mathbf{k}_1\|OX$ and lies in the plane perpendicular to the cone axis. For the value H_c of the field determined from the condition $\cos\theta = 1$ (4), the cycloid collapses, i.e., we have a "continuous" phase transition to the FM state.

In a similar way, we can study the superstructure formed along the y-axis. The formulas obtained in this case are similar to (1)–(4) in which the following substitution is made: $\mathbf{L}_1 \to \mathbf{L}_2$ and $\mathbf{k}_1 \to \mathbf{k}_2$. While solving problem of combining cycloidal structures, we must write the equation for the density of potential with derivatives along the x- and y-axes. Substituting $\varphi_x = k_1 x, \varphi_y = k_2 y$ into this equation and minimizing it in k_1 and k_2, we obtain

$$k_1 = -\frac{\Delta FL_1}{F^2\alpha_1 + \alpha_2(L_1^2 + L_2^2)};$$

$$k_2 = -\frac{\Delta FL_2}{F^2\alpha_1 + \alpha_2(L_1^2 + L_2^2)}. \qquad (5)$$

It follows from (5) that $k_1 = k_2$ only for $L_1 = L_2$. In this case, the resultant vector of propagation $\mathbf{k}$ forms equal angles with the x- and y-axes. If $L_1 \neq L_2$, then $k_1 \neq k_2$, and the value of k can be determined from the equation

$$[\delta_2 + \alpha_2 k^2][(\delta_1 + \alpha_1 k^2)(\delta_2 + \alpha_2 k^2) - \Delta^2 k^2] = 0, \qquad (6)$$

where $k^2 = k_1^2 + k_2^2$. This equation has three solutions, namely,

$$k_{(1)}^2 = -\frac{\delta_2}{2\alpha_2}; \qquad (7a)$$

$$k_{(2,3)}^2 = -\frac{\alpha_1\delta_2 + \alpha_2\delta_1 - \Delta^2}{2\alpha_1\alpha_2}$$
$$\pm \frac{1}{2\alpha_1\alpha_2}\sqrt{(\alpha_1\delta_2 + \alpha_2\delta_1 - \Delta^2)^2 - 4\delta_1\delta_2\alpha_1\alpha_2}. \qquad (7b)$$

It can be seen that the sign of Δ is immaterial for the formation of an incommensurate structure. The solution $k_{(1)}^2$ takes place under the condition $\alpha_2 > 0, \delta_2 < 0$, i.e., we require that $T < T_N$. In this case, $F=0$ and $L_1 = \lambda L_2$, where $\lambda = -k_1/k_2$ ($k_1 \neq 0, k_2 \neq 0$), i.e., k_1 and k_2 have different signs. However, such a relation is ruled out, and k_1 and k_2 must have the same sign, i.e., solution (7a) is deprived of physical meaning. Relation (7b) has two solutions. Let us consider the conditions for the existence of each solution in different temperature intervals.

We assume that $T_C > T_N$. In this case, it can be seen from (7b) that at $T=T_C$ ($\delta_1 = 0, \delta_2 = a_2(T_C - T_N)$), one of the solutions (k_2^2) on the PT line, for which the second term has the "+" sign, is positive for $\Delta^2 \geq \alpha_1 a_2(T_C - T_N)$. This is a sufficient condition for the formation of a superstructure through a first-order phase transition in temperature from the paraphase.[7] Such a transition is impossible for $\Delta^2 < \alpha_1 a_2(T_C - T_N)$, and $k_{(2)}^2 = 0$ on the PT line. If $T < T_C$, i.e., $\delta_1 < 0$ and $\delta_2 > 0$, we have $k_2^2 > 0$, and a continuous PT from the paraphase to an incommensurate structure occurs even when the sufficient condition is not satisfied. The solution $k_{(3)}^2$ is negative everywhere and has no physical meaning.

A different situation takes place for $T=T_N$. In this case, we have

$$k_{(2)}^2 = 0; \quad k_{(3)}^2 = \frac{\Delta^2 + \alpha_2 a_1(T_C - T_N)}{\alpha_1\alpha_2}. \qquad (8)$$

The solution $k_{(2)}^2$ describes a continuous PT from an incommensurate to an FM structure, while $k_{(3)}^2$ describes a first-order PT from FM to a superstructure with a jump in $\mathbf{k}$ irrespective of the relation between Δ and $(T_C - T_N)$, and the sufficient condition can be disregarded.

For $\delta_1 = 0$, we obtain

$$\left|\frac{F}{L_{1,2}}\right| = \left|\frac{\Delta k_{1,2}}{2\alpha_1 k^2}\right| \gg 1, \qquad (9)$$

i.e., $F \gg L_1$, and we have an FM cycloidal structure with a "latent" transverse AFM. If $L_1 = L_2 = 0$, we have $\mathbf{S}_1\|\mathbf{S}_2\|\mathbf{S}_3$. For small L_1 and L_2 perpendicular to $\mathbf{F}$, deviation from collinearity is required. Similarly, it follows from the condition $\delta_2 = 0$ that $F \ll L_1$. This gives an AFM cycloid with a "latent" transverse FM. For $F=0$, a triangular 120° AFM ordering appears. A weak transverse FM appears when spins deviate from the basal plane.

In the second case, we have $\Delta\varphi = \varphi_3 - \varphi_1 = 0; \pm \pi$; $\varphi_{1x}' = \varphi_{3x}' = 0$; $\varphi_1 = 0; \pm \pi/2$. The variation of the functional gives the set of Euler equations

$$L_1^2\alpha_2\theta_{1x}'' \pm \Delta FL_1\theta_{3x}'\cos(\theta_3 \mp \theta_1) = -\tfrac{1}{2}\beta_2 L_1^2\sin 2\theta_1,$$

$$F^2 \alpha_1 \theta_{3x}'' \mp \Delta F L_1 \theta_{1x}'' \cos(\theta_3 \mp \theta_1) = -\frac{1}{2} \beta_1 F^2 \sin^2 2\theta_3$$

$$+\frac{1}{2} FH \sin \theta_3. \tag{10}$$

Here and below, the upper sign corresponds to $\Delta\varphi=0$, while the lower sign to $\Delta\varphi=\pm\pi$. In the absence of anisotropy and for $H=0$, the solution of system (10) is a function of the type $\theta_3=\pm kx$, describing a cycloidal structure for $\varphi_1=0$ with rotation of vectors $\mathbf{F}$ and $\mathbf{L}_1$ in the $z0x$ plane and a spiral structure for $\varphi_1=\pm\pi/2$ with rotation of vectors $\mathbf{F}$ and $\mathbf{L}_1$ in the $Z0Y$ plane. The quantity $\theta_3 \mp \theta_1=\psi$ turns out to be constant. In this case,

(1) if $\Delta>0$, $\psi=-\pi/2$ for $\theta_{3x}' \pm \theta_{1x}'>0$ and

$\psi=\pi/2$ for $\theta_{3x}' \pm \theta_{1x}'<0$;

(2) if $\Delta<0$, $\psi=\pi/2$ for $\theta_{3x}' \pm \theta_{1x}'>$ and

$\psi=-\pi/2$ for $\theta_{3x}' \pm \theta_{1x}'<0$.

It follows hence that the vector $\mathbf{L}_1$ always leads the vector $\mathbf{F}$ for any direction of rotation and for $\Delta>0$. If $\Delta<0$, the vector $\mathbf{F}$ leads the vector $\mathbf{L}_1$. Since the Euler angles θ_1 and θ_2 vary from 0 to π, the total period of the incommensurate structure described here has to be ''glued'' from quarters. For $\Delta<0$, we have the following relations for finding $\mathbf{F}$ in I–IV quadrants: $\theta_1+\theta_3=\pi/2$, $\theta_3-\theta_1=-\pi/2$, $\theta_1+\theta_3=3\pi/2$, $\theta_3-\theta_1=\pi/2$ respectively. For $\Delta<0$, we have the following relations: $\theta_3-\theta_1=-\pi/2$, $\theta_3+\theta_1=\pi/2$, $\theta_3-\theta_1=\pi/2$, $\theta_1+\theta_3=3\pi/2$ respectively. The angles θ_1 and θ_3 are measured from the z-axis, the upper left quarter plays the role of the first quadrant, and the remaining quadrants are counted in the counterclockwise direction. The solutions of system (10) are a sort of ''domain'' structures formed from 1/4 of the total period of the superstructure. A ''domain'' in this case is a region in the crystal, in which irreducible vectors turn through an angle of $\pi/2$. Clearly, the solutions for which the phase of the vectors $\mathbf{F}$ and $\mathbf{L}_1$ do not coincide at domain walls, i.e., the angles θ_1 and θ_3 change jumpwise, can be ''glued.'' In this case, we must be sure that the conditions of leading are observed. Forming various combinations of ''domains,'' we can obtain a number of magnetic structures:

(a) two ''domains'' ensuring the rotation of the long-period structure through π are ''glued'' together. After this, the vectors $\mathbf{F}$ and $\mathbf{L}_1$ return jumpwise to their initial positions (Fig. 1a);

(b) two ''domains'' each of which ensures the rotation of irreducible vectors through $\pi/2$ in opposite directions are ''glued'' together; in this case, one of the vectors $\mathbf{F}$ or $\mathbf{L}_1$ undergoes a jump through an angle π at the boundary of these ''domains'' (Fig. 1b).

When a field is applied ($\beta_1=\beta_2=0$ as before), the following relations are used for finding the solutions: $\theta_3=kx+\psi_3$, $\theta_3 \pm \theta_1=\pi/2+n\pi\pm\psi_1$, where $\psi_1\sim H$ and $\psi_3\sim H$. In this case, the quantities θ_1 and θ_3 have the form (rotation in the counterclockwise direction)
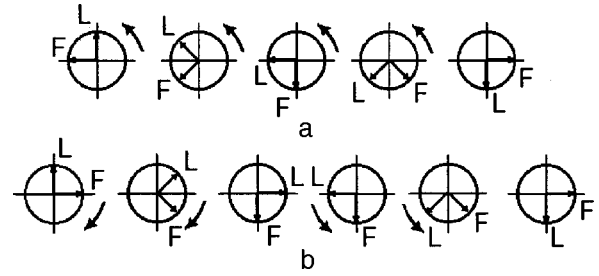

FIG. 1. Structures composed from fragments of superstructures ensuring the rotation of long-period structures through an angle π (a) or the rotation of irreducible vectors through $\pi/2$ in opposite directions (b). Arrows show the direction of rotation.

$$\theta_3=f_1(kx)-R_1\sin(kx),   \theta_1=f_2(kx)-R_1\sin(kx), \tag{11}$$

where

$$R_1=\frac{H(k\alpha_2 L_1-\Delta F)}{2k^2[\alpha_1\alpha_2 L_1 Fk-\Delta(F^2\alpha_1+L_1^2\alpha_2)]};$$

$$R_2=\frac{\Delta HF}{2k^2[\alpha_1\alpha_2 FL_1 k-\Delta(\alpha_2 L_1^2+\alpha_1 F^2)]},$$

and we obtain the following expressions for determining $\mathbf{F}$ in quadrants I–IV:

I. $f_1(kx)=kx$; $f_2(kx)=\pi/2-kx$;

II. $f_1(kx)=kx$; $f_2(kx)=-\pi/2+kx$; $R_2\rightarrow-R_2$,

III. $f_1(kx)=2\pi-kx$; $f_2(kx)=-\pi/2+kx$;

$$R_1\rightarrow-R_1,   R_2\rightarrow-R_2;$$

IV. $f_1(kx)=2\pi-kx$; $f_2(kx)=5\pi/2-kx$;

$$R_1\rightarrow-R_1. \tag{12}$$

The value of kx in (11) and (12) varies from 0 to 2π. It should be noted that in an applied field H, the vectors $\mathbf{F}$ and $\mathbf{L}_1$ are orthogonal only for values of x corresponding to $\sin(kx)=0$. It can be seen from (12) that the extent of smallness of H is determined from the relations $|R_1|\ll 1$ and $|R_2|\ll 1$. In this case, the approximation $F=$const, $L=$const is still valid, and the hodographs of F and L_1 are circles. Owing to the presence of terms in (11) proportional to H and responsible for the emergence of harmonics, the vectors $\mathbf{F}$ and $\mathbf{L}_1$ do not rotate uniformly any longer for $0\leq kx\leq 2\pi$. It follows from (11) that the vector components F_z,F_y,L_{1z}, and L_{1y} for $H\neq 0$ have a peculiar spatial modulation during which harmonics appear. In the corresponding expansions, all harmonics are taken into account, but only F_z and L_{1y} contain terms independent of kx and ensuring a permanent shift. This leads to a distortion of the uniform distribution of the vector $\mathbf{F}$ over the circle. The curves describing the dependences $F_z(kx)$ and $F_y(kx)$ for $R_1>0$ (which is observed for rather large values of $|\Delta|$) are shown in Fig. 2a. It can be seen that the minimum of $F_z(kx)$ in the vicinity of the point $kx=\pi$ becomes sharper, while the maximum at $x=0$ becomes flatter than for an ordinary sinusoid. At the same time, the extrema of $F_y(kx)$ become sharper and
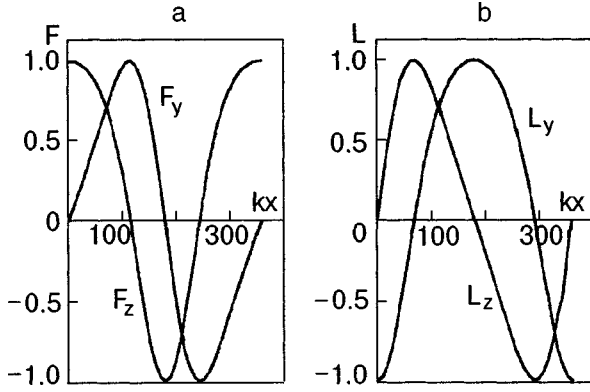
FIG. 2. Dependences $F_z(kx)$ and $F_y(kx)$ (a) and $L_z(kx)$, $L_y(kx)$ (b) in a weak field.

FIG. 3. Dependences $F_z(kx)$ and $F_y(kx)$ (a) and $L_z(kx)$, $L_y(kx)$ (b) for a weak anisotropy.

are displaced to the point $kx = \pi$. All this indicates the predominant direction of $kx = 2\pi n$, i.e., along the field. The distribution of the vector $\mathbf{L}_1$ is also distorted. For $R_2 < 0$, the shape of the $L_{1y}(kx)$ coincides with F_z and L_{1z} with F_y. Consequently, the vector $\mathbf{L}_1$ "sticks" in the basal plane synchronously with $\mathbf{F}$ in the direction determined by the condition of leading. If $R_2 > 0$, the AFM vector, as before, has a predominant direction in the basal plane, but now for $kx = \pi$. The extrema of L_{1z} are displaced to the points $kx = 2\pi n$. Consequently, in this case the directions of "sticking" between the vectors $\mathbf{F}$ and $\mathbf{L}$ are not synchronized.

We obtain the following dependence of the vector of propagation on magnetic field:

$$k = k_1 \left\{ 1 - \frac{3}{4} \frac{F^2 \alpha_1 R_1^2 + L_1^2 \alpha_2 R_2^2}{F^2 \alpha_1 + L^2 \alpha_2} - \frac{1}{16}(R_1 + R_2)^2 \right.$$
$$\left. - \frac{3}{8} R_1 R_2 \right\}, \tag{13}$$

where k_1 is defined by formula (5). Since R_1 and R_2 depend on the field linearly, the magnitude of the wave vector decreases with increasing H. However, an example when the vector of propagation increases with H is also known.[7] An expression similar to (13) in which L_1 is replaced by L_2 and k_1 by k_2 can also be obtained for a superstructure with $k \| 0Y$.

In the case when field is equal to zero, but a weak anisotropy takes place (β_1 and β_2 are of the same order of smallness), the solutions for the angles θ_1 and θ_3 are sought in the same form as for $H \neq 0$, but $\psi_1 \sim \beta_1, \psi_3 \sim \beta_1$. In this case, we obtain (for the rotation in the counterclockwise direction)

$$\theta_3 = f_1(kx) + R_1 \sin 2kx; \quad \theta_1 = f_2(kx) + R_2 \sin 2kx, \tag{14}$$

where

$$R_1 = \frac{1}{8k^2 \alpha_1} \left[\beta_1 + \frac{\Delta L_1^2 (\alpha_2 \beta_1 + \alpha_1 \beta_2)}{4k \alpha_1 \alpha_2 F L_1 - \Delta (F^2 \alpha_1 + L_1^2 \alpha_2)} \right];$$

$$R_2 = \frac{1}{8k^2 \alpha_1} \left[\beta_1 + \frac{L_1 (\alpha_2 \beta_1 + \alpha_1 \beta_2)(\Delta L_1 - 4F \alpha_1 k)}{4k \alpha_1 \alpha_2 F L_1 \pm \Delta (F^2 \alpha_1 + L_1^2 \alpha_2)} \right]$$
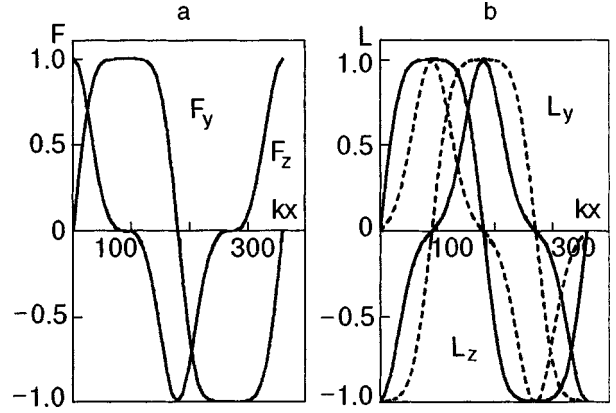
and $f_1(kx), f_2(kx)$, and the signs of R_1 and R_2 are determined by relations (12). The extent of weakness of anisotropy is defined by the inequalities $|R_1| \ll 1, |R_2| \ll 1$; in this case, the approximation $F = \text{const}$, $L_1 = \text{const}$ is also valid.

The expansion of the functions F_z, F_y, L_{1z}, L_{1y} into a Fourier series taking into account (14) contains, in addition to the fundamental harmonic, only even harmonics and no shear terms. Depending on the signs of anisotropy constants β_1 and β_2, we have either an "easy" axis ($R_1 < 0$), or an "easy" plane ($R_1 > 0$). In the presence of anisotropy of the "easy" plane type, $F_y(kx)$ has a plateau in the vicinity of the points $kx = \pi/2, 3\pi/2$, and the dependence $F_z(kx)$ is characterized by narrow sharp extrema (Fig. 3). This indicates the "sticking" of the vector $\mathbf{F}$ in the basal plane on both sides of the z-axis. The sign reversal of R_1 for invariable signs of β_1 and β_2 leads to the change in the type of anisotropy. In this case, the $F_z(kx)$ curve acquires two plateaus at $kx = 0$ and π, while $F_y(kx)$ has sharp extrema. Consequently, for $R_1 < 0$ the "sticking" occurs along the z-axis. If R_1 and R_2 have the same sign, the behavior of FM and AFM vectors is synchronized (solid curves in Fig. 3b), i.e., the AFM vector has a predominant distribution in the direction perpendicular to $\mathbf{F}$. For opposite signs of R_1 and R_2, synchronization vanishes (dashed curves in Fig. 3b), and both vectors are "stuck" in identical directions.

The dependence of the modulus $\mathbf{k}$ of the propagation vector on anisotropy is defined by the formula

$$k = k_1 \left\{ 1 - 2 \frac{F^2 \alpha_1 R_1^2 + L_1^2 \alpha_2 R_2^2}{F^2 \alpha_1 + L^2 \alpha_2} - \frac{1}{16}(R_1 + R_2)^2 \right.$$
$$\left. - \frac{15}{4} R_1 R_2 \right\}, \tag{15}$$

which shows that increase in anisotropy leads to a decrease in k.

ROTATION OF THE ROTATION PLANE FOR IRREDUCIBLE VECTORS

Let us consider the possibility of mutual transformations of the spiral and cycloidal structures. For the sake of sim-
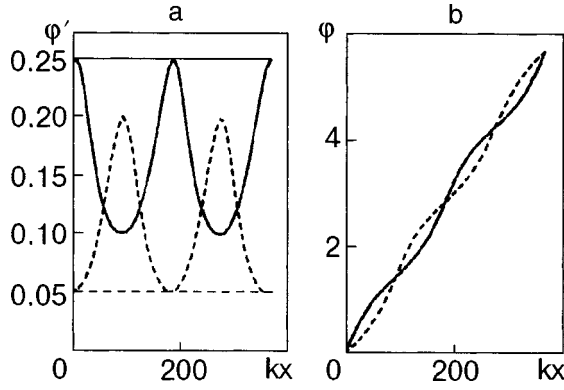
FIG. 4. Dependences $\varphi'(kx)$ (a) and $\varphi(kx)$ (b). Solid curves correspond to $F^2\alpha_1 - L_1^2\alpha_2 > 0$ and dashed curves to $F^2\alpha_1 - L_1^2\alpha_2 < 0$.

plicity, we consider the rotation of the plane of rotation of the vectors $\mathbf{F}$ and $\mathbf{L}_1$ around the z-axis. In this case, $\varphi_1 = \varphi_3 \pm \pi n$ and $\varphi_1' = \varphi_3'$.

The variation of the functional gives the following set of Euler equations in the absence of anisotropy in zero field:

$$\varphi_x''[F^2\alpha_1 \sin 2\theta_3 + L_1^2\alpha_1 \sin 2\theta_1] + \varphi_x'[\theta_3' F^2\alpha_1 \sin 2\theta_3$$

$$+ \theta_1' L_1^2\alpha_1 \sin 2\theta_1] = 0;$$

$$F^2\alpha_1 \theta_{3x}'' \pm \Delta F L_1 \theta_{1x}' \cos(\theta_3 \pm \theta_1)$$

$$= \frac{1}{2} F^2\alpha_1 (\varphi_x')^2 \sin 2\theta_3;$$

$$L_1^2\alpha_1 \theta_{1x}'' \mp \Delta F L_1 \theta_{3x}' \cos(\theta_3 \pm \theta_1)$$

$$= \frac{1}{2} L_1^2\alpha_2 (\varphi_x')^2 \sin 2\theta_1. \tag{16}$$

The solution of this system can be found assuming that the value of φ_x' is small in the form (for the fourth quadrant)

$$\theta = kx + \psi_3;$$

$$\theta_1 = \theta_3 - \frac{\pi}{2} + \psi_1 = kx - \pi/2 + \psi_3 + \psi_1, \tag{17}$$

where $\psi_1 \sim (\varphi_x')^2$ and $\psi_3 \sim (\varphi_x')^2$. In this case, the first integral of the first equation in (16) for $F^2\alpha_1 \neq L_1^2\alpha_2$ has the form

$$\varphi_x' = C[(F^2\alpha_1 - L_1^2\alpha_2)\sin^2 kx + L_1^2\alpha_2]^{-1}, \tag{18}$$

where C is the integration constant which remains indefinite since the initial conditions are not specified. The extent of smallness of φ_x' can be determined from the condition

$$|C| \ll |(F^2\alpha_1 - L_1^2\alpha_2)\sin^2 kx + L_1^2\alpha_2|. \tag{19}$$

Inequality (19) shows that φ_x' never vanishes and its sign is determined by the sign of C. For $F^2\alpha_1 = L_1^2\alpha_2$, the quantity φ_x' is constant, i.e., the plane of rotation of the vectors $\mathbf{F}$ and $\mathbf{L}_1$ rotates uniformly around the z-axis. Otherwise, the velocity of rotation is an oscillating function of x. Oscillations of $\varphi_x'(x)$ occur either above or below the straight line $C/L_1^2\alpha_2$ (Fig. 4a). Subsequent integration of (18) under the assumption $|F^2\alpha_1 - L_1^2\alpha_2| < |L_1^2\alpha_2|$ gives

$$\varphi(x) = \frac{C}{k\sqrt{F^2L^2\alpha_1\alpha_2}} \arctan\left\{\left(\frac{F^2\alpha_1}{L_1^2\alpha_2}\right)^{1/2} \tan(kx)\right\} + \varphi_0,$$
$$\tag{20}$$

where $\varphi_0 = 0$ since this constant defines the reference point. The curves describing the dependences $\varphi(x)$ for various relations between $F^2\alpha_1$ and $L_1^2\alpha_2$ are shown in Fig. 4b. For $F^2\alpha_1 = L_1^2\alpha_2$, the $\varphi(x)$ dependence is linear, i.e., $\varphi(x) = px$, where the integration constant p plays the role of the vector of propagation of a new incommensurate structure formed by the rotation of the plane of rotation of the vectors $\mathbf{F}$ and $\mathbf{L}_1$.

If we assume that $|F^2\alpha_1 - L_1^2\alpha_2| \ll |L_1^2\alpha_2|$, the right-hand sides of the second and third equations in (16) can be expanded into a power series in $(F^2\alpha_1 - L_1^2\alpha_2)$. Confining the analysis to the first two terms of the expansion, we obtain additional terms containing $\sin(4kx)$ as a factor. This is equivalent to the emergence of the fourth-order anisotropy. The solution of system (16) in this case assumes the form

$$\theta_3 = f_1(kx) - R_1 \sin(2kx) - R_2 \sin(4kx),$$

$$\theta_1 = f_2(kx) - R_3 \sin(2kx) + R_4 \sin(4kx), \tag{21}$$

where

$$R_1 = \frac{C^2}{8L_1^6\alpha_2^3 k^2}(F^2\alpha_1 - 3L_1^2\alpha_2)\left[-1 + \frac{2\Delta k L_1}{F\alpha_1(q^2 + 4k^2)}\right];$$

$$R_2 = \frac{C^2(F^2\alpha_1 - L_1^2\alpha_2)}{64L_1^6\alpha_2^3 k^2}\left[1 + \frac{4\Delta k L_1}{F\alpha_1(q^2 + 16k^2)}\right];$$

$$R_3 = \frac{C^2}{8L_1^6\alpha_2^3 k^2}(F^2\alpha_1 - 3L_1^2\alpha_2)\left[-1\right.$$

$$\left. + \frac{2k(4kF\alpha_1 - \Delta L_1)}{F\alpha_1(q^2 + 16k^2)}\right];$$

$$R_4 = \frac{C^2(F^2\alpha_1 - L_1^2\alpha_2)}{64L_1^6\alpha_2^3 k^2}\left[1 + \frac{4k(\Delta L_1 - 16kF\alpha_1)}{F\alpha_1(q^2 + 16k^2)}\right];$$

$$q^2 = -\frac{k\Delta}{F\alpha_1 L_1\alpha_2}(F^2\alpha_1 + L_1^2\alpha_2).$$

For the quadrants, we have

I. $f_1(kx) = kx;$ $f_2(kx) = \pi/2 - kx;$

II. $f_1(kx) = kx;$ $f_2(kx) = kx - \pi/2;$

$R_3 \rightarrow -R_3;$ $R_4 \rightarrow -R_4;$

III. $f_1(kx) = 2\pi - kx;$ $f_2(kx) = kx - \pi/2;$

$R_i \rightarrow -R_i$ $(i = 1,2,3,4);$

IV. $f_1(kx) = 2\pi - kx;$ $f_2(kx) = 5\pi/2 - kx;$

$R_1 \rightarrow -R_1;$ $R_2 \rightarrow -R_2.$

The expansion of F_z, F_y, L_{1z}, and L_{1y} into a Fourier series contain no shear terms and only odd harmonics. The corresponding expressions are cumbersome and are not given here.

Thus, we obtain a structure with irreducible vectors **F** and L_1 rotating in a plane that in turn rotates around the principal axis of the crystal. We refer to this structure as a ''rotating skew spiral'' (R$\widetilde{S}\widetilde{S}$) in analogy with the $\widetilde{S}\widetilde{S}$ structure in Ref. 6.

In the case of a uniform rotation in the rotation plane, i.e., for $F^2\alpha_1 = L_1^2\alpha_2$ and $\varphi_x' = $ const, the right-hand sides of the second and third equations of system (16) describe a second-order anisotropy of the ''easy'' axis type. The corresponding solutions are given by formulas (21) in which we must put $R_2 = R_4 = 0$. In this case, $\theta_3 = f(x) - |R|\sin(2kx)$ and the rotation of the plane of rotation of the vectors **F** and L_1 must lead to ''sticking'' of the vector **F** in the directions $\theta_3 = \pi n$ ($n = 0,1$), i.e., the rotational axis z. This phenomenon was called by us the ''anticentrifugal'' effect.

In the general case, when $F^2\alpha_1 \neq L_1^2\alpha_2$, a fourth-order anisotropy must appear in accordance with (21). Owing to this term, a relatively weak ''sticking'' of the vector **F** occurs for $\theta_3 = 0$, $\pi/2, \pi$ irrespective of the sign of R_2.

CONCLUSION

It is proved that spiral and cycloidal structures are limiting cases. The R$\widetilde{S}\widetilde{S}$ structure (rotating skew spiral) predicted by us is an intermediate structure around which the plane of rotation of irreducible vectors rotates, thus ensuring a smooth transition from the spiral to the cycloidal structure and vice versa. Such a possibility leads to the emergence of anisotropy of the ''easy'' axis type. This phenomenon is known as the ''anticentrifugal'' effect. Besides, it was found that ''domains'' over whose length irreducible vectors are turned through $\pi/2$ can exist. These ''domains'' can be ''glued'' together, i.e., structures with a phase jump of irreducible vectors at the boundary can be created.

*E-mail: zavarot@host.dipt.donetsk.ua

[1] I. E. Dzyaloshinskiĭ, Zh. Éksp. Teor. Fiz. **47**, 992 (1964) [Sov. Phys. JETP **20**, 665 (1964)].

[2] A. Michelson, Phys. Rev. B **B16**, 572 (1977).

[3] V. G. Bar'yakhtar, E. P. Stephanovskiĭ, and D. A. Yablonskiĭ, JETP Lett. **42**, 317 (1985).

[4] V. G. Bar'yakhtar and E. P. Stephanovskiĭ, Fiz. Tverd. Tela (Leningrad) **11**, 1946 (1969) [Sov. Phys. Solid State **11**, 1566 (1969)].

[5] I. E. Chupis, Fiz. Nizk. Temp. **12**, 330 (1986) [Sov. J. Low Temp. Phys. **12**, 188 (1986)].

[6] Yu. A. Izyumov, Usp. Fiz. Nauk **144**, 439 (1984) [Sov. Phys. Usp. **27**, 845 (1984)].

[7] V. G. Bar'yakhtar and E. P. Stephanovskiĭ, Fiz. Nizk. Temp. **22**, 904 (1996) [Low Temp. Phys. **22**, 693 (1996)].

[8] H. Fujii, T. Hokabe, and K. Eguchi, J. Phys. Soc. Jpn. **51**, 414 (1982).

[9] Yu. M. Gufan, E. I. Kut'in, V. L. Lorman, *et al.*, JETP Lett. **46**, 287 (1987).

[10] D. A. Yablonskiĭ and L. I. Medvedeva, Physica B **167**, 125 (1990).

[11] E. P. Stephanovskiĭ and A. L. Sukstanskiĭ, Zh. Éksp. Teor. Fiz. **104**, 3434 (1993) [JETP **77**, 628 (1993)].

[12] G. M. Fikhtengol'ts, *Differential and Integral Calculus*, vol. 3, [in Russian], Nauka, Moscow (1966).

Translated by R. S. Wadhwa

Magnetic properties of periodic nonuniform spin-1/2*XX* chains in a random Lorentzian transverse field

Oleg Derzhko

Institute for Condensed Matter Physics, 1 Svientsitskii St., L'viv, 290011, Ukraine;
Chair of Theoretical Physics, Ivan Franko L'viv State University, 12 Drahomanov St., L'viv, 290005,
Ukraine*

Using continued fractions we examine the density of states, transverse magnetization and static transverse linear susceptibility of a few periodic nonuniform spin-1/2*XX* chains in a random Lorentzian transverse field. © *1999 American Institute of Physics.*
[S1063-777X(99)00606-4]

The one-dimensional spin-1/2*XY* model was introduced in the early 60s by a number of authors.[1] They recognized that several statistical mechanics calculations for that spin model could be performed exactly because it can be rewritten as a model of noninteracting spinless fermions with the help of the Jordan-Wigner transformation. Evidently, the formulation of the spin-1/2*XY* chain in terms of fermions allows one to give a magnetic interpretation to the results derived for one-dimensional tight-binding spinless fermions. As an example of where this relationship has been exploited one can cite the papers on the Lloyd model[2,3] and corresponding papers on the spin-1/2*XX* chain in a random Lorentzian transverse field.[4,5] The work reported in the present paper has been inspired by some results on one-dimensional tight-binding Hamiltonians for periodically modulated lattices[6,7] and spinless Falicov-Kimball model.[8,9] Combining the approach developed in those papers and the treatment of the Lloyd model presented in Refs. 2 and 3 we shall calculate exactly the random-averaged one-fermion Green's functions (that yield the density of states and therefore the thermodynamics) for the periodic nonuniform spin-1/2*XX* chain in a random Lorentzian transverse field. We shall treat a few particular chains in order to discuss the changes in the density of states and magnetic properties induced by periodic nonuniformity and diagonal disorder. It should be noted, in passing, that the periodic nonuniform spin-1/2*XX* chain was considered in several papers dealing with a spin-1/2*XX* chain with two and more sublattices[10,11] and the spin-Peierls instability in a spin-1/2*XX* chain[12] (see also Refs. 13–18). However, the latter papers concentrated mainly on the influence of the structural degrees of freedom upon the magnetic ones, rather than on the properties of a magnetic chain with regularly alternating exchange couplings. One should also mention a study of a spin-1/2*XX* model on a one-dimensional superlattice[19] (such a model can be viewed as a nonuniform chain with periodically varying exchange coupling) but consideration was restricted to the excitation spectrum. Our communication is also related to the work in Ref. 20 and may be viewed as a further study of the effects of periodic nonuniformity and randomness on magnetic properties of spin-1/2 chains.

Let us consider a cyclic nonuniform *XX* chain of $N \to \infty$ spins 1/2 in a transverse field described by the Hamiltonian

$$H = \sum_{n=1}^{N} \Omega_n s_n^z + 2 \sum_{n=1}^{N} I_n (s_n^x s_{n+1}^x + s_n^y s_{n+1}^y)$$
$$= \sum_{n=1}^{N} \Omega_n \left(s_n^+ s_n^- - \frac{1}{2} \right) + \sum_{n=1}^{N} I_n (s_n^+ s_{n+1}^- + s_n^- s_{n+1}^+).$$

$$(1)$$

Here Ω_n is the transverse field at the site n, and is assumed to be a random variable with the Lorentzian probability distribution

$$p(\Omega_n) = \frac{1}{\pi} \frac{\Gamma_n}{(\Omega_n - \Omega_{0n})^2 + \Gamma_n^2},$$

$$(2)$$

Ω_{0n} is the mean value of the transverse field at the site n, and Γ_n is the width of its distribution. $2I_n$ is the exchange coupling between the sites n and $n+1$. After making use of the Jordan-Wigner transformation the model is recast into a chain of spinless fermions governed by the Hamiltonian

$$H = \sum_{n=1}^{N} \Omega_n \left(c_n^+ c_n - \frac{1}{2} \right) + \sum_{n=1}^{N} I_n (c_n^+ c_{n+1} - c_n c_{n+1}^+) \quad (3)$$

(the boundary term that is non-essential for the calculation of thermodynamic quantities has been omitted). Note, that for the non-random case ($\Gamma_n = 0$) assuming the transverse field in (3) to be uniform one arises at the Hamiltonian considered in Ref. 6. In addition, after substitution $\Omega_n \to U w_n$, $I_n \to -t$, Eq. (3) transforms into the Hamiltonian of a one-dimensional spinless Falicov-Kimball model in the notations used in Refs. 8 and 9. In model (3), considered here, not only the transverse fields that are independent random Lorentzian variables having the mean values and widths of their distribution, but also the exchange couplings between neighboring spins, vary from site to site.

Let us introduce the temperature double-time Green's functions $G_{nm}^{\mp}(t) = \mp i \theta(\pm t) \langle \{c_n(t), c_m^+(0)\} \rangle$,

$$G^{\mp}_{nm} = \frac{1}{2\pi} \int_{-\infty}^{\infty} d\omega \exp(-i\omega t) G^{\mp}_{nm}(\omega \pm i\varepsilon), \varepsilon \to +0,$$

where the angular brackets denote the thermodynamic average. Utilizing a set of equations for $G^{\mp}_{nm} \equiv G^{\mp}_{nm}(\omega \pm i\varepsilon)$, and performing random averaging using contour integral,[2-5] one finds the following set of equations for the random-averaged Green's functions

$$(\omega \pm i\Gamma_n - \Omega_{0n})\overline{G^{\mp}_{nm}} - I_{n-1}\overline{G^{\mp}_{n-1,m}} - I_n\overline{G^{\mp}_{n+1,m}} = \delta_{nm}. \tag{4}$$

Here $\overline{(\ldots)} \equiv \int_{-\infty}^{\infty} d\Omega_1 p(\Omega_1) \ldots \int_{-\infty}^{\infty} d\Omega_N p(\Omega_N)(\ldots)$. Our task is to evaluate the diagonal random-averaged Green's functions $\overline{G^{\mp}_{nm}}$, the imaginary parts of which give the random-averaged density of states $\overline{\rho(\omega)}$

$$\overline{\rho(\omega)} = \mp \frac{1}{\pi N} \sum_{n=1}^{N} \mathrm{Im} \overline{G^{\pm}_{nn}}, \tag{5}$$

that in its turn, yields thermodynamic properties of spin model (1). It is a simple matter to obtain from Eq. (4) the following representation for $\overline{G^{\mp}_{nn}}$

$$\overline{G^{\mp}_{nn}} = \frac{1}{\omega \pm i\Gamma_n - \Omega_{0n} - \Delta_n^- - \Delta_n^+},$$

$$\Delta_n^- = \cfrac{I_{n-1}^2}{\omega \pm i\Gamma_{n-1} - \Omega_{0,n-1} - \cfrac{I_{n-2}^2}{\omega \pm i\Gamma_{n-2} - \Omega_{0,n-2} - \ddots}},$$

$$\Delta_n^+ = \cfrac{I_n^2}{\omega \pm i\Gamma_{n+1} - \Omega_{0,n+1} - \cfrac{I_{n+1}^2}{\omega \pm i\Gamma_{n+2} - \Omega_{0,n+2} - \ddots}}. \tag{6}$$

Eqs. (5) and (6) are extremely useful for examining thermodynamic properties of periodic nonuniform spin-1/2 XX chain in a random Lorentzian transverse field when periodic continued fractions emerge. It should be emphasized that the continued fraction representation of the one-particle Green's functions for the model of tight-binding electrons is well known in solid state theory. As an example let us refer here to a number of original and review papers.[21] In what follows we shall calculate the relevant continued fractions exactly (it becomes possible since they are periodic) that will permit us to reveal the effects of regular nonuniformity on the magnon band structure.

Consider, at first, a non-random case. For a regular alternating chain $\Omega_1 I_1 \Omega_2 I_2 \Omega_3 I_3 \Omega_1 I_1 \Omega_2 I_2 \Omega_3 I_3 \ldots$ one generates periodic continued fractions having a period 3, and after some calculations we obtain

$\rho(\omega)$

$$= \begin{cases} 0, & \text{if } \omega < c_6, c_5 < \omega < c_4, c_3 < \omega < c_2, c_1 < \omega, \\ \dfrac{1}{3\pi} \dfrac{|X(\omega)|}{\sqrt{C(\omega)}}, & \text{if } c_6 < \omega < c_5, c_4 < \omega < c_3, c_2 < \omega < c_1; \end{cases}$$

$$X(\omega) = I_1^2 + I_2^2 + I_3^2 - (\omega - \Omega_1)(\omega - \Omega_2)$$
$$- (\omega - \Omega_1)(\omega - \Omega_3) - (\omega - \Omega_2)(\omega - \Omega_3),$$

$$C(\omega) = 4I_1^2 I_2^2 I_3^2 - [I_1^2(\omega - \Omega_3) + I_2^2(\omega - \Omega_1) + I_3^2(\omega - \Omega_2)$$
$$- (\omega - \Omega_1)(\omega - \Omega_2)(\omega - \Omega_3)]^2$$
$$= -\prod_{j=1}^{6} (\omega - c_j). \tag{7}$$

Here $c_1 \geqslant \ldots \geqslant c_6$ denote six roots of the equation $C(\omega) = 0$ that can be found by solving two cubic equations. For a regular alternating chain

$$\Omega_1 I_1 \Omega_2 I_2 \Omega_3 I_3 \Omega_4 I_4 \Omega_1 I_1 \Omega_2 I_2 \Omega_3 I_3 \Omega_4 I_4 \ldots$$

periodic continued fractions having period 4 emerge, and after some calculations we find

$\rho(\omega)$

$$= \begin{cases} 0, & \text{if } \omega < d_8, d_7 < \omega < d_6, d_5 < \omega < d_4, \\ & \quad d_3 < \omega < d_2, d_1 < \omega, \\ \dfrac{1}{4\pi} \dfrac{|W(\omega)|}{\sqrt{D(\omega)}}, & \text{if } d_8 < \omega < d_7, d_6 < \omega < d_5, \\ & \quad d_4 < \omega < d_3, d_2 < \omega < d_1; \end{cases}$$

$$W(\omega) = I_1^2(2\omega - \Omega_3 - \Omega_4) + I_2^2(2\omega - \Omega_1 - \Omega_4)$$
$$+ I_3^2(2\omega - \Omega_1 - \Omega_2) + I_4^2(2\omega - \Omega_2 - \Omega_3)$$
$$- (\omega - \Omega_1)(\omega - \Omega_2)(\omega - \Omega_3) - (\omega - \Omega_1)$$
$$\times (\omega - \Omega_2)(\omega - \Omega_4) - (\omega - \Omega_1)(\omega - \Omega_3)$$
$$\times (\omega - \Omega_4) - (\omega - \Omega_2)(\omega - \Omega_3)(\omega - \Omega_4),$$

$$D(\omega) = 4I_1^2 I_2^2 I_3^2 I_4^2 - [(\omega - \Omega_1)(\omega - \Omega_2)(\omega - \Omega_3)$$
$$\times (\omega - \Omega_4) - I_1^2(\omega - \Omega_3)(\omega - \Omega_4) - I_2^2(\omega - \Omega_1)(\omega$$
$$- \Omega_4) - I_3^2(\omega - \Omega_1)(\omega - \Omega_2) - I_4^2(\omega - \Omega_2)(\omega - \Omega_3)$$
$$+ I_1^2 I_3^2 + I_2^2 I_4^2]^2 = -\prod_{j=1}^{8} (\omega - d_j). \tag{8}$$

Here, $d_1 \geqslant \ldots \geqslant d_8$ are the eight roots of the equation $D(\omega) = 0$ that can be found by solving two equations of 4th order. Let us note that all c_j and d_j are real since they can be viewed as eigenvalues of symmetric matrices.[6]

The simplest periodic nonuniform spin-1/2 XX chain in a random Lorentzian transverse field $\Omega_{01}\Gamma_1 I_1 \Omega_{02}\Gamma_2 I_2 \Omega_{01}\Gamma_1 I_1 \Omega_{02}\Gamma_2 I_2 \ldots$ requires a calculation of periodic continued fractions with period 2. The random-averaged density of states for this case becomes

$$\overline{\rho(\omega)} = \frac{1}{2\pi} \frac{|Y(\omega)|}{B(\omega)};$$

$$Y(\omega) = (\Gamma_1 + \Gamma_2)\sqrt{\frac{B(\omega) + B'(\omega)}{2}} - \mathrm{sgn}\, B''(\omega)(2\omega$$
$$- \Omega_{01} - \Omega_{02})\sqrt{\frac{B(\omega) - B'(\omega)}{2}},$$

$$B(\omega) = \sqrt{(B'(\omega))^2 + (B''(\omega))^2},$$

$$B'(\omega) = [(\omega - \Omega_{01})(\omega - \Omega_{02}) - \Gamma_1\Gamma_2 - I_1^2 - I_2^2]^2 - [(\omega$$
$$- \Omega_{01})\Gamma_2 + (\omega - \Omega_{02})\Gamma_1]^2 - 4I_1^2 I_2^2,$$

$$B''(\omega) = 2[(\omega - \Omega_{01})(\omega - \Omega_{02}) - \Gamma_1\Gamma_2 - I_1^2 - I_2^2][(\omega$$
$$- \Omega_{01})\Gamma_2 + (\omega - \Omega_{02})\Gamma_1]. \tag{9}$$

In principal, there are no difficulties in considering more complicated periodic nonuniform chains apart from the fact that the calculations become somewhat cumbersome.

Let us turn to a discussion of the results obtained for the density of states. First, note that in the limit of a uniform transverse field and exchange coupling, Eqs. (7) and (8) reproduce the well-known result for the uniform spin-1/2XX chain in a transverse field: $\rho(\omega) = 1/\pi\sqrt{4I^2 - (\omega - \Omega)^2}$ if $4I^2 - (\omega - \Omega)^2 > 0$ and $\rho(\omega) = 0$, otherwise. This result for the uniform chain also follows from (9) if $\Omega_{01} = \Omega_{02} = \Omega$, $\Gamma_1 = \Gamma_2 = 0$, $I_1 = I_2 = I$. The density of states (9) contains the result for uniform spin-1/2XX chain in a random Lorentzian transverse field[4] $\overline{\rho(\omega)} = \mp(1/\pi)$ $\times \text{Im}[1/\sqrt{(\omega \pm i\Gamma - \Omega_0)^2 - 4I^2}]$ if $\Omega_{01} = \Omega_{02} = \Omega_0$, $\Gamma_1 = \Gamma_2 = \Gamma$, $I_1 = I_2 = I$. In addition, the density of states (9), in the non-random limit $\Gamma_1 = \Gamma_2 = 0$, coincides with the density of states (8) with $\Omega_1 = \Omega_3$, $\Omega_2 = \Omega_4$, $I_1 = I_3$, $I_2 = I_4$, i.e., for a regular alternating chain $\Omega_1 I_1 \Omega_2 I_2 \Omega_1 I_1 \Omega_2 I_2 \dots$ as should be expected.

In Figs. 1–3 we display the density of states, together with both the dependences of the transverse magnetization

$$\overline{m_z} = -\frac{1}{2}\int_{-\infty}^{\infty} dE \overline{\rho(E)} \tanh\frac{E}{2kT} \tag{10}$$

on the transverse field at zero temperature, and the static transverse linear susceptibility

$$\overline{\chi_{zz}} = -\frac{1}{kT}\int_{-\infty}^{\infty} dE \overline{\rho(E)} \frac{1}{4\cosh^2(E/2kT)} \tag{11}$$

on temperature, for the few particular chains considered. Initially, let us discuss a non-random case. The main result of introducing the nonuniformity is a splitting of the initial magnon band with the edges $\Omega - 2|I|$, $\Omega + 2|I|$ into several subbands. The edges of the subbands are determined by the roots of equations $C(\omega) = 0$, $D(\omega) = 0$. The quantity $\rho(\omega)$ is positive inside the subbands, tends to infinity inversely proportionally to the square root of ω when ω approaches the subbands edges, and is equal to zero outside the subbands. For special values of parameters, the roots of the equations that determine the subbands edges may become multiple, the zeros in denominator and numerator in the expression for the density of states cancel each other, and as a result one observes a smaller number of subbands. In Figs. 1a and 2a, we show $\rho(\omega)$ for some periodic nonuniform chains having periods 3 and 4 to demonstrate the energy band scheme in the presence of nonuniformity. Note that the splitting caused by periodic nonuniformity is not surprising, since the periodic nonuniform chain can be viewed as a uniform chain with a crystalline unit cell containing several sites of the initial lattice. On the other hand, one expects several sub-

FIG. 1. Density of states (a), transverse magnetization versus transverse field Ω at $T=0$ (b), and static transverse linear susceptibility versus temperature at $\Omega=0$ (c), for the nonuniform chain $\Omega I_1 \Omega I_2 \Omega I_3 \Omega I_1 \Omega I_2 \Omega I_3 \dots$, $I_1 = 0.5$, $I_2 = 0.5$, $I_3 = 0.5$ (solid lines); $I_2 = 0.5$, $I_3 = 1$ (dashed lines); $I_2 = 0.25$, $I_3 = 1$ (dotted lines).

bands for a crystal having several atoms per unit cell (see for example Ref. 22). We now turn to the density of states given by (9). First, note that in the non-random case one finds two magnon subbands the edges of which are given by
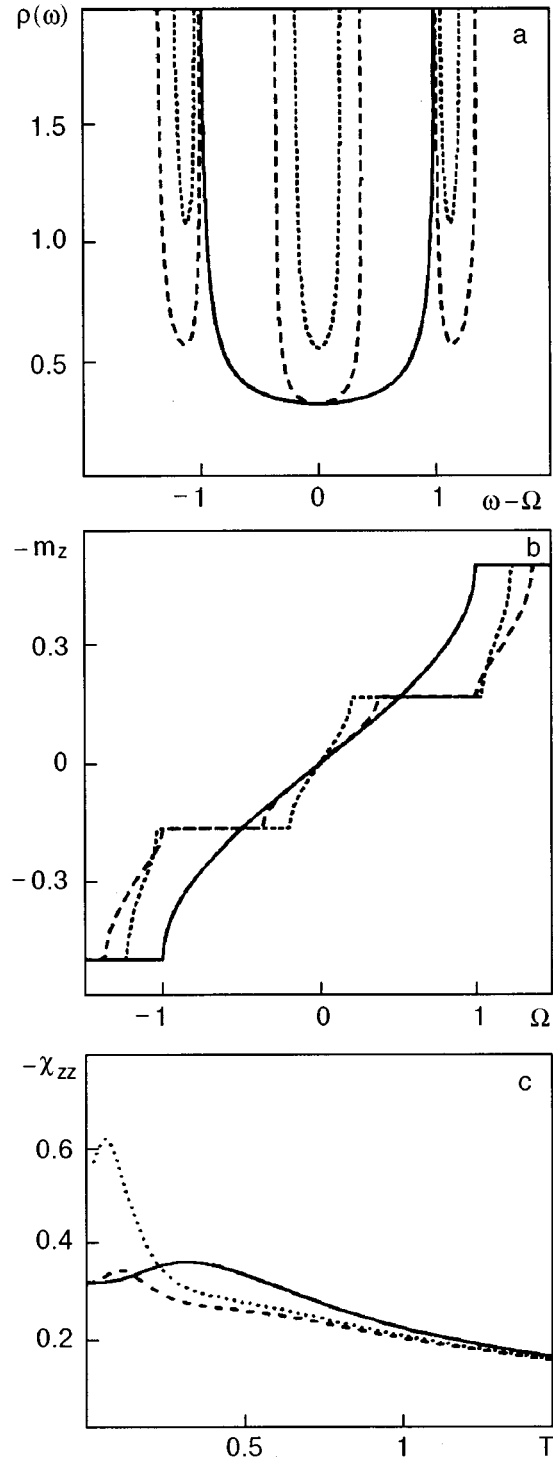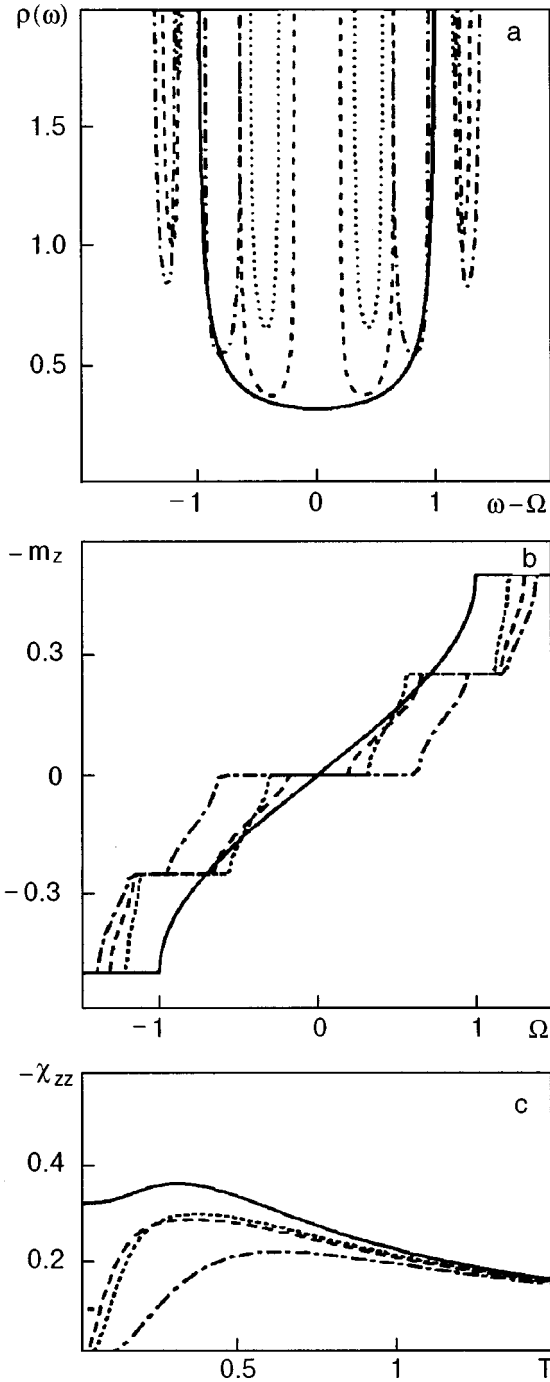
FIG. 2. Density of states (a), transverse magnetization versus transverse field Ω at $T=0$ (b), and static transverse linear susceptibility versus temperature at $\Omega=0$ (c), for the nonuniform chain $\Omega I_1 \Omega I_2 \Omega I_3 \Omega I_4 \Omega I_1 \Omega I_2 \Omega I_3 \Omega I_4 \ldots$, $I_1=0.5$, $I_2=0.5$, $I_3=0.5$, $I_4=0.5$ (solid lines); $I_2=0.5$, $I_3=0.5$, $I_4=1$ (dashed lines); $I_2=0.5$, $I_3=0.25$, $I_4=1$ (dotted lines); $I_2=1$, $I_3=0.25$, $I_4=1$ (dash-dotted lines).

$$\{b_1, b_2, b_3, b_4\} = \left\{ \frac{1}{2} \left[\Omega_1 + \Omega_2 \right. \right.$$

$$\left. \left. \pm \sqrt{(\Omega_1 - \Omega_2)^2 + 4(|I_1| \pm |I_2|)^2} \right] \right\} \quad (12)$$

(Fig. 3a). Introduction of the uniform diagonal Lorentzian disorder $\Gamma_1 = \Gamma_2 = \Gamma$ results in smearing out of the edges of the subbands (Fig. 3b). For extremely nonuniform diagonal

Lorentzian disorder $\Gamma_1 = 0$, $\Gamma_2 \neq 0$ the changes in the $\overline{\rho(\omega)}$ with increasing of the strength of disorder are more complicated (Fig. 3c). In the case when $\Omega_{01} \neq \Omega_{02}$ one may find that for a small strength of disorder only one subband is mainly smoothed, but with increases in the strength of disorder both subbands become smeared out.

The described dependences of the density of magnon states on introduction of periodic nonuniformity and disorder affects the behavior of thermodynamic quantities of the spin model. For example, the temperature dependence of the specific heat $\overline{c} = \int_{-\infty}^{\infty} dE \overline{\rho(E)} (E/2kT)^2 / \cosh^2(E/2kT)$ for a nonrandom periodic chain may exhibit a two-peak structure consisting of low-temperature and high-temperature peaks. Let us comment in some detail on the magnetic properties of the spin chains considered. The splitting of the magnon band into subbands caused by nonuniformity has interesting consequences for those properties. Consider for example the transverse magnetization (10). Since for $T \to 0$, $\tanh(E/2kT)$ tends either to -1 if $E<0$, or to 1 if $E>0$, one immediately finds because of the appearance of subbands that the low-temperature dependence of m_z against Ω in the non-random case must be composed of sharply increasing parts (when, with increasing Ω, $E=0$ moves inside each subband from its top to its bottom) separated by horizontal parts (when, with increasing of Ω, $E=0$ moves inside the gaps). Evidently a number of plateaus in the low-temperature dependence of the transverse magnetization on the transverse field is determined by a number of subbands. Moreover, the larger the gap in the density of states, the longer is the corresponding plateau. Every cusp in the the dependence of the transverse magnetization on Ω induces a singularity in the dependence of the static transverse linear susceptibility (11) on Ω. One can easily show that the dependence $-\overline{\chi_{zz}}$ against Ω, at $T=0$, is the same as the dependence of $\overline{\rho(\omega)}$ against $\Omega - \omega$. The latter dependence can be derived from the densities of states depicted in Figs. 1–3. The value of $-\overline{\chi_{zz}}$ at $T=0$ in the temperature dependence of $\overline{\chi_{zz}}$ at $\Omega=0$ is determined by the value of $\overline{\rho(0)}$. Therefore, the nonuniformity and randomness may essentially affect this value as well as the temperature dependence of the static transverse linear susceptibility. In different temperature regions one may find both an enhancement (and even a divergence), or suppressing of the curves $-\overline{\chi_{zz}}$ versus T. This can be seen nicely in Figs. 1c, 2c, 3g, 3h, and 3i.

To summarize, using continued fractions we have obtained rigorously the density of magnon states for periodic nonuniform spin-1/2 XX chain in a random Lorentzian transverse field. Continued fraction representation of the solution of Eq. (4) is extremely useful for calculation of the density of magnon states. The attractive features of this approach can be seen even for the uniform chain. In this case one omits performing twice the Fourier transformation while solving Eq. (4) in a standard manner and evaluates the desired $\overline{\rho(\omega)}$ straightforwardly. The advantages of the continued fraction approach becomes clear while treating periodic chains already with the smallest period of 2. Periodic nonuniformity
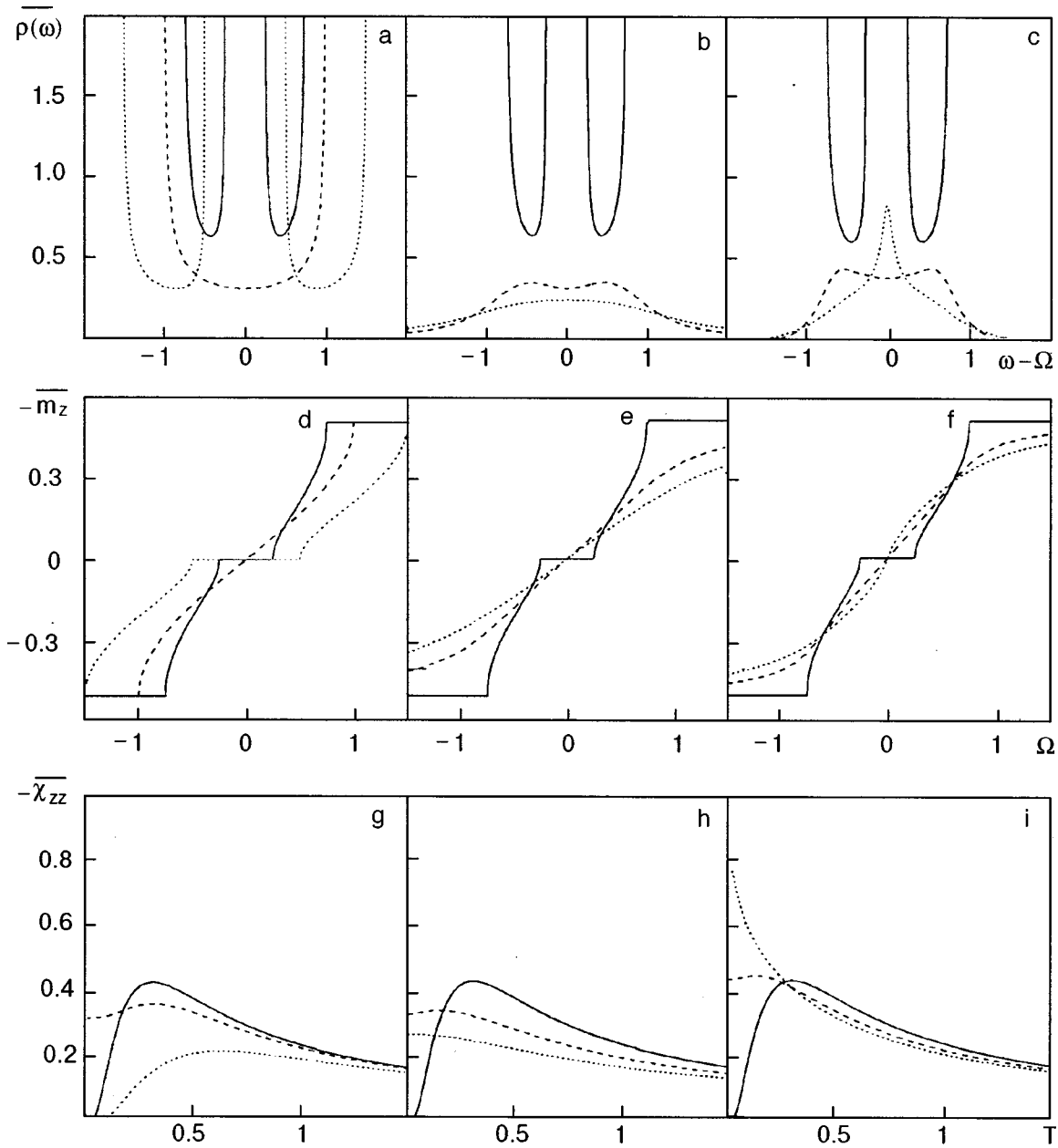
FIG. 3. Density of states (a, b, c) transverse magnetization versus transverse field Ω at $T=0$ (d, e, f) and static transverse linear susceptibility versus temperature at $\Omega=0$ (g, h, i) for the nonuniform random chain $\Omega_{01}\Gamma_1 I_1 \Omega_{02}\Gamma_2 I_2 \Omega_{01}\Gamma_1 I_1 \Omega_{02}\Omega_2 I_2 \ldots$, $I_1=0.5$, $\Omega_{01}=\Omega_{02}=\Omega$. a, d, g: non-random case $\Gamma_1=\Gamma_2=0$, $I_2=0.25$ (solid lines), $I_2=0.5$ (dashed lines), $I_2=1$ (dotted lines) b, e, h uniform disorder $I_2=0.25$, $\Gamma_1=\Gamma_2=0$ (solid lines), $\Gamma_1=\Gamma_2=0.5$ (dashed lines), $\Gamma_1=\Gamma_2=1$ (dotted lines); c, f, i nonuniform disorder $I_2=0.25$, $\Gamma_1=0$, $\Gamma_2=0$ (solid lines), $\Gamma_2=0.5$ (dashed lines), $\Gamma_2=1$ (dotted lines).

leads to a splitting of the magnon band into subbands that in its turn leads to the appearance of new cusps and singularities in the low-temperature dependences of the transverse magnetization and the static transverse linear susceptibility on transverse field, respectively. In the random case the spectacular changes in these dependences are smoothed. Periodic nonuniformity and randomness may either enhance or suppress the temperature dependence of $-\overline{\chi_{zz}}$. Changing the degree of periodic nonuniformity one may to some extent influence the detailed shapes $\overline{m_z}$ or $\overline{\chi_{zz}}$ against Ω, or $\overline{\chi_{zz}}$ against T. The described approach may be of considerable use for examining simple models of spin-Peierls instabilities,

especially in the presence of disorder. Analysis of the thermodynamic properties of non-random and random Lorentzian periodic nonuniform spin-1/2XX chains in a transverse field and their stability with respect to a lattice distortion will be given in a separate paper.

*E-mail: derzhko@icmp.lviv.ua

[1] E. Lieb, T. Schultz, and D. Mattis, Ann. Phys. (N.Y.) **16**, 407 (1961); S. Katsura, Phys. Rev. **127**, 1508 (1962); S. A. Pikin and V. M. Tsukernik, Zh. Éksp. Teor. Fiz **50**, 1377 (1966) Sov. Phys. JETP **23**, 914 (1966).

[2] P. Lloyd, J. Phys. **C2**, 1717 (1969); T. P. Eggarter, J. Math. Phys. **15**, 7 (1974).

[3] W. John and J. Schreiber, Phys. Status Solidi B **66**, 193 (1974); J. Richter, Phys. Status Solidi B **87**, K89 (1978); K. Handrich and S. Kobe, Amorphe Ferro- und Ferrimagnetika, Akademie-Verlag, Berlin, (1980) (in German).

[4] E. Barouch and J. Oppenheim, Physica (Amsterdam) **76**, 410 (1974); H. Nishimori, Phys. Lett. **A100**, 239 (1984); O. V. Derzhko and T. M. Verkholyak, Fiz. Nizk. Temp. **23**, 977 (1997) [Low Temp. Phys. **23**, 733 (1997)].

[5] O. Derzhko and J. Richter, Phys. Rev. B **55**, 14 298 (1997); O. Derzhko and J. Richter, Phys. Rev. B **59**, 100 (1999).

[6] S. W. Lovesey, J. Phys. C **21**, 2805 (1988).

[7] Ch. J. Lantwin and B. Stewart, J. Phys. A **24**, 699 (1991).

[8] J. K. Freericks and L. M. Falicov, Phys. Rev. B **41**, 2163 (1990).

[9] R. Lyzwa, Physica A **192**, 231 (1993).

[10] V. M. Kontorovich and V. M. Tsukernik, Zh. Éksp. Teor. Fiz. **53**, 1167 (1967) [Sov. Phys. JETP **26**, 687 (1968)].

[11] A. A. Zvyagin, Phys. Lett. A **158**, 333 (1991); A. A. Zvyagin Fiz. Nizk. Temp. **18**, 788 (1992) [Sov. J. Low Temp. Phys. **18**, 558 (1992)].

[12] P. Pincus, Solid State Commun. **9**, 1971 (1971).

[13] R. A. T. Lima and C. Tsallis, Phys. Rev. B **27**, 6896 (1983).

[14] K. Okamoto and K. Yasumura, J. Phys. Soc. Jpn. **59**, 993 (1990).

[15] K. Okamoto, J. Phys. Soc. Jpn. **59**, 4286 (1990).

[16] K. Okamoto, Solid State Commun. **83**, 1039 (1992).

[17] Y. Saika and K. Okamoto, cond-mat/9510114.

[18] A. Fujii, cond-mat/9707137.

[19] L. L. Goncalves and J. P. de Lima, J. Magn. Magn. Mater. **140−144**, 1606 (1995).

[20] O. Derzhko and O. Zaburannyi, J. Phys. Stud. **2**, 128 (1998); O. Derzhko, O. Zaburannyi, and J. W. Tucker, J. Magn. Magn. Mater. **186**, 188 (1998).

[21] V. I. Peresada, V. N. Afanasiev, and V. S. Borovikov, Fiz. Nizk. Temp. **1**, 461 (1975) [Sov. J. Low Temp. Phys. **1**, 227 (1975)], R. Haydock, V. Heine, and M. J. Kelly, J. Phys. C **5**, 2845 (1972); R. Haydock, V. Heine, and M. J. Kelly, J. Phys. C **8**, 2591 (1975); E. S. Syrkin and S. B. Feodosiev, Fiz. Nizk. Temp. **20**, 586 (1994) [Low Temp. Phys. **20**, 463 (1994)]; M. A. Mamalui, E. S. Syrkin, and S. B. Feodosiev, Fiz. Tverd. Tela **38**, 3683 (1996) [Phys. Solid State **38**, 2006 (1996)]; R. Haydock, Solid State Phys. **35**, 215 (1980); M. J. Kelly, Solid State Phys. **35**, 295 (1980).

[22] A. S. Davydov, *Tjeorija tvjerdogo tjela*, Nauka, Moskwa (1976).

Effect of pressure on magnetic properties of the compound MnSi

A. S. Panfilov

B. Verkin Institute for Low Temperature Physics and Engineering, National Academy of Sciences of the Ukraine, 310164 Kharkov, Ukraine*
(Submitted December 14, 1998; revised February 5, 1999)
Fiz. Nizk. Temp. **25**, 582–586 (June 1999)

Magnetic susceptibility of the weak itinerant-electron ferromagnet MnSi ($T_C \simeq 30$ K) is studied in the paramagnetic state under hydrostatic pressure up to 2 kbar in the temperature interval 78–300 K. An analysis of the experimental data using the Stoner model modified to account for the spin fluctuations leads to the estimate for the volume derivative of effective electron–electron interaction parameter $d \ln J / d \ln V = -1.4 \pm 0.1$ and of the density of electron states at the Fermi level $d \ln N(E_F) / d \ln V = 2 \pm 0.5$. A noticeable volume dependence of J points towards a significant role of electron correlations in the magnetism of this compound. © *1999 American Institute of Physics.* [S1063-777X(99)00706-9]

1. INTRODUCTION

Intermetallic compound MnSi (having a cubic crystal structure of the type B20) is a metal in which magnetic ordering occurs at temperatures below $T_C \simeq 30$ K.[1,2] In zero magnetic field, the magnetically ordered state is characterized by a helicoidal spin structure with a wavelength 180 Å along the direction [111], and by the spontaneous magnetic moment $M_0 = 0.4 \mu_B$ per Mn atom at zero temperature. In comparatively weak magnetic fields ($H \geqslant H_c \simeq 0.6$ T at T=4.2 K), the helicoidal ordering is replaced by ferromagnetic ordering with quite large values of susceptibility of the paraprocess ($\chi_{hf} \simeq 2.9 \times 10^{-3}$ emu/mole.[3])

At $T > T_c$, the temperature dependence of the magnetic susceptibility of MnSi can be described quite well by the Curie–Weiss law up to 300 K, and noticeable departures from this dependence are observed only at higher temperature.[4] The corresponding value of the effective moment per Mn atom $M_{\mathrm{eff}} \simeq 2.2 \mu_B$ is much larger than the spontaneous moment, which is typical of itinerant ferromagnets.

Calculations of the electron structure of the paramagnetic state[5–7] show that MnSi has a high density of states at the Fermi level and a large value of the exchange-enhanced spin paramagnetism, but the Stoner criterion for an itinerant-electron ferromagnet is not fulfilled in this compound. However, spin-polarized computations indicate[6] that the ground state is magnetically ordered. On the other hand, the Fermi level of the paramagnetic phase lies near the minimum of the density of states curve $N(E)$. For a dominating role of the single-particle excitations, this should lead to an increase in the magnetic susceptibility χ upon an increase in temperature.[6,7] However, such a behavior seems contrary to the experiments. A detailed analysis of calculations of the paramagnetic density of states shows[8] that a slight displacement of the Fermi level ($\simeq -2$ mRyd) results not only in a qualitatively correct form of the dependence $\chi(T)$, but also in the fulfillment of Stoner's criterion due to a significant increase in the density of states at the Fermi level. However,

it has not been possible so far to provide a consistent description of the magnetic properties of MnSi at finite temperature using Stoner's standard model.

In an attempt to interpret the data on paramagnetic diffusive scattering of neutrons as well as the dependence $\chi(T)$, Edwards[9] went farther than the hypotheses of Stoner's model and proposed that slowly fluctuating magnetic moments (having an amplitude $\sim 1 \mu_B$) arise in Mn atoms in MnSi upon an increase in temperature. These induced moments were later presented[10] as thermal excitations of spin fluctuations (SF) in the Stoner continuum. Such a modification of Stoner's model taking SF into account considerably improves the agreement between this model and experimental results for MnSi, especially for the dependence $\chi(T)$ and the quantity T_C.[10,11] Hence it can be assumed that SF play a significant role in the temperature dependence of the magnetic properties of the compound under consideration.

Another distinguishing feature of MnSi is that its magnetic characteristics are highly sensitive to pressure. Thus, a pressure $P \sim 15$ kbar completely suppresses the magnetically ordered state.[12,13] The high experimental values of the volume derivatives of Curie temperature ($d \ln T_C / d \ln V \sim 50$)[3,13,14] and spontaneous magnetic moment ($d \ln M_0 / d \ln V = 16$)[3] confirm the itinerant nature of magnetism of MnSi, and at the same time emphasize the significant role of the fine structure of $N(E)$ near the Fermi level in determining the peculiarities of its magnetic properties.[3]

Lerch and Jarlborg[6] calculated the spin-polarized state in MnSi as a function of the lattice parameter a in the local spin-density approximation (LSDA). The resulting estimates of the spontaneous magnetic moment ($M_0 \simeq 0.85 \mu_B$ per Mn atom) and its volume derivative ($d \ln M_0 / d \ln V \simeq 3$) corresponding to the experimental value $a = 8.60$ a.u. differ significantly from the above experimental data. This discrepancy points towards the problem typical of the LSDA technique and concerning the description of the spin-polarized state (in particular, the dependence of its properties on volume). Thus, the weak dependence of the effective exchange-correlation interaction parameter for electrons in
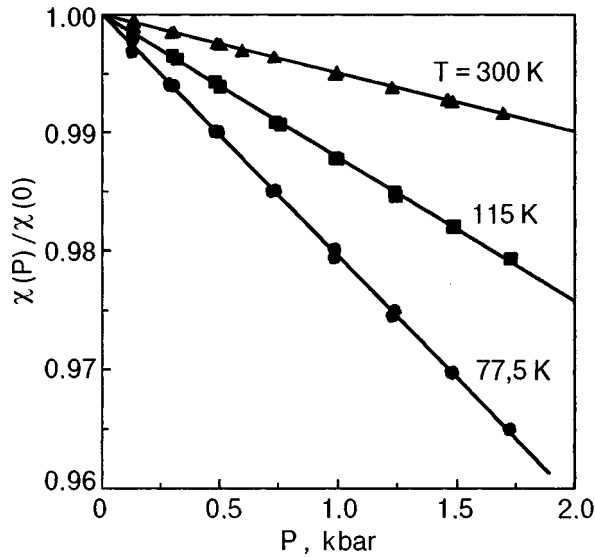
FIG. 1. Pressure dependence of magnetic susceptibility at various temperatures, normalized to the value of the susceptibility at $P=0$.

TABLE I. Experimental values of magnetic susceptibility, its pressure and volume derivatives, and bulk modulus for MnSi at various temperatures.

T, K	$10^4 \chi$ emu/mol	$d \ln \chi / dP$, 1/Mbar	B, Mbar	$d \ln \chi / d \ln V$
77.5	128.1	-20.4 ± 1.0	1.355	27.7 ± 1.5
115.4	70.6	-12.1 ± 0.7	1.350	16.4 ± 1.0
300.0	23.4	-5.0 ± 0.4	1.325	6.6 ± 0.5

$$\frac{d \ln \chi(T)}{d \ln V} = \frac{d \ln C}{d \ln V} + \frac{1}{T-\Theta}\frac{d\Theta}{d \ln V} \equiv \frac{d \ln C}{d \ln V}$$

$$+ \frac{\chi(T)\Theta}{C}\frac{d \ln \Theta}{d \ln \Theta}. \quad (1)$$

It can be seen from Fig. 2 that in accordance with the above formula, the experimental values of $d \ln \chi / d \ln V$ are a linear function of susceptibility defining the parameters

$$\frac{d \ln C}{d \ln V} = 2 \pm 0.5, \quad \frac{d \ln \Theta}{d \ln V} = 45 \pm 5. \quad (2)$$

The last parameter was estimated by using the values $C \simeq 0.63$ K·emu/mole and $\Theta \simeq 28$ K, corresponding to our data and close to those obtained by Ishikawa et al.[2] The values of $d \ln \Theta / d \ln V$ obtained above are in good agreement with the values $d \ln T_C / d \ln V \simeq 53$ and 60 obtained from magnetization studies under pressure,[3] as well as electrical resistance and differential magnetic susceptibility studies.[14]

Note that the values of $d \ln \chi / d \ln V$ obtained by us from direct measurements of the susceptibility of MnSi under pressure are in accord with the magnetostriction data for $T > T_C$ obtained by Fawcett et al.,[22] which in turn are about half the analogous values obtained by Matsunaga et al.[23] The values of the magnetovolume constant $C_V = \partial \ln V(T,H)/\partial M^2(T,H)$ for para- and ferromagnetic states also differ by a factor of about two: $C_V = 0.56 \times 10^{-10}$ (emu/mole)$^{-2}$ at $T = 77.5$ K (our results) and 0.93

transition metals and their compounds on the atomic spacing predicted by the LSDA[6,15,16] contradicts the available results of studies of the magnetic susceptibility of exchange-enhanced spin paramagnets[17] and magnetovolume effect in itinerant-electron ferromagnets[18] under pressure. Additional experimental data for a wider range of investigated materials are required for determining the applicability of the LSDA method and the approximations used therein for describing the magnetic properties of transition metals.

In the present work, we study the effect of pressure on the magnetic susceptibility of MnSi in the paramagnetic state. The experimental data were analyzed by using the Stoner model taking SF into consideration. The obtained estimates of the volume derivative of the density of states at the Fermi level and of the exchange-correlation electron interaction parameter are compared with those obtained theoretically for MnSi. Preliminary results of investigations were published in Ref. 7.

2. EXPERIMENTAL TECHNIQUE AND RESULTS

The magnetic susceptibility χ of the MnSi single crystal was studied under hydrostatic pressure up to 2 kbar at fixed temperatures 77.5, 115.4 and 300 K. Measurements were made in a magnetic field $H \simeq 1.5$ T by using a pendulum magnetometer placed directly in the high-pressure cell.[19] The pressure was created by gaseous helium with the help of a membrane compressor.[20] The relative error of measurements did not exceed 0.05%. The obtained experimental dependences $\chi(P)$ (Fig. 1) are linear within this error limit. Table I contains the values of the corresponding derivatives $d \ln \chi / dP$. Bulk moduli B from Ref. 21 were used for converting these derivatives into volume derivatives.

In the framework of the Curie–Weiss law, a phenomenological description of the volume effects in the magnetic susceptibility of MnSi at various temperatures can be given in terms of volume derivatives of the Curie constant C and the paramagnetic Curie temperature Θ:
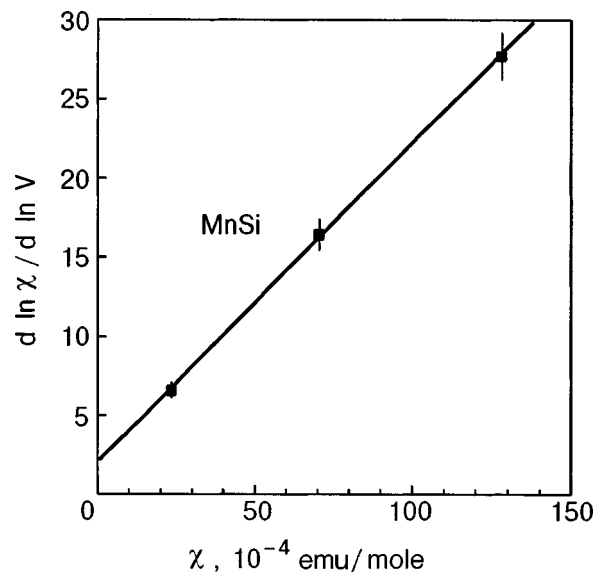

FIG. 2. The derivative $d \ln \chi / d \ln V$ as a function of the magnetic susceptibility.

$\times 10^{-10}(\text{emu/mole})^{-2}$ at $T = 4.2\,\text{K}$ (magnetostriction data for $H \geqslant H_c$).[23] The origin of these discrepancies is not known so far.

3. DISCUSSION OF RESULTS

The simplified version of the modification of Stoner's model taking into account the temperature-induced spin fluctuations leads to the following expression for the volume-enhanced spin-susceptibility χ:[24-26]

$$\frac{1}{\chi(T)} = \frac{1}{\chi_P} - J + \lambda_0 T, \tag{3}$$

where $\chi_P = \mu_B^2 N(E_F)$ is the unperturbed Pauli spin susceptibility which depends weakly on temperature, $N(E_F) \equiv N$ the density of states at the Fermi level, J the effective exchange-correlated parameter of interaction between band electrons, and $\lambda_0 T$ the SF contribution in which the constant λ_0 is determined by the properties of the band structure.[26] In this case, the temperature dependence of susceptibility, assumed to be related with the SF term, is characterized by the Curie–Weiss law with the parameters

$$C = \lambda_0^{-1}, \quad \Theta = \frac{C}{\chi_P}(J\chi_P - 1). \tag{4}$$

Differentiating Eq. (3) with respect to volume, we obtain for the magnetovolume effect $d\ln\chi/d\ln V$ the expression

$$\frac{d\ln\chi(T)}{d\ln V} = \frac{d\ln N}{d\ln V} + J\chi(T)\left[\frac{d\ln N}{d\ln V} + \frac{d\ln J}{d\ln V}\right.$$
$$\left. - \frac{\lambda_0 T}{J}\left(\frac{d\ln\lambda_0}{d\ln V} + \frac{d\ln N}{d\ln V}\right)\right]. \tag{5}$$

This expression is assumed to be valid for the compound MnSi. Indeed, the observed linear dependence of the experimental values of $d\ln\chi/d\ln V$ on χ (Fig. 2) is in accord with Eq. (5) if we treat the parameters $d\ln N/d\ln V, J$ and $d\ln J/d\ln V$ appearing in it as constants and disregard the contribution $(\lambda_0 T/J)(d\ln\lambda_0/d\ln V + d\ln N/d\ln V)$ associated with the SF mechanism. The smallness of this contribution in MnSi is due to two reasons. The first reason is the smallness of the factor $\lambda_0 T/J$ in the investigated temperature interval. Assuming that $\chi(T)$ is determined mainly by the SF effects (see Eqs. (3) and (4)) and using the value of the Curie constant $C = 0.63\,\text{K}\cdot\text{emu/mole}$ and the theoretical value $J = 1.05 \times 10^4$ mole/emu,[7] we obtain $\lambda_0 T/J \leqslant 0.05 \ll 1$ for $T \leqslant 300\,\text{K}$. Moreover, in view of the closeness of the quantities $d\ln C/d\ln V$ and $d\ln N/d\ln V$ following from a comparison of Eqs. (1) and (5) for $\chi = 0$, we obtain $d\ln\lambda_0/d\ln V + d\ln N/d\ln V \approx 0$. Thus, the final expression for the magnetovolume effect in MnSi assumes the form

$$\frac{d\ln\chi(T)}{d\ln V} \simeq \frac{d\ln N}{d\ln V} + J\chi(T)\left(\frac{d\ln N}{d\ln V} + \frac{d\ln J}{d\ln V}\right). \tag{6}$$

This expression does not contain explicitly specific mechanisms of thermal excitations determining the quantity $\chi(T)$ appearing in it, and is valid for all types of excitations under the condition that their temperature-dependent corrections to Stoner product $J\chi_P$ are comparatively small.

Fitting of parameters (6) to the experimental data (Fig. 2) gives

$$\frac{d\ln N}{d\ln V} + \frac{d\ln J}{d\ln V} = 0.19 \pm 0.05, \tag{7}$$

$$\frac{d\ln N}{d\ln V} = 2 \pm 0.5. \tag{8}$$

The theoretical value $J = 1.05 \times 10^4$ mole/emu[7] used here is in accord with the data obtained by other authors (1.14×10^4 mole/emu,[27] and 1.37×10^4 mole/emu[6]).

The estimate obtained for the volume derivative of the density of states (8) coincides with the theoretical values $d\ln N/d\ln V = 1.60$[6] and 1.66[7] within the error in determining the former. The mean value 1.63 ± 0.03 of the latter, which is more precise estimate for $d\ln N/d\ln V$ in comparison with (8), was used in (7) for determining the volume derivative of the interaction parameter

$$\frac{d\ln J}{d\ln V} = -1.4 \pm 0.1. \tag{9}$$

This quantity is in good agreement with the value -1.3 ± 0.1 obtained[28] in analogous investigations for the system $Fe_{1-x}Co_xSi$ of alloys related to MnSi, thus confirming its reliability. At the same time, it differs considerably from the value $\simeq -0.1$ calculated for MnSi in the LSDA method.[6] This is yet another evidence of inapplicability of local approximation of the spin density functional for describing the magnetic properties of systems with a large spatial inhomogeneity of the electron density, e.g., d-metals and their compounds.

It is assumed that correlation effects, which are presented more appropriately by the Hubbard model,[29,30] play a significant role in systems with narrow bands. In this model, the relation between the interaction parameter J and the width W of the d-band is determined by the balance between the gain in potential energy U of intraatomic Coulomb repulsion and the loss in their kinetic (band) energy, and the volume dependence of J is determined by the expression[29,30]

$$\frac{d\ln J}{d\ln V} = \frac{d\ln W}{d\ln V}f(U/W, Q). \tag{10}$$

Here, the coefficient $f(\leqslant 1)$ depends on the ratio U/W, occupancy Q of the d-band, and the type of the crystal structure, while the intraatomic potential energy U is assumed to be independent of the volume. It follows from Eq. (10) that dependence of J on volume is determined by the width of the d-band. For $U \gg W$, it becomes the only energy parameter with which the behavior of J correlates.[32] This determines the lower limit of the values of $d\ln J/d\ln V \geqslant d\ln W/d\ln V = -5/3$.[33]

The value of $d\ln J/d\ln V \simeq -1.4$ obtained in the present work for MnSi confirms the noticeable volume dependence of J predicted by the Hubbard model. This indicates a significant role of electron correlations in the magnetism of MnSi and supports the applicability of the model for transition metals. At the same time, only a qualitative agreement has been obtained[34] between the experimental data on the

volume dependence of J in specific d-metals and their compounds and the available theoretical results obtained by using the Hubbard model.[29–31] It should be certainly interesting to carry out further experimental and theoretical studies of the properties of electron–electron interactions for such systems.

The author is indebted to A. A. Frolov for kindly supplying the monocrystalline MnSi sample, and to Prof. I. V. Svechkarev for his fruitful remarks during a discussion of the results.

*E-mail: panfilov@ilt.kharkov.ua

[1] H. J. Williams, J. H. Wernick, R. C. Sherwood, and G. K. Wertheim, J. Appl. Phys. **37**, 1256 (1966).

[2] Y. Ishikawa, K. Tajima, D. Bloch, and M. Roth, Solid State Commun. **19**, 525 (1976).

[3] D. Bloch, J. Voiron, V. Jaccarino, and J. H. Wernick, Phys. Lett. **51A**, 259 (1975).

[4] H. Yasuoka, V. Jaccarino, R. C. Sherwood, and J. H. Wernick, J. Phys. Soc. Jpn. **44**, 842 (1978).

[5] O. Nakanishi, A. Yanase, and A. Hasegawa, J. Magn. Magn. Mater. **15-18**, 879 (1980).

[6] P. Lerch and T. Jarlborg, J. Magn. Magn. Mater. **131**, 321 (1994).

[7] G. E. Grechnev, A. S. Panfilov, and I. V. Svechkarev, J. Magn. Magn. Mater. **157-158**, 711 (1996).

[8] G. E. Grechnev, to be published.

[9] D. M. Edwards, J. Phys. F **12**, 1789 (1982).

[10] S. N. Evangelou and D. M. Edwards, J. Phys. C **16**, 2121 (1983).

[11] G. G. Lonzarich and E. Taillefer, J. Phys. C **18**, 4339 (1985).

[12] J. D. Thompson, Z. Fisk, and G. G. Lonzarich, Physica B **161**, 317 (1989).

[13] C. Pfleiderer, R. H. Friend, G. G. Lonzarich *et al.*, in *Proceedings Int. Conf. Phys. Transition Metals*, Darmstadt, Germany (1992), [ed. by P. M. Oppeneer and J. Kübler], World Scientific, Singapore (1993).

[14] C. Pfleiderer, G. J. McMullan, S. R. Julian, and G. G. Lonzarich, Phys. Rev. B **13**, 8330 (1997).

[15] O. K. Andersen, J. Madsen, U. K. Poulsen *et al.*, Physica B & C **86−88**, 249 (1977).

[16] Y. Ohta and M. Shimizu, J. Phys. F **13**, L123 (1983).

[17] A. S. Panfilov and I. V. Svechkarev, in *Proceedings Int. Conf. Phys. Transition Metals*, Darmstadt, Germany (1992), [ed. by P. M. Oppeneer and J. Kübler], World Scientific, Singapore (1993), p. 699.

[18] M. Shimizu, J. Magn. Magn. Mater. **20**, 47 (1980).

[19] A. S. Panfilov, Fiz. Tekh. Vysok. Davl. **2**, 61 (1992).

[20] M. D. Bondarenko, Prib. Tekh. Eksp. , No. 4, 223 (1973).

[21] G. P. Zinoveva, L. P. Andreeva, and P. V. Geld, Phys. Status Solidi A **23**, 711 (1974).

[22] E. Fawcett, J. P. Maita, and J. H. Wernick, J. Magn. Magn. Mater. **1**, 29 (1970).

[23] M. Matsunaga, Y. Ishikawa, and T. Nakajima, J. Phys. Soc. Jpn. **51**, 1153 (1982).

[24] Y. Ishikawa, Y. Noda, Y. J. Uemura *et al.*, Phys. Rev. B **31**, 5884 (1985).

[25] T. Moriya and A. Kawabata, J. Phys. Soc. Jpn. **34**, 63 (1973); **35**, 669 (1973).

[26] M. Shimizu, Physica **159**, 26 (1989).

[27] M. Shimizu, A. Kunihara, and A. Tamaoki, Phys. Lett. **99A**, 107 (1983).

[28] A. S. Panfilov, I. V. Svechkarev, and L. F. Romasheva, Fiz. Nizk. Temp. **19**, 284 (1993) [Low Temp. Phys. **19**, 200 (1993)].

[29] A. B. Kaiser, A. M. Olés, and G. Stollhoff, Phys. Scr. **37**, 935 (1988).

[30] P. Fulde, Physica B **159**, 50 (1989).

[31] G. Stollhoff, A. M. Olés, and V. Heine, Phys. Rev. B **41**, 7028 (1990).

[32] N. D. Lang and H. Ehrenreich, Phys. Rev. **168**, 605 (1968).

[33] V. Heine, Phys. Rev. **153**, 673 (1967).

[34] A. B. Kaiser, Physica **161**, 311 (1989).

Translated by R. S. Wadhwa

Anomalies in microwave absorption in quasi-one-dimensional $CsMnCl_3 \cdot 2H_2O$ in a pulsed magnetic field

A. G. Anders and M. I. Kobets

B. Verkin Institute for Low Temperature Physics and Engineering, National Academy of Sciences of the Ukraine, 310164 Kharkov, Ukraine*
(Submitted December 18, 1998)
Fiz. Nizk. Temp. **25**, 587–591 (June 1999)

Intense microwave absorption is observed in quasi-one-dimensional antiferromagnet $CsMnCl_3 \cdot 2H_2O$ in the frequency range below the gap in the spin-wave spectrum. The absorption is observed for the polarization $\mathbf{h} \| \mathbf{H}$ in a pulsed external field directed along the ''hard'' anisotropy axis. It is proposed that the absorption is associated with the frustration of the interchain magnetic order due to a pulse of the applied field. © *1999 American Institute of Physics.*
[S1063-777X(99)00806-3]

Low-dimensional magnets exhibiting a strong spatial anisotropy of exchange interactions are characterized by a complex microwave energy absorption spectrum. The quasi-one-dimensional biaxial antiferromagnet $CsMnCl_3 \cdot 2H_2O$ with the Neel temperature $T_N = 4.89$ K is an example of such a spectrum.[1,2] In addition to uniform antiferromagnetic resonance (AFMR) bands corresponding to excitation of magnons with the wave vector $\mathbf{k} = 0$, it displays a magnetic-dipole subthreshold two-magnon absorption which is linear in power and associated with simultaneous excitation of two spin waves with $\mathbf{k}_1 = -\mathbf{k}_2$ as a result of decay of a microwave field quantum. The behavior of this spectrum for different orientations of the applied field and its transformation upon a change in frequency and temperature were analyzed in detail in Refs. 1 and 2 A fragment of the frequency–field dependence of absorption bands in the case when the applied field $\mathbf{H}$ is oriented along ''hard'' anisotropy axis $\mathbf{a}$ is presented in Fig. 1. In experiments,[1,2] these dependences were obtained by the traditional radiospectroscopic method using a slow field scanning at fixed frequencies of microwave excitation.

Our experiments in pulsed external fields revealed a new peculiar type of microwave energy absorption. Additional absorption is observed for the applied field orientation $\mathbf{H} \| \mathbf{a}$ in the frequency range lying below the gap ν_1 in the spin-wave spectrum of the system. The experiments were carried out on a radiospectrometer with a reflecting resonator (wave of the H_{10n} type) at the output microwave generator power level $P < 10$ mW in the frequency range $\nu_0 = 18$–35 GHz, the duration of magnetic field pulse was $\tau = 20$ ms for the sinusoidal pulse, the temperature range of observations was 1.6–2 K, and the absorption signal was detected by an oscillograph.

The main features of this absorption are as follows. The absorption is observed only at frequencies $\nu_0 < \nu_1$ for the polarization $\mathbf{h} \| \mathbf{H} \| \mathbf{a}$ of the magnetic component of the microwave field. The absorption spectrum contains two bands whose peak intensity is comparable with the peak intensity of the uniform resonance line. The shape of the bands is

symmetric, the left slope sometimes displaying a structure with a low resolution. The absorption has peculiar time characteristics depicted schematically in Fig. 2. The delay time τ_1 of the first band relative to the beginning of the field pulse depends explicitly on the amplitude, and hence on the steepness of the field pulse front since the field pulse duration remained unchanged under the experimental conditions. For a constant field pulse amplitude, the value of τ_1 increases with decreasing working frequency. For a small amplitude (case 3 in Fig. 2), the delay time can exceed the field pulse duration: $\tau_1 > \tau$.

The delay time τ_1 for the second band exceeds τ_1 considerably (by a factor of 10 and more) and decreases with the field pulse amplitude. Finally, it was found that the second absorption band is observed even in the case of a delay in the feeding of microwave radiation to the sample by the time $\tau_{del} \simeq 0.1$ s, which is considerably longer than τ_1 and the field pulse duration τ.

Thus, the absorption being detected is a result of action of the magnetic field pulse, while the microwave illumination of the sample plays the role of a tool for detecting the consequences of such a pulse. We can assume that such an action causes a renormalization of the magnon spectrum of the system, which is similar to that observed during crystal heating and leading to a decrease in the value of the energy gap in the spectrum to $\nu_1 < \nu_0$. This must cause the emergence of absorption at the working frequency ν_0 since it corresponds to the excitation of a uniform AFMR mode with $\mathbf{k} = 0$ for the field direction $\mathbf{H} \| \mathbf{a}$. In this case, the absorption corresponds to the first of the observed bands separated from the beginning of the pulse by the time τ_1, longer delay times corresponding to lower frequencies of the working range.

The rate of subsequent cooling of the magnon subsystem, which is associated with the removal of heat to the helium bath through the phonon subsystem of the crystal, is determined by specific features of experimental technique, i.e., the method of fixation of the sample to the resonator wall, the pressure of the heat-exchange gas, and so on. The process is accompanied by an increase in the natural resonant
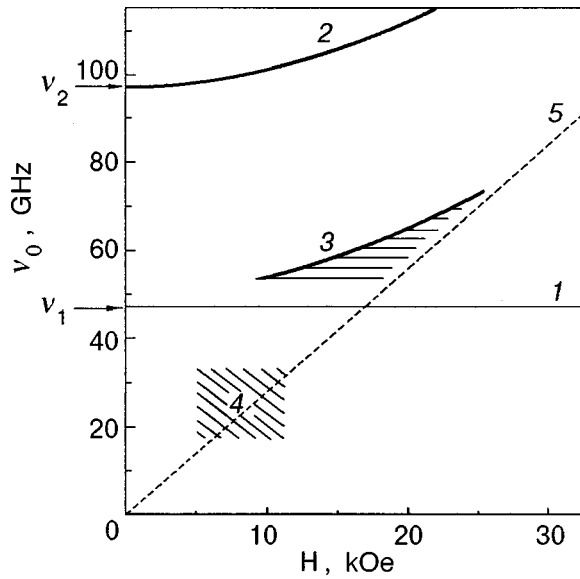
FIG. 1. Frequency-field diagram of microwave absorption bands in $CsMnCl_3 \cdot 2H_2O$ for the applied field orientation $\mathbf{H} \| \mathbf{a}$ at $T = 2$ K. Solid lines *1* and *2* correspond to uniform AFMR bands (excitations with $\mathbf{k} = 0$). Band *3* is the difference process of the subthreshold two-magnon absorption of magnons from branches *1* and *2* (excitations with $\mathbf{k}_1 = -\mathbf{k}_2$). Absorption *4* is observed under pulsed scanning of the field; straight line *5* describes the frequency–field dependence of resonant absorption of the standard sample DPPH (diphenyl pipicrylhydrosil).

frequency of the magnon subsystem and repeated resonant absorption at the instant τ_2 at the same working frequency ν_0, which naturally occurs after a time period much longer than τ_1.

It should be noted, however, that the heating of the crystal must be quite strong in this case. According to the results of investigation of temperature dependences of the gaps in the AFMR spectrum of $CsMnCl_3 \cdot 2H_2O$,[3] a decrease in the
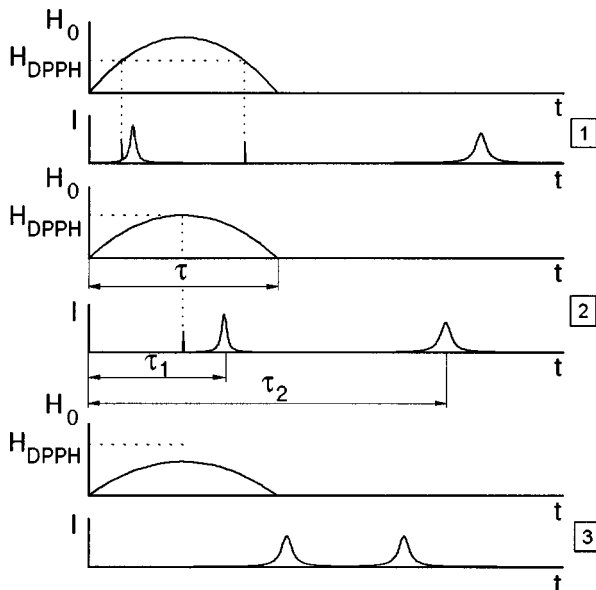

FIG. 2. Transformation of the absorption band with intensity I_0 observed at a fixed frequency upon a change in the magnetic field pulse amplitude H_0; H_{DPPH} is the value of the field corresponding to the EPR absorption in the standard sample.

value of ν_1 to the working frequency range ν_0 must correspond to an increase in the temperature of the magnon subsystem of the sample from the initial temperature by ~ 1.5–2 K.

At the same time, we must eliminate the effect of the trivial source of heating due to eddy currents induced by the field pulse in the resonator. In order to prevent a possible heat transfer from the resonator walls to the sample, the latter was coated in some experiments with a heat-proof paraffin coating, which did not lead to any noticeable change in the observed effects. Besides, when the sample without a heat–proof coating was turned through an angle of 90°, so that the applied field $\mathbf{H}$ was oriented along the easy axis $\mathbf{b}$, the uniform AFMR line observed in the working frequency range in fields $H \sim 10$–15 kOe does not change the value of resonant field. This indicates the constancy of the sample temperature for moderate values of the field pulse amplitude H_0 used by us.

The increase in spin temperature mentioned above corresponds to an increase in the magnetic energy of the crystal due to the interaction of the external field pulse with the induced magnetic moment of the sample, formed due to the tilting of magnetic sublattices in the direction of the field perpendicular to the "easy" axis:

$$E_M = \mathbf{M} \cdot \mathbf{H} = N g S \mu_B \int_0^\tau (H_0^2/H_e) \sin(\pi t/\tau) dt.$$

Here N is the number of Mn^{2+} ions with the effective g-factor $g = 2$ and spin $S = 5/2$ in the sample, μ_B Bohr's magneton, and H_e the exchange field amounting to 230 kOe in $CsMnCl_3 \cdot 2H_2O$. Since the contribution of the phonon subsystem to the heat capacity of this crystal is virtually zero at temperatures $T \leqslant 2$ K,[4] the increment of the spin temperature for a sample with typical size $5 \times 2 \times 0.5$ mm^3 at $T = 1.5$ K and the specific heat $C = 0.5$ J/mole·K amounts to $\Delta T_s \simeq 1.5$ K.

According to estimates obtained in Ref. 5, the spin–spin relaxation time τ_s in this case is rather short and amounts to $\sim 10^{-8}$ s for the exchange parameter $J = 3$ K in chains of Mn^{2+} ions. For $t > \tau_s$, the spin subsystem must go over to the quasi-equilibrium state for the given temperature increment. However, the spin–phonon relaxation time

$$\tau_{sl}^{-1} = \frac{\Theta_c}{\hbar} \frac{T}{\rho a^2 s^2} \left(\frac{T}{\Theta_c}\right)^{5/2} \exp(-\Theta_D^2/4\Theta_c T)$$

turns out to be considerably longer and amounts to $\tau_{sl} = 10^{-2}$ s (which is comparable with the duration of the field pulse) for values of the exchange parameters $\Theta_c = 30$ K, the average velocity of sound $s = 2$ km/s, the density of the substance $\rho = 2.84$ g/cm^3, and the Debye temperature $\Theta_D = 56$ K for $T = 2$ K.

Thus, the magnon subsystem of the crystal should display heating and subsequent cooling for such relations of time periods, i.e., we should expect the approximate equality $\tau_1 \approx \tau_s$ and $\tau_2 \approx \tau_{sl}$. In the time interval $\tau_1 - \tau_2$, the system must be under conditions close to adiabatic. Besides, a similar overheating of the magnon subsystem must also be observed for the field direction along the "intermediate"

axis **c**. However, the experimental results indicate that, first, the values of the parameters τ_1 and τ_2 differ noticeably from these estimates, and second, $\mathbf{H} \| \mathbf{a}$ is the predominant direction of the field for the observation of the effect. Consequently, it would be interesting to study the processes of system excitation at the beginning of the field pulse, when we can expect that the regime remains adiabatic, as well as the state of the system in the interval $\tau_1 - \tau_2$, where adiabaticity is apparently violated. It should be borne in mind that the magnon subsystem in such a noticeably overheated state must be essentially nonlinear.

The initial process of excitation can be associated with the generation of stationary nonlinear states of the type of solitons or domain walls, which can exist in $CsMnCl_3 \cdot 2H_2O$ for the given orientation of the external and rf magnetic fields.[4] The possibility of impact excitation of solitons by spatially homogeneous as well as spatially localized pulsed magnetic field was investigated in Refs. 5 and 6 where the magnetic system was regarded as essentially nonlinear system. In this case, the time of relaxation of soliton excitations to the magnon subsystem of the crystal can be evaluated on the basis of the results obtained by Kivshar' and Malamed.[7] This time for $CsMnCl_3 \cdot 2H_2O$ is quite short and amounts to $\tau_{sol\text{-}s} = E_0 / \eta c^2 \simeq 10^{-8}$ s (E_0 and c are the energy and limiting velocity of a domain wall, and η the viscosity parameter), which is comparable with the time τ_s of stabilization of the quasi-equilibrium distribution inside the magnetic subsystem, which is determined by exchange scattering of magnons. In this case, the efficiency of generation of stationary nonlinear states might prove to be quite high. According to estimates, an overheating by 2 K of the magnon system for a sample of the size indicated above may result in the formation of $\sim 10^{18}$ kinks in chains of Mn^{2+} ions, which amounts to $\sim 5\%$ of the total number of magnetic sites in the crystal. However, the formation of nonlinear states along interchain directions with a weak exchange coupling is many times more advantageous from the energy point of view, and their realization must naturally lead to the suppression of interchain correlations.

At the same time, the interaction of the pulsed field with the magnetic subsystem in $CsMnCl_3 \cdot 2H_2O$ can have an origin differing basically from that of nonlinear states associated with peculiarities of its magnetic structure. It should be recalled that an orthorhombic unit cell of a crystal with the space group P_{cca} contains four magnetic ions Mn^{2+} occupying pairwise equivalent positions.[10] Magnetic ions occupying inequivalent sites in a unit cell along the **a** direction are coupled through a strong antiferromagnetic exchange interaction $J = 3$ K and form chains that are the basis of the quasi-one-dimensional magnetic structure of this crystal. Weak exchange interaction J_1 and J_2 between chains along the directions **b** and **c** are also antiferromagnetic, their values being $J_1/J \sim 10^{-2}$ and $J_2/J \sim 10^{-4}$. A magnetic unit cell of $CsMnCl_3 \cdot 2H_2O$ is formed due to doubling of the parameter b, and hence this crystal is an eight-sublattice antiferromagnet, although it is regarded as a two-sublattice antiferromagnet in most of publications devoted to an analysis of magnetic and resonant properties.

Neighboring ions in a chain can be coupled though an antisymmetric exchange interaction of the type $D_{jl}[\mathbf{S}_j \times \mathbf{S}_l]$, and the spin Hamiltonian of the form

$$H_D = \sum_j D_j (S_j^z S_{j+1}^x - S_j^x S_{j+1}^z), \tag{1}$$

where the x-, y-, and z-axes are parallel to the a, b and c direction in the cell respectively, was taken into account by Nagata and Hirosawa[11] who analyzed the EPR linewidth for this compound. An interaction of type (1) in the magnetically ordered state leads to tilting of magnetic moments of adjacent cites of a chain and to the formation of the ferromagnetic moment of the chain as a whole, which is directed along the axis **a**. It is compensated by the opposite moment in a neighboring chain, and hence the magnetic unit cell has zero spontaneous ferromagnetic moment.

The value of the parameter D_j can be estimated proceeding from the results obtained in Ref. 11 concerning the contribution of antisymmetric exchange to the EPR linewidth. It amounts to $\sim 5 \times 10^{10} \, s^{-1}$, which leads to the value $M_F = (D_j/2J) g S \mu_B \approx 0.05 \mu_B$ of the ferromagnetic moment of the chain in the ground state (per site).

Since the interchain coupling corresponds to the "weak" exchange field $H_{e1} = 2J_1 S k_B / g \mu_B \approx 500$ Oe, the external field of the orientation $\mathbf{H} \| \mathbf{a}$ for $H \geqslant H_{e1}$ must cause a phase transition associated with a reorientation of ferromagnetic moments for half the chains. This can lead to an additional heating of the sample by $\Delta T \simeq 0.25$ K provided that the entire energy $E_M = M_F H$ liberated in such a transition is transformed into heat.

In this case, the observed effects should be explained by taking into account the peculiarities o the magnetically ordered state of the quasi-one-dimensional magnetic system. As a matter of fact, the equilibrium magnetic structure fluctuates quite strongly along links between chains virtually in the entire temperature range of the antiferromagnetic state of $CsMnCl_3 \cdot 2H_2O$ except the millikelvin region. For this reason, the temperature dependence of the magnon spectrum of the system (including its gaps) essentially reflects just the extent of increase in these fluctuations, and hence the dynamics of interchain disordering, which attain maximum values at the Neel temperature $T_N = 4.89$ K, while the short-range antiferromagnetic order in the chain is preserved up to $T \simeq 30$ K.

The phase transition induced by the applied field inevitably generates phase separation of the system, as a result of which the interchain correlation radius characterizing quantitatively the extent of interchain ordering, decreases abruptly and becomes apparently smaller than the size of the sample in the direction of weak exchange. The temperature of the phonon reservoir remains unchanged during the action of the field pulse, and hence the magnon subsystem of the crystal turns out to be overheated and more disordered against its background than the equilibrium structure for the given temperature, which must be manifested in the corresponding decrease in the values of energy gaps in the magnon spectrum. It should be noted that the limiting case of interchain disordering and vanishing of the interchain correlation radius corresponds to the Mermin–Wagner theorem[12]

concerning the absence of a long-range magnetic order, and naturally to the disappearance of energy gaps in the spectrum of a one-dimensional magnet.

In this case, the value of the delay parameter τ_1 determined by the rate of interchain disordering must depend on the steepness of the field pulse since (see above) the process of disordering itself starts from the phase transition for $H \geqslant H_{e1}$. The parameter τ_2 is determined by the rate of reconstruction of interchain correlations, during which the inverse phase transition to the pure antiferromagnetic phase must occur. The time characteristics of these processes can differ apparently in view of the presence of the external field in the former and its absence in the latter case. However, it should be borne in mind in any case that processes of domain transformations accompanying the phase separation during phase transitions are of the long-period diffusive type as a rule. Since the thermodynamic potentials of the corresponding phases differ insignificantly in our case, we must expect a considerable relaxation time of nonequilibrium structures. These periods of time must be increased additionally due to natural defects in the crystal.

Thus, the main qualitative characteristics of the microwave absorption observed in $CsMnCl_3 \cdot 2H_2O$ in pulsed magnetic fields can be explained by the dynamics of violation and restoration of the long-range magnetic order in interchain directions in the crystal.

It should be noted in conclusion that the decrease in the gap widths in the energy spectrum of $CsMnCl_3 \cdot 2H_2O$ in an external pulsed magnetic field was also observed (but not interpreted) in Ref. 13. An analysis of the exciton–magnon absorption spectrum in this crystal revealed a considerable (approximately by a factor of 1.5 and more) decrease in the gap widths measured in the pulsed field as compared to their value in static fields.

*E-mail: aanders@ilt.kharkov.ua

[1] A. G. Anders, A. I. Zvyagin, and A. I. Petutin, Fiz. Nizk. Temp. **3**, 649 (1977) [Sov. J. Low Temp. Phys. **3**, 316 (1977)].

[2] A. G. Anders, A. I. Zvyagin, and A. I. Petutin, Fiz. Nizk. Temp. **6**, 491 (1980) [Sov. J. Low Temp. Phys. **6**, 234 (1980)].

[3] A. G. Anders, A. I. Petutin, Yu. V. Pereverzev, and A. I. Zvyagin, Fiz. Nizk. Temp. **5**, 604 (1979) [*sic*].

[4] K. Kopinga, Phys. Rev. B **16**, 427 (1977).

[5] A. I. Akhiezer, V. G. Bar'yakhtar, and S. V. Peletminskiĭ, *Spin Waves* [in Russian], Nauka, Moscow (1967).

[6] B. A. Ivanov and A. K. Kolezhuk, Fiz. Nizk. Temp. **17**, 343 (1991) [Sov. J. Low Temp. Phys. **17**, 177 (1991)]; Fiz. Nizk. Temp. **21**, 355 (1995) [Low Temp. Phys. **21**, 275 (1995)].

[7] Yu. S. Kivshar' and B. A. Malomed, Fiz. Tverd. Tela (Leningrad) **31**, 209 (1989) [Sov. Phys. Solid State **31**, 293 (1989)]; Fiz. Met. Metalloved. No. **3**, 5 (1990).

[8] I. L. Lyubchanskiĭ, V. L. Sobolev, and T. K. Soboleva, Fiz. Nizk. Temp. **13**, 1061 (1987) [Sov. J. Low Temp. Phys. **13**, 603 (1987)].

[9] B. A. Ivanov, A. L. Sukstanskiĭ, and E. V. Tartakovskaya, Fiz. Nizk. Temp. **13**, 982 (1987) (1987) [Sov. J. Low Temp. Phys. **13**, 560 (1987)].

[10] S. J. Jensen, P. Andersen, and S. E. Rasmussen, Acta Chem. Scand. **16**, 189 (1962).

[11] K. Nagata and T. Hirosawa, J. Phys. Soc. Jpn. **40**, 1584 (1976).

[12] N. D. Mermin and H. Wagner, Phys. Rev. Lett. **17**, 1133 (1966).

[13] V. P. Novikov, I. S. Kachur, and V. V. Eremenko, Fiz. Nizk. Temp. **7**, 223 (1981) [Sov. J. Low Temp. Phys. **7**, 108 (1981)].

Peculiarities of thermodynamics of $2D$ Heisenberg magnets on a triangular lattice

T. N. Antsygina

B. Verkin Institute for Low Temperature Physics and Engineering, National Academy of Sciences of the Ukraine, 310164 Kharkov, Ukraine*
(Submitted February 5, 1999)
Fiz. Nizk. Temp. **25**, 592–599 (June 1999)

Thermodynamic and magnetic properties of $2D$ Heisenberg ferro- and antiferromagnets with a spin of 1/2 on a triangular lattice are investigated theoretically. The formalism of two-time Green's functions and the decoupling procedure explicitly taking into account the presence of a short-range order and not requiring the existence of a long-range order in the system are used. The energy, heat capacity, and susceptibility of magnets are expressed in terms of correlation functions for which a self-consistent system of equations is obtained. The system is solved numerically in the entire temperature range. Analytic asymptotic forms of the above quantities are constructed in the limits of high and low temperatures. The results of analysis are compared with analogous data for square lattices as well as with the high-temperature expansions available in literature. © *1999 American Institute of Physics.*
[S1063-777X(99)00906-8]

1. INTRODUCTION

At the present time, the theory of low-dimensional magnetic systems is an extensive and thoroughly investigated branch of solid-state physics.[1,2] Nevertheless, theoretical investigations in this field continue to be important in view of a number of unsolved basic problems and the appearance of new experimental results on the thermodynamics of such systems. In most cases of practical importance, the observed physical patterns can be successfully described on the basis of the traditional Heisenberg model. The one-dimensional case has been investigated most comprehensively (see, for example, Ref. 2). In an analysis of two-dimensional ($2D$) systems, main attention was paid to square lattices[1–5] in connection with the description of the properties of high-T_c superconductors which are $2D$ antiferromagnetic insulators in the undoped state. The thermodynamics of $2D$ magnets on a triangular lattice has been studied less extensively. However, the interest in such systems has increased in recent years due to intense experimental studies of ^{3}He films on graphite,[6–10] whose physical properties in the millikelvin temperature range are completely determined by the dynamics of the nuclear spin subsystem on a triangular lattice.

A correct interpretation of the experimental results mentioned above requires the knowledge of thermodynamic functions of a magnet in the entire temperature range. At the same time, only high-temperature expansions for ferro- and antiferromagnets[11] and asymptotic forms for the ferromagnetic case for $T \to 0$ are known for spin systems on a triangular lattice.[5] Thus, it is important to obtain theoretical results describing the behavior of the systems under consideration in the entire temperature range by using a unified approach.

In this paper, the heat capacity and magnetic susceptibility of $2D$ spin ferro- and antiferromagnetic (FM and AFM) systems with a spin 1/2 on a triangular lattice are calculated

theoretically by using the Heisenberg model. Analytic asymptotic forms are constructed for internal energy, heat capacity, and magnetic susceptibility in the limits of low and high temperatures. The obtained results are compared with similar data obtained for square lattices.

2. FORMULATION OF THE PROBLEM AND BASIC EQUATIONS

Let us consider a Heisenberg system with spin $S = 1/2$, whose Hamiltonian has the form

$$H = -\frac{J}{2} \sum_{\mathbf{f}, \delta} \mathbf{S}_\mathbf{f} \mathbf{S}_{\mathbf{f}+\delta}, \tag{1}$$

where J is the exchange constant ($J > 0$ in the ferromagnetic and $J < 0$ in the antiferromagnetic case), $\mathbf{S}_\mathbf{f}$ the operator of spin at site $\mathbf{f}$, and δ the vector defining the coordinates of nearest neighbors. A distinguishing feature of low-dimensional isotropic magnetic systems is that they do not have a long-range order at any finite temperature (the Mermin–Wagner theorem[12]) so that the thermodynamic average $\langle S^z \rangle = 0$. Thus, the theory must be constructed in terms of the quantities describing the short-range order, i.e., in rerms of the correlation functions. Such a method of calculation was proposed by Kondo and Yamaji[13] for $1D$ systems and generalized to the case of $2D$ magnets on square lattices in Ref. 3. We shall follow this procedure here for analyzing the Heisenberg system on a triangular lattice.

The method of calculations is based on the formalism of two-time Green's functions[14] and can be described as follows. The equation of motion for Fourier time transforms $\langle\langle S_\mathbf{f}^z | S_{\mathbf{f}'}^z \rangle\rangle_\omega$ of Green's function is

$$\omega\langle\langle S_{\mathbf{f}}^z|S_{\mathbf{f}'}^z\rangle\rangle_\omega = iJ\sum_\delta \ (\langle\langle S_{\mathbf{f}}^x S_{\mathbf{f}+\delta}^y|S_{\mathbf{f}'}^z\rangle\rangle_\omega$$

$$-\langle\langle S_{\mathbf{f}}^y S_{\mathbf{f}+\delta}^x|S_{\mathbf{f}'}^z\rangle\rangle_\omega). \tag{2}$$

The equations for $\langle\langle S_{\mathbf{f}}^x|S_{\mathbf{f}'}^x\rangle\rangle_\omega$ and $\langle\langle S_{\mathbf{f}}^y|S_{\mathbf{f}'}^y\rangle\rangle_\omega$ can be obtained from (2) by cyclic permutation. Then we must write equations for the functions appearing on the right-hand side of (2) (for the sake of brevity, we give here only one equation):

$$\omega\langle\langle S_{\mathbf{f}}^x S_{\mathbf{f}+\delta}^y|S_{\mathbf{f}'}^z\rangle\rangle_\omega = \frac{i}{2\pi}(\Delta_{\mathbf{f}+\delta,\mathbf{f}'}\langle S_{\mathbf{f}}^x S_{\mathbf{f}+\delta}^x\rangle$$

$$-\Delta_{\mathbf{f},\mathbf{f}'}\langle S_{\mathbf{f}}^y S_{\mathbf{f}+\delta}^y\rangle)$$

$$+iJ\sum_{\delta'} \ (\langle\langle S_{\mathbf{f}}^y S_{\mathbf{f}+\delta'}^z S_{\mathbf{f}+\delta}^y|S_{\mathbf{f}'}^z\rangle\rangle_\omega$$

$$-\langle\langle S_{\mathbf{f}}^z S_{\mathbf{f}+\delta'}^y S_{\mathbf{f}+\delta}^y|S_{\mathbf{f}'}^z\rangle\rangle_\omega$$

$$+\langle\langle S_{\mathbf{f}}^x S_{\mathbf{f}+\delta}^z S_{\mathbf{f}+\delta+\delta'}^x|S_{\mathbf{f}'}^z\rangle\rangle_\omega$$

$$-\langle\langle S_{\mathbf{f}}^x S_{\mathbf{f}+\delta}^x S_{\mathbf{f}+\delta+\delta'}^z|S_{\mathbf{f}'}^z\rangle\rangle_\omega) \tag{3}$$

($\Delta_{\mathbf{f},\mathbf{f}'}$ is the Kronecker symbol). On the second step, we carry out decoupling of higher functions on the right-hand side of (3). In order to illustrate the procedure of decoupling, we consider, for example, the first term in the sum over δ'. We write this term in an identical form

$$\langle\langle S_{\mathbf{f}}^y S_{\mathbf{f}+\delta'}^z S_{\mathbf{f}+\delta}^y|S_{\mathbf{f}'}^z\rangle\rangle_\omega = \Delta_{\delta,\delta'}\langle\langle S_{\mathbf{f}}^y S_{\mathbf{f}+\delta}^z S_{\mathbf{f}+\delta}^y|S_{\mathbf{f}'}^z\rangle\rangle_\omega + (1$$

$$-\Delta_{\delta,\delta'})\langle\langle S_{\mathbf{f}}^y S_{\mathbf{f}+\delta}^z S_{\mathbf{f}+\delta'}^y|S_{\mathbf{f}'}^z\rangle\rangle_\omega, \tag{4}$$

separating explicitly its terms for coinciding ($\delta=\delta'$) and different ($\delta\neq\delta'$) values of δ and δ'. Since the spin of 1/2 satisfies the equality $S^z S^y = -(i/2)S^x$, the first term on the right-hand side of (4) has the form

$$\Delta_{\delta,\delta'}\langle\langle S_{\mathbf{f}}^y S_{\mathbf{f}+\delta}^z S_{\mathbf{f}+\delta}^y|S_{\mathbf{f}'}^z\rangle\rangle_\omega = -\frac{i}{2}\Delta_{\delta,\delta'}\langle\langle S_{\mathbf{f}}^y S_{\mathbf{f}+\delta}^x|S_{\mathbf{f}'}^z\rangle\rangle_\omega \tag{5}$$

and hence can be reduced to a function of the same type as the function on the left-hand side of (3). In the second term on the right-hand side of (4), the order of Green's functions can be reduced only as a result of decoupling. Following the method proposed by Kondo and Yamaji,[13] we carry out decoupling according to the algorithm

$$\langle\langle S_{\mathbf{f}}^y S_{\mathbf{f}+\delta}^z S_{\mathbf{f}+\delta'}^y|S_{\mathbf{f}'}^z\rangle\rangle_\omega \rightarrow \alpha\langle S_{\mathbf{f}}^y S_{\mathbf{f}+\delta'}^y\rangle\langle\langle S_{\mathbf{f}+\delta}^z|S_{\mathbf{f}'}^z\rangle\rangle_\omega. \tag{6}$$

Here, in contrast to the standard method of decoupling, we introduce the coefficient α which is chosen in such a way that the kinematic relation

$$\langle\mathbf{S}^2\rangle = S(S+1) = 3/4 \tag{7}$$

is satisfied.

It is interesting to note that this original decoupling procedure is quite effective as compared to the generally accepted method in which $\alpha\equiv 1$. In particular, the fulfillment of condition (7) automatically leads to coincident tempera-

ture dependences of correlation functions[3,13] with the corresponding expressions derived from direct high-temperature expansions.

Applying the above procedure of decoupling to all higher-order Green's functions appearing on the right-hand side of (3), we obtain a complete system of equations containing correlators (ν runs through the values x,y,z)

$$c_1 = 4\langle S_{\mathbf{f}}^\nu S_{\mathbf{f}+\delta}^\nu\rangle; \tag{8}$$

$$c_2 = 4\langle S_{\mathbf{f}}^\nu S_{\mathbf{f}+\delta+\delta'}^\nu\rangle; \quad \delta\neq-\delta'. \tag{9}$$

According to definition (8), the function c_1 takes into account spin correlations at site $\mathbf{f}$ with the neighbors located on the first coordination sphere. The second correlation function c_2 describes correlations between spins separated by two steps along the translation vectors δ. Starting from this moment, the type of the lattice under investigation plays the fundamental role. For example, the condition $\delta\neq-\delta'$ for a square lattice is a necessary and sufficient condition for defining the correlator (9) unambiguously since in this case we necessarily leave the limits of the first coordination sphere in this lattice after two steps. In the case of a triangular lattice, however, there are ways consisting of two steps and leading to a spin on the first coordination sphere, which corresponds to correlations between nearest neighbors that have already been taken into account while writing c_1. Thus, while defining c_2 on a triangular lattice, we must require that the following condition hold in addition to (9):

$$\delta+\delta'\neq\delta''. \tag{10}$$

It should be noted that in the case of a square as well as a triangular lattice, the function (9) describes correlations with all neighbors lying on the second as well as the third coordination spheres. Condition (10) must be taken into account correctly in the evaluation of the corresponding sums over δ' appearing on the right-hand side of (3) after decoupling.

We carry out the Fourier coordinate transformation for $\langle\langle S_{\mathbf{f}}^z|S_{\mathbf{f}'}^z\rangle\rangle_\omega$ and determine Fourier transforms of Green's function:

$$G(\omega,\mathbf{k}) = \sum_{\mathbf{f}} \ \langle\langle S_{\mathbf{f}}^z|S_{\mathbf{f}'}^z\rangle\rangle_\omega \exp(i\mathbf{k}\mathbf{f}). \tag{11}$$

As a result of solution of the set of equations for Green's functions, we obtain

$$G(\omega,\mathbf{k}) = \frac{Jzc_1}{4\pi}\frac{1-\gamma_{\mathbf{k}}}{\omega^2-\omega_{\mathbf{k}}^2}. \tag{12}$$

Here

$$\gamma_{\mathbf{k}} = \frac{1}{z}\sum_\delta \ \exp(i\mathbf{k}\delta) \tag{13}$$

(z is the coordination number; $z=6$ for a triangular and $z=4$ for a square lattice),

$$\omega_{\mathbf{k}}^2 = \frac{J^2 z}{2}(1-\gamma_{\mathbf{k}})[\Delta+\tilde{c}_1 z(1-\gamma_{\mathbf{k}})], \tag{14}$$

$$\Delta = 1-5\tilde{c}_1+3\tilde{c}_2, \tag{15}$$

and $\tilde{c}_i = \alpha c_i$ $(i=1,2)$. Using spectral relations for Green's functions,[14] we arrive at the following set of equations defining the functions α, $\tilde{c}_1$, and $\tilde{c}_2$:

$$\alpha = \frac{Jz\tilde{c}_1}{N} \sum_{\mathbf{k}} g(\mathbf{k}); \tag{16}$$

$$1 = \frac{Jz}{N} \sum_{\mathbf{k}} \gamma_{\mathbf{k}} g(\mathbf{k}); \tag{17}$$

$$\tilde{c}_2 = \frac{Jz\tilde{c}_1}{3N} \sum_{\mathbf{k}} f(\gamma_{\mathbf{k}}) g(\mathbf{k}), \tag{18}$$

where N is the total number of lattice sites,

$$g(\mathbf{k}) = \frac{1 - \gamma_{\mathbf{k}}}{\omega_{\mathbf{k}}} \coth \frac{\omega_{\mathbf{k}}}{2T}; \tag{19}$$

and the function $f(\gamma_{\mathbf{k}})$ for a triangular lattice has the form

$$f(\gamma_{\mathbf{k}}) = 6\gamma_{\mathbf{k}}^2 - 2\gamma_{\mathbf{k}} - 1. \tag{20}$$

For a $2D$ magnet on a triangular lattice, the set of equations (16)–(18) has the same structure as the equations for α, $\tilde{c}_1$, and $\tilde{c}_2$ in the case of a square lattice.[3] However, this similarity is only formal. The basic difference between these two systems lies not only in different values of the coordination numbers, but first of all in the type of the structural factor $\gamma_{\mathbf{k}}$ as well as the form of the function $f(\gamma_{\mathbf{k}})$ which in the case of a square lattice is defined as[3]

$$f(\gamma_{\mathbf{k}}) = 4\gamma_{\mathbf{k}}^2 - 1. \tag{21}$$

It will be proved below that these differences lead to notably different behaviors of thermodynamic functions for lattices of the two types.

3. ASYMPTOTIC BEHAVIOR OF CORRELATION FUNCTIONS IN THE LIMITS OF HIGH AND LOW TEMPERATURES

The set of equations (16)–(18) for the functions α, $\tilde{c}_1$, and $\tilde{c}_2$ looks formally identical for the FM and the AFM case, but an analysis of these equations is determined essentially by the sign of the correlation constant J. In particular, the sign of J determines the sign of the correlation function $\tilde{c}_1$. The solution of this system for arbitrary temperatures can be obtained only numerically. In the limit of high and low temperatures, the set of equations (16)–(18) can be solved analytically. Below, we shall obtain the asymptotic forms of solutions for $T \gg |J|$ and $T \to 0$ for both types of lattices. It is convenient to introduce the parameter $\theta = T/J$ that can be positive or negative depending on the sign of J.

In the range of high temperatures ($|\theta| \gg 1$), the system of equations is solved by expansion in reciprocal powers of the parameter θ. In this case, all calculations are identical for both types of lattices as well as for FM and AFM. Confining the analysis to terms of the order of θ^{-2}, we arrive at the following result:

$$\alpha = 1 + \frac{A}{\theta}; \quad \tilde{c}_1 = \frac{1}{4\theta}\left(1 + \frac{2A}{\theta}\right); \quad \tilde{c}_2 = \frac{5}{48\theta^2}, \tag{22}$$

where we have introduced the notation

$$A = \frac{z-5}{4}. \tag{23}$$

It can be seen from (22) that expressions for FM and AFM differ in the sign of the exchange constant J, while the results obtained for triangular and square lattices in this approximation differ in the value of the parameter A containing the coordination number z.

In contrast to the high-temperature limit, an analysis of asymptotic forms in the low-temperature limit is more complicated and has peculiarities for FM or AFM systems as well as for triangular and square lattices. For this reason, each of the cases listed above should be analyzed separately.

First of all, we consider the function $g(\mathbf{k})$ appearing in all the equations of the system (16)–(18), which is a Fourier transform of the correlator $\langle S_0^z S_{\mathbf{f}}^z \rangle$ accurate to within a factor:

$$\langle S_{\mathbf{k}}^z S_{-\mathbf{k}}^z \rangle = \frac{Jzc_1}{4} g(\mathbf{k}). \tag{24}$$

As in Ref. 3, we can prove that the function $g(\mathbf{k})$ for $T \to 0$ and for vectors $\mathbf{k}$ close to $\mathbf{k}_0$ assumes the Ornstein–Zernike form

$$g(\mathbf{k}) \simeq \frac{26T}{(Jz)^2 |\tilde{c}_1|} \frac{1}{(\mathbf{k}_0 - \mathbf{k})^2 + \xi^{-2}}, \tag{25}$$

where the parameter ξ plays the role of correlation length. In each of the cases listed below, the parameters appearing in relation (25) are defined as

$$\mathbf{k}_0 = 0; \quad \xi = \sqrt{z\tilde{c}_1/4\Delta}, \tag{26}$$

for FM on a square or a triangular lattice, where Δ is defined by relation (15),

$$\mathbf{k}_0 = (\pi, \pi); \quad \xi = \sqrt{|\tilde{c}_1|/\Delta_1}; \quad \Delta_1 = 1 - 3|\tilde{c}_1| + 3\tilde{c}_2 \tag{27}$$

for AFM on a square lattice, and finally

$$\mathbf{k}_0 = (0, 2\pi/3); \quad \xi = \sqrt{3|\tilde{c}_1|/4\Delta_2}; \quad \Delta_2 = 1 - 4|\tilde{c}_1| + 3\tilde{c}_2 \tag{28}$$

for AFM on a triangular lattice.

Let us return to the system of equations (16)–(18). Obviously, the last two equations ((17) and (18)) form a complete system for the correlation functions $\tilde{c}_1$ and $\tilde{c}_2$. Having defined these functions, we can determine the parameter α with the help of Eq. (16). In order to construct asymptotic forms for $T \to 0$ and to carry out subsequent numerical calculations, it is convenient to use in the system of equations (16)–(18) the functions Δ, Δ_1, or Δ_2 instead of the function $\tilde{c}_2$ in each of the cases (26)–(28).

Let us first consider a ferromagnet ($J > 0$). The calculations presented below are valid for both types of lattices. After we go over from the variable $\tilde{c}_2$ to the quantity Δ, Eqs. (16) and (17) remain unchanged, and Eq. (18) taking into account definition (15) is transformed into

$$\Delta = 1 - 2\tilde{c}_1 - \frac{Jz\tilde{c}_1}{N} \sum_{\mathbf{k}} (z\gamma_{\mathbf{k}} + 1)(1 - \gamma_{\mathbf{k}}) g(\mathbf{k}). \tag{29}$$

For our subsequent analysis, it is convenient to introduce the density of states

$$w(x) = \frac{1}{N} \sum_{\mathbf{k}} \delta(x - \gamma_{\mathbf{k}}), \tag{30}$$

with the help of which the system of equations (17) and (29) is transformed to

$$y = 2 \int_{-1}^{1} dx x w(x) \frac{1-x}{\Omega(x)} \coth \frac{\Omega(x)}{\lambda}, \tag{31}$$

$$\eta y^2 z = 1 - y^2 - y \int_{-1}^{1} dx w(x) \frac{(1-x)^2 (zx+1)}{\Omega(x)}$$

$$\times \coth \frac{\Omega(x)}{\lambda}. \tag{32}$$

Here, we have introduced the following new variables y and η (instead of $\tilde{c}_1$ and Δ):

$$y = \sqrt{2 \tilde{c}_1}; \quad \eta = \Delta / y^2 z, \tag{33}$$

as well as the following notation:

$$\Omega(x) = \sqrt{(1-x)(1-x+2\eta)}; \quad \lambda = \frac{4\theta}{zy}. \tag{34}$$

An analysis shows that the function y for $T \to 0$ remains finite ($y \to 1$), while $\eta \to 0$. Since the integrand in (32) has no singularities for $\eta \to 0$, we can put $\eta = 0$ on both sides of Eq. (32), which is converted into an equation for y:

$$1 - y^2 = y \int_{-1}^{1} dx w(x)(1-x)(zx+1) \coth \frac{(1-x)}{\lambda}. \tag{35}$$

After a number of transformations, this equation in the lowest approximation in θ is transformed to

$$1 - y^2 = y \lambda^2 (1+z) w(1) \int_{0}^{\infty} du u (\coth u - 1).$$

Evaluating the integral and taking into account the first relation in (33), we obtain the following expression for $\tilde{c}_1$:

$$\tilde{c}_1 \simeq \frac{1}{2} - \frac{2\pi^2}{3} \frac{1+z}{z^2} w(1) \theta^2. \tag{36}$$

Using Eqs. (16) and (31) and the second relation from (33), we obtain the following expressions for α and Δ:

$$\alpha \simeq \frac{3}{2} - \frac{4\pi^2}{3z} w(1) \theta^2, \tag{37}$$

$$\Delta \simeq \theta \exp\left(- \frac{z}{8 w(1) \theta} \right). \tag{38}$$

Expressions (36)–(38) are valid both for a square and for a triangular lattice and differ only in the values of the parameters z and $w(1)$ ($z = 4$ and $w(1) = 1/\pi$ for a square lattice and $z = 6$, $w(1) = \sqrt{3}/2\pi$ for a triangular lattice).

Let us go over to the construction of low-temperature asymptotic forms for antiferromagnets ($J < 0$, $\theta < 0$). In this case, the correlation function $\tilde{c}_1$ is negative, and we shall henceforth consider $|\tilde{c}_1|$ for convenience. Besides, it was mentioned above that instead of the function $\tilde{c}_2$ in Eq. (18), we must introduce the functions Δ_1 (for a square lattice) and Δ_2 (for a triangular lattice) defining the temperature depen-

dence of the correlation length (see (27) and (28)). In contrast to FM, square and triangular lattices should be analyzed separately for AFM. This is primarily due to a considerable difference in the temperature dependences of Δ_1 and Δ_2. Indeed, $\Delta_1 \to 0$ as $T \to 0$ for a square lattice, while the value of Δ_2 for a triangular lattice remains finite at any temperature. The calculation of the low-temperature asymptotic forms of $|\tilde{c}_1|$ and Δ_1 on a square lattice is generally similar to that used in an analysis of FM, although initial equations in this case turn out to be more complicated. In the first nonvanishing approximation in θ, the final result has the form

$$|\tilde{c}_1| \simeq \frac{1}{2a_1^2} - \frac{\zeta(3)}{\pi} |\theta|^3, \tag{39}$$

$$\alpha \simeq 1 + \frac{1}{2a_1^2} - \frac{\zeta(3)}{\pi} |\theta|^3, \tag{40}$$

$$\Delta_1 \simeq \frac{\theta^2}{2} \exp\left(- \pi \frac{1 - 2a_1 a_2}{2a_1^2 |\theta|} \right). \tag{41}$$

Here

$$a_1 = \int_{-1}^{1} dx w(x) \sqrt{1 - x^2} \simeq 0.842;$$

$$a_2 = \int_{-1}^{1} dx w(x) \frac{x^2}{\sqrt{1 - x^2}} \simeq 0.551, \tag{42}$$

and $\zeta(3) \simeq 1.202$ is a particular value of the zeta-function.

In an analysis of AFM on a triangular lattice, it is convenient to write the system of equations (17) and (18) by using the equality $\coth(x/2) = 1 + 2n(x)$, where $n(x) = (e^x - 1)^{-1}$ is the Bose distribution function. This gives

$$|\tilde{c}_1| = - \frac{6|J||\tilde{c}_1|}{N} \sum_{\mathbf{k}} \frac{\gamma_{\mathbf{k}} (1 - \gamma_{\mathbf{k}})}{\omega_{\mathbf{k}}} \left[1 + n\left(\frac{\omega_{\mathbf{k}}}{T} \right) \right], \tag{43}$$

$$\Delta_2 = 1 + \frac{6|J||\tilde{c}_1|}{N} \sum_{\mathbf{k}} (6\gamma_{\mathbf{k}}^2 + 2\gamma_{\mathbf{k}} - 1) \frac{1 - \gamma_{\mathbf{k}}}{\omega_{\mathbf{k}}} \left[1 \right.$$

$$\left. + n\left(\frac{\omega_{\mathbf{k}}}{T} \right) \right]. \tag{44}$$

Since Δ_2 remains finite at all temperatures, the term containing $n(\omega_{\mathbf{k}}/T)$ vanishes for $T \to 0$. The system of transcendental equations obtained in this case defines $|\tilde{c}_1|$ and Δ_2 in the zeroth approximation and can be solved only numerically. The leading term from the addends containing $n(\omega_{\mathbf{k}}/T)$ is found to be of the order of $|\theta|^3$. Indeed, these terms can be written in the form

$$Q \equiv \frac{12|J||\tilde{c}_1|}{N} \sum_{\mathbf{k}} F(\gamma_{\mathbf{k}}) \frac{1 - \gamma_{\mathbf{k}}}{\omega_{\mathbf{k}}} n\left(\frac{\omega_{\mathbf{k}}}{T} \right), \tag{45}$$

where $F(\gamma_{\mathbf{k}}) = - \gamma_{\mathbf{k}}$ for (43) and $F(\gamma_{\mathbf{k}}) = 6\gamma_{\mathbf{k}}^2 + 2\gamma_{\mathbf{k}} - 1$ for (44). Using expression (30) for density of states, we go over in (45) from the sum over $\mathbf{k}$ to the integral with respect to x. After a sequence of transformations, we obtain

$$Q \simeq \frac{8\,\zeta(3)|\tilde{c}_1|F(1)}{\pi\sqrt{3}(\Delta_2 + 9|\tilde{c}_1|)^2}|\theta|^3. \tag{46}$$

Substituting (46) into (43) $(F(1) = -1)$ and into (44) $(F(1) = 7)$ and solving the obtained system of equations in the perturbation theory, we find that

$$|\tilde{c}_1| \simeq 0.289 + 0.194|\theta|^3, \tag{47}$$

$$\alpha \simeq 1.347 + 0.986|\theta|^3, \tag{48}$$

$$\Delta_2 \simeq 0.102 - 0.168|\theta|^3. \tag{49}$$

It should be noted that the range of applicability of asymptotic forms (47)–(49) for $2D$ antiferromagnets is rather narrow as in the one-dimensional case.[13]

On the basis of the low-temperature asymptotic forms presented here, we can conclude that the behavior of $2D$ Heisenberg systems is basically determined by the type of the lattice on which these systems are considered. For a square lattice at $T = 0$, the correlation length $\xi \to \infty$ for both FM and AFM, and accordingly the long-range order always exists in the system irrespective of the sign of J. At the same time, for a triangular lattice, there is no long-range order in AFM at $T = 0$ ($\xi = \text{const}$) in contrast to the case of FM.

4. HEAT CAPACITY AND SUSCEPTIBILITY OF 2*D* MAGNETS

The thermodynamic functions of the system we are interested in can be expressed in terms of $\tilde{c}_1$, $\tilde{c}_2$, and α. All the extensive quantities are given per lattice site. The internal energy E is the average value of Hamiltonian (1):

$$E \simeq -\frac{3}{8}Jzc_1, \tag{50}$$

and heat capacity C at constant volume is given by

$$C = \frac{\partial E}{\partial T}, \tag{51}$$

while the magnetic susceptibility of the system is defined as

$$\chi \simeq \frac{1}{T}\lim_{\mathbf{k}\to 0}\langle S_{\mathbf{k}}^z S_{-\mathbf{k}}^z\rangle = \frac{c_1}{J\Delta}. \tag{52}$$

Before analyzing the results of numerical calculations, we write the asymptotic expressions for internal energy, heat capacity, and susceptibility of $2D$ Heisenberg magnets. In the limit of high temperatures, expressions for these quantities are formally the same for FM and AFM on triangular and square lattices and differ only in the sign of J and the value of z. Taking into account (22), we obtain

$$E \simeq -\frac{3Jz}{32\theta}\left(1 + \frac{A}{\theta}\right), \tag{53}$$

$$C \simeq \frac{3z}{32\theta^2}\left(1 + 2\frac{A}{\theta}\right), \tag{54}$$

$$\chi \simeq \frac{1}{4T(1 - z/4\theta)}. \tag{55}$$

Expressions (53)–(55) exactly coincide with the corresponding results obtained by direct high-temperature expansion
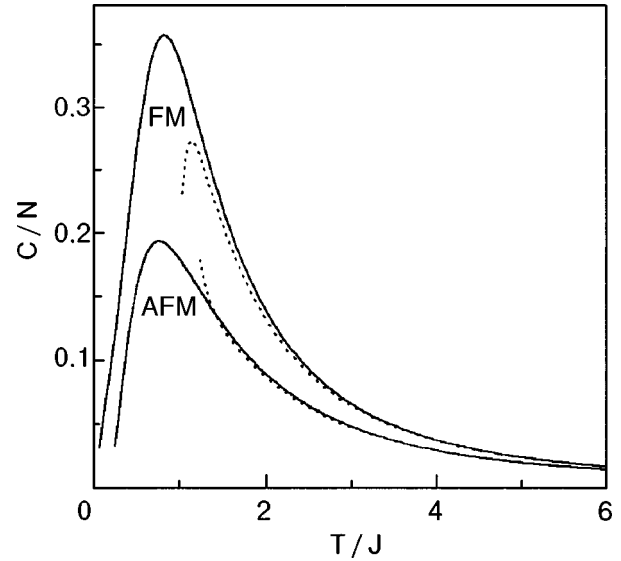

FIG. 1. Heat capacities of FM and AFM on a triangular lattice. The dotted curves correspond to relevant high-temperature expansions.

(see, for example, Refs. 11 and 15). Taking into account expressions (36)–(38), we obtain for FM with both types of lattices at low temperatures

$$E \simeq -\frac{Jz}{8}\left[1 - \frac{4\pi^2(z+3)}{9z^2}w(1)\theta^2\right], \tag{56}$$

$$C \simeq \frac{\pi^2(z+3)}{9z}w(1)\theta, \tag{57}$$

$$\chi \simeq \frac{1}{3T}\exp\left(\frac{z}{8\theta w(1)}\right). \tag{58}$$

It should be noted that expression (57) coincides with the similar formula in Ref. 5. Thus, the heat capacity of ferromagnets for $T \to 0$ is a linear function of temperature, which is in accord with the theory of spin waves.

For AFM on a square lattice for $T \to 0$, we have

$$E \simeq -\frac{3}{2}|J|\left(1 - A_1 - \frac{\zeta(3)}{\pi}A_1^2|\theta|^3\right), \tag{59}$$

$$C \simeq \frac{9}{2\pi}\zeta(3)A_1^2\theta^2, \tag{60}$$

$$\chi|J| \simeq \frac{A_1}{8}\left(1 + \frac{\zeta(3)}{\pi}A_1|\theta|^3\right). \tag{61}$$

Here $A_1 = 2a_1^2/(1 + 2a_1^2) \simeq 0.586$, and a_1 is defined in accordance with (43).

Finally, taking into account (47)–(49), we obtain for AFM on a triangular lattice

$$E \simeq -0.482 + 0.029|\theta|^3, \tag{62}$$

$$C \simeq 0.087\theta^2, \tag{63}$$

$$\chi|J| \simeq 0.0794 - 0.052|\theta|^3. \tag{64}$$

The asymptotic forms given above make it possible to find certain qualitative peculiarities in the temperature dependences of thermodynamic parameters of $2D$ magnets on
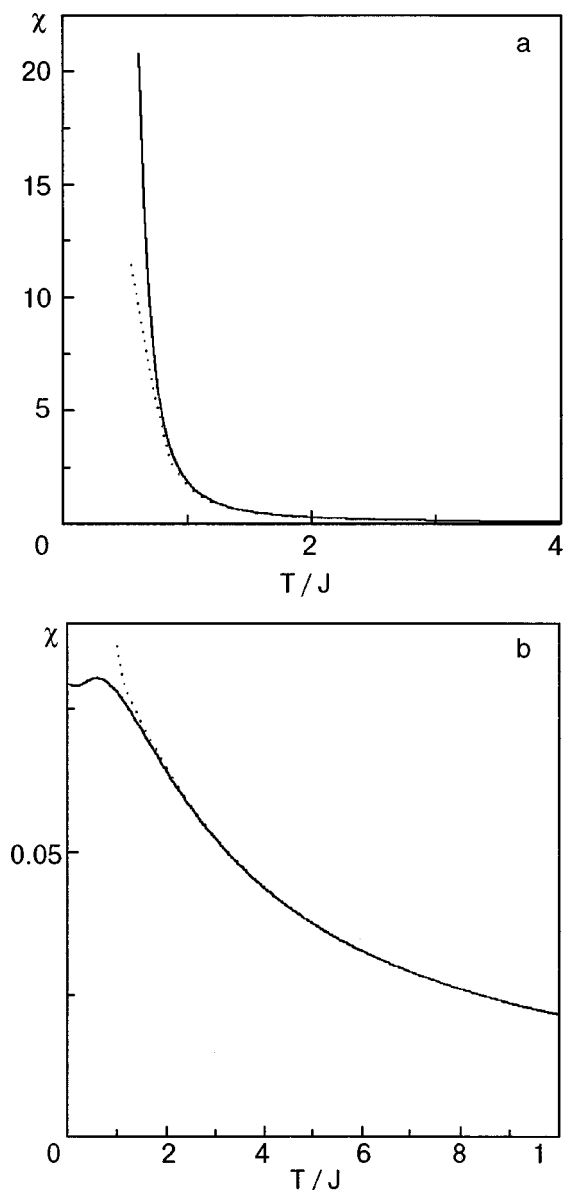
FIG. 2. Magnetic susceptibilities for FM (a) and AFM (b) on a triangular lattice. The dotted curves correspond to relevant high-temperature expansions.[11]

various lattices. For example, for a triangular lattice, the heat capacity of FM at low as well as high temperatures must be higher than the heat capacity of AFM, while the opposite relation is observed for a square lattice.

In order to obtain quantitative temperature dependences of the thermodynamic functions E, C, and χ over the entire temperature range, we must solve numerically the system of transcendental equations (16)–(18) and determine the quantities $\tilde{c}_1$, $\tilde{c}_2$, and α as functions of temperature. Then we

must calculate the internal energy, heat capacity and susceptibility of the magnet using formulas (50)–(52).

Figure 1 shows temperature dependences of the heat capacity for FM and AFM on a triangular lattice. The dotted curves show the results obtained by high-temperature expansions.[11] It can be seen that the heat capacity of FM in the entire temperature range lies above the heat capacity of AFM. The temperature behavior of magnetic susceptibility for FM and AFM on a triangular lattice is illustrated in Fig. 2 which also shows the corresponding curves obtained on the basis of high-temperature expansion.[11]

In conclusion, note that the advantage of the used approach is that it enables us to calculate from a common point of view the thermodynamics of two-dimensional isotropic Heisenberg magnets in the entire temperature range. Moreover, the results of calculations are in excellent agreement with the predictions of high-temperature expansions. It should also be noted that Siqueira et al.[7] presented the results of experimental measurements of heat capacity for ^{3}He films at various coverages corresponding to ferro- and antiferromagnetic exchange in the spin subsystem. It was found that the value of C at the heat capacity peak is twice as high for FM as for AFM. Figure 1 shows that the proposed theory leads to the same relation. Thus, we can conclude that the obtained results correctly describe the physical pattern of the phenomena under consideration.

*E-mail: antsygina@ilt.kharkov.ua

[1] M. Roger and J. H. Hetherington, Rev. Mod. Phys. **55**, 1 (1983).
[2] T. N. Antsygina and V. A. Slyusarev, Fiz. Nizk. Temp. **21**, 127 (1995) [Low Temp. Phys. **21**, 93 (1995)].
[3] T. N. Antsygina and V. A. Slyusarev, Fiz. Nizk. Temp. **19**, 67 (1993) [Low Temp. Phys. **19**, 48 (1993)].
[4] T. N. Antsygina and V. A. Slyusarev, Fiz. Nizk. Temp. **18**, 261 (1992) [Sov. J. Low Temp. Phys. **18**, 179 (1992)].
[5] K. Yamaji and J. Kondo, Phys. Lett. **45**, 317 (1973).
[6] D. S. Greywall, Phys. Rev. B **41**, 1842 (1990).
[7] M. Siqueira, J. Nièki, B. Cowan, and J. Saunders, Phys. Rev. Lett. **78**, 2600 (1997).
[8] K. Ishida, M. Morishita, K. Yawata, and H. Fukuyama, Phys. Rev. Lett. **79**, 3451 (1997).
[9] C. Bauerle, J. Bossy, Yu. M. Bunkov et al., J. Low Temp. Phys. **110**, 345 (1998).
[10] M. Roger, C. Bauerle, Yu. M. Bunkov et al., Phys. Rev. Lett. **80**, 1308 (1998).
[11] N. Eltner, R. Singh, and A. P. Yang, Phys. Rev. Lett. **71**, 1629 (1993).
[12] H. Mermin and N. D. Wagner, Phys. Rev. Lett. **17**, 1133 (1966).
[13] J. Kondo and K. Yamaji, Prog. Theor. Phys. **47**, 807 (1972).
[14] D. N. Zubarev, *Nonequilibrium Statistical Thermodynamics* [in Russian], Nauka, Moscow (1971).
[15] G. S. Rushbrooke, G. A. Baker, Jr., and P. J. Wood, in *Phase Transition and Critical Phenomena*, vol. 3 (ed. by C. Domb and M. S. Green), Academic Press, New York (1974).

Translated by R. S. Wadhwa

LOW-DIMENSIONAL AND DISORDERED SYSTEMS

Deceleration of charged particles in a two-dimensional electron gas with impurity states of electrons

A. M. Ermolaev and Babak Haghighi

Kharkov State University, 310077 Kharkov, Ukraine
(Submitted January 15, 1999)
Fiz. Nizk. Temp. **25**, 600–608 (June 1999)

Differential cross-section of inelastic scattering and loss function of fast charged particles in a two-dimensional electron gas are calculated at low temperatures, taking into account the localization of electrons at impurity atoms. The contribution of one-particle and collective excitations of the electron gas to the scattering cross-section and loss function is considered. One-particle excitations are manifested in the existence of a threshold of scattering cross-section and loss function, associated with a transition of localized electrons to the conduction band. Localization of electrons leads to a decrease in the frequency of two-dimensional plasmons. Consequently, the plasma loss lines in the energy spectrum of electrons passing through a two-dimensional electron gas are displaced towards lower frequencies and are broadened. Numerical estimates are obtained for the inversion layer at the boundary between silicon and silicon dioxide. © *1999 American Institute of Physics.* [S1063-777X(99)01006-3]

INTRODUCTION

Characteristic losses of energy of fast electrons occupy a significant place among the mechanisms of deceleration of charged particles in matter. The method of characteristic energy losses is used successfully for studying the properties of plasma,[1] solids,[2,3] and quantum liquids.[4] This method was also used to prove the collective nature of narrow lines in the energy spectrum of electrons passing through a thin film of metal or reflected at its surface.[4,5] This led to the discovery of plasma waves in metals whose existence was predicted earlier by Pines and Bohm.[3,6]

The advantage of the method of characteristic losses lies in that it can be used to obtain information about collective as well as single-particle excitations in conductors. As a rule, the loss spectrum of the electron energy contains two lines, viz., a broad line associated with the excitation of electron–hole pairs, and a narrow line connected with plasmon excitation. The resolution of these lines is hampered by the excitation of surface plasmons,[7] transitions between bands,[2] and other factors responsible for electron deceleration in matter.

In view of the enhanced interest to the physics of two-dimensional electron systems,[8] it seems expedient to use the characteristic loss method for studying the properties of a two-dimensional electron gas. As in the three-dimensional case, it is important to distinguish between the plasma losses and the losses associated with one-particle excitations. The theory of plasma losses of particle energy in a two-dimensional electron gas was developed in Refs. 9 and 10. The three-dimensional scattering of electrons by the classical two-dimensional electron gas was considered by Fetter[9] who showed that the energy spectrum of electrons passing through an electron layer contains a narrow plasma line. The position of this line defines the spectrum of two-dimensional plasmons in a nondegenerate electron gas, while its width describes the Landau damping. The theory developed by Fetter[9] is used for electrons at the surface of liquid helium, as well as for other classical systems.

Bret and Deutsch[10] considered the deceleration of a charged particle moving in an electron layer. The electron–electron interaction in the layer was taken into account in the random phase approximation.[3] The results were obtained for any degree of degeneracy of electrons. It was mentioned that in contrast to the three-dimensional case, the plasmon contribution to the loss function in the two-dimensional case is smaller than the contribution of one-particle excitations. This is due to the activationless spectrum of two-dimensional longwave plasmons.

The influence of impurity atoms on deceleration of particles was not considered in Refs. 9 and 10. However, impurities do not play a trivial role in two-dimensional systems. Impurity atoms not only restrict the mean free path of conduction electrons, but also change their energy spectrum. In the two-dimensional case, even an extremely weak impurity attractive potential can lead to the formation of a bound state.[11] This leads to the emergence of an additional mechanism of deceleration of particles associated with the ionization of impurity atoms. Moreover, the bound state causes deformation of the plasmon spectrum, which must affect the characteristic loss spectrum.

In this work, we consider the effect of impurity states in a two-dimensional electron gas on the deceleration of charged particles caused by one-particle and collective excitations. The general formulas for scattering cross-section and loss function for a charged particle in a two-dimensional

electron gas are given in Sec. 1. Section 2 is devoted to the losses of particle energy caused by one-particle excitations of electrons localized at impurities, while characteristic losses are described in Sec. 3. The results of computations are described briefly in Conclusion.

1. SCATTERING CROSS-SECTION AND STOPPING POWER OF A TWO-DIMENSIONAL ELECTRON GAS

Let us consider a two-dimensional electron gas in the plane $z=0$ separating half-spaces with permittivities ε_1 and ε_2. We assume that a particle of mass M and charge Ze moves in the plane of the electron layer.[10] The Hamiltonian of Coulomb interaction of the particle with the two-dimensional electron gas is defined as[1,9]

$$V = Z\bar{e}^2 \int d^2r \int d^2r' \frac{N(\mathbf{r})n(\mathbf{r}')}{|\mathbf{r}-\mathbf{r}'|}, \qquad (1)$$

where $\mathbf{r}$ and $\mathbf{r}'$ are two-dimensional radius-vectors, $N(\mathbf{r})$ and $n(\mathbf{r})$ are density operators of the particle and the electron gas, and

$$\bar{e} = e\left(\frac{2}{\varepsilon_1+\varepsilon_2}\right)^{1/2}.$$

Going over to Fourier components in Eq. (1), we obtain

$$V = Z\bar{e}^2 \int \frac{d^2q}{2\pi} \frac{n(\mathbf{q})}{q} e^{i\mathbf{qr}}, \qquad (2)$$

where $n(\mathbf{q})$ and $2\pi/q$ are the Fourier components of the functions $n(\mathbf{r})$ and r^{-1} respectively. We use the symbol $|\alpha\rangle$ to denote the stationary state of a two-dimensional electron gas with energy E_α, while $\mathbf{p}$ and σ stand for the momentum and spin quantum number of the particle incident on the electron gas. The matrix element of the operator (2) between states $|\alpha \mathbf{p}\sigma\rangle$ and $|\alpha'\mathbf{p}'\sigma'\rangle$ is defined as

$$\langle \alpha'\mathbf{p}'\sigma'|V|\alpha \mathbf{p}\sigma\rangle = 2\pi Z\bar{e}^2 |\mathbf{p}-\mathbf{p}'|^{-1}\langle \alpha'|n(\mathbf{p}'$$
$$-\mathbf{p})|\alpha\rangle \delta_{\sigma'\sigma}. \qquad (3)$$

The area occupied by the electron gas and the quantum constant are assumed to be equal to unity.

The probability of transition $\mathbf{p}\to\mathbf{p}'$ in unit time in the Born approximation in V can be presented in the form[3,9]

$$W(\mathbf{q},\omega) = (2\pi)^3 Z^2 \bar{e}^4 n_e q^{-2} S(\mathbf{q},\omega), \qquad (4)$$

where $\mathbf{q}=\mathbf{p}-\mathbf{p}'$ and $\omega=E_p-E_{p'}$ describe the momentum and energy losses for the incident particle as a result of scattering, n_e is the surface density of electrons,

$$S(\mathbf{q},\omega) = \frac{1}{n_e} \sum_{\alpha\alpha'} w_\alpha |\langle \alpha'|n(-\mathbf{q})|\alpha\rangle|^2 \delta(\omega - E_{\alpha'} + E_\alpha) \qquad (5)$$

is the dynamic structural factor for a two-dimensional electron gas,[3,4,9] and w_α is the Gibbs' distribution function.

The double differential two-dimensional scattering cross-section of particles in the interval of angles $d\varphi$ with energy loss in the interval $d\omega$ is defined as

$$\frac{d^2\sigma}{d\omega d\varphi} = \frac{2\pi n_e}{p}\left(MZ\frac{\bar{e}^2}{q}\right)^2 S(\mathbf{q},\omega), \qquad (6)$$

where

$$q^2 = 4M\left\{E - \frac{\omega}{2} - [E(E-\omega)]^{1/2}\cos\varphi\right\}, \qquad (7)$$

$E=E_p$ is the particle energy, and φ is the scattering angle. The dynamic structural factor appearing in Eq. (6) is connected with the retarding polarization operator Π through the relation[9,12]

$$S(\mathbf{q},\omega) = -\frac{1}{\pi n_e}(n_\omega+1)\operatorname{Im}\Pi(\mathbf{q},\omega), \qquad (8)$$

where $n_\omega = (e^{\beta\omega}-1)^{-1}$ is Planck's distribution function and β the reciprocal temperature. The probability of transition (4) is associated with the imaginary part of the polarization operator:

$$W(\mathbf{q},\omega) = 8\pi^2 Z^2 \bar{e}^4 q^{-2}(n_\omega+1)[-\operatorname{Im}\Pi(\mathbf{q},\omega)]. \qquad (9)$$

In the random phase approximation, the polarization operator is presented as the sum of ''loop'' diagrams[12] and is equal to

$$\Pi(\mathbf{q},\omega) = \frac{P(\mathbf{q},\omega)}{1-\nu_q P(\mathbf{q},\omega)}, \qquad (10)$$

where P corresponds to a simple loop in which Green's electron functions are calculated by taking impurity scattering into account, and $\nu_q = (2\pi\bar{e}^2)/q$ is the Fourier component of the Coulomb interaction energy for two-dimensional electrons. In the linear approximation in concentration of impurity atoms, $P=P_0+\delta P$, where P_0 is the polarization operator for the free electron gas, and the contribution δP is due to the electron localization in the field of impurity atoms.[13] The function P_0 was evaluated by Stern[14] for a degenerate electron gas and by Platzman and Tzoar[15] for a nondegenerate gas. The same function was calculated by Bret and Deutsch[10] for any degree of degeneracy of electrons. The contribution δP is defined as[13]

$$\delta P(\mathbf{q},\omega) = 2\int \frac{d^2k}{(2\pi)^2}\int_{-\infty}^{+\infty} d\varepsilon\, \delta\rho(\mathbf{k}+\mathbf{q},\varepsilon)[f(\varepsilon)$$
$$-f(\varepsilon_k)]\left(\frac{1}{\varepsilon-\varepsilon_k+\omega+i0}+\frac{1}{\varepsilon-\varepsilon_k-\omega-i0}\right), \qquad (11)$$

where ε_k is the energy of an electron with momentum k, f is the Fermi distribution function, and

$$\delta\rho(\mathbf{k},\varepsilon) = |\nu_0|n_i(\varepsilon-\varepsilon_k)^{-2}\delta[1-\nu_0 F(\varepsilon)] \qquad (12)$$

describes the contribution of localized electrons to the spectral density of Green's function averaged over the configuration of impurity atoms. Here ν_0 is a constant characterizing the intensity of short-range impurity potential, n_i the number density of impurity atoms, and $F(\varepsilon)$ the function appearing in I. M. Lifshitz' equation for local levels

$$1-\nu_0 F(\varepsilon) = 0. \qquad (13)$$

This function is connected with the electron density of states g through the Hilbert transformation

$$F(\varepsilon) = \int_{-\infty}^{+\infty} d\varepsilon' \frac{g(\varepsilon')}{\varepsilon - \varepsilon'}.$$

If the energy spectrum of two-dimensional electrons contains only one local level $\varepsilon_l = -|\varepsilon_l|$, the real and imaginary parts of the polarization operator (11) can be defined as

$$\mathrm{Re}\,\delta P(\mathbf{q}, \omega) = -\frac{mrn_i}{\pi} \int_0^\infty d\varepsilon [f(\varepsilon_l) - f(\varepsilon)]$$

$$\times \frac{\varepsilon - \varepsilon_l + \varepsilon_q}{[(\varepsilon - \varepsilon_l + \varepsilon_q)^2 - 4\varepsilon\varepsilon_q]^{3/2}(\varepsilon - \varepsilon_l - \omega)}$$

$$+ (\omega \to -\omega), \tag{14}$$

$$\mathrm{Im}\,\delta P(\mathbf{q}, \omega) = -mrn_i [f(\varepsilon_l) - f(\varepsilon_l + \omega)]\theta(\omega$$

$$- \omega_g)\omega_+ [\omega_+^2 - 4\varepsilon_q(\omega + \varepsilon_l)]^{-3/2}$$

$$- (\omega \to -\omega), \tag{15}$$

where m is the electron mass,

$$r = \left| \left[\frac{dF}{d\varepsilon} \right]_{\varepsilon = \varepsilon_l} \right|^{-1}$$

is the residue of the amplitude of electron scattering by an impurity atom at the pole ε_l, $\omega_g = |\varepsilon_l|$ is the threshold activation frequency for a localized electron, $\omega_\pm = \omega \pm \varepsilon_q$, θ is the Heaviside function, and $(\omega \to -\omega)$ denotes a term which differs from the preceding term only in the sign of the frequency. It can be seen from formulas (14) and (15) that $\varepsilon_q/|\varepsilon_l|$ is the parameter determining the role of spatial dispersion δP of the polarization operator. If this parameter is small, we can confine the analysis to the longwave approximation. In this case, we obtain from (14) the following expression for degenerate electrons:

$$\mathrm{Re}\,\delta P = \frac{mrn_i}{\pi\omega^2} \ln \left| 1 - \left(\frac{\omega}{\varepsilon_F - \varepsilon_l} \right)^2 \right|, \tag{16}$$

where ε_F is the Fermi energy for a two-dimensional electron gas.

The energy lost by a charged particle in unit time is given by[1]

$$\frac{dE}{dt} = \int \frac{d^2 p'}{(2\pi)^2} \omega W(\mathbf{q}, \omega). \tag{17}$$

It is associated with the imaginary part of the polarization operator through the relation

$$\frac{dE}{dt} = 2Z^2 \bar{e}^4 \int d^2 p' \frac{\omega}{q^2}(n_\omega + 1)[-\mathrm{Im}\,\Pi(\mathbf{q}, \omega)]. \tag{18}$$

While calculating this quantity, we must take into account the contribution (11) due to localization of two-dimensional electrons at impurity atoms.

It can be seen from formulas (10) and (18) that the stopping power of a two-dimensional electron gas is due to one-particle as well as collective excitations. The contribution of one-particle excitations determines the peculiarities of the numerator in (10), while the contribution of collective excitations determines the zeros in the denominator. We shall consider these contributions separately.

2. CONTRIBUTION OF ONE-PARTICLE EXCITATIONS TO THE STOPPING POWER OF A TWO-DIMENSIONAL ELECTRON GAS

2.1. Two-dimensional scattering

The Coulomb interaction of two-dimensional electrons can be disregarded while calculating the contribution of one-particle excitations to the energy loss for a test particle. In this case, the transition probability (9) can be presented as follows in the linear approximation in the concentration of impurity atoms

$$W = W_0 + \delta W, \tag{19}$$

where W_0 is the probability of transition in a free electron gas,[9] and δW is the contribution of localized electrons. It follows from formulas (9) and (15) that this contribution is defined as

$$\delta W(q, \omega) = 8\pi^2 mZ^2 \bar{e}^4 rn_i q^{-2}(n_\omega + 1)\{[f(\varepsilon_l) - f(\varepsilon_l$$

$$+ \omega)]\theta(\omega - \omega_g) \times \omega_+ [\omega_+^2 - 4\varepsilon_q(\omega$$

$$+ \varepsilon_l)]^{-3/2} - (\omega \to -\omega)\}. \tag{20}$$

The first term on the right-hand side of Eq. (20) is associated with transitions of electrons localized at impurity atoms to the two-dimensional conduction band. Such transitions are accompanied by a decrease in the particle energy. The second term describes induced transitions of band electrons to the local level. Since $n_{-\omega} + 1 = -n_\omega$, this contribution vanishes at zero temperature. It follows from formula (20) that δW as a function of the energy loss ω of the particle has a threshold for the activation energy ω_g of a localized electron. As the temperature tends to zero, the difference in Fermi functions in (20) displaces the threshold to the point $\omega_g + \varepsilon_F$ in accordance with Pauli's exclusion principle. For $\varepsilon_q \ll \omega_g$, we obtain the following expression from (20) for the probability of transition of delocalized electrons to the conduction band:

$$\delta W(q, \omega) = \frac{8\pi^2 mZ^2 \bar{e}^4 rn_i}{q^2 \omega^2} \theta(\omega - \omega_g)(n_\omega + 1)[f(\varepsilon_l)$$

$$- f(\varepsilon_l + \omega)]. \tag{21}$$

In this case, the cross-section of inelastic two-dimensional scattering of electrons is defined as

$$\frac{d^2\sigma}{d\omega d\varphi} = \frac{2m(MZ\bar{e}^2)^2 rn_i}{pq^2 \omega^2} \theta(\omega - \omega_g)(n_\omega + 1)[f(\varepsilon_l)$$

$$- f(\varepsilon_l + \omega)]. \tag{22}$$

The loss q of the particle momentum appearing in formulas (21) and (22) is connected with the energy loss ω through the relation (7). If ω is fixed, the cross-section (22) as a function of scattering angle attains its maximum value for $\varphi = 0$ and decreases for $\varphi \to \pm\pi$. As the scattering angle varies from 0 to π, the cross-section (22) decreases by a factor of

$$\left[\frac{1+(1-\omega/E)^{1/2}}{1-(1-\omega/E)^{1/2}}\right]^2$$

For $\varphi=0$, the cross-section (22) as a function of ω has a threshold at $\omega=\omega_g$. With increasing ω, the cross-section passes through a peak and then decreases.

If the velocity of the incident particle exceeds the Fermi velocity of electrons, the particle momentum loss is small. In this case, we can use the longwave approximation for the polarization operator. Hence formulas (17) and (21) lead to the following expression for the particle energy loss in unit time due to ionization of impurity atoms:

$$\frac{d}{dt}\delta E = 2mZ^2\bar{e}^4 r n_i \int d^2p' \frac{n\omega+1}{\omega q^2}\{\theta(\omega-\omega_g)[f(\varepsilon_l)$$

$$-f(\varepsilon_l+\omega)]-(\omega\to-\omega)\}. \qquad (23)$$

Integration with respect to the scattering angle φ can be carried out quite easily:

$$\int_0^{2\pi}\frac{d\varphi}{c-\cos\varphi}=\frac{2\pi\sin c}{(c^2-1)^{1/2}}, \quad |c|>1.$$

This gives

$$\frac{d}{dT}\delta E = 2\pi mZ^2\bar{e}^4 r n_i \int_0^E \frac{d\omega}{\omega^2}(n_\omega+1)[f(\varepsilon_l)-f(\varepsilon_l$$

$$+\omega)]+2\pi mZ^2\bar{e}^4 r n_i \int_{-E}^0 \frac{d\omega}{\omega^2}n_\omega[f(\varepsilon_l)-f(\varepsilon_l$$

$$+\omega)]. \qquad (24)$$

The first term in this formula is associated with transitions of localized electrons to the band, while the second term is connected with transitions of band electrons to the local level. At zero temperature, we obtain from (24) the relation

$$\frac{d}{dt}\delta E = \frac{2\pi mZ^2\bar{e}^4 r n_i}{E}\theta(E-\varepsilon_F-\omega_g)\left(\frac{E}{\varepsilon_F+\omega_g}-1\right). \qquad (25)$$

The stopping power (25) of a two-dimensional gas has a threshold at the point $E_0=\varepsilon_F+\omega_g$. The value of $(d/dt)\delta E$ increases with E and attains saturation for $E\gg E_0$. The ratio of the maximum value of (25) to the stopping power of free two-dimensional electron gas[10] is

$$A=\frac{mr}{\pi\varepsilon_F}\frac{n_i}{n_e}\left(1+\frac{\omega_g}{\varepsilon_F}\right)^{-1}.$$

Using the value

$$r=\frac{2\pi|\varepsilon_l|}{m},$$

for the residue r calculated for a shallow donor ($m|\nu_0|\ll1$),[16] we obtain

$$A=2\frac{n_i}{n_e}\frac{\omega_g}{\varepsilon_F}\left(1+\frac{\omega_g}{\varepsilon_F}\right)^{-1}. \qquad (26)$$

2.2. Three-dimensional scattering

The scattering of electrons incident at any angle on a two-dimensional electron gas was considered by Fetter,[9] who showed that for a beam of electrons that has crossed the electron layer, the cross-section of differential scattering in a solid angle dO with energy loss in the interval $d\omega$ is defined as

$$\frac{d^2\sigma}{d\omega dO}=n_e\frac{k'}{k}[a(\mathbf{k}-\mathbf{k}')^2]^{-2}S(\mathbf{q},\omega), \qquad (27)$$

where $\mathbf{k}$ and $\mathbf{k}'$ are the electron momenta before and after scattering, $\mathbf{q}$ is the projection of the vector $\mathbf{k}-\mathbf{k}'$ on the plane occupied by the electron gas, $\omega=\varepsilon_k-\varepsilon_{k'}$, and $a=(2m\bar{e}^2)^{-1}$ is the effective Bohr radius. The dynamic structural factor appearing in formula (27) is connected with the imaginary part of the polarization operator of a two-dimensional electron gas through the relation (8). Using formula (15), we obtain the contribution of the local state of an electron to the scattering cross-section (27):

$$\frac{d^2\sigma}{d\omega dO}=\frac{mrn_ik'}{\pi k}[a(\mathbf{k}-\mathbf{k}')^2]^{-2}(n_\omega+1)\{[f(\varepsilon_l)-f(\varepsilon_l$$

$$+\omega)]\theta(\omega-\omega_g)\omega_+[\omega_+^2-4\varepsilon_q(\omega+\varepsilon_l)]^{-3/2}$$

$$-(\omega\to-\omega)\}. \qquad (28)$$

As in the case of two-dimensional scattering, this cross-section at finite temperatures has a threshold at the point $\omega=\omega_g$. At zero temperature, the threshold is located at the point $\varepsilon_F+\omega_g$.

3. CHARACTERISTIC ELECTRON ENERGY LOSSES IN A TWO-DIMENSIONAL ELECTRON GAS

The electron energy losses caused by the excitation of plasma waves in a two-dimensional electron gas were taken into account by the zeros in the denominator of formula (10). The positions of the zeros can be determined from the dispersion equation for plasmons:

$$1-\nu_q P(\mathbf{q},\omega)=0. \qquad (29)$$

The solution of this equation has the form $\omega=\omega_q-i\gamma_q$, where ω_q is the plasmon spectrum and γ_q is the damping decrement. For $\gamma_q\ll\omega_q$, the imaginary part of the polarization operator near the root of the dispersion equation (29) has the form

$$\text{Im}\,P(\mathbf{q},\omega)=-\frac{\pi}{\nu_q^2}\left|\left[\frac{\partial}{\partial\omega}\text{Re}\,P(\mathbf{q},\omega)\right]_{\omega=\omega_q}\right|^{-1}[\delta(\omega-\omega_q)$$

$$+\delta(\omega+\omega_q)]. \qquad (30)$$

Taking into account the finite magnitude of γ_q, we can replace the δ-functions in the above equation by Lorentzian curves.

Outside the region of collisionless attenuation of plasma waves, the real part of the polarization operator of a degenerate two-dimensional electron gas in the absence of impurity atoms is defined as[8,14,17]

$$\operatorname{Re} P_0(\mathbf{q},\omega) = -\frac{m}{\pi} + \frac{m^2}{\pi q^2}\{[(\omega+\Omega_+)(\omega-\Omega_-)]^{1/2}$$

$$-[(\omega-\Omega_+)(\omega+\Omega_-)]^{1/2}\}, \qquad (31)$$

where $\Omega_\pm = q\nu_F \pm \varepsilon_q$, ν_F is the Fermi velocity, and $\omega \geq \Omega_+$. Taking into account Eq. (31), we can present the solution of the dispersion equation (29) in the form[17]

$$\omega_q = \left(\frac{2\pi\bar{e}^2 n_e q}{m}\right)^{1/2}(1+aq)\left(1+\frac{aq}{2}\right)^{-1/2}$$

$$\times\left[1+\frac{aq^3}{2k_F^2}\left(1+\frac{aq}{2}\right)\right]^{1/2}, \qquad (32)$$

where k_F is the Fermi momentum. In the longwave limit $aq \ll 1$ and $q \ll k_F$, we obtain from formula (32)

$$\omega_q = \left(\frac{2\pi\bar{e}^2 n_e q}{m}\right)^{1/2}. \qquad (33)$$

This expression is a solution of Eq. (29) if we use the long-wave approximation for the polarization operator:

$$P_0(\mathbf{q},\omega) = \frac{q^2 n_e}{m(\omega+i\nu)^2}. \qquad (34)$$

Here ν is the frequency of collisions of electrons with impurity atoms associated only with potential scattering. The damping decrement of longwave plasmons in a degenerate electron gas is equal to the collision frequency ν.

For $\mathbf{q} = \mathbf{k} - \mathbf{k}'$, the cross-section of three-dimensional electron scattering by a strongly degenerate two-dimensional electron gas near the root (33) of the dispersion equation is given by

$$\frac{d^2\sigma}{d\omega dO} = \frac{n_e^{1/2}k'}{2\pi^{3/2}(aq)^{3/2}kq}(n_{\omega_q}+1)\frac{\gamma_q}{(\omega-\omega_q)^2+\gamma_q^2}. \qquad (35)$$

The first term in this equation, which is proportional to n_{ω_q}, describes induced emission of plasmons by electrons, while the second term describes spontaneous emission.

A consideration of electron localization in the field of impurity atoms changes the plasmon spectrum and the damping decrement.[13] Taking into account formulas (16) and (34) in the dispersion equation (29), we obtain the plasmon spectrum taking the local level into consideration:

$$Q = \frac{1}{2}x^2\left\{1+\left[1-\frac{b}{x^4}\ln\left|1-x^2\right|\right]^{1/2}\right\}, \qquad (36)$$

where

$$Q = q\frac{2\pi\bar{e}^2 n_e}{m}(\varepsilon_F+\omega_g)^{-2},$$

$$x = \frac{\omega}{\varepsilon_F+\omega_g}, \quad b = \frac{8}{\pi}\frac{1}{a^2 n_e}\frac{n_i}{n_e}\frac{\omega_g}{\varepsilon_F}\left(1+\frac{\omega_g}{\varepsilon_F}\right)^{-4}. \qquad (37)$$

In the absence of electron localization, we obtain from formula (36) the dispersion relation (33):

$$Q_0 = x^2. \qquad (38)$$

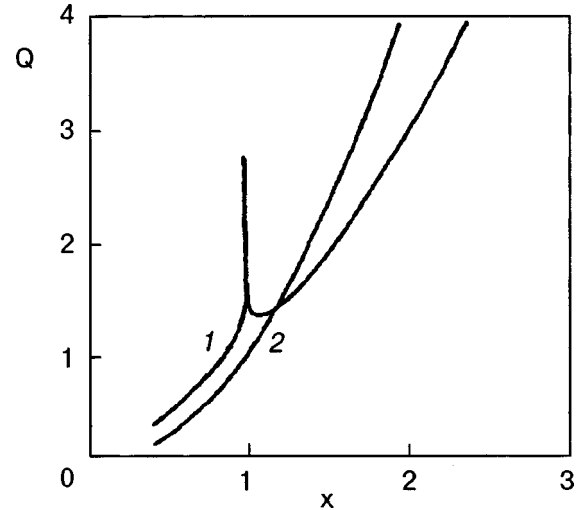The dependence (36) is plotted in Fig. 1 (curve 1) for the

FIG. 1. Plasmon dispersion relation (36) taking local level into consideration (curve 1) and disregarding localization (curve 2).

following values of the parameters of inversion layer at the boundary between silicon and silicon dioxide[8]: $m = 10^{-28}$ g, $n_e = 10^{12}$ cm^{-2}, $n_i/n_e = 10^{-3}$, $\omega_g/\varepsilon_F = 1$, $\varepsilon_1+\varepsilon_2 = 15$. Curve 2 corresponds to the dispersion relation (38) for long-wave plasmons. It can be seen from Fig. 1 that electron localization leads to a decrease in the frequency of longwave plasmons. Such a decrease for low electron densities was observed experimentally[18] and attributed to the drag of the effective mass of the conduction electrons in (33). It can be seen from formula (36) that the decrease in the plasmon frequency may also be due to a decrease in the threshold frequency $\omega' = \omega_g + \varepsilon_F$ in samples with a low electron density. If ω' decreases, the separation between dispersion curves 1 and 2 in Fig. 1 increases in conformity with the experimental observations.[18]

If we take into account the finite width of the local level ν_0, the logarithmic singularity in Eq. (36) is blurred. At the point ω', the argument of the logarithm is found to be equal to

$$2\frac{\upsilon_0}{\omega'}[1+(\nu_0/2\omega')^2]^{1/2}.$$

For $\nu_0/\omega_g = 0.1$ and the above values the parameters, we obtain $\nu_0/\omega' = 0.05$, $Q' = 1.003$ being the value of the dimensionless plasmon wavenumber (37) at the point ω'. In this case, $q' = 2.05\times10^6$ cm^{-1} and $\omega' = 6.28\times10^{13}$ s^{-1}.

The damping decrement of plasmons with spectrum (36) is equal to
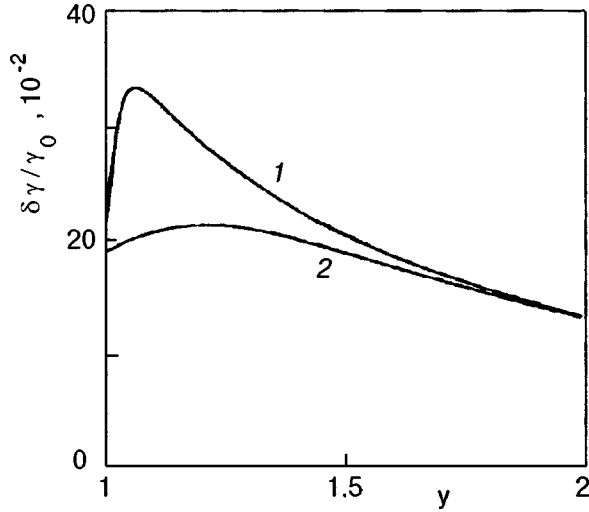
$$\gamma = \nu + \delta\xi, \qquad (39)$$

where

FIG. 2. Contribution (40) of local electron states to the damping decrement of plasmons. Curve 1 corresponds to $\beta\varepsilon_F = 100$, and curve 2 to $\beta\varepsilon_F = 10$.

$$\frac{\delta\gamma}{\nu} = \frac{\pi^{3/2}}{(aq_m)^{1/2}} \frac{n_i}{n_e} \frac{\omega_g}{\nu} \frac{n_e^{1/2}}{q_m} y^{-3/2} \theta(y-1)$$

$$\times \left\{ \frac{1}{1 + \exp[-\beta\varepsilon_F(1 + \omega_g/\varepsilon_F)]} \right.$$

$$\left. - \frac{1}{1 + \exp[-\beta\varepsilon_F(1 + \omega_g\varepsilon_F(1 - y^{1/2}))]} \right\}. \qquad (40)$$

Here

$$y = \frac{q}{q_m}, \quad aq_m = \frac{1}{2}\left(ak_F \frac{\omega_g}{\varepsilon_F}\right)^2 = 0.08.$$

The dependence of the decrement (40) on y is plotted in Fig. 2, where we have used the above values of the parameters and assumed that $\omega_g/\nu = 10$. Curve 1 is obtained for $\beta\varepsilon_F = 100$ and curve 2 for $\beta\varepsilon_F = 10$.

The cross section of electron scattering by plasmons with spectrum (36) coincides with formula (35) in which ω_q is the spectrum (36) and γ_q is the damping decrement (39). Taking the local level into account, the maximum value of the cross-section (35) at the point q' can be presented in the form

$$\left(\frac{d^2\sigma}{d\omega dO}\right)_m = \frac{1}{2\pi^3} \frac{k'}{k} \frac{(m\omega')^3}{n_e q'^4 \gamma_{q'}}. \qquad (41)$$

Substituting into this equation the above values of the parameters and $\omega'/\varepsilon = 0.1$, the ratio of the maximum values of the cross-sections at the point q' taking local level into consideration and disregarding it can be presented in the following form:

$$\frac{1}{Q'^4}\left(1 + \frac{\delta\gamma_{q'}}{\nu}\right)^{-1} = 4.58 \times 10^{-2}.$$

In this case, $\gamma_{q'} = 3.29 \times 10^{12}\,\text{s}^{-1}$. The decrease in the cross section due to the electron localization effect is caused by a sharp increase in momentum transfer at the threshold frequency.

The energy loss for a charged particle as a result of spontaneous and induced emission of two-dimensional plasmons can be obtained from formulas (18) and (30):

$$\frac{dE}{dt} = \frac{Z^2}{2\pi} \int d^2p'\, \omega(n_\omega + 1)$$

$$\times \left[\left[\frac{\partial}{\partial\omega}\text{Re}\,P(\mathbf{q},\omega)\right]_{\omega=\omega_q}\right]^{-1} \delta(\omega - \omega_q). \qquad (42)$$

Going over to integration with respect to ω and φ, we obtain

$$\frac{dE}{dt} = \frac{MZ^2}{2\pi} \int_0^{2\pi} d\varphi\, \omega_q(n_{\omega_q} + 1) \left|\frac{\partial}{\partial\omega_q}\text{Re}\,P(\mathbf{q},\omega_q)\right|^{-1}, \qquad (43)$$

where $\mathbf{q}$ is equal to the value given by (7) in which we must put $\omega = \omega_q$. In the absence of electron localization and for an incident particle velocity exceeding the Fermi velocity, we can use the longwave approximation (34) for the polarization operator. In this case, formula (43) leads to the following expression for the degenerate electrons:

$$\frac{dE}{dt} = \frac{2\pi^2 MZ^2\bar{e}^4 n_e}{m}, \qquad (44)$$

This expression was derived by Bret and Deutsch.[10] In view of the electron localization, we must take (16) and (36) into account in formula (43). The resulting integral (43) can be evaluated only numerically.

CONCLUSION

We have studied the effect of local states of electrons in the field of isolated impurity atoms on the stopping power of a degenerate two-dimensional electron gas. The importance of this problem stems from the fact that impurity atoms cause a significant alteration of the energy spectrum of two-dimensional systems. Even an insignificant attractive impurity detaches from the lower edge of the conduction band local levels which must be taken into account while calculating the energy loss for charged particles in two-dimensional conductors. Localization of electrons is manifested in the spectrum of energy losses in charged particles caused by one-particle as well as collective excitations. For a low concentration of impurity atoms, the loss function contains a term associated with the transitions of electrons localized at impurities to the conduction band. The stopping power of a system as a loss function of the particle energy has a threshold at the activation energy of the localized electron. By observing this singularity, we obtain the binding energy of impurity electrons in the two-dimensional case.

Electron localization lowers the frequency of two-dimensional plasmons, as was actually observed in experiments. This effect is manifested in the displacement of the characteristic electron energy loss line to the low-frequency region and to its additional broadening. Measurement of the position and width of this line enables us to obtain the spectrum and damping decrement of plasmons in imperfect two-dimensional conductors.

[1] A. I. Akhiezer, I. A. Akhiezer, R. V. Polovin *et al.*, *Plasma Electrodynamics* [in Russian], Nauka, Moscow (1974).

[2] A. R. Shul'man (Ed.), *Characteristic Electron Energy Losses in Solids* [in Russian], Foreign Lang. Publ. House, Moscow (1959).

[3] D. Pines, *Elementary Excitations in Solids*, New York (1963).

[4] D. Pines and Ph. Noziere, *The Theory of Quantum Liquids*, New York (1966).

[5] H. Watanabe, J. Phys. Soc. Jpn. **11**, 112 (1956).

[6] D. Pines and D. Bohm, Phys. Rev. **85**, 338 (1952).

[7] R. H. Ritchie, Phys. Rev. **106**, 874 (1957).

[8] T. Ando, A. Fowler, and F. Stern, *Electronic Properties of Two-dimensional Systems*, American Physical Society, New York (1982).

[9] A. L. Fetter, Phys. Rev. B **10**, 3739 (1974).

[10] A. Bret and C. Deutsch, Phys. Rev. E **48**, 2994 (1993).

[11] L. D. Landau and E. M. Lifshitz, *Quantum Mechanics* [in Russian], Nauka, Moscow (1989).

[12] A. L. Fetter and J. D. Walecka, *Quantum Theory of Many-particle Systems*, McGraw-Hill, New York (1971).

[13] A. M. Ermolaev and Babak Haghighi, Kharkov State Univ. Newsletter, No. 418, 13 (1998).

[14] F. Stern, Phys. Rev. Lett. **18**, 546 (1967).

[15] P. M. Platzman and N. Tzoar, Phys. Rev. B **13**, 3197 (1976).

[16] N. V. Gleĭzer and A. M. Ermolaev, Fiz. Nizk. Temp. **23**, 73 (1997) [Low Temp. Phys. **23**, 55 (1997)].

[17] E. A. Andryushin and A. P. Silin, Fiz. Tverd. Tela **35**, 324 (1993) [Phys. Solid State **35**, 164 (1993)].

[18] S. J. Allen, D. C. Tsui, and R. A. Logan, Phys. Rev. Lett. **38**, 980 (1977).

Translated by R. S. Wadhwa

Dynamics of formation of soliton conductivity in a 2*D*-array of linear chains containing commensurate charge density waves near the contact with a normal metal

Yurij V. Pershin and Alexander S. Rozhavsky

*B. Verkin Institute for Low Temperature Physics and Engineering, 47 Lenin Avenue, 310164, Kharkov, Ukraine**

We make a numerical study of the conversion of conduction electrons into charge density wave (CDW) topological solitons at the interface between a normal metal and a 2*D*-array of the CDW-carrying linear chains. The interplay of commensurability potential, interchain interaction, and electric field on the dynamics of soliton formation is studied. When the interchain interaction exceeds the commensurability energy, the dynamic mechanism of creation of fractionally charged solitons near the contact is suppressed and specific contact nonlinearity in transport current is not observed. © *1999 American Institute of Physics.* [S1063-777X(99)01106-8]

INTRODUCTION

Some quasi-one-dimensional metallic alloys undergo phase transition to the Peierls dielectric (PD) state at low temperatures (see, e.g.,[1–3]). PD is characterized by a complex order parameter $\Delta \exp(i\varphi)$, where Δ is the gap in a single-electron spectrum and phase gradients define the collective charge transfer: CDW conductivity. Topologically stable nonlinear phase excitations, in particular, solitons and antisolitons, serve as the elementary CDW charge carriers. The soliton description is more or less successful in explanation of the nonlinear bulk transport (see, e.g., the Reviews 1 and 2). However, one principal aspect of CDW-physics, viz, the problem of interaction of the current-carrying CDW-phase deformations with conduction electrons, in particular, the nature of CDW/metal electrode interface phenomena, is not yet entirely understood and controversial explanations still arises.

To describe the process of charge transformation at the CDW/normal metal interface, the ideology of phase slip centers (PCS) which exploits the analogy between the PSC and dislocations had been put forward (see, e.g., Refs. 4–7). The physics behind the PSC is the strongly pronounced polaron effect:[3] i.e., conduction electrons imbedded in the conduction band of a quasi-one-dimensional semi-conductor are unstable against self-trapping and subsequent absorption by the valence band where they are finally converted into CDW phase solitons.[9] Interchain interaction provides aggregation of solitons into dislocation-like loops: PSCs. Charge transformation takes place near the contact with a normal metal. In the cited publications[4–7] (see also references therein), the PSCs were treated as the static objects.

Dynamics of conversion was studied in a series of pioneer papers.[8–10] It was shown that prior to formation of PSC conduction solitons manifest highly nontrivial individual behavior, and the proper hierarchy of time scales which governs the charge transformation was established. Self-trapping is connected with local gap deformations in conducting chains. The potential barrier for the self-trapping is $\sim\Delta$, and during the time $\sim\hbar/\Delta$ the quasiparticles spectrum is matched to a local value $\Delta(\mathbf{r},t)$; the time of the gap deformation is of order of $\bar{\omega}^{-1}$ ($\bar{\omega}$ is the frequency of the Peierls phonons which is of the order of the Debye frequency[2,3]), the interchain interaction being of order T_c (T_c is the temperature of the Peierls transition), it defines the time $\hbar/T_c$ of the interchain phase coherence onset. In a weakly coupled array of highly conducting chains, when $T_c \ll \hbar\bar{\omega} \ll \Delta$, the self-trapping of electrons occurs in individual chains independently[3,4] and the charge transformations proceeds in two steps, each characterized by its own time: transfer of conduction electrons into the valence band in a single chain at $\tau_\Delta \sim \bar{\omega}^{-1}$, and formation of a collective charge carrier in this chain at $\tau_\varphi \gg \tau_\Delta$. The time τ_φ is the intrinsic scale of the CDW-phase Hamiltonian,[2–4] at $t < \tau_\varphi$ individual charge carriers obey the Lagrange equations supplemented by the boundary conditions. The latters are formed during the time $t < \tau_\Delta$;[7] the initial phase perturbation is localized near the interface over the distance of the order of $V_F\tau_\Delta \sim \xi_0 = \hbar V_F/\Delta$; where ξ_0 is the amplitude coherence length in PD. The jump $\delta\varphi$ of the initial phase profile $\varphi(t=0)$ is defined by the charge conservation law in the process of self-trapping. Indeed, the collective CDW charge density ρ in a single chain is related to phase gradient via the Fröhlich relation:

$$\rho = \frac{e}{\pi} \frac{\partial\varphi}{\partial x}. \tag{1}$$

When q electrons are converted into the CDW-condensate, the phase acquires a local deformation with the net phase shift:

$$\delta\varphi = \varphi(x=\infty) - \varphi(x=-\infty) = q\pi. \tag{2}$$

It was shown in[9] that during the elementary act of self-trapping at the metal/PD interface the charge $2e$ is transformed into a CDW in a single chain, i.e. two electrons with

opposite spins are self localized during the time $\bar{\omega}^{-1}$. This process resembles the Andreev reflection in superconductors. Thus, the initial condition to the phase equations of motion leads to $q = -2$ in Eq. (2). As the scale ξ_0 is much less than any intrinsic length in the phase Hamiltonian,[2–4] we can formulate the initial condition as a point-like step function with the height equal to -2π.[7]

In our previous publications[8,10] we have studied the evolution of the initial CDW profile both analytically and numerically in two models, when self-trapping occurs:

1) in a central chain which belongs to a cluster of nearest chains containing an incommensurate CDW. The electric field was not taken into account;[8]

2) in an isolated chain containing commensurate CDW in the presence of a dc-electric field.[10]

It was shown that the initial condition always transforms into stable topological Sine-Gordon (SG) solitons. In the model of nearest chains cluster each soliton has charge $2e$, and the role of the bulk term in the SG equation plays the role of interaction between chains of the type $\sin(\varphi_0 - \varphi_1)$, where φ_0 and φ_1 are the phases in the central and nearest chains. In a commensurate CDW we have observed the effect of a charge fractionalization (see, e.g., Refs. 1 and 2) when the initial profile decays into M fractionally charged solitons (an integer $M > 2$ is an index of commensurability) each carrying charge:

$$q_s = 2e/M. \tag{3}$$

It was shown in Ref. 10 that soliton-antisoliton pairs with charges $\pm q_s$ (3) are created in a dc-electric field from an initial CDW profile, thus giving rise to an additional contact non-linearity in the CDW-conductivity.

It is certainly interesting to study the evolution of initial CDW profile and interaction of phases in different chains in a more general 2D model, which takes into account the effects of commensurability, inter-chain interaction and electric field. This problem is not integrable; it is solved numerically in this paper.

MODEL

Consider the 2D-array of the CDW-containing chains which occupy the semi-axis $x \geqslant 0$. The Lagrangian of the system is (see, e.g., Ref. 2):

$$L = \frac{1}{\pi \hbar V_F} \sum_i \left[\frac{\Delta^2}{\bar{\omega}^2} \left(\frac{\partial \varphi_i}{\partial t} \right)^2 - \frac{\hbar^2 V_F^2}{4} \left(\frac{\partial \varphi_i}{\partial x} \right)^2 \right.$$

$$+ \frac{\Delta^2}{\bar{\omega}^2} \frac{2}{M^2} \omega_0^2 \cos M \varphi_i + 2 T_c^2 \cos(\varphi_i - \varphi_{i-1})$$

$$\left. + \frac{e}{\pi} \hbar V_F E(\varphi_i - \tilde{\varphi}) \right], \tag{4}$$

where φ_i denotes the phase in the i-th chain, ω_0 is the commensurability frequency, and $\tilde{\varphi}$ is the phase at $x \to +\infty$. Such form of the last term in Eq. (4) takes into account the renormalization of the phase in each chain in the presence of an electric field.

The equation of motion for the Lagrangian (4) has the form:

$$\frac{\partial^2 \chi_i}{\partial t^2} - \frac{\partial^2 \chi_i}{\partial y^2} + A \sin M(\chi_i + \tilde{\varphi}) + B \sin(\chi_i - \chi_{i-1})$$

$$+ B \sin(\chi_i - \chi_{i+1}) = \varepsilon, \tag{5}$$

where

$$y = \frac{2\Delta}{\hbar V_F \bar{\omega}} x, \quad \varepsilon = \frac{e}{2\pi} \hbar V_F \frac{\bar{\omega}^2}{\Delta^2} E,$$

$$A = \frac{\omega_0^2}{M}, \quad B = \frac{\bar{\omega}^2}{\Delta^2} T_c^2, \quad \text{and} \quad \chi_i = \varphi_i - \tilde{\varphi}. \tag{6}$$

In a nonzero field E the ground state is:

$$\tilde{\varphi} = \arcsin(\varepsilon). \tag{7}$$

Equation (7) implies the restriction on the electric field whereby the stable phase configuration exists:

$$\left| \frac{\varepsilon}{A} \right| < 1. \tag{8}$$

Only the fields that obey the condition (8) are considered further.

Equation (5) is supplemented by the initial and boundary conditions which describe conversion of the pair of electrons into a CDW-profile in a central chain ($i = 0$) (see the above discussion of the hierarchy of times in this problem):

$$\left. \frac{\partial \chi_i}{\partial t} \right|_{t=0} = 0, \tag{9a}$$

$$\chi_i(t=0) = -2\pi \theta(\bar{\xi}_0 - y) \delta_{i0}, \tag{9b}$$

$$\chi_i(y=0) = -2\pi \delta_{i0}, \tag{9c}$$

where $\delta_{ij} = 1$, $i = j$ and $\delta_{ij} = 0$, $i \neq j$; $\bar{\xi}_0$ is the coherence length $\xi_0 = \hbar V_F / \Delta$ in units (6), $\bar{\xi}_0 \ll 1$; and $\theta(y)$ is the Heavyside step function.

In what follows, we solve Eq. (5) with the conditions (9) numerically by means of the method of finite differences. The difference equation corresponding to Eq. (5) has the form

$$\frac{\chi_{i,k+1,l} + \chi_{i,k-1,l} - 2\chi_{i,k,l}}{(\Delta t)^2} - \frac{\chi_{i,k,l+1} + \chi_{i,k,l-1} - 2\chi_{i,k,l}}{(\Delta y)^2}$$

$$+ A \sin M(\chi_{i,k,l} + \varphi_0) + B \sin(\chi_{i,k,l} - \chi_{i+1,k,l})$$

$$+ B \sin(\chi_{i,k,l} - \chi_{i-1,k,l}) = \varepsilon, \tag{10}$$

where Δt is the time step, Δy is coordinate step, and $\chi_{i,k,l} = \chi_i(\Delta t k, \Delta y l)$. Equation (10) is solved for different values of parameters and at different envelope functions in (9b). The results presented are obtained for $\max(k) = 1000$ ($\max(k)$ is the number of sites). It is found in particular that neither changing the shape of the initial perturbation (9b) (rectangular or triangular step) nor increasing the number of sites provides any significant effect on the solution of Eq. (10).
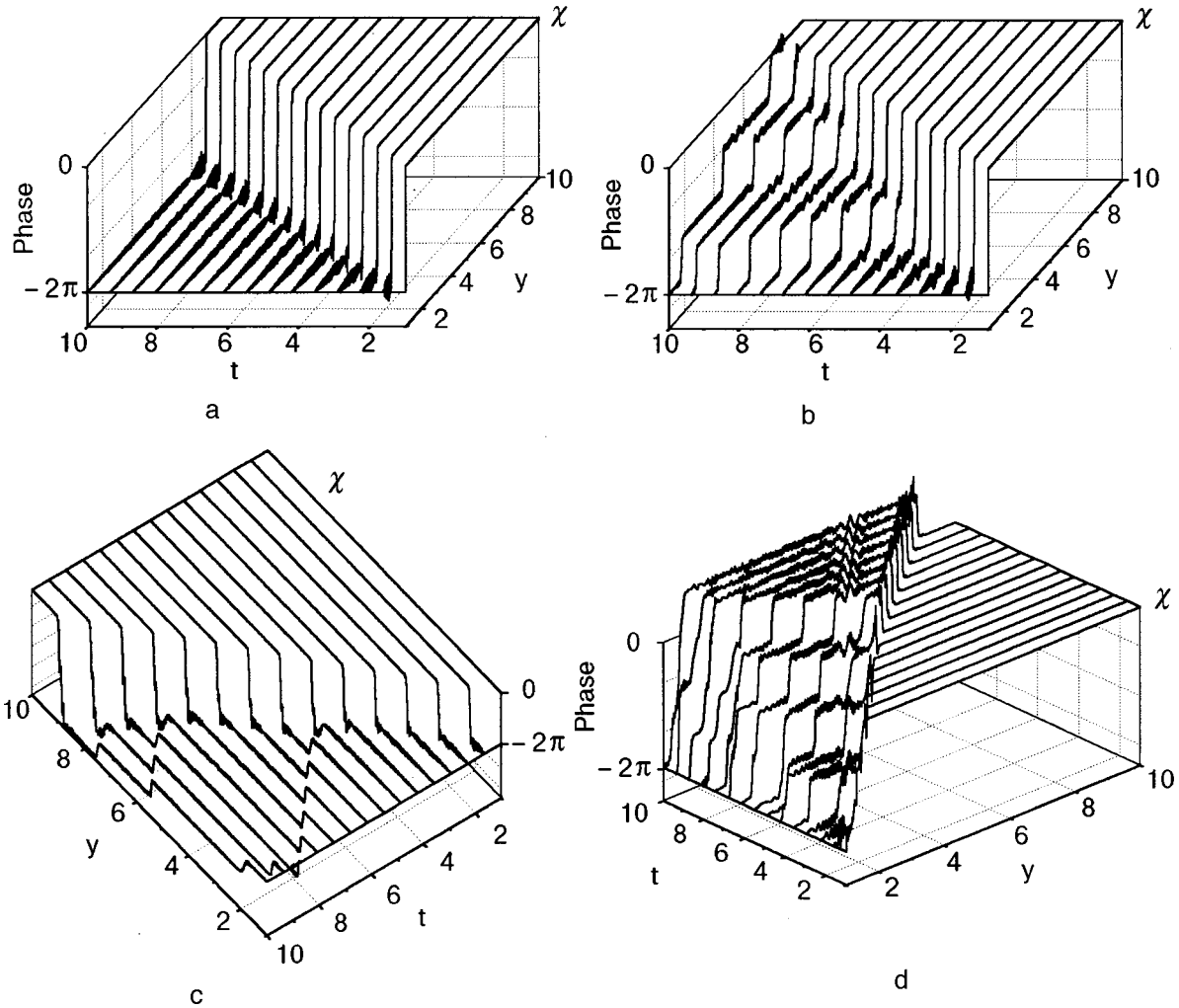
FIG. 1. Dynamics of conversion of the electrons to the commensurate one-dimensional CDW. $A = 1$: a—accelerating field: $\varepsilon = 0.05$; b—decelerating field: $\varepsilon = -0.05$; c—accelerating field: $\varepsilon = 0.2$. The mechanism of the pair creation is observed: d—decelerating field: $\varepsilon = -0.2$. The mechanism of the pair creation is observed.

CONVERSION IN A SINGLE CHAIN

Dynamics of conversion of conduction electrons into a one-dimensional CDW was studied in.[10] The system is described by the reduced equation (5):

$$\frac{\partial^2 \chi}{\partial t^2} - \frac{\partial^2 \chi}{\partial y^2} + A \sin M(\chi + \tilde{\varphi}) = \varepsilon. \tag{11}$$

In weak decelerating and accelerating fields ($|\varepsilon/A| < 0.1$) the dynamics of phase develops along conventional lines. In an accelerating field the initial profile propagates along the chain keeping safe its "«step-like»" form (9b) (Fig. 1a). In a weakly decelerating field (Fig. 1b), the initial profile loses its stability after some time and splits into commensurability solitons (3), which reverse their direction of motion, and eventually collect near $x = 0$. The radiation propagating with the maximum velocity is clearly observed.

The picture changes drastically when $|\varepsilon/A|$ exceeds a threshold field ε_T. In this case the charge creation during the evolution of the initial profile is observed both in accelerating (Fig. 1c) and decelerating fields (Fig. 1d). The reversal of the sign of created charges with the change of the field direction unambiguously indicates that the mechanism of the charge formation is the polarization of a CDW vacuum: at $\varepsilon > 0$, the soliton (s) and antisoliton ($\bar{s}$) move pro- and contra the electric field correspondingly; at $\varepsilon < 0$ soliton and antisoliton change their positions. Such a mechanism of the charge creation is responsible for the specific nonlinearity of the contact conductivity:[10]

$$j \sim \frac{E \sqrt{E - E_T}}{B + \sqrt{E - E_T}}. \tag{12}$$

Note that the threshold field E_T, which defines the onset of the nonlinear contact conductivity (12), is different from the one normally observed in bulk transport.[1,2] The latter is of electrostatic origin and of course cannot appear in numerical simulation of Eq. (11). The microscopic origin of the threshold (11) is the concurrence between the energy of soliton-antisoliton confinement in a moving phase profile and the electric field, which tends to dissolve the $s\bar{s}$-bound state.[10]
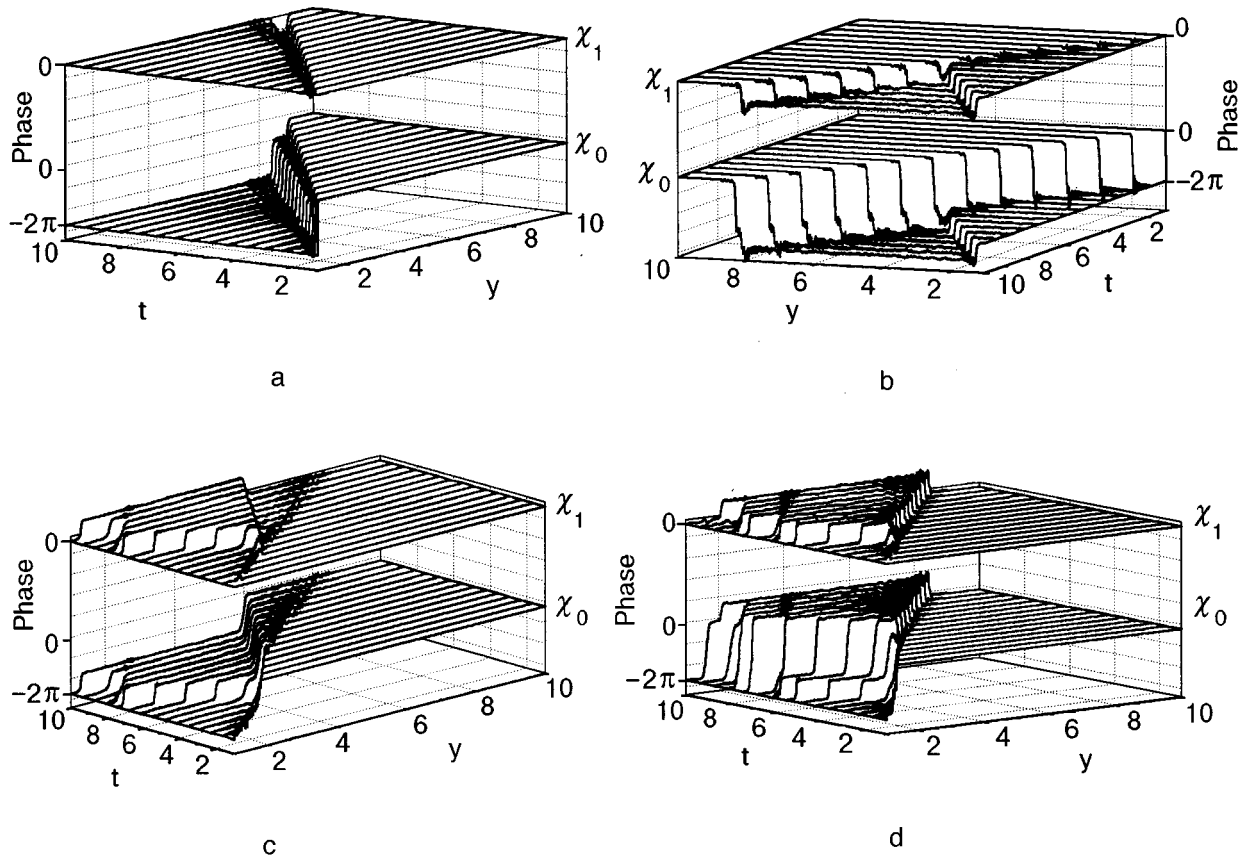
FIG. 2. Dynamics of conversion of the electrons to the cluster of the nearest chains. $N=2$, $B=1$: a—incommensurate chains: $\varepsilon=0$, $A=0$. The initial condition transforms to a 2π-kink surrounded by dipoles; b—commensurate chains, accelerating field: $\varepsilon=0.4$, $A=1$. The mechanism of the pair creation is observed; c—commensurate chains, decelerating field: $\varepsilon=-0.2$, $A=1$. The mechanism of the pair creation is observed; d—commensurate chains, decelerating field: $\varepsilon=-0.3$, $A=1$. The mechanism of the pair creation is observed.

CONVERSION IN A 2D-CLUSTER OF NEAREST CHAINS

In this model we consider the conversion in a central chain which is surrounded by N symmetrically arranged nearest chains. The symmetry of the problem allows us to describe the dynamics of conversion by the following two equations:

$$\frac{\partial^2 \chi_0}{\partial t^2} - \frac{\partial^2 \chi_0}{\partial y^2} + A \sin M(\chi_0 + \tilde{\varphi}) + NB \sin(\chi_0 - \chi_1) = \varepsilon,$$
(13a)

$$\frac{\partial^2 \chi_1}{\partial t^2} - \frac{\partial^2 \chi_1}{\partial y^2} + A \sin M(\chi_1 + \tilde{\varphi}) + B \sin(\chi_1 - \chi_0) = \varepsilon,$$
(13b)

where χ_0 is the phase in the central chain and χ_1 in neighboring ones. Equations (13) are supplemented by the conditions (9). Equations (13) differ from Eq. (11) by the interchain interaction term $B \sin(\chi_0 - \chi_1)$.

The oversimplified problem (without the electric field and commensurability potential) was solved analytically in Ref. 8. It was shown in Ref. 8 that pair of self-trapped conduction electrons transforms into a charged 2π-kink localized in a central chain and surrounded by dipoles in neighboring chains. The result of a numerical study of same problem is plotted in Fig. 2a. There are two distinctions between the results obtained analytically and numerically. First

is the existence of the radiation (Fig. 2a) which has been dropped in.[8] Second, decrease of the velocity of the 2π-kink (Fig. 2a), which is the typical feature of the soliton-type solutions in the discrete Sine-Gordon equation.[11,12] The inclusion of the commensurability [$A \neq 0$ in Eq. (13)] results in suppression of the charged dipoles.

Taking into account the electric field in the r.h.s. of Eqs. (13) leads to various pictures, which depend on the equation parameters. As in the model of a single chain, the threshold field is observed, which is higher that in the one-dimensional model and which depends on the number of neighboring chains N, the parameters A and B, and sign of the field. Increasing the number of chains leads to increasing the threshold field. In weak accelerating fields ($\varepsilon/A < 0.3$) charged 2π-kink moves in the central chain and only the radiation is observed in the neighboring chains. In higher accelerating fields ($\varepsilon/A > 0.3$) fractional charge creation is observed (Fig. 2b); it occurs in the central and in neighboring chains simultaneously, which explains the enhancement of the threshold field.

Figures 2c and 2d show the solutions of Eqs. (13) in decelerating fields. The dynamics in weak decelerating fields ($|\varepsilon/A| < 0.15$) is analogous to the corresponding result for a single chain. The initial profile, which moves opposite the field, loses its velocity after some time and localizes near
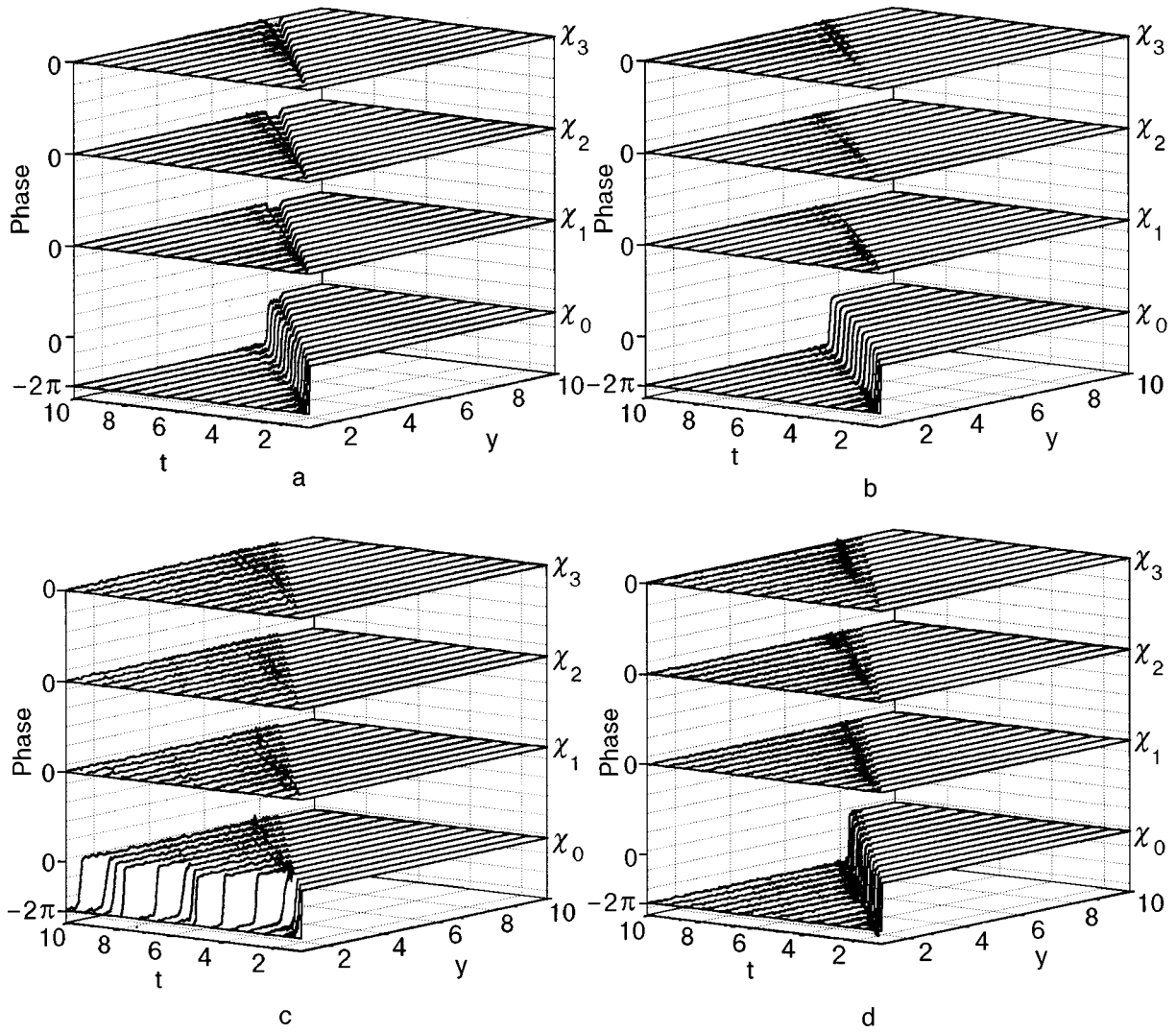
FIG. 3. Dynamics of conversion of the electrons to the $2D$-array of chains. $B=1$: a—incommensurate chains: $\varepsilon=0$, $A=0$. The initial condition transforms to a 2π-kink surrounded by dipoles; b—commensurate chains: $\varepsilon=0$, $A=1$. Commensurability leads to the suppression of the dipoles; c—commensurate chains, decelerating field: $\varepsilon=-0.5$, $A=1$. The initial condition transforms to a 2π-kink decelerating by the field; d—commensurate chains, accelerating field: $\varepsilon=0.5$, $A=1$. The initial condition transforms to a 2π-kink accelerating by the field.

$x=0$. In higher fields ($|\varepsilon/A|>0.15$) the charge creation is observed (Figs. 2c and 2d). The charge creation occurs in the neighboring chains only (Fig. 2c) or in the central and in the neighboring chains simultaneously (Fig. 2d), but always solitons and antisolitons in the neighboring chains form bound states with solitons and antisolitons in the central chain. It must be emphasized that the value of the threshold field depends on the sign of the applied field. In our opinion, this is artifact of the model; actually, in real experiment one has a symmetric system with two metal/CDW interfaces, and E_T is independent on the sign of ε.

BEYOND THE CLUSTER APPROXIMATION

Consider the finite number of chains arranged symmetrically relative to the central chain. We start from the model without electric field and commensurability term (Fig. 3a). The picture obtained is in its common features similar to Fig. 2a. The charged 2π-kink moves in the central chain and is surrounded by dipoles and radiation in the array of chains.

With increase in the size of array, the dipoles will be spread in the direction perpendicular to x. The amplitude of radiation is approximately the same in all the chains.

Figure 3b shows the solutions of Eq. (5) at $\varepsilon=0$. The commensurability suppresses the charged dipoles. The 2π-kink moves in the central chain, losing its velocity.

In the presence of an electric field (Figs. 3c and 3d), effects of the soliton-antisoliton pairs creation and fractional charge solitons (3) are not observed. In the decelerating field (Fig. 3c) the 2π-kink looses velocity and localizes near $x=0$. In the accelerating field (Fig. 3d), the 2π-kink accompanied by radiation moves into the bulk.

In Fig. 4 the soliton-soliton interaction for the solitons located in the neighboring chains is studied. This problem is interesting in the context of the problem of the solitons aggregation into the macroscopic phase-slip centers. The 2π-kink localized in the center of the first chain is prepared in the following way: the initial condition for this chain is chosen in the form:
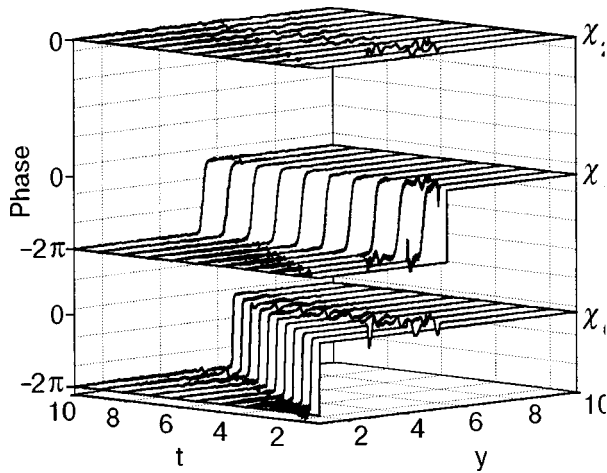
FIG. 4. Interaction between the solitons in the neighboring chains. $\varepsilon = 0$, $A = B = 1$. The soliton-soliton interaction leads only to small phase shift of the solitons.

$$\varphi_1(t=0) = -2\pi\theta\left(\frac{l}{2} - y\right), \tag{14}$$

where l is the length of the chain. Then, after some time, the condition (14) decays into the stable 2π-kink accompanied by the radiation, which spreads in both directions in all the chains. The velocity of this kink is zero due to the symmetrical initial condition (14) contrary to the initial condition (9b) which produces the kink with a nonzero velocity. Before the collision we put the radiation equal to zero. Hence, we have the static 2π-kink in the first chain and the moving 2π-kink in the zero chain. From Fig. 1b we see that the velocity of the kinks does not change after collision. The collision results only in the small space shift of the kinks, which means that the aggregation of such solitons into macroscopic phase-slip centers does not occur in this model.

CONCLUSIONS

In this paper we have studied several models describing the dynamics of conversion of conduction electrons into topological solitons of the commensurate charge density wave.

In an incommensurate CDW, in the absence of electric field, the initial condition transforms into the 2π-kink localized in the central chain and surrounded by charged dipoles in the other chains. The commensurability leads to suppression of such dipoles. In the presence of electric field when $B/A \ll 1$ and the field being sufficiently large, the mechanism of topological charge creation is observed. If $B/A < 1$ (which is more realistic) the fractional charge conductivity and creation of the soliton-antisoliton pairs are suppressed. The 2π-kink is localized in the central chain and is surrounded by the radiation in the other chains. The soliton velocity depends on the field.

In the framework of this model the soliton-soliton interaction does not lead to the aggregation of the solitons into macroscopic phase-slip centers.

*E-mail: pershin@hotmail.com

[1] *Electronic Properties of Inorganic Quasi One-Dimensional Compounds*, P. Monceau (Ed.), Riedel Company, Dordrecht (1985), Parts 1 and 2, *Density Waves in Solids*, G. Grüner (Ed.), Addison-Wesley, Reading, Massachusets (1994).
[2] I. V. Krive, A. S. Rozhavsky, and I. O. Kulik, Fiz. Nizk Temp. **12**, 635 (1986) [Sov. J. Low Temp. Phys. **12**, 360 (1986)].
[3] S. Brazovskii and N. Kirova, *Electron Self-Localization and Periodic Superstructures in Quasi One Dimensional Dielectrics*, Sov. Sci. Rev. A: Phys., I. M. Khalatnikov (Ed.), Harwood Academic Publishers, 6 (1984).
[4] S. Brazovskii and S. Matveenko, J. Phys. I (Paris) **1**, 269 (1991); J. Phys. I (Paris) **1**, 1173 (1991).
[5] D. Feinberg and J. Friedel, J. Phys. (Paris) **49**, 485 (1988).
[6] J. C. Gill, J. Phys. C **19**, 6589 (1986).
[7] S. Ramakrishna, M. P. Maher, V. Ambegaokar, and U. Eckern, Phys. Rev. Lett. **68**, 2066 (1992).
[8] A. S. Kovalev, Yu. V. Pershin, and A. S. Rozhavsky, Phys. Rev. B **53**, 16227 (1996); Fiz. Nizk. Temp. **22**, 322 (1996) [Low Temp. Phys. **22**, 253 (1996)].
[9] I. V. Krive, A. S. Rozhavsky, and V. A. Rubakov, Pis'ma Zh. Éksp. Teor. Fiz **46**, 99 (1987) [JETP Lett. **46**, 121 (1987)].
[10] A. S. Rozhavsky, Yu. V. Pershin, and A. S. Kovalev, Fiz. Nizk. Temp. **23**, 1325 (1997) [Low Temp. Phys. **23**, 996 (1997)].
[11] Yu. S. Kivshar and A. M. Kosevich, Pis'ma Zh. Éksp. Teor. Fiz **37**, 542 (1983) [JETP Lett. **37**, 648 (1983)].
[12] I. Ishimori and T. Munakata, J. Appl. Phys. **51**, 3367 (1982).

Structural phase transformation and limited miscibility in Jahn–Teller systems

M. A. Ivanov

Institute of Metal Physics, National Academy of Sciences of the Ukraine, 252680 Kiev, Ukraine*

N. K. Tkachev

Institute of High-Temperature Electrochemistry, Ural Branch of the Russian Academy of Sciences, 620219 Ekaterinburg, Russia**

A. Ya. Fishman

Institute of Metallurgy, Ural Branch of the Russian Academy of Sciences, 620016 Ekaterinburg, Russia***
(Submitted January 18, 1999)
Fiz. Nizk. Temp. **25**, 616–624 (June 1999)

Immiscibility of crystal systems with Jahn–Teller (JT) ions is studied at low temperatures. Phase transformations under which concentrated JT systems are separated into phases with a high and low concentration of JT ions with structural JT transformations are analyzed. A dependence of the phase diagram topology on the ratio between the cooperative interaction energy in the JT subsystem and the intensity of random crystal fields acting on the JT ions is established. The possibility of low-temperature three-phase equilibrium of two cubic and a tetragonal phase with different concentrations of JT centers is demonstrated for a high degree of substitutional-type disorder. © *1999 American Institute of Physics.* [S1063-777X(99)01206-2]

INTRODUCTION

In the present communication, we analyze the origin of immiscibility (or rather weak miscibility) of different components in crystals with the cooperative Jahn–Teller (JT) effect. The substitution of orbitally nondegenerate ions for JT ions in such systems can lead to a separation into phases with a higher and lower concentrations of JT ions at low temperatures similar to that in some doped magnetic materials (see, for example, Ref. 1). Structural phase transformations of the displacement type are related to a certain extent to phase transitions of separation type due to the fact that in both cases the system has a tendency to lower its free energy as a result of maximum possible splitting of degenerate states. This also applies to JT crystals with cooperative structural phase transition of the first and second order. Peculiarities of the phenomena under consideration is associated to a considerable extent with random crystal fields which are always present in disordered systems. Like cooperative interactions between JT ions, such random fields can serve as the main mechanism of splitting of degenerate states, and hence can considerably affect the phase equilibrium in binary mixtures under investigation.

Structural phase transformations (PT) and other properties of JT systems in random crystal fields were investigated by many authors (see, for example, Refs. 2 and 3). It was proved that such fields reduce the transition temperature and the order parameter and can suppress the PT completely in the case of quite high intensities. Obviously, random crystal fields must also affect the position of the boundaries of immiscibility regions in systems with structural PT. Besides, such fields themselves can lead to thermodynamic instability of some phase states. The interest to the influence of random

crystal fields on the thermodynamic properties and phase transformations in JT systems is considerably stimulated by the advances in experimental investigations of crystals with anomalous magnetoresistance, doped fullerites, HTSC oxides, etc., i.e., the materials in which centers with a degenerate or pseudo-degenerate ground state strongly affect their properties.

We shall analyze phase diagrams of quasi-binary systems with the substitution of an ion with a nondegenerate ground state for a JT ion. For the sake of definiteness, we consider crystals in which JT structural transformations of the ''ferro''-type occur (main attention will be paid to systems with second-order structural PT). It will be proved that the form of a phase diagram is determined to a considerable extent by the scale of variation of dispersion of random crystal fields upon the replacement of JT ions.

1. MODEL OF STRUCTURAL PT ASSOCIATED WITH THE COOPERATIVE JT EFFECT

Let us consider for simplicity structural transformations of the ''ferro''-type in cubic crystals with doubly degenerate JT ions. The Hamiltonian of the JT subsystem in the molecular-field approximation can be written in the form

$$H = \sum_s \left[(\lambda \sigma + h_{sz}) \sigma_{sz} + h_{sx} \sigma_{sx} \right],$$

$$\sigma_{sz} = \begin{pmatrix} -1 & 0 \\ 0 & 1 \end{pmatrix}, \quad \sigma_{sx} = \begin{pmatrix} 0 & 1 \\ 1 & 0 \end{pmatrix}, \tag{1}$$

where λ is the parameter of the cooperative interaction between JT ions, h_{sz} and h_{sx} are the components of $2D$ random crystal field at the sth JT ion, σ_{sz} and σ_{sx} the orbital opera-

tors defined in the space of wave functions of an orbital doublet, and σ denotes the quantum-statistical average $(\langle \dots \rangle_T)$ and the average over the configuration of random fields $(\langle \dots \rangle_c)$ of the operator $\sigma_z (\sigma \equiv \langle \langle \sigma_z \rangle_T \rangle_c)$. In Hamiltonian (1), we have omitted the terms describing unharmonic interactions at a JT ion.[4] We assume that these terms are much smaller than the energy λ of cooperative interaction. As a result, the structural phase transformations are second-order PT.[5] A nonzero order parameter σ in the model under investigation corresponds to the emergence of tetragonal deformation of the lattice $e_{zz} - (e_{xx} + e_{yy})/2$.

The order parameter σ is defined by the following equation:

$$\sigma = \left\langle \{(\lambda \sigma + h_z)/E(\sigma,\mathbf{h})\} \tanh \frac{E(\sigma,\mathbf{h})}{T} \right\rangle_c ,$$

$$E(\sigma,\mathbf{h}) = \sqrt{(\lambda \sigma + h_z)^2 + h_x^2}. \tag{2}$$

Here and below, we use for configuration averaging the random-field distribution function $f(\mathbf{h}) \equiv f(h_z, h_x)$ of the Gaussian type[3]:

$$f(\mathbf{h}) = \frac{1}{\pi \Delta^2} \exp\left\{ -\frac{h_z^2 + h_x^2}{\Delta^2} \right\}, \tag{3}$$

where Δ is the dispersion of random crystal fields.

An analysis of the dependences of the order parameter σ and the temperature T_D of the structural phase transformation from the ''para''- to the ''ferro''-phase on the dispersion Δ can be carried out using the expressions[6]

$$\sigma = 2 \exp\left[-\left(\frac{\lambda \sigma}{\Delta}\right)^2 \right] \int_0^\infty y$$

$$\times \exp(-y^2) I_1\left(\frac{2 y \lambda \sigma}{\Delta}\right) \tanh\left(\frac{y \Delta}{T}\right) dy, \tag{4}$$

$$2 \frac{\lambda}{\Delta} \int_0^\infty y^2 \exp(-y^2) \tanh\left(\frac{y \Delta}{T_D}\right) dy = 1, \tag{5}$$

where $I_1(x)$ is a Bessel function of the imaginary argument.

In the absence of random fields, when $\Delta \to 0$, the structural phase transformation temperature T_D is equal to λ. In the region of critical values of Δ for which the PT disappears in the system $(T_D(\Delta) \to 0)$, the solutions of Eqs. (4) and (5) can be written in the form

$$\left(\frac{T_D}{\Delta}\right)^3 = \frac{2\sqrt{\pi}}{3 \zeta(3)} \left(1 - \frac{\Delta}{\Delta_0}\right), \quad \Delta_0 = \frac{\sqrt{\pi}}{2} \lambda, \tag{6}$$

$$\sigma^2 = \left(\frac{\Delta}{\lambda}\right)^3 \left[\left(\frac{2\lambda}{\Delta}\right) J_1\left(\frac{T}{\Delta}\right) - 1 \right] \left[2 J_1\left(\frac{T}{\Delta}\right) - J_2\left(\frac{T}{\Delta}\right) \right]^{-1}$$

$$= \left(\frac{2\Delta}{\lambda}\right)^2 \left(1 - \frac{\Delta}{\Delta_0}\right) \left[1 - \left(\frac{T}{T_D}\right)^3 \right], \tag{7}$$

$$J_1\left(\frac{T}{\Delta}\right) = \int_0^\infty y^2 \exp(-y^2) \tanh\left(\frac{y \Delta}{T}\right) dy,$$

$$J_2\left(\frac{T}{\Delta}\right) = \int_0^\infty y^4 \exp(-y^2) \tanh\left(\frac{y \Delta}{T}\right) dy, \tag{8}$$

where $\zeta(y)$ is the Riemann zeta-function, and expressions for $J_1(T/\Delta)$ and $J_2(T/\Delta)$ in the asymptotic limit $T/\Delta \ll 1$ have the form

$$J_1\left(\frac{T}{\Delta}\right) = \frac{\sqrt{\pi}}{4} - \frac{3}{8} \zeta(3) \left(\frac{T}{\Delta}\right)^3,$$

$$J_2\left(\frac{T}{\Delta}\right) = \frac{3\sqrt{\pi}}{8} - \frac{45}{32} \zeta(5) \left(\frac{T}{\Delta}\right)^5. \tag{9}$$

Phase transformation in the JT system is completely suppressed by random crystal fields when $\Delta > \Delta_0 = (\sqrt{\pi}/2)\lambda$, i.e., when their dispersion becomes larger than the energy of the cooperative interaction between degenerate centers.

Typical temperature dependences of the order parameter σ for various values of dispersion Δ are presented in Fig. 1. It can be seen that an increase in dispersion of random fields reduces the order parameter σ (Fig. 1a) as well as the phase transformation temperature T_D (Fig. 1b).

The above expressions allow us to analyze the phase states of systems with JT ions for various types of substitutions in the crystal lattice, including the substitution of orbitally nondegenerate ions for JT centers. We must only specify the dependences of the molecular field parameters and random-field dispersion on the concentration of the replaced centers.

2. MODEL OF THE MIXTURE

Let us consider the model of a mixture in which the free energy is determined by the splitting of degenerate centers, and the configuration entropy corresponds to a random distribution of JT ions in the mixture. In this case, the free energy of a quasi-binary system in the mean-field approximation per structural unit can be written in the form

$$F = c_{JT} F_{JT} + F_{id},$$

$$F_{JT} = \frac{\lambda \sigma^2}{2} - T \left\langle \ln\left\{ 2 \cosh\left(\frac{E(\sigma,\mathbf{h})}{T}\right) \right\} \right\rangle_c$$

$$= \frac{\lambda \sigma^2}{2} - 2T \exp\left\{ -\left(\frac{\lambda \sigma}{\Delta}\right)^2 \right\} \int_0^\infty y$$

$$\times \exp(-y^2) I_0\left(\frac{2 y \lambda \sigma}{\Delta}\right) \ln\left\{ 2 \cosh\left(\frac{y \Delta}{T}\right) \right\} dy,$$

$$F_{id} = T[c_{JT} \ln c_{JT} + (1 - c_{JT}) \ln(1 - c_{JT})], \tag{10}$$

where the parameters λ, Δ, and σ depend on the concentration c_{JT} of the JT centers.

Expressions (10) allow us to calculate the chemical potentials μ_a (of components with JT ions), μ_b (of component with orbitally nondegenerate ions), and the exchange chemical potential μ of the quasi-binary system under investigation[7–9]:

$$\mu = \frac{\partial F}{\partial c_{JT}} \equiv \mu_a - \mu_b = F_{JT} + c_{JT} \frac{\partial F_{JT}}{\partial c_{JT}} + T \ln\left(\frac{c_{JT}}{1 - c_{JT}}\right), \tag{11}$$

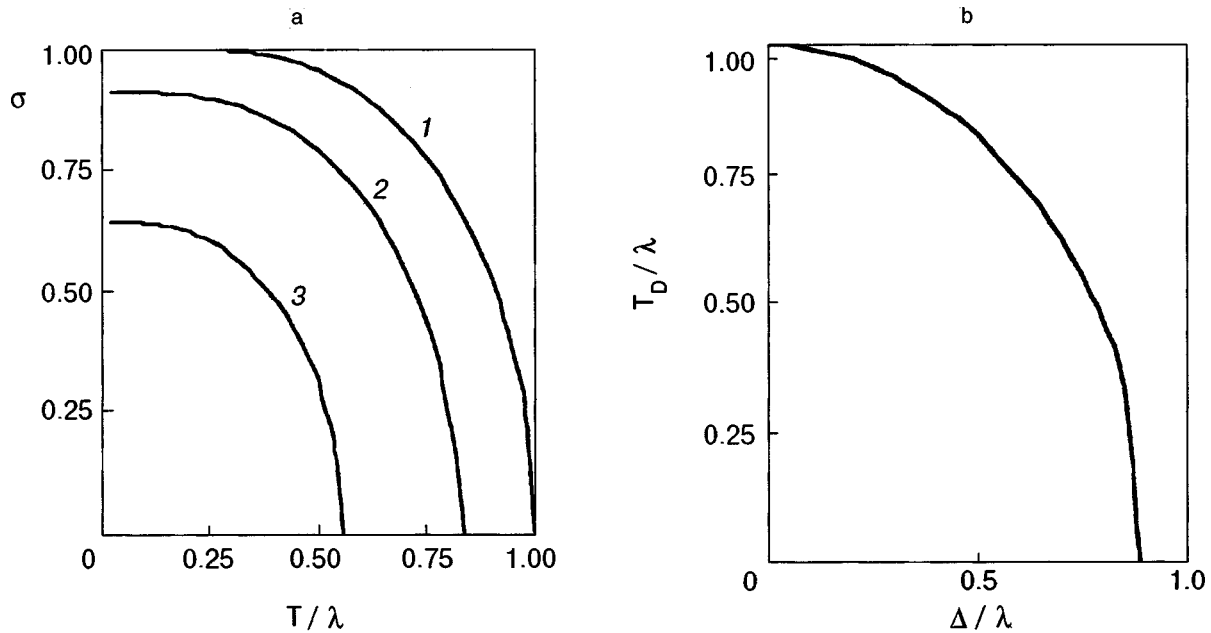FIG. 1. Effect of random fields on temperature dependence of the order parameter σ (a) and the structural transition temperature T_D (b). Curves *1, 2* and *3* correspond to the values 0, 0.5, and 0.75 respectively of the parameter Δ/λ.

$$\mu_a = F + (1 - c_{JT})\mu = F_{JT} + c_{JT}(1 - c_{JT})\frac{\partial F_{JT}}{\partial c_{JT}}$$

$$+ T\ln c_{JT}. \tag{12}$$

We disregard the effects associated with a change in the volume as a result of doping.

Expressions (11) and (12) make it possible to calculate binodals, i.e., temperature dependences of concentrations of components in two equilibrium phases (with the same values of μ and μ_a).

The boundaries of the region of absolute instability of the solution to phase separation are determined by the condition[10]

$$\frac{\partial^2 F}{\partial c_{JT}^2} = \frac{\partial \mu}{\partial c_{JT}} = 0. \tag{13}$$

In the case of phase separation, Eq. (13) defines the spinodal curve $T_s(c_{JT})$. The peak of this dependence is attained at the critical point T_{crit}, i.e., at coinciding peaks of the spinodal and binodal (phase-separation *domes*).[7]

Let us first consider the phase states of the system in the absence of random fields. In this case, the expressions (11) and (12) for chemical potentials and (13) for the concentration dependence of spinodal can be transformed to

$$\mu = \frac{\sigma^2}{2}\left[\lambda - c_{JT}\frac{\partial \lambda}{\partial c_{JT}}\right] - T\ln\left\{2\cosh\left(\frac{\lambda\sigma}{T}\right)\right\}$$

$$+ T\ln\left(\frac{c_{JT}}{1 - c_{JT}}\right), \tag{14}$$

$$\mu_a = \frac{\sigma^2}{2}\left[\lambda - c_{JT}(1 - c_{JT})\frac{\partial \lambda}{\partial c_{JT}}\right] - T\ln\left\{2\cosh\left(\frac{\lambda\sigma}{T}\right)\right\}$$

$$+ T\ln c_{JT}, \tag{15}$$

$$T_s(c_{JT}) = c_{JT}(1 - c_{JT})\left\{\sigma^2\left(\frac{\partial \lambda}{\partial c_{JT}} + \frac{1}{2}c_{JT}\frac{\partial^2 \lambda}{\partial c_{JT}^2}\right)\right.$$

$$\left. + c_{JT}\left(\frac{\partial \lambda}{\partial c_{JT}}\right)^2 \frac{1 - \sigma^2}{T_s(c_{JT}) - \lambda(1 - \sigma^2)}\right\}. \tag{16}$$

If we assume that

$$\lambda = \lambda_0 c_{JT}, \tag{17}$$

the equation for the spinodal curve (16) can be simplified considerably:

$$T_s(c_{JT}) = \lambda_0 c_{JT}(1 - c_{JT}\sigma^2), \tag{18}$$

and the temperature of the structural PT is found to be $T_D = \lambda_0 c_{JT}$. In this case, the peak of the phase-separation dome T_{crit} is at the point of intersection of the spinodal with the straight line $T(c_{JT}) = 0.5\lambda_0(1 - c_{JT})$. It can also be easily verified that the critical point of mixing in this case is $T_{\text{crit}} \approx 0.322\lambda_0$, while the critical concentration $c_{\text{crit}} \approx 0.355$, i.e., $T_D(c_{\text{crit}} > T_{\text{crit}}$. The corresponding equilibrium phase diagram (binodal) and the spinodal curve are shown in Fig. 2. It should be noted that the spinodal curve is always within the region of existence of the ''ferro''-phase. As a result, the line of structural transformations $T_D(c_{JT})$ intersects the binodal at a point lying on the left of c_{crit} and below T_{crit}. Consequently, ordered JT ''ferro''-phases with different order parameters practically coexist near the top of the phase-separation dome. In other words, different values of uniform JT deformations are observed in these phases at a given temperature. In the entire remaining temperature range (below the point of intersection of the $T_D(c_{JT})$ curve with the binodal), phase separation into the ''para''-phase deplete in JT ions and a more concentrated ''ferro''-phase takes place.
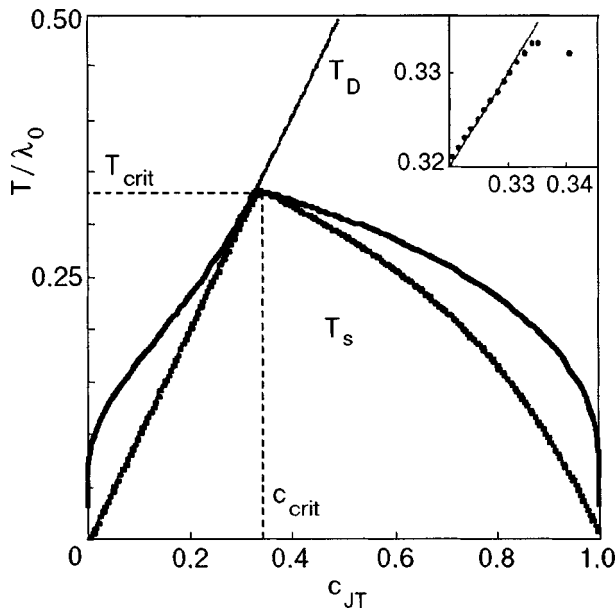
FIG. 2. Phase diagram of solid solution in the absence of random fields. The outer curve corresponds to binodal and the inner curve to the absolute instability boundary (spinodal). The straight line (T_D) shows the boundary of the low-symmetry phase for a random distribution of the components to be mixed.

3. PHASE-SEPARATION OF JT SYSTEM IN RANDOM CRYSTAL FIELDS

In order to analyze the influence of random fields on PT in crystals with JT ions, we must specify explicitly the concentration dependence of dispersion of these fields. We choose for this quantity the following approximation leading

to known concentration dependences in asymptotic limits of low concentrations of the sources of random field ($c_{JT} \ll 1$ or $(1 - c_{JT}) \ll 1$):

$$\Delta(c_{JT}) = d[c_{JT}(1 - c_{JT})]^{1/2}. \qquad (19)$$

The origin and the value of parameter d are associated either with the difference in the sizes of the substituting ion and the ion being replaced, or with the difference in their charges.[3]

It can be seen from formulas (6) and (16) that the structural phase transformation in a system with a random distribution of JT ions for the given concentration dependence of dispersion occurs only for concentrations $c_{JT} > c_0$, where $c_0 = [1 + \pi \lambda_0^2/(4d^2)]^{-1}$. Consequently, the boundaries of the region of absolute instability of the mixture considered above (the region of spinodal phase separation in the "ferro"-phase) must also be displaced towards higher values of c_{JT}. The corresponding concentration dependences of the structural phase transition temperature are shown by dotted curves in Fig. 3a.

It is significant that a mixture with a random distribution of the two types of ions in the concentration range $c_{JT} < c_0$, i.e., in the "para"-phase also, is unstable to spinodal phase separation of a different type (additional segment with $\partial \mu / \partial c_{JT} \leq 0$). This segment of the spinodal is approximately described by the equation

$$T_s^{(1)} = \frac{3\sqrt{\pi}}{8} d[c_{JT}(1 - c_{JT})]^{1/2} \left(1 - 4c_{JT} + \frac{8}{3} c_{JT}^2\right). \qquad (20)$$

Thus, the quasi-binary system under investigation is thermodynamically unstable in the entire low-concentration range at low temperatures, i.e., it is advantageous from the energy point of view for a system with JT ions in random
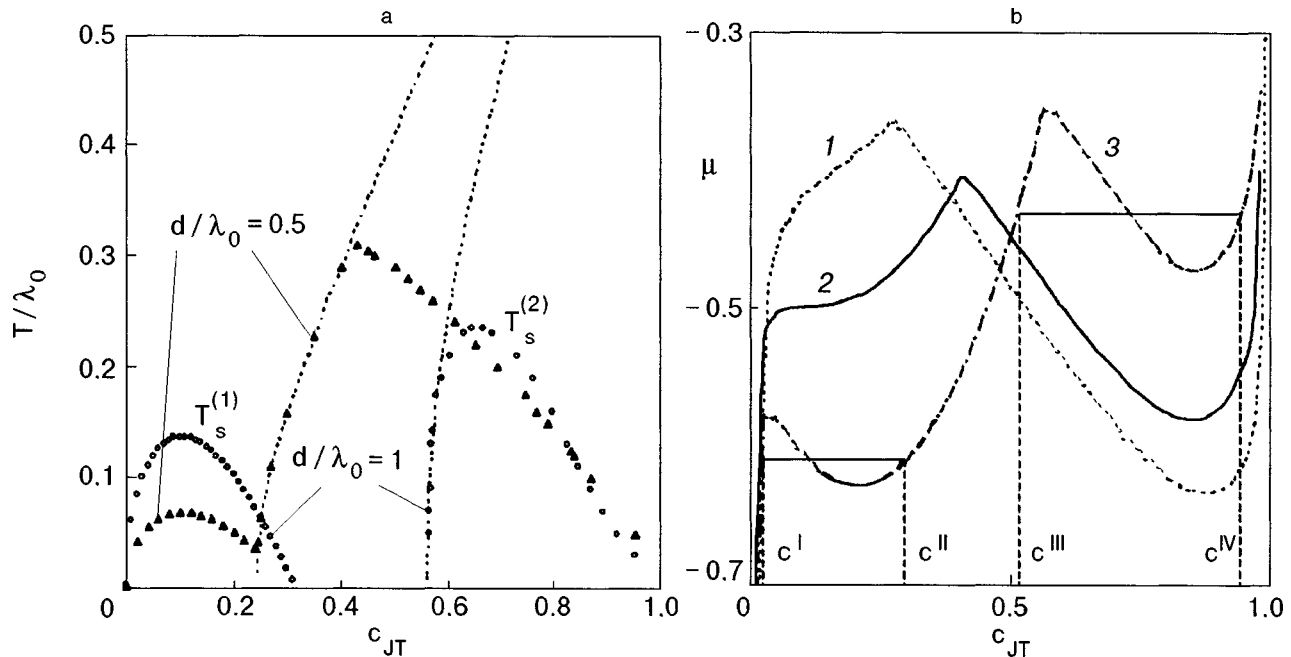

FIG. 3. (a) Configurations of the regions of spinodal decompositions of the "para"-"para" ($T_s^{(1)}$) and "ferro"-"para" ($T_s^{(2)}$) types in systems with different intensities of random fields. Dotted curves show the boundaries of structural PT for a random distribution of components being mixed in crystals. (b) Effect of random fields on concentration dependences of exchange potential for $T/\lambda_0 = 0.1$. Curves *1, 2* and *3* correspond to values of the parameter $d/\lambda_0 = 0.5$, 0.72, and 1 respectively. For $d/\lambda_0 = 1$, Maxwell's construction is carried out for two immiscibility regions.
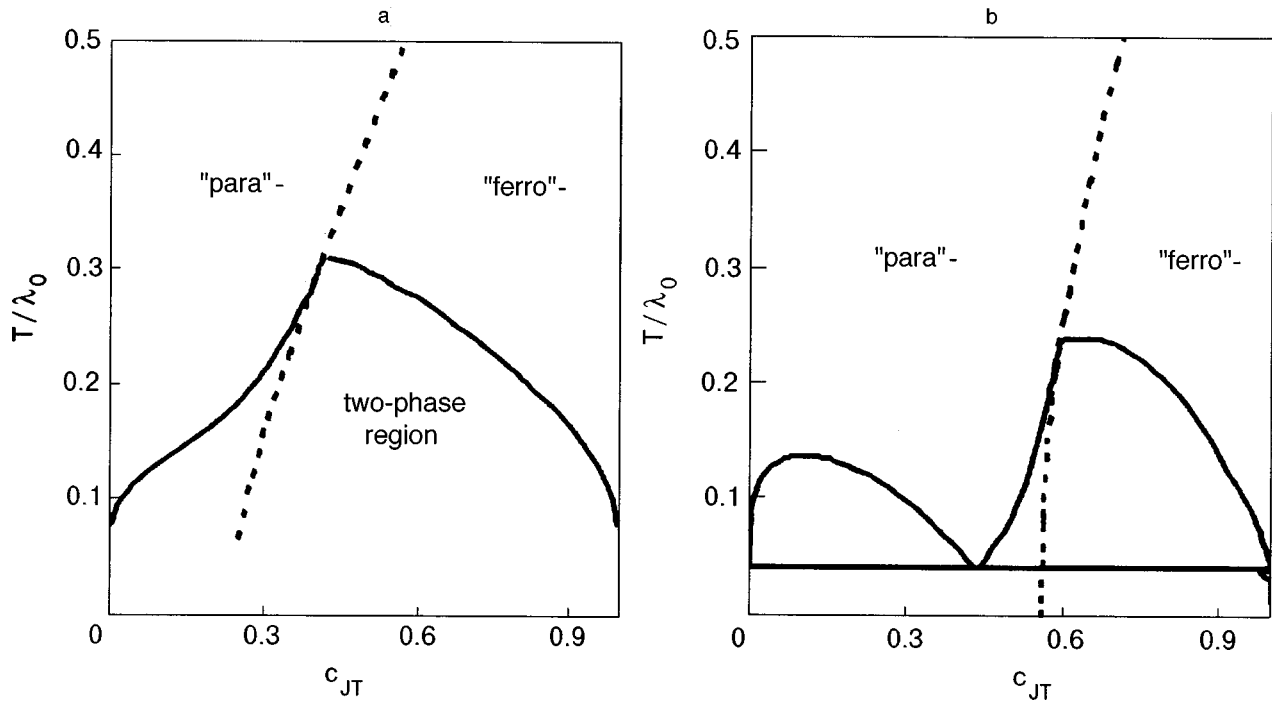
FIG. 4. Phase diagrams of solid solutions for various intensities of random fields ($d/\lambda_0 = 0.5$ (a) and 1 (b)).

crystal fields to undergo phase separation (at $T \neq 0$ K) into phases with relatively high and low concentrations of degenerate centers. The difference from a similar tendency for systems with cooperative JT effect lies in the fact that both states mentioned above are highly symmetric, i.e., ''para''-phases (c^{I} and c^{II} in Fig. 3b). It should be noted that such a behavior of dilute JT systems in random crystal fields is rather universal and is apparently not confined to approximations (3) and (19) used here.

The top of the dome of absolute immiscibility for a limited solubility of these ''para''-phases is attained for $c_{\mathrm{crit}}^{(1)} = 0,11$, $T_{\mathrm{crit}}^{(1)} = 0,14d$ ($T_{\mathrm{crit}}^{(1)}/d = (3\sqrt{\pi}/8)\sqrt{c_{\mathrm{crit}}^{(1)}(1 - 3,5c_{\mathrm{crit}}^{(1)})}$).

Typical concentration dependences of spinodals ($T_s^{(1)}$ and $T_s^{(2)}$) in the entire range of variation of c_{JT} in Fig. 3a. The curve describing the concentration dependence of chemical potential (Fig. 3b) indicates the position of the spinodal and binodal instability boundaries of the mixture at a fixed temperature. It can be seen that as the parameter d/λ_0 increases, the region of absolute instability of the solution is divided into two regions corresponding to the spinodal phase separation of the ''para''-''para'' type ($T_s^{(1)}$) and of the ''para''-''ferro'' type ($T_s^{(2)}$). It should be noted that the upper boundary of the value of d in the adopted model is the quantity $d_{\max} \approx 1.02\lambda_0$. This limitation corresponds to the condition for the minimum value of chemical potential of the components for the stoichiometric composition when $T \to 0$ K.

The results of analysis of the equilibrium phase diagram of the system under consideration (the boundaries of binodal phase separation) are presented in Fig. 4. It can be seen that a noticeable change in the phase diagram topology due to random fields occurs for values of d comparable with the cooperative interaction parameter λ_0. For $d/\lambda_0 < 0.72$, the

boundary of the immiscibility region for equilibrium ''ferro''- and ''para''-phases lies above the miscibility gap for two ''para''-phases (Fig. 4a). For $d/\lambda_0 = 0.72$, the boundary touches the peak $T_{\mathrm{crit}}^{(1)}$, and a triple point appears on the phase diagram for $d/\lambda_0 > 0.72$ (Fig. 4b). The position of this point of three-phase equilibrium on the diagram changes upon an increase in the parameter d/λ_0 as follows: it coincides with $T_{\mathrm{crit}}^{(1)}, c_{\mathrm{crit}}^{(1)}$ for $d = 0.72\lambda_0$ and is displaced to the values $T = 0$ K and $c_{JT} \simeq 0.32$ for $d \to d_{\max}$. The asymptotic description of the corresponding phase boundaries in the region $c_{JT} < c_0$ is given by the formula

$$T^{(1)}(c_{JT}) = \left\{ -\frac{3\sqrt{\pi}}{4} d[c_{JT}(1 - c_{JT})]^{1/2} \left(1 - \frac{2}{3}c_{JT} \right) + \frac{\lambda_0}{2} \right\} \frac{1}{\ln c_{JT}}. \qquad (21)$$

Noticeable variations of phase diagram due to random fields can also be noted in the region $c_{JT} > c_0$. As the value of d/λ_0 increases, the one-phase region of existence of the ''ferro''-phase becomes narrower, which is accompanied by an increase in the corresponding values of $T_{\mathrm{crit}}^{(2)}$ and $c_{\mathrm{crit}}^{(2)}$. In this case, the region in which the mixture undergoes the separation into two ''ferro''-phases expands to a certain extent. It should be noted that in the absence of random fields, the values of T_{crit} and c_{crit} lie near the line of second-order phase transformations for a crystal with a random distribution of ions to be mixed. Such a topology of phase boundaries leads to a change in the type of critical behavior of phase separation.[10,11] As a result (Fig. 5), the temperature dependence of the concentration difference Δc for two coexisting ''ferro'' phases near the critical temperature T_{crit} is described by the function $(1 - T/T_{\mathrm{crit}})^\beta$ with the exponent
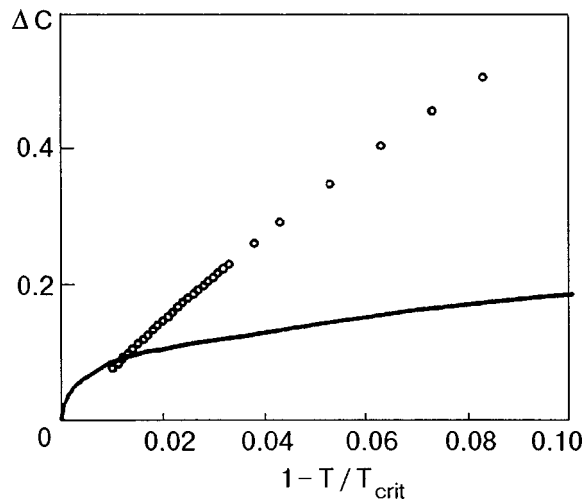
FIG. 5. Temperature dependences of the concentration difference Δc for JT ions in coexisting phases in random fields ($d/\lambda_0 = 1$ corresponds to the solid curve) and in the absence of such fields ($\bigcirc$).

FIG. 6. Phase diagram of a JT system in the presence of an additional contribution to the free energy of the solution ($W = -0.3$, 0, 0.5, 1, 1.5, and 2).

$\beta \simeq 1$ instead of the value $\beta = 0.5$ typical of the mean-field theory.[11] Such a topology of phase boundaries is responsible for ''crossover'' near Lifshitz multicritical points even in the absence of critical fluctuations and leads to a change in the critical behavior of phase separation. Figure 5 shows that we are dealing with a situation similar to that observed for a mixture of liquid isotopes ^{4}He–^{3}He, where the curve of transitions to the superfluid state for solutions enriched by ^{3}He terminates at the critical point of mixing. Random fields displace the point of phase separation from the second-order PT curve, thus restoring the mean-field shape of the limited miscibility dome.

Let us now consider possible reasons behind the change in the structure of phase diagrams under investigation from a different point of view. We primarily take into account the possibility of other (not JT) mechanisms of formation of free energy of the mixture. Such an analysis with an additional contribution of the type $\Delta F = W c_{JT}(1 - c_{JT})$ to the energy of mixing was carried out by us for JT systems with relatively weak random crystal fields ($d \ll \lambda_0$) in order to separate the corresponding effects.

Figure 6 shows the transformation of the phase diagram in the presence of additional contributions to the mixing energy of the solution, which are not associated with splitting of degenerate levels. It can be seen that the variations of the phase diagram due to an increase in the energy W are similar to a certain extent to those considered earlier for JT ions in random fields with increasing parameter d. The most pronounced difference is associated with the reduction effects for the cooperative JT transition (T_D, σ, etc.) in random fields. Thermodynamic parameters (such as heat capacity which is peculiar for random fields)[12] in one-phase regions will also display considerably different behavior.

A similar behavior is also observed for a wide class of JT systems with a structural first-order PT (see, for example, Ref. 13). In contrast to the system considered above, such systems display the coincidence of the critical point of mix-
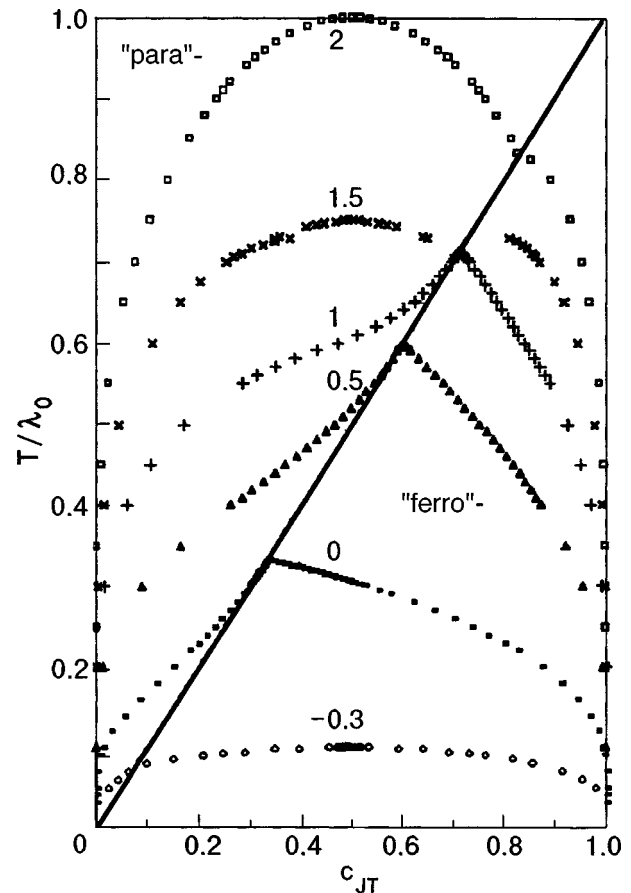
ing with the PT temperature in a pure compound with JT ions.

CONCLUSION

The analysis carried out by us here proved that limited miscibility is manifested to a certain extent in partially ordered crystal systems with Jahn–Teller ions. The variety of its possible manifestations must reflect different origin of degenerate or pseudo-degenerate states and accordingly the mechanisms of their splitting (orbital magnetism, spin–orbit interaction, etc.). Random crystal fields in systems with degenerate centers change significantly the shape of phase diagrams of the phase-separation type and lead to a number of other consequences. In this case, the same mechanism operates for all types of PT. It is associated with the tendency of JT ions at low temperatures to be in the phase with the maximum possible splitting of degenerate levels.

The results of analysis of possible instability regions for one-phase states makes it possible to predict anomalous behavior of some parameters of crystal systems, in which the equilibrium state of the JT subsystem (with cooperative interactions or random crystal fields at JT ions) is not realized in the low-temperature region in view of kinetic limitations. This primarily refers to the formation of thermodynamic properties typical of glass-like states (spin glass, Jahn–Teller glass,[12,14] etc.). The genesis of the corresponding region on

the diagram of metastable phase states with phase separation (or spinodal decomposition) regions on the equilibrium phase diagram can be traced.

*E-mail: ivanov@imp.kiev.ua
**E-mail: n.tkachev@ihte.uran.ru
***E-mail: fishman@imet.erl.e-burg.su

[1] J. L. Moran-Lopez *et al.* (Eds.), *Structural and Phase Stability of Alloys*, Plenum Press, New York (1992).
[2] G. A. Gehring, S. J. Switenby, and M. R. Wells, Solid State Commun. **18**, 31 (1976).
[3] M. A. Ivanov, V. Ya. Mitrofanov, L. D. Falkovskaya, and A. Ya. Fishman, J. Magn. Magn. Mater. **35**, 26 (1983).
[4] F. S. Ham, *Jahn–Teller Effects in Electron Paramagnetic Resonance Spectra. Electron Paramagnetic Resonance*, Plenum Press, New York (1972).
[5] J. Kanamori, J. Appl. Phys. **31**, 14S (1960).
[6] M. A. Ivanov, V. Ya. Mitrofanov, V. B. Fetisov, and A. Ya. Fishman, Fiz. Tverd. Tela (St. Petersburg) **37**, 3226 (1995) [Phys. Solid State **37**, 1774 (1995)].
[7] I. Prigogine and R. Defay, *Chemische Thermodynamik*, Deutsche Verlag für Grundstoffindustrie, Leipzig (1962).
[8] P. De Gennes, *Scaling Concepts in Polymer Physics*, Cornell Univ. Press, Ithaca (USA) (1979).
[9] G. S. Zhdanov and A. G. Khundzhua, *Lectures in Solid State Physics: Principles of Construction, Real Structure, and Phase Transformations* [in Russian], Izd. MGU, Moscow (1988).
[10] L. D. Landau and E. M. Lifshitz, *Statistical Physics* [in Russian], Nauka, Moscow (1976).
[11] M. E. Fisher, J. Stat. Phys. **75**, 1 (1994).
[12] M. A. Ivanov, V. Ya. Mitrofanov, and A. Ya. Fishman, Fiz. Tverd. Tela (Leningrad) **20**, 3023 (1978) [Sov. Phys. Solid State **20**, 1744 (1978)].
[13] P. Holba, M. A. Khilla, and S. Krupicka, J. Phys. Chem. Solids **34**, 387 (1973).
[14] F. Mehran and E. W. H. Stevens, Phys. Rev. B **27**, 2899 (1983).

Translated by R. S. Wadhwa

Interaction of nonuniform elastic waves with two-dimensional electrons in AlGaAs–GaAs–AlGaAs heterostructures

D. V. Fil'

Institute of Single Crystals, National Academy of Sciences of the Ukraine, 310001 Kharkov, Ukraine*

The interaction of a double-layer electron system in a AlGaAs–GaAs–AlGaAs heterostructure with nonuniform elastic modes localized in the GaAs layer is considered. The dependence of the interaction constant on the ratio between the thickness of the GaAs layer and the wavelength is calculated in a system with interfaces parallel to the (001) plane for waves with the wave vector directed along the [110] axis, the polarization vector lying in the $(1\bar{1}0)$ plane. It is shown that the interaction constant attains its maximum value for the wavelength of the order of the thickness of the GaAs layer. The renormalization of the velocity of elastic waves is found for the case when the electron system is under the conditions of the fractional quantum Hall effect. It is shown that for some modes, the dependence of the velocity renormalization on the wave vector is modified qualitatively upon a transition of the electron system to a state corresponding to the Halperin wave function. © *1999 American Institute of Physics.*
[S1063-777X(99)01306-7]

The method of surface acoustic waves (SAW) has been widely used recently for an analysis of dynamic parameters of two-dimensional electron layers in AlGaAs heterostructures.[1,2] Since AlGaAs possesses piezoelectric properties, SAW generate an alternating electric field. The interaction of this field with two-dimensional electrons leads to a renormalization of the velocity and attenuation of SAW. Measurements of these quantities can be used for obtaining the frequency and momentum dependence of the conductivity of the electron subsystem. The method is especially effective for an analysis of quantum Hall systems for which the conductivity depends considerably on the applied magnetic field.

The two-dimensional electron layer lies at a certain distance d_0 from the sample surface, and hence the interaction of SAW with electrons depends on the parameter qd_0 (q is the wave vector of an elastic wave). As the value of this parameter increases, the matrix elements of interaction decrease exponentially, i.e., the method is ineffective for an analysis of dynamic characteristics of the electron system for large q. In this case, a nonuniform elastic wave which is localized near the electron layer due to acoustic inhomogeneity of the heterostructure can be an alternative to SAW.

We consider the heterostructure $Al_xGa_{1-x}As$–GaAs–$Al_xGa_{1-x}As$ in which electron layers lie at the interfaces AlGaAs–GaAs as the system in which a localization of elastic wave is possible. Heterostructures of this type are used for studying quantum Hall effect in double-layer systems.[3,4] Elastic waves localized in the central layer (the wave amplitudes in the banks decreases exponentially with increasing distance from the interface) can propagate in the structure under investigation. This system was used by us earlier[5] to study the interaction of $2D$ electrons with a non-uniform transverse elastic wave with a displacement vector parallel to the interface. Here we continue the investigations started in Ref. 5 and consider nonuniform elastic waves for which the displacement vector lies in the plane determined by the wave vector and the normal to the interfaces (like SAW, these waves are polarized elliptically). It follows from the results obtained here that the interaction of such waves with electrons can be considerably stronger that for waves considered in Ref. 5.

1. MODEL GEOMETRY AND DISPERSION EQUATIONS

Let us consider a system in which a GaAs layer of thickness $2a$ is bounded by two $Al_{0.3}Ga_{0.7}As$ with thicknesses much larger than the wavelength of elastic modes. We choose interfaces parallel to the (001) plane. We direct the wave vector of the elastic mode along the [110] axis and make use of the fact that elastic moduli c_{ik} weakly depend on the Al concentration (we assume that their values are the same for the two media). Acoustic inhomogeneity of the system is determined by the difference in densities ($\rho_1 = 5.3\,\text{g/cm}^3$ for GaAs and $\rho_2 = 4.8\,\text{g/cm}^3$ for $Al_{0.3}Ga_{0.7}As$).

We consider an elastic mode with the displacement vector component

$$u_i(\mathbf{r},z,t) = u_i(z)\exp(i\mathbf{q}\mathbf{r} - i\omega_q t), \tag{1}$$

where $w_q = vq, v$ is the velocity of the elastic mode, $i = x,z$, the x-axis is chosen along the [110] direction, the z-axis is chosen along the [001] direction, and the vector $\mathbf{r}$ lies in the (001) plane. We write the wave equations for the components $u_i(z)$ in the form

$$(c_{44}\partial_z^2 - c'_{11}q^2 + \rho_\alpha\omega^2)u_x + iq(c_{12}+c_{44})\partial_z u_z = 0,$$

$$iq(c_{12}+c_{44})\partial_z u_x + (c_{11}\partial_z^2 - c_{44}q^2 + \rho_\alpha\omega^2)u_z = 0, \tag{2}$$

where $c'_{11}=0.5(c_{11}+c_{12}+2c_{44})$; $\alpha=1,2$ corresponds to the number of the medium. The solution of system (2) has the form

$$u_i^\alpha(z)=\sum_k A_{ik}^\alpha \exp(-y_k^\alpha zq),\tag{3}$$

where y_k^α are the roots of the characteristic equation

$$y^4+2b_\alpha y^2+c_\alpha=0\tag{4}$$

with

$$b_\alpha=\frac{1}{2c_{11}c_{44}}[(c_{12}+c_{44})^2+c_{11}(\rho_\alpha v^2-c'_{11})$$
$$+c_{44}(\rho_\alpha v^2-c_{44})],$$

$$c_\alpha=\frac{1}{c_{11}c_{44}}(\rho_\alpha v^2-c'_{11})(\rho_\alpha v^2-c_{44}).\tag{5}$$

If we take into account the equality of elastic moduli in the two media, the boundary conditions are reduced to the continuity of u_i and $\partial_z u_i$ at the interfaces. The localized mode corresponds to the solution vanishing for $z\rightarrow\pm\infty$. The structure of the localized solution at the banks is similar to the structure of SAW at the surface of a cubic crystal (see, for example, Ref. 6). Such a solution appears if Eq. (4) for $\alpha=2$ has no purely imaginary roots. If elastic moduli satisfy the inequality

$$(c_{12}+c_{44})^2-c_{11}(c'_{11}-c_{44})<0,\tag{6}$$

a localized solution appears for $v<c_{44}/\rho_2$. If the opposite inequality holds, the velocity of the localized mode is $v<v_{m2}$, where v_{m2} is the root of the equation $D_2(v)=b_2^2-c_2=0$ ($v_{m2}<c_{44}/\rho_2$). In the system under investigation (the values of elastic moduli will be given below), the second case is realized. For $v<v_{m2}$, Eq. (4) with $\alpha=2$ gives

$$y=\pm(\lambda\pm i\varphi),\tag{7}$$

where

$$\lambda=[(\sqrt{c_2}-b_2)/2]^{1/2},\quad \varphi=[(\sqrt{c_2}+b_2)/2]^{1/2}.\tag{8}$$

For medium 1, the solution of Eq. (2) satisfying the boundary conditions corresponds to cases when Eq. (4) has either two real and two imaginary roots, or the four imaginary roots

$$y_{1,2}=\pm\kappa=\pm(\sqrt{D_1}-b_1)^{1/2},$$
$$y_{3,4}=\pm i\xi=\pm i(\sqrt{D_1}+b_1)^{1/2},\tag{9}$$

where $D_1=b_1^2-c_1$. (The quantity κ is real-valued for $v>c_{44}/\rho_1$ and imaginary for $v_{m1}<v<c_{44}/\rho_1$, where v_{m1} is the root of the equation $D_1(v)=0$.)

Taking into account the symmetry in z, we have two types of solutions of wave equations with the given boundary conditions (we denote them as I and II)

$$u_x^p(z)=C^p f_x^p(z),\quad u_z^p(z)=iC^p f_x^p(z),\tag{10}$$

where C^p is the normalization factor, $p=$I,II. For mode I, $f_x^I(z)$ is an odd function of z and $f_z^I(z)$ is an even function. For mode II, $f_x^{II}(z)$ is odd, and $f_z^{II}(z)$ is even.
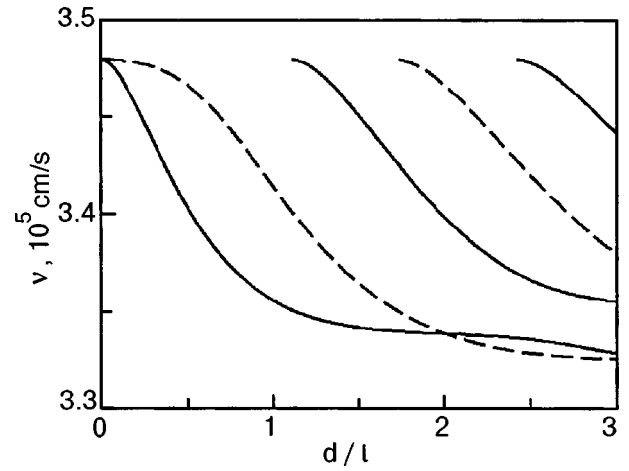

FIG. 1. Dependence of the velocities of elastic modes on the ratio of the thickness d of the central layer and the wavelength l. Solid curves correspond to type I modes and dashed curves to type II modes.

The dispersion equation for v is determined from the equality to zero of the determinant of the system of linear equations for the coefficients A_{ik}^α. The equations follow from the wave equations (2) and the boundary conditions. For mode I, the dispersion equation has the form

$$R_1\tanh\kappa qa\tan\xi qa+R_2\tanh\kappa qa$$
$$+R_3\tan\xi qa+R_4=0,\tag{11}$$

For mode II, we have

$$R_1\coth\kappa qa\cot\xi qa-R_2\coth\kappa qa$$
$$+R_3\cot\xi qa-R_4=0,\tag{12}$$

where

$$R_1=(\kappa m_\kappa+\xi m_\xi)(\varphi m_\lambda-\lambda m_\varphi);$$

$$R_2=m_\varphi m_\xi(\lambda^2+\varphi^2)-\varphi\xi(m_\varphi^2+m_\lambda^2)$$
$$-\kappa m_\kappa(\xi m_\varphi-\varphi m_\xi);$$

$$R_3=-m_\varphi m_\kappa(\lambda^2+\varphi^2)+\varphi\kappa(m_\varphi^2+m_\lambda^2)bf+\xi m_\xi(\varphi m_\kappa$$
$$-\kappa m_\varphi);$$

$$R_4(\kappa m_\xi-\xi m_\kappa)(\varphi m_\lambda+\lambda m_\varphi);$$

$$m_\kappa=\frac{\kappa(c_{12}+c_{44})}{c_{11}\kappa^2-c_{44}+\rho_1 v^2};\quad m_\xi=\frac{\xi(c_{12}+c_{44})}{-c_{11}\xi^2-c_{44}+\rho_1 v^2};$$

$$m_\lambda=\frac{\lambda c_{44}(R-1)}{c_{12}+c_{44}};\quad m_\varphi=\frac{\varphi c_{44}(R+1)}{c_{12}+c_{44}};$$

$$R=\left(\frac{c_{11}(\rho_2 v^2-c'_{22})}{c_{44}(\rho_2 v^2-c_{44})}\right)^{1/2}.$$

The result of numerical solution of Eqs. (11) and (12) for the parameters $c_{11}=12.3$, $c_{12}=5.7$, $c_{44}=6.0$ (all of them in the units of 10^{11} dyne/cm^2) are presented in Fig. 1 as a function of the ratio of the central layer thickness ($d=2a$) and the wavelength l of the elastic mode. The curves in the figure show that the system is characterized by two activationless modes (of types I and II). A decrease in the wavelength gives
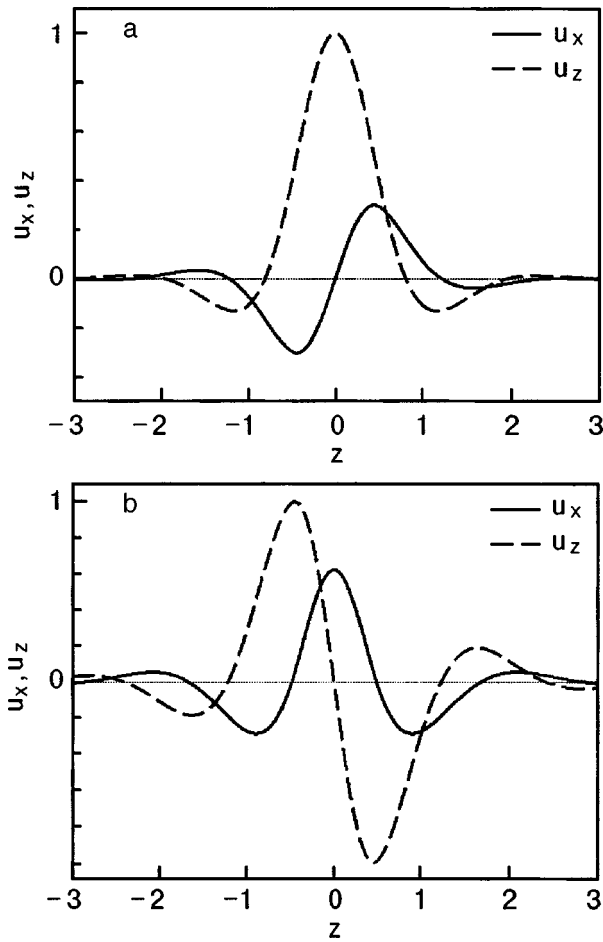
FIG. 2. Dependence of the displacement vector component (in relative units) on z (in the units of wavelength) for $d/l=1$ for type I mode (a) and type II mode (b).
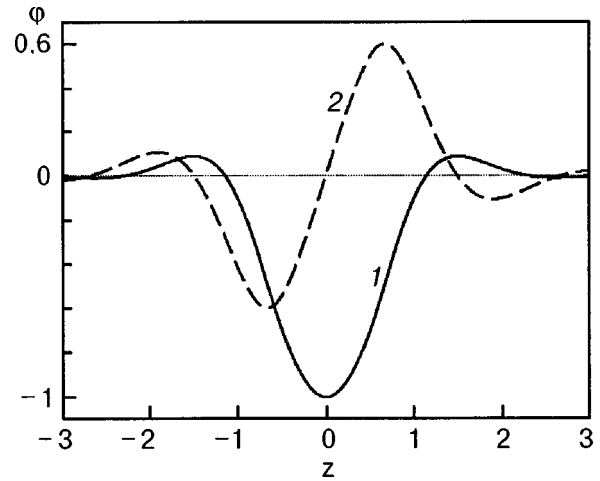

FIG. 3. Dependence of the electric potential (in relative units) on z (in the units of wavelength) for $d/l=1$ for type I mode (curve 1) and type II mode (curve 2).

rise to additional modes whose frequencies lie above the gapless modes. We shall consider below only the results for activationless modes. The quantities $f_i^p(z)$ are written in the form of simple analytic functions of z, whose coefficients have a cumbersome dependence on q and v. We do not write here their explicit expressions. By way of illustration, Fig. 2 shows the plots of the functions $u_x(z)$ and $u_z(z)$ for $d/l=1$.

2. PIEZOELECTRIC INTERACTION CONSTANTS

Let us calculate the renormalization of velocity of the nonuniform elastic mode determined by the interaction with the double-layer electron system with the coordinates $z_{1(2)}=\pm a$ of the layers. We shall use the approach similar to that developed by Knäbchen et $al.$[7] We write the Hamiltonian of elastic oscillations in terms of the creation and annihilation operators for phonons (b^+,b):

$$H_u=\sum_{\mathbf{q}} \omega_{\mathbf{q}}(b_{\mathbf{q}}^+ b_{\mathbf{q}}+\tfrac{1}{2}). \qquad (13)$$

We choose the Hamiltonian of interaction between electrons and phonons in the form

$$H_{\text{int}}=\frac{1}{\sqrt{S}}\sum_{\mathbf{q},m} \int d^2 r g_{qm}\Psi_{\mathbf{r}m}^+ \Psi_{\mathbf{r}m} e^{i\mathbf{qr}}(b_{\mathbf{q}}+b_{-\mathbf{q}}^+), \qquad (14)$$

where $\Psi^+(\Psi)$ are the creation (annihilation) operators for electrons, m the number of the electron layer, and S the area of the layers.

In order to find the matrix elements g_{qm}, we write the interaction of an elastic wave with electrons in the form

$$H=\sum_m \int d^2 r \varphi_{\mathbf{r}m}\Psi_{\mathbf{r}m}^+ \Psi_{rm}, \qquad (15)$$

where $\varphi_{\mathbf{r}m}$ is the scalar potential of the electric field generated by the elastic mode in the layer m. The value of φ is determined by the solution of the Poisson equation

$$\Delta\varphi=-(4\pi/\varepsilon)\beta_{i,jk}\partial_i u_{jk}, \qquad (16)$$

where ε is the dielectric constant, $\beta_{i,jk}$ is the piezoelectric tensor, and u_{jk} the strain tensor. If we choose the coordinate axes along the directions [100], [010], [001], the tensor $\hat{\beta}$ for the system under investigation has nonzero components (having the same value denoted by β) for $i\neq j\neq k$. The substitution of (10) into (16) (taking into account a transition to a rotated system of coordinates) gives the following equation for the Fourier component of electric potential:

$$(\partial_z^2-q^2)\varphi_q(z)=i(4\pi\beta/\varepsilon)C^p g^p(z), \qquad (17)$$

where

$$g^p(z)=q^2 f_z^p(z)-2q\partial f_x^p(z). \qquad (18)$$

We assume that the constants ε and β are the same for the entire system. In this case, the boundary conditions are reduced to the requirement of continuity of $\varphi_q(z)$ and $\partial_z\varphi_q(z)$ at the interfaces. The solution of Eq. (17) taking into account the boundary conditions has the form

$$\varphi_q(z)=i(4\pi\beta/\varepsilon)C^p\chi_p(z), \qquad (19)$$

where $\chi_{\text{I}}(z)$ is an even function and $\chi_{\text{II}}(z)$ an odd function. We omit cumbersome analytic expressions for the function $\chi_p(z)$. By way of illustration, Fig. 3 shows the dependences

$\varphi_q(z)$ for $d/l=1$ (we used the values of the constants C^p calculated below).

In order to determine the normalization constant, we write the displacement components in the form

$$u_i(\mathbf{r},z,t)=\sum_{\mathbf{q}} C^p f_i^p(z)e^{i\mathbf{q}\mathbf{r}}(b_{\mathbf{q}}+b_{-\mathbf{q}}^+) \qquad (20)$$

and substitute expansion (20) into the expression for elastic energy. Equating the result and Eq. (13), we obtain the following expression for the quantity C^p:

$$C^p(Sv I^p)^{-1/2}, \qquad (21)$$

where

$$I^p=4q\int_0^{\infty} dz\rho(z)(|f_x^p(z)|^2+|f_z^p(z)|^2). \qquad (22)$$

Note that the dependence on q in the expression for I^p (and hence for C^p) can be reduced to the dependence on the parameter qa.

Going over in (19) to operators b and substituting the obtained expression into Eq. (15), we obtain the following expression for matrix elements in (14):

$$g_{qm}=i(4\pi\beta e/\varepsilon\sqrt{v I^p})\chi_p(z_m). \qquad (23)$$

The renormalization of the velocity Δv of the elastic mode and the damping factor Γ determined by interaction (14) satisfy the equation

$$\frac{\Delta v}{v}-i\frac{\Gamma}{q}=\frac{1}{vq}g_{mq}^* D_{mm'}(q,\omega_q)g_{m'q}, \qquad (24)$$

where $D_{mm'}$ is the density-density response function for electrons. In the random-phase approximation, the quantities D are defined as

$$\hat{D}(q,\omega)=[\hat{I}-\hat{D}^{(0)}(q,\omega)\hat{V}(q)]^{-1}\hat{D}^{(0)}(q,\omega), \qquad (25)$$

where

$$V_{mm'}(q)=\frac{2\pi e^2}{\varepsilon q}[\delta_{mm'}+(1-\delta_{mm'})e^{-qd}] \qquad (26)$$

are the Fourier components of Coulomb interaction and $D^{(0)}$ is the density–density response function for the system without the Coulomb interaction. The quantities $D^{(0)}$ are connected with the longitudinal electron conductivity through the relation

$$D_{mm'}^0(q,\omega)=-\frac{iq^2}{\omega e^2}\sigma_{xx}^{mm'}(q,\omega), \qquad (27)$$

were $\sigma^{11}=\sigma^{22}$ and $\sigma^{12}=\sigma^{21}$ are the conductivity components diagonal and nondiagonal in the layers. Here and below, we consider the case of two equivalent layers. It should be noted that in the case of electron gas, the nondiagonal components in the layers vanish in the random-phase approximation. For a composite fermion gas that will be considered in the next section, these quantities may have nonzero values due to statistical interaction between layers.

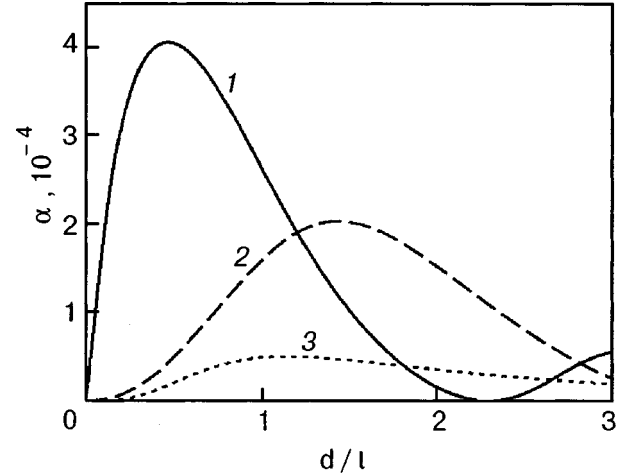Substituting expressions (23), (25)–(27) into (24), we obtain

FIG. 4. Dependence of the piezoelectric coupling constant on the parameter d/l. Curve 1 corresponds to α_+ for type I mode, curve 2 to α_- for type II mode, and curve 3 to α_- for the transverse mode.[5]

$$\frac{\Delta v}{v}-i\frac{\Gamma}{q}=\alpha_+\frac{-i\sigma_{xx}^+(q,vq)/\sigma_M^+}{1+i\sigma_{xx}^+(q,vq)/\sigma_M^+}$$
$$+\alpha_-\frac{-i\sigma_{xx}^-(q,vq)/\sigma_M^-}{1+i\sigma_{xx}^-(q,vq)/\sigma_M^-}, \qquad (28)$$

where $\sigma_{xx}^{\pm}=\sigma_{xx}^{11}\pm\sigma_{xx}^{12}$, $\sigma_M^{\pm}=v\varepsilon/2\pi[1\pm\exp(-\delta)]$, and

$$\alpha_{\pm}=\frac{4\pi\beta^2}{\varepsilon v^2 I^p}\frac{|\chi_p(a)\pm\chi_p(-a)|^2}{1\pm\exp(-qd)}. \qquad (29)$$

The functions $\alpha_{\pm}$ are analogs of the constants of piezoelectric coupling introduced in an analysis of interaction of SAW with two-dimensional electrons. It can be seen from formula (29) that only the coefficient α_+ differs from zero for a mode of type I and only the coefficient α_- for type II.

Figure 4 shows the dependences of α_+ for mode I and α_- for mode II on the ratio d/l. We used the parameters $\beta=4.5\times10^4$ dyne$^{1/2}$/cm and $\varepsilon=12.5$. For the sake of comparison, Fig. 4 also shows the dependence of α_- on d/l for the case analyzed in Ref. 5 (transverse mode polarized in the plane (001)). It can be seen from the plots that the interaction of electrons with elastic modes polarized elliptically in a plane defined by the wave vector and a normal to the interfaces is much stronger than the interaction with the transverse mode. It should be noted, however, that the case considered in Ref. 5 has the advantage that only one localized mode exists (if the thickness of the central layer is not too large as compared to the wavelength), its frequency being lower than that of the bulk modes. (For the case considered here, bulk transverse modes with the displacement vector directed along [110] have a frequency lower than the frequencies of modes I and II.)

3. RENORMALIZATION OF THE VELOCITY OF ELASTIC MODE UNDER PHASE TRANSITIONS IN THE ELECTRON SYSTEM WITH FRACTIONAL QUANTUM HALL EFFECT

We apply the results obtained in the previous sections to analyze the possibility of observing phase transitions in double-layer electron systems under the conditions of the

fractional quantum Hall effect. We shall describe the Hall system by using the model of composite fermions (the corresponding model for a double-layer system was developed by Lopez and Fradkin).[8] In this model, the Hall system is described as a system of composite Fermi particles carrying a fictitious statistical charge and the flux of statistical gauge field. In the case of a double-layer system, we introduce two types of statistical charges corresponding to two layers and two types of gauge fields. In the general case, a composite quasiparticle carries field fluxes of two types, namely, an even number ψ of field flux quanta corresponding to its statistical charge, and an integral number s of field flux quanta corresponding to statistical charges of quasiparticles in the adjacent layers. For $s \neq 0$, such a model corresponds to states described by the Halperin wave function.[9] In the framework of the approach developed by Lopez and Fradkin,[8] the state with $s \neq 0$ can be interpreted as a phase with statistical interaction between the layers.

In the mean field approximation, statistical fields partially screen the external magnetic field B. The effective magnetic field is defined as

$$B_{\rm eff} = B[1 - \nu(\psi + s)], \tag{30}$$

where ν is the filling factor per layer. The fractional quantum Hall effect corresponds to filling factors for which the value of $B_{\rm eff}$ corresponds to the integral number N of filled Landau levels:

$$\nu = \frac{N}{N(\psi + s) \pm 1}, \tag{31}$$

where the upper sign corresponds to $B_{\rm eff} > 0$ and the lower sign to $B_{\rm eff} < 0$. It can be seen from formula (31) that a fixed filling factor can correspond to different sets of the parameters ψ and s (for different phases).

In an analysis of incompressible states (corresponding to filling factors (31)), it is convenient to express σ_{xx} in terms of the components of polarization tensor $\hat{\Pi}$:

$$\sigma_{xx}^{+(-)} = -\frac{i}{\omega} \Pi_{xx}^{+(-)} = -\frac{i\omega}{q^2} \Pi_{00}^{+(-)}, \tag{32}$$

where $\Pi^{+(-)} = \Pi^{11} \pm \Pi^{12}$; Π^{11}, Π^{12} are the diagonal and nondiagonal components of polarization tensor in layers. Using the approach developed in Ref. 5, we obtain the following expression for the quantities $\Pi_{00}^{+(-)}$:

$$\Pi_{00}^{+(-)} = -\frac{e^2 q^2}{2\pi\omega_c} \frac{S_0}{\Delta^{+(-)}}, \tag{33}$$

where

$$S_0 = \Sigma_0 - \frac{m^* - m_b}{m^* N} [\Sigma_0(\Sigma_2 + N) - \Sigma_1^2], \tag{34}$$

$$\Delta^{+(-)} = [1 - (\psi \pm s)\Sigma_1]^2 - (\psi \pm s)^2 \Sigma_0(\Sigma_2 + N)$$

$$\qquad - \frac{m^* - m_b}{m^* N} F, \tag{35}$$

$$F = \Sigma_2 + N + (\omega/\omega_c)^2 S_0, \tag{36}$$

$$\Sigma_j = [\sin(\beta_{\rm eff})]^j e^{-x}$$

$$\times \sum_{n=0}^{N-1} \sum_{m=N}^{\infty} \frac{n!}{m!} \frac{x^{m-n-1}(m-n)}{(\omega/\omega_c)^2 - (m-n)^2} [L_n^{m-n}(x)]^{2-j}$$

$$\times \left[(m-n-x)L_n^{m-n}(x) + 2x \frac{dL_n^{m-n}(x)}{dx} \right]^j. \tag{37}$$

In formulas (33)–(37), $\omega_c = 2\pi n_0/m^* N$ is the effective cyclotron frequency, $x = (q\lambda_{\rm eff})^2/2$, where $\lambda_{\rm eff} = (N/2\pi n_0)^{1/2}$ is the effective magnetic length $L_n^{m-n}(x)$ is the generalized Laguerre polynomial, m^* the effective mass of composite fermions, m_b the band mass of electrons, and n_0 is the average number density for electrons. Substituting (32) and (33) into (28), we obtain

$$\frac{\Delta v}{v} = \alpha_+ \frac{E_q^+ S_0}{\Delta_+ - E_q^+ S_0} + \alpha_- \frac{E_q^- S_0}{\Delta_- - E_q^- S_0}, \tag{38}$$

where $E_q^{+(-)} = (e^2 q/\varepsilon\omega_c)[1 \pm \exp(-qd)]$ (the damping factor Γ is equal to zero in this case).

Let us consider by way of an example the filling factor $\nu = 1/5$. In the absence of statistical interaction between layers, the filling corresponds to the parameters $\psi = 4$, $s = 0$, and $N = 1$. As the layers become closer to one another, a transition to the phase with $\psi = 2$, $s = 2$, and $N = 1$ becomes possible. It can be seen from formulas (34)–(37) that in this case the first term in formula (38) does not change. Consequently, the quantity Δv for type I mode is conserved under such a transition. On the contrary, for type II mode a jump in phase velocity is observed since in this case the dependence on Δ_- which is a function of the difference $\psi - s$ is preserved in formula (38). The jump must be observed upon a change in the separation between layers, which is apparently difficult to realize in experiments. However, the effect can be observed indirectly while measuring the dependence of Δv on the wave vector. If we use the value of velocity for the filling factor $\nu = 1$ as the bare value (the value of Δv for $\nu = 1$ is also determined by formula (38) for $m^* = m_b$, $\psi = s = 0$, $N = 1$), the above dependence differs qualitatively for $s = 0$ and $s \neq 0$. This is illustrated in Fig. 5 which shows the dependence of $\Delta v/v$ (measured from the velocity value for $\nu = 1$) on reciprocal wavelength. We used for calculations the parameters $n_0 = 10^{11}\,{\rm cm}^{-2}$, $d = 500\,{\rm \AA}$, $m_b = 0.07 m_e$, $m^* = 4 m_b$ (m_e is the electron mass).

It can be seen from formula (31) that a situation is possible when a phase transition occurs with sign reversal of $B_{\rm eff}$. For example, for $\nu = 2/7$, the phase without statistical interaction between the layers corresponds to $\psi = 4$, $s = 0$, $N = 2$ ($B_{\rm eff} < 0$), while in the presence of such an interaction a phase with $\psi = 2$, $s = 1$, $N = 2$ ($B_{\rm eff} > 0$) is possible. In this case, the jump in phase velocity takes place for a mode of type I as well as a mode of type II. However, the qualitative dependence $\Delta v(q)$ changes insignificantly under such a phase transition. The plots illustrating the last statement are not given here.

The type-I mode for which the peak of interaction lies in a region corresponding to longer waves than for a type II mode can be used for indirect observation of the dependence of effective magnetic length on filling factor. Figure 6 shows
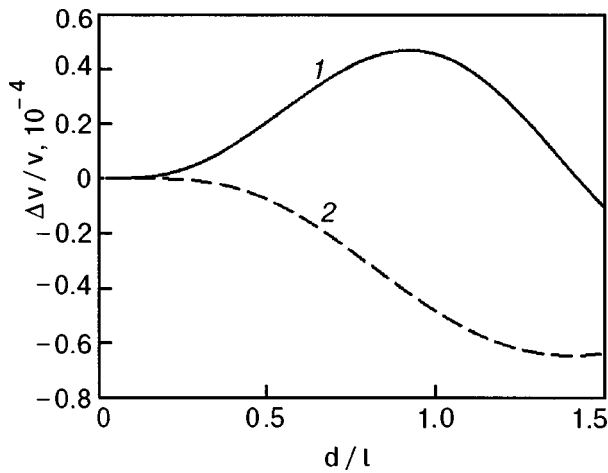
FIG. 5. Dependence of the velocity renormalization on reciprocal wavelength for type II mode for the filling factor $\nu=1/5$. Curve *1* corresponds to the phase $\psi=4$, $s=0$ and curve *2* to the phase $\psi=2$, $s=2$.

the dependences $\Delta v(d/l)$ (the value of Δv is measured from the value of velocity for $\nu=1$) for $s=0$ for filling factors $\nu=1/3, 2/5, 3/7$ ($\psi=2$ and $N=1,2,3$ respectively). It can be seen from Fig. 6 that the quantity Δv oscillates as a function of $1/l$. The decrease in the period of oscillations as ν approaches $1/2$ reflects the increase in effective magnetic length for such a sequence of filling factors.
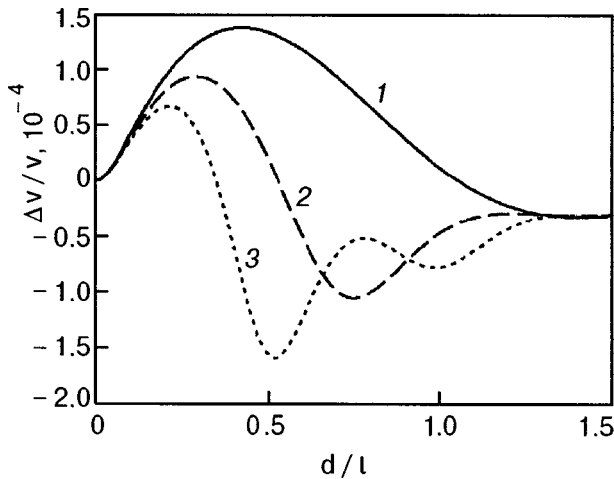

FIG. 6. Dependence of the velocity renormalization on reciprocal wavelength for type I mode: Curve *1* corresponds to $\nu=1/3$, curve *2* to $\nu=2/5$, and curve *3* to $\nu=3/7$.

Thus, we have analyzed theoretically the interaction of double-layer electron system formed at the edges of a wide quantum well in the AlGaAs–GaAs–AlGaAs heterostructure with nonuniform elastic modes localized in the central layer of the heterostructure and having the elliptic polarization in the plane determined by the direction of the wave vector of a wave and the normal to the interface. The dependence of the coupling constant determined by the piezoelectric mechanism on the ratio of the width of the quantum well and the wavelength is found. It is shown that the coupling constant increases with decreasing wavelength and attains its maximum value for a wavelength coinciding in order of magnitude with the width of the GaAs layer. The position of the peak is determined by the type of the nonuniform mode. The effect considered here can be used for studying dynamic parameters of two-dimensional electron systems for large wave vectors, i.e., in the case when the interaction with the surface acoustic wave is suppressed exponentially due to the finite depth of the electron layer in the heterostructure. The renormalization of the phase velocity of nonuniform elastic modes is calculated for a double-layer electron system under the conditions of the fractional quantum Hall effect. It is shown that the dependence of the velocity renormalization on the wave vector may change qualitatively upon a transition of the Hall system to a state described by the Halperin wave function.

[1] A. Wixforth, J. P. Kotthaus, and G. Weinmann, Phys. Rev. Lett. **56**, 2104 (1986); A. Wixforth, J. Scriba, M. Wassermeier *et al.*, Phys. Rev. B **40**, 7874 (1989).

[2] R. L. Willett, M. A. Paalanen, and R. R. Ruel *et al.*, Phys. Rev. Lett. **65**, 112 (1990); M. A. Paalanen, R. L. Willett, and P. B. Littlewood *et al.*, Phys. Rev. B **45**, 11342 (1992); R. L. Willett, R. R. Ruel, K. W. West, and L. N. Pfeiffer, Phys. Rev. Lett. **71**, 3846 (1993); R. L. Willett, R. R. Ruel, and M. A. Paalanen *et al.*, Phys. Rev. B **47**, 7344 (1993); R. L. Willett, K. W. West, and L. N. Pfeiffer, Phys. Rev. Lett. **75**, 2988 (1995); *ibid.* **78**, 4478 (1997).

[3] Y. W. Suen, L. W. Engel, and M. B. Santos *et al.*, Phys. Rev. Lett. **68**, 1379 (1992).

[4] G. S. Boebinger, H. W. Jiang, L. N. Pfeiffer, and K. W. West, Phys. Rev. Lett. **64**, 1793 (1990); J. P. Eisenstein, G. S. Boebinger, and L. N. Pfeiffer *et al.*, Phys. Rev. Lett. **68**, 1383 (1992); S. Q. Murphy, J. P. Eisenstein, and G. S. Boebinger *et al.*, Phys. Rev. Lett. **72**, 728 (1994).

[5] D. V. Fil', Fiz. Nizk. Temp. **25**, 376 (1999) [Low Temp. Phys. **25**, 274 (1999)] (D. V. Fil' cond-mat/9812166).

[6] J. Farnell in *Physical Acoustics. Principles and Methods* (ed. by W. Mason and R. Thurston), vol. VI, Academic Press, New York (1968–1970).

[7] A. Knäbchen, Y. B. Levinson, and O. Entin-Wohlman, Phys. Rev. B **54**, 10696 (1996).

[8] A. Lopez and E. Fradkin, Phys. Rev. B **51**, 4347 (1995).

[9] B. I. Halperin, Helv. Phys. Acta **56**, 75 (1983).

Translated by R. S. Wadhwa

BRIEF COMMUNICATIONS

Kinetic properties of the HTSC compound Ag–Bi2223

B. A. Merisov, G. Ya. Khadjai, M. A. Obolensky

Kharkov State University, 310077 Kharkov, Ukraine*

N. T. Cherpak

Institute of Radiophysics and Electronics, National Academy of Sciences of the Ukraine, 310085 Kharkov, Ukraine

P. Haldar and D. Hazelton

Intermagnetics General Corporation, Latham, NY12110, USA

Thermal conductivity $\lambda(T)$ and resistivity $\rho(T)$ of the HTSC compound Ag–Bi2223 ($T_c \simeq 107$ K; $\Delta T_c \simeq 2$ K) produced by the Intermagnetics General Corporation (USA) were measured in the temperature intervals 4.2–300 K and T_c–300 K respectively. Away from the SC transition, the values of $\lambda(T)$ and $\rho(T)$ are determined by the silver content. For $T > 60$ K, irregular thermal conductivity oscillations are observed in the vicinity of the superconducting transition against the background of the dependence $\lambda(T)$ typical of silver. The position and amplitude of the oscillations are not affected by temperature cycling. A sharp minimum on the $\lambda(T)$ dependence, whose depth is much larger than the estimated contribution of thermal conductivity of Bi2223 to the thermal conductivity of the system, is observed at T_c. © *1999 American Institute of Physics.* [S1063-777X(99)01406-1]

Temperature dependences of thermal conductivity λ and resistivity ρ of the superconducting composite material Ag–HTSC are studied.

The investigated material was in the form of a ribbon of cross-section 3.68×0.206 mm^2 produced by the Intermagnetics General Corporation (USA). A mixture of silver powder and the HTSC compound Bi2223 having volume fractions of 70 and 30% respectively were packed in a silver casing. The initial purity of silver was 99.95%. The sample was about 5 cm long. The resistivity $\rho(T)$ was measured by the four-probe method, while the thermal conductivity $\lambda(T)$ was measured by using the *steady axial heat* flow technique. The charge and thermal fluxes were directed along the ribbon. The thermometers were attached to the sample for $\lambda(T)$ measurement at the same points as the potential leads for $\rho(T)$ measurement, and hence the geometrical factors coincide in both cases. The temperature dependence of ρ was measured in the interval between T_c and 300 K with an average error not exceeding 0.5%. The dependence $\lambda(T)$ was measured in the interval 4.2–300 K with an average error 2%.

The superconducting transition temperature T_c, determined from the position of the $d\rho/dT$ peak, was found to be 107 K with a transition width of about 2 K. The $\rho(T)$ dependence of the composite is a linear function of temperature in the interval 108–300 K, and $\rho(300\,\text{K}) = 3.87 \times 10^{-8}$ $\Omega \cdot$m, which is about twice as large as the data available in literature for pure silver.[1]

The $\lambda(T)$ dependence of the composite in the investigated temperature range is typical for the thermal conductivity of pure silver (Fig. 1). The thermal conductivity peak lies at 15 K, which is in accord with the data obtained in Refs. 2 and 3, but the thermal conductivity at the peak is about half the value given in these works. Above 100 K, the thermal conductivity of the composite depends weakly on temperature and amounts to about 210 W/(m·K). In this region, the thermal conductivity of silver samples with different degrees of purity is close to 430 W/(m·K) (see, for example, Ref. 4), which is almost double the value obtained by us. Thus, the characteristic values of $1/\rho$ and λ are about half the values given in the literature for pure silver. The measured values of conductivity indicate that the outer silver shell occupies about half the cross-sectional area of the ribbon. The remaining silver is in the form of interlayers between HTSC particles.

The obtained results can be discussed conveniently by using the Lorentz function

$$L(T) = \lambda(T)\rho(T)/T. \qquad (1)$$

Figure 2 shows the values of $L(T)$ for silver having various degrees of purity, calculated by using the data presented in Refs. 1–4, as well as for the composite material studied in this work. It can be seen that the $L(T)$ curves for silver with different degrees of purity are close to each other and tend to the Sommerfeld value $L_0 = 2.45 \times 10^{-8}$ WΩ/K^2 upon an increase in temperature, which is typical of metallic

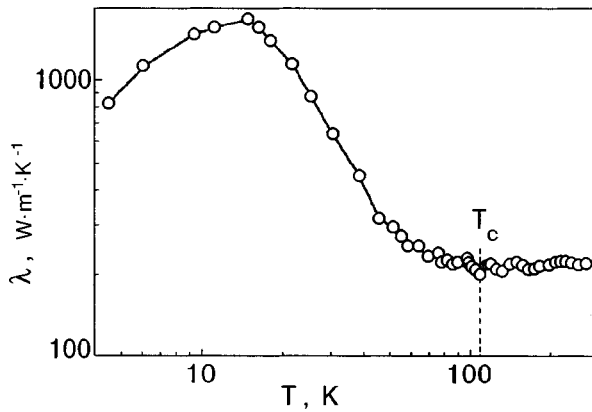FIG. 1. Temperature dependence of the thermal conductivity of the composite Ag–Bi2223.

FIG. 3. Thermal conductivity (curve *1*) and electric resistivity (curve *2*) of the composite Ag–Bi2223 in the vicinity of the superconducting transition.

conductivity at temperatures higher than the Debye temperature. For the composite, $L(T) > L_0$, and increases with temperature. This is probably due to the additional contribution to $\rho(T)$ (1) associated with the presence of two components, especially with the scattering at interfaces.

At low temperatures, the thermal conductivity of quite pure metals is described by the Wilson formula[5]

$$T/\lambda(T) = \rho_0/L_0 a T^3, \tag{2}$$

which is also applicable to the composite investigated by us in the temperature range 4.2–46 K. Here, ρ_0 is the residual resistivity of the composite and a is a constant. The value of ρ_0 in formula (2) is equal to $1.14 \times 10^{10} \, \Omega \cdot m$. Thus, the ratio $\rho(300\,K)/\rho(4.2\,K)$ characterizing the purity of the silver matrix is close to 300.

At $T > 60\,K$, irregular oscillations of thermal conductivity of the composite are observed against the background of the $\lambda(T)$ dependence typical of pure metals in this temperature range (Fig. 3). The oscillation amplitude is about 10% of the thermal conductivity in this temperature range, i.e., several times larger than the characteristic values of the thermal conductivity of bismuth-based HTSC (see, for example, Refs. 6 and 7). Multiple temperature cycling (from 4.2 to 300 K) does not affect the obtained results.
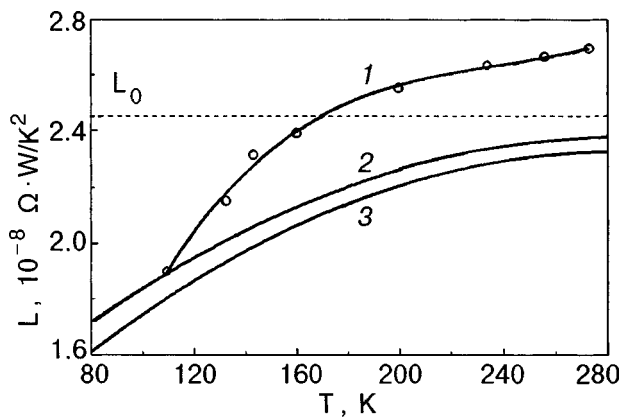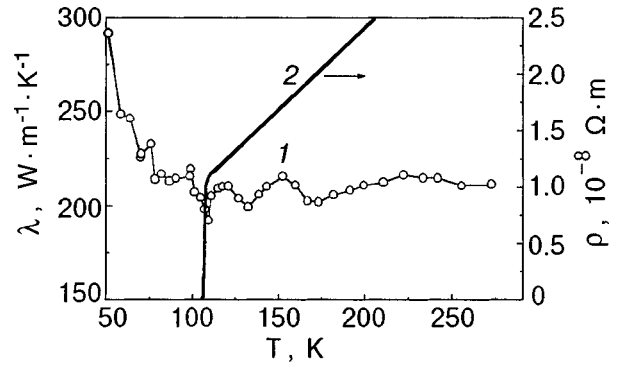
It can be assumed that such a behavior of thermal conductivity is associated with the emergence of the effect of Andreev reflection of quasiparticles in a mesoscopic system of nonsuperconductor–superconductor junctions in the investigated heterophase system.

On the temperature scale, the deepest and sharpest thermal conductivity minimum coincides with T_c. Such a sharp decrease in thermal conductivity and electrical resistivity indicates the elimination of superconducting electrons from the heat transport process. Such a behavior of $\lambda(T)$ and $\rho(T)$ in the vicinity of T_c was indicated by us earlier.[8]

Analogous behavior of some physical characteristics was also observed in several superconducting composites, including HTSC. In Refs. 9 and 10, such a behavior of heat capacity, linear expansion coefficient, and thermal conductivity of Y-based HTSC was attributed by the authors to lattice instability caused by migration of superstoichiometric oxygen. For the superconducting composite Nb–Cu, such a behavior of thermal conductivity was observed at 50–60 K,[11] i.e., far from the superconducting transition ($T_c = 9.1$ K). Simultaneously, a decrease in the internal friction and a splitting of the natural frequency of flexural vibrations of the sample into three components was observed upon a decrease in temperature.

Apparently, such structural instabilities are characteristic of spatially inhomogeneous materials including high-temperature superconductors and composites, and may be manifested near the superconducting transition or away from it.

Note that the thermal expansion of Bi-based HTSC has a considerable anisotropy[12,13] while the thermal expansion coefficient is about half its value for silver. The data presented in Refs. 12–15 can provide a very rough estimate of the stresses emerging in the composite sample upon cooling from 300 to 100 K. Such an estimate leads to a value of the order of 10^8 Pa. Such anisotropic stresses may stimulate the emergence of structural instabilities in the investigated two-phase composite, which may also lead to the observed non-monotonic behavior of thermal conductivity.

FIG. 2. Temperature dependence of the Lorentz function of composite Ag–Bi2223 (curve *1*) and silver of different purities (curves *2, 3*).[1,3]

*E-mail: boris.a.merisov@univer.kharkov.ua

[1] F. Pawlek and D. Hogalla, Cryogenics **6**, 14 (1966).

[2] H. M. Rosenberg, Philos. Trans. R. Soc. London, Ser. A **247**, 441 (1955).

[3] G. K. White, Proc. Phys. Soc. London **A66**, 844 (1953).

[4] C. Y. Ho, R. W. Powell, and P. E. Liley, J. Phys. Chem. Ref. Data, **3**, Suppl. No. 1 (1974).

[5] J. M. Ziman, *Electrons and Phonons*, Clarendon Press, Oxford (1960).

[6] S. D. Peacor and C. Uher, Phys. Rev. B **39**, 11 559 (1989).

[7] M. F. Crommie and A. Zettl, Phys. Rev. B **41**, 10 978 (1990); *ibid.* **43**, 408 (1991).

[8] B. A. Merisov, G. Ya. Khadjai, M. A. Obolenskiĭ, and O. A. Gavrenko, Fiz. Nizk. Temp. **14**, 643 (1988) [Sov. J. Low Temp. Phys. **14**, 355 (1988)].

[9] B. Ya. Sukharevskiĭ, E. O. Tsybul'skiĭ, N. E. Pis'menova *et al.*, Fiz. Nizk. Temp. **14**, 1108 (1988) [Sov. J. Low Temp. Phys. **14**, 608 (1988)].

[10] B. A. Merisov, G. Ya. Khadjaĭ, O. A. Gavrenko, and A. P. Voronov, Fiz. Nizk. Temp. **16**, 389 (1990) [Sov. J. Low Temp. Phys. **16**, 216 (1990)].

[11] O. A. Gavrenko, B. A. Merisov, and G. Ya. Khadjaĭ, Metallofizika i Noveĭshie Tekhnologii **15**, 1215 (1996).

[12] I. A. Gospodarev, A. P. Isakina, A. I. Prokhvatilov *et al.*, Fiz. Nizk. Temp. **16**, 673 (1990) [Sov. J. Low Temp. Phys. **16**, 396 (1990)].

[13] R. H. Arendt, M. F. Garbauskas, C. A. Meyer *et al.*, Physica C **182**, 73 (1991).

[14] G. W. Kaye and T. H. Laby (Eds.), *Tables of Physical and Chemical Constants*, Longman, Green and Co., London (1962).

[15] J. Dominec, C. Laermans, A. Vanelstraete, and V. Plechacek, *High-T_c Superconductor Materials* in *Proceedings 14th EMRS Symposium* [Ed. by H.-U. Habermeier, E. Kaldis, and J. Schoenes], North-Holland (1990).

Translated by R. S. Wadhwa